

Energy Conversion in Plasmas out of Local Thermodynamic Equilibrium: A Kinetic Theory Perspective

Mahmud Hasan Barbhuiya

Dissertation Submitted to
The Eberly College of Arts and Sciences
at West Virginia University
in partial fulfillment of the requirements
for the degree of

Doctor of Philosophy
in
Physics

Paul Cassak, Ph.D., Chair
Earl Scime, Ph.D.
Weichao Tu, Ph.D.
Michael Shay, Ph.D.

Department of Physics and Astronomy

Morgantown, West Virginia, USA
2023

Keywords: plasmas, kinetic theory, energy conversion, non-local thermodynamic
equilibrium, magnetic reconnection
Copyright 2023 Mahmud Hasan Barbhuiya

Abstract

Energy Conversion in Plasmas out of Local Thermodynamic Equilibrium: A Kinetic Theory Perspective

Mahmud Hasan Barbhuiya

The study of energy conversion in collisionless plasmas that are not in local thermodynamic equilibrium (LTE) is at the leading edge of plasma physics research. Plasma constituents in such systems can exhibit highly structured phase space densities that deviate significantly from that of a Maxwellian. A standard approach has emerged in recent years for investigating energy conversion between bulk flow and thermal energy in collisionless plasmas using the non-LTE generalization of the first law of thermodynamics. The primary focus is placed on pressure-strain interaction (PS) term, with a particular emphasis on its non-LTE piece called Pi – D. Recent studies have found that Pi – D can be negative, which makes its identification as collisionless viscous heating counterintuitive. A kinetic understanding of Pi – D has been limited. We argue that the non-LTE generalization of the first law of thermodynamics and subsequent attempts to extend thermodynamics overlooks the kinetic aspects associated with phase space densities having arbitrary shapes that can deviate significantly from a Maxwellian. Only changes in work due to compression that changes the zeroth moment of the phase space density, *i.e.*, the number density, and Pi – D and heat flux which change the second moment, *i.e.*, effective temperature are considered by the non-LTE generalization of the first law of thermodynamics. However, it remains agnostic to energy conversion associated with changes to any higher moment of the phase space density. We address these limitations by first developing a kinetic understanding of Pi – D and introducing an alternative decomposition of the PS term in Cartesian coordinates which separates the physics of converging/diverging flows from shear deformation. We further find that in magnetic field-aligned coordinates, the PS term can be decomposed into eight groups of terms, each corresponding to a different physical mechanism. Lastly, we develop a first-principles theory of the energy conversion associated with all higher moments of the phase space density. Using particle-in-cell simulations of a well understood non-LTE system, *i.e.*, two-dimensional antiparallel magnetic reconnection, we first examine the decompositions of PS term in both Cartesian and magnetic field-aligned coordinates. This enables us to identify the predominant mechanisms contributing to positive and negative PS terms during reconnection, thereby facilitating the interpretation of numerical and observational data. Additionally, simulation results reveal that energy conversion associated with higher-order moments can be locally significant by being a substantial fraction of the internal energy and even surpassing it in regions characterized by strongly non-LTE phase space densities. These results may be useful in numerous plasma settings, such as heliospheric, planetary, and astrophysical plasmas, and for other non-LTE phenomenon such as turbulence, shocks and wave-particle interactions.

Dedication

I dedicate this dissertation to my wife, Dipshikha Das, who for reasons beyond me, has been my unwavering companion for the last decade (and more), whom I have known for half of our lives, and who played a pivotal role in enabling me to pursue my childhood dream of becoming a scientist!

Acknowledgments

My Ph.D. journey was not linear which, as I have discovered in later years, is a “feature” not a “bug”. Thus, firstly I would like to express my gratitude to the Department of Physics and Astronomy for allowing individuals like me to switch fields and advisors. This leads me to my final (Ph.D.) advisor Prof. Paul Cassak who decided to take me under his wings half a decade ago, even though he was not looking to expand his group. I have not thanked him enough so here it is again - thanks, Paul, for your guidance, for amusing my random queries, be it about plasma physics, or science in general or philosophical, and for allowing me to work the way I prefer which is most likely not the best and healthy way of working (but I do tend to take breaks and I am quoting you here “wander in the forests somewhere” whenever I feel the need). To Prof. Weichao Tu, (who incidently was my first teacher of anything plasma physics and taught a great magnetohydrodynamics course back in the spring of 2018), for being generous with her time and serving on my committee. To my committee member Prof. Earl Scime, for not allowing me to join your experimental group, but then being an excellent guide (pun intended!) by teaching me some “real” (experimental) plasma physics through our collaborations and talks over the years in the hallway of the third floor of White Hall. Finally, to my committee member, Prof. Michael Shay, for his conscientious thoughts on our collaborative work, and for being the voice of god (which is an inside joke!) when needed.

I am greatly indebted to Sameer Patel, with whom I have engaged in numerous thought-provoking discussions about physics, while we were both starting our journeys of trying to switch majors from engineering to physics. This leads to special thanks to MOOCs (Massive Open Online Courses) such as edX, and Coursera which were a tremendous help as I was teaching myself college-level physics and mathematics.

At the Department of Physics and Astronomy, I would like to express my sincere thanks to Dr. Ben Woods, for our long conversations and discussions about our respective work, which has helped in broadening my knowledge of physics beyond plasma physics, and for being a good friend. I also thank Dr. Raju Bhai KC for his invaluable technical assistance. I am grateful to Dr. Amber Kiana and Dr. Ashok Choudhary for their companionship and encouragement throughout this journey.

I extend my appreciation to office-mates Dr. Milton Arencibia and Xingzhi Lyu where the former’s guidance and knowledge of plasma physics in my first few years were of tremendous help, and the latter’s barrage of questions has kept me on my toes, and who has served as my guinea pig at times when dealing with confirmation bias in data analysis. I would also like to thank my newer office-mate Hasith Perera and Regis John for helping refresh my knowledge. Much thanks goes to Dr. Subash Adhikari for extending my knowledge by providing his know-how of turbulence and by being there whenever I needed help venturing into this still newer field of study.

The faculty members at our department have all played a crucial role in my academic development. I express my sincere gratitude to Prof. Duncan Lorimer, Prof. Tudor Stanescu (for actually introducing me to magnetic reconnection), and Prof. Aldo Romero. Additionally, I am deeply grateful to Prof. Art Weldon and

the late Prof. Leo Golubovic and , who generously helped me solve complex mathematical problems when I got stuck doing analytical derivations, and for always entertaining my curiosity.

Prof. Jan Egedal deserves special acknowledgment for generously providing the data used in my ever first article and engaging in insightful conversations during our limited interactions, whenever and wherever we meet. I am also grateful to Dr. Vadim Roytershteyn for his ideas and expertise in our collaborations.

The one and only Dr. Marc Swisdak deserves special mention for his substantial contributions in tackling p3d coding challenges, and so does Dr. Haoming Liang for being my second mentor as I was starting and whenever Paul was busy. I am thankful to Dr. Matt Argall for teaching me a thing or two about “real” measurements of space plasmas and being an excellent collaborator. I am also grateful to Woo-Sun and Rebecca from NERSC for providing help with esoteric challenges which have a habit of spontaneously popping up.

Special thanks goes to Viola and Miranda in the main office at our department who have always been there and have provided invaluable support (on multiple occasions) with navigating the treacherous waters that is academic paperwork.

I am immensely grateful to my wife for her unwavering support and understanding throughout this endeavor, mostly during the last half year as I progressed towards my defense. I did not make it easy for being around me and thus her constant presence has been invaluable for keeping my sanity and strength. I extend my deepest appreciation to my mother who was my first teacher and taught me algebra (among other things mathematics) back in school, my father, and my brother, as well as other family members, for their love, encouragement, and belief in my abilities.

I am humbled and honored to have had such incredible support from all these individuals, without whom my achievements would not have been possible, so thank you all!

This dissertation work was supported by Department of Energy, NASA, and the National Science Foundation. Computational resources were provided by NERSC.

Table of Contents

List of Tables	x
List of Figures	xi
1 Introduction	1
1.1 Motivation behind the work	1
1.2 Temperature and thermodynamic equilibrium	5
1.3 Kinetic theory - a brief primer	8
1.3.1 Phase space and its discretization for large N particles	8
1.3.2 Time evolution of the distribution function	13
1.3.3 Maxwell's Equations in kinetic theory	16
1.3.4 Entropy in kinetic theory	18
1.4 Fluid description of plasmas from kinetic theory	19
1.4.1 Fluid equations	20
1.4.2 Energy time evolution equations	21
1.4.3 Magnetohydrodynamics (MHD) - a primer	23
1.5 Magnetic reconnection	27
1.5.1 Magnetic reconnection - where does it take place?	28
1.5.2 Basic theory of magnetic reconnection	30
1.5.3 Collisionless reconnection	39
1.6 Motivation for studying non-LTE energy conversion in reconnection	44
1.7 Outline of the dissertation	48
2 Numerical simulations	51
2.1 General description of the simulations	51
2.2 Normalized units of simulated quantities	52
2.2.1 Governing equations and normalization	52
2.3 System setup	55
2.3.1 Plasma system at initialization	55
2.3.2 Simulation parameters at initialization	58
2.4 Kinetic entropy-based quantities	61
2.4.1 Velocity-space grid optimization	61
2.4.2 Velocity-space kinetic entropy density flux	62
2.4.3 Velocity-space thermal kinetic entropy density flux	64
2.4.4 Relative entropy density	68
2.4.4.1 Implementation in p3d	68
2.4.4.2 Subtlety with relative entropy calculation	70
2.4.4.3 Lagrangian time derivative of relative entropy per particle	73
2.5 Dynamics of the reconnecting system	74

3	Pressure-Strain Interaction: I. On Compression, Deformation, and Implications For Pi-D	79
3.1	Introduction	79
3.2	An Alternate Decomposition of Pressure-Strain Interaction	87
3.3	Physical Interpretation of Pressure-Strain Interaction	89
3.3.1	Fluid Description of the Pressure-Strain Interaction	91
3.3.2	Kinetic Description of PDU	92
3.3.3	Kinetic Description of $\text{Pi} - D_{\text{shear}}$	97
3.4	Kinetic Interpretation of Normal Deformation and Implications for the Sign of $\text{Pi} - D$	102
3.5	Discussion and Conclusions	106
4	Pressure-Strain Interaction: II. Decomposition in Magnetic Field-Aligned Coordinates	111
4.1	Introduction	111
4.2	Theory	114
4.2.1	Pressure-Strain Interaction in Magnetic Field-Aligned Coordinates	114
4.2.2	Example of Torsion for a Helical Magnetic Field	119
4.3	Physical Picture of the Pressure-Strain Interaction in Field-Aligned Coordinates	121
4.3.1	Parallel Flow Compression/Expansion: $-PS_1 = -P_{\parallel}(\nabla_{\parallel}u_{\parallel})$	123
4.3.2	Perpendicular Flow Compression/Expansion: $-PS_2 = -P_{\kappa\kappa}(\nabla_{\kappa}u_{\kappa}) - P_{nn}(\nabla_nu_n)$	124
4.3.3	Parallel Flow Sheared in the Perpendicular Direction: $-PS_3 = -P_{b\kappa}(\nabla_{\kappa}u_{\parallel}) - P_{bn}(\nabla_nu_{\parallel})$	124
4.3.4	Perpendicular Flow Shear: $-PS_4 = -P_{b\kappa}(\nabla_{\parallel}u_{\kappa}) - P_{bn}(\nabla_{\parallel}u_n) - P_{\kappa n}(\nabla_{\kappa}u_n + \nabla_nu_{\kappa})$	125
4.3.5	Perpendicular Geometrical Compression/Expansion: $-PS_5 = u_{\kappa}P_{b\alpha}W_{\alpha\kappa}$	126
4.3.6	Torsional Geometrical Compression: $-PS_6 = -u_{\kappa}P_{n\alpha}W_{\alpha\tau}$	127
4.3.7	Parallel Geometrical Shear: $-PS_7 = -u_{\parallel}P_{\kappa\alpha}W_{\alpha\kappa}$	129
4.3.8	Torsional Geometrical Shear: $-PS_8 = u_nP_{\kappa\alpha}W_{\alpha\tau}$	130
4.4	Discussion and Conclusions	131
5	Pressure-Strain Interaction: III. Particle-in-Cell Simulations of Magnetic Reconnection	135
5.1	Introduction	135
5.2	Numerical Simulation Setup	139
5.3	Simulation results - Cartesian Coordinates	142
5.3.1	Overview	142
5.3.2	Decomposition of Pressure-Strain Interaction in Cartesian Coordinates	143
5.3.3	Largest Contributions to Pressure-Strain Interaction in Cartesian Coordinates	146

5.4	Simulation Results - Magnetic Field-Aligned Coordinates	150
5.4.1	Overview	150
5.4.2	Decomposition of Pressure-Strain Interaction in Field-Aligned Coordinates	153
5.4.3	Largest Contributions to the Pressure-Strain Interaction in Field-Aligned Coordinates	157
5.5	Discussion and Conclusions	163
6	Energy Conversion in higher-order moments in plasmas	172
6.1	Introduction	172
6.2	Theory	175
6.3	Simulation Results	180
6.4	Discussion	183
6.5	Supplemental Material for <i>Quantifying Energy Conversion in Higher Order Phase Space Density Moments in Plasmas</i>	186
6.5.1	Derivation of Kinetic Entropy Evolution Equation	186
6.5.2	Derivation of Generalized Work Term	189
6.5.3	Derivation of Generalized Energy Term	190
6.5.4	Derivation of Generalized Heat Term	191
6.5.5	Derivation of Relative Energy Per Particle Rate for a Bi- Maxwellian Plasma	194
6.5.6	Numerical Simulation Methodology	197
6.5.7	Additional Comments on the Relation to Previous Work . . .	199
7	Conclusion	207
7.1	Summary and discussion	207
7.2	Future work and concluding remarks	214
A	Electron heating due to non-Maxwellian ring distributions	217
A.1	Introduction	217
A.2	Theory	224
A.3	Simulations	229
A.4	Methods and Results	233
A.4.1	Presence of ring distributions	233
A.4.2	Parametric dependence of ring distribution major and minor radii	236
A.4.3	Relation of ring distributions to temperature and magnetic field profiles	243
A.4.4	Confirmation that ring distributions are caused by remagne- tization	248
A.5	Discussion and Applications	250
A.6	Conclusions	258

B	Kinetic Entropy-Based Measures of Distribution Function Non-Maxwellianity: Theory	264
B.1	Kaufmann and Paterson Kinetic Entropy-based Non-Maxwellianity	264
B.2	Theory of the Kaufmann and Paterson Non-Maxwellianity	266
B.2.1	Basic Properties of Kaufmann and Paterson Non-Maxwellianity	266
B.2.2	Kaufmann and Paterson Non-Maxwellianity for Two Beams	269
B.2.3	Kaufmann and Paterson Non-Maxwellianity for Bi-Maxwellian Distributions	271
B.2.4	Kaufmann and Paterson Non-Maxwellianity for Egedal Dis- tributions	272
B.2.5	Kaufmann and Paterson Non-Maxwellianity for Ring Distri- butions	277
C	Kinetic Entropy in an EDR - Theory, Observations, and Simulations of Ki- netic Entropy in a Magnetotail Electron Diffusion Region	280
C.1	Review of Kinetic Entropy with a Uniform Velocity Space Grid	280
C.2	Simulation	284
C.3	Results	291
C.3.1	Comparison between Observations and the PIC Simulation	291
C.3.2	Kinetic Entropy: Application	293
C.4	Data Availability	298

List of Tables

A.1	Numerical parameters for two sets of simulations with varying (top) upstream total temperature $T_{TOT,up}$ and (bottom) upstream number density n_{up} . l_x and l_z are system sizes along \hat{x} and \hat{z} , respectively, w_0 is the initial current sheet thickness, Δx is the grid scale along \hat{x} and \hat{z} , and Δt is the time step.	231
A.2	Data from the fitting method described in Sec. A.4.2 for all simulations. The first column gives the value being varied, and $n_r, v_{\perp 0}$, and v_{Th} are the ring density, major radius, and minor radius. The σ values are standard deviations from the mean from cuts in the $\perp 1$ and $\perp 2$ directions, and 95% err is the error calculated using 95% confidence bounds from the fit.	237
A.3	Upstream plasma parameters from the simulations using the method described in Sec. A.4.2. The first column gives the value being varied, $B_{up,e}$ is the upstream magnetic field, n_{up} is the upstream density, and $T_{e,up}$ is the upstream temperature at the EDR edge. The last two columns give the theoretical predictions for the major radius $v_{\perp 0}$ and minor radius v_{Th} based on the upstream values using Eqs. (A.2) and (A.3), respectively.	239

List of Figures

1.1	Sketch of a one-dimensional Maxwellian distribution function, where the black curve shows the distribution of particles as a function of velocity.	7
1.2	Sketch of a discretized phase space where the red lines show the uniformly spaced grid with phase space area $\Delta x \Delta v$ for a 2-D phase space. Green circles show the N particles populating this phase space. For illustrative purposes, there are phase space bins shown with few or no particles.	9
1.3	Sketch of a discretized phase space bin with particles (shown by green circles) moving in the phase space from location 1 denoted by (x, v) to location 2 denoted by $(x + \Delta x, v + \Delta v)$, with the phase space bin at location 2 losing some particles due to sinks (denoted by missing green-colored particles) and gaining few particles due to sources (denoted by dark green circles) that can abruptly change f	14
1.4	Sketch of the 2-D geometry of reconnection, tilted in the $x - y$ plane. Please refer to the text for a detailed description.	33
1.5	Sketch of the 2-D geometry of anti-parallel reconnection. Please refer to the text for a description.	39
2.1	Plot of the magnetic field perturbation of the form given by Eq. (2.8) shown in panel (a) and Eq. (2.9) shown in panel (b) that seed an X-O line pair in lower current sheet at $(x, y) = (9.6, 1.6)$ and upper current sheet at $(x, y) = (3.2, 4.8)$ when simulation is initialized, shown by a sketch in panel (c).	59
2.2	Plot of the total energy density (panel (a)) and change in total energy density (panel (b)), for the whole simulation domain, as a function of time.	60
2.3	A 1-D cut (taken at the lower X-line) of the kinetic entropy density for electron s_e centered around the lower X-line at $t = 0$ displaying its profile. In black is shown the simulated s_e for $\Delta v_e = 1.33$, and in red dashed is shown the theoretical profile.	62
2.4	A 1-D cut (taken at the lower X-line) of the z -component of velocity-space kinetic entropy density flux $\mathcal{J}_{v,z}$ for electrons centered around the lower X-line at $t = 0$ displaying its profile. In black is shown the simulated curve and in red dashed is shown the theoretical profile, given by Eq. (2.13).	64

2.5	1-D cut (taken and centered around the lower X-line) of the z -component of velocity-space thermal kinetic entropy density flux $\mathcal{J}_{\text{th},v,z}$ for electrons at $t = 0$. Panels (a) and (b) show $\mathcal{J}_{\text{th},v,z}$ simulated from our implementation in <code>p3d</code> and post-processed, respectively. The green curve in panel (a) shows the profile of the weight of the macroparticles, the red dashed line denotes the theoretical value and the black curves are the simulated values in panels (a) and (b). In panel (c), the difference between the simulated $\mathcal{J}_{\text{th},v,z}$ shown in panel (a) and (b) is plotted, where we observe less than a 1% error when comparing the two methods of obtaining $\mathcal{J}_{\text{th},v}$	66
2.6	1-D cut (taken and centered around the lower X-line) of relative entropy for electrons at $t = 0$ using $\text{PPG} = 25,600$. Panel (a) shows relative entropy density $s_{v,\text{rel}}$ and (b) shows relative entropy per particle $s_{v,\text{rel}}/n$ simulated from our implementation in <code>p3d</code> . The green curve in panel (a) shows the the non-uniform macroparticles weight, red dashed line denotes the theoretical value and the black curves denote the simulated values in panels (a) and (b). Panels (c) and (d) repeat panel (b) but for $\text{PPG} = 6400$ and $\text{PPG} = 400$ simulations, respectively.	71
2.7	Plots of 1-D cuts (taken and centered around the lower X-line) for electrons at $t = 0$. In black, red, and green are simulated s_v/n , the simulated $s_{v,\mathcal{E}}/n$, and the computed value of $s_{v,\text{rel}}/n$, respectively.	72
2.8	Plots of $d(s_{v,\text{rel}})/dt$ for electrons at $t = 13$ are shown. Panel (a) and (b) show 2D plots centered around the lower X-line, with the former displaying data from <code>p3d</code> implementation of relative entropy density and the latter data obtained via post-processing. Panel (c) and (d) show overplots of the 1-D cuts (taken and centered at the X-line) of data shown in panel (a) (in black color) and (b) (in red color), with former showing the horizontal cut and the latter showing the vertical cut.	75
2.9	Plot of reconnection rate E and its instantaneous time rate of change dE/dt as a function of time in black and red, respectively, for the lower current sheet.	76
2.10	1-D cuts of $\text{Pi} - \text{D}$ for electrons (taken and centered at the lower X-line), with panel (a) showing the horizontal cut and panel (b) showing the vertical cut. In both panels, various smoothing procedures are overplotted with the raw simulation data (black curves) and are color-coded as described in the legend.	78

3.1	Sketch of representative contributions to the pressure-strain interaction in the fluid description. Black shapes are the initial fluid elements, and bold arrows show the bulk flow directions. The dashed arrows map the change between initial and final shapes of the fluid elements. (a) Pressure dilatation (red), showing compression, (b) normal deformation (blue), and (c) shear deformation (green). Panels (a) and (b) are essentially copies of Figure 1 from Ref. (Del Sarto & Pegoraro, 2018); panel (c) is new. Modified with permission from Figure 1 of “Shear-induced pressure anisotropization and correlation with fluid vorticity in a low collisionality plasma,” by Daniele Del Sarto and Francesco Pegoraro, Monthly Notices of the Royal Astronomical Society, 475 , 181 (2018).	90
3.2	Sketches showing the physical interpretation of PDU, <i>i.e.</i> , heating via converging flow, in kinetic theory, ignoring body forces and collisions for simplicity. Magenta ellipses denote a 2D slice of the phase space density f in the (v_x, v_z) plane given by bi-Maxwellian distributions with $P_{\parallel} > P_{\perp}$, where x is a perpendicular direction and z is parallel. (a) Phase space densities at initial time $t = t_0$ at three locations at and near $z = 0$. The vertical bulk flow velocity u_z , denoted by the magenta arrows, is converging in the parallel direction. (b) The phase space density at $z = 0$ at a slightly later time $t = t_0 + dt$. The phase space densities labeled 1, 2, and 3 in panel (a) evolve to their associated positions labeled in panel (b). The phase space density at this time is broader in v_z , implying an increase in thermal energy density. Note, $\text{Pi} - \text{D}$ is positive for this case. (c) and (d) are analogous for the same phase space density except with converging bulk flow in x . There is an increase in the thermal energy density in the phase space density at $x = 0$ at $t = t_0 + dt$ in panel (d). Interestingly, $\text{Pi} - \text{D}$ is negative for this case.	94
3.3	Sketch illustrating the kinetic theory explanation of why $\text{Pi} - \text{D}_{\text{shear}}$ leads to heating or cooling. (a) Array of sketches at locations in position space (x, z) near the origin at the initial time t_0 . Each sketch contains a phase space density f in the (v_x, v_z) plane in blue and red, where blue represents relatively low f and red represents relatively high f . Such phase space densities have $P_{xz} < 0$. The placement of the phase space density in each axis system reveals its bulk flow \mathbf{u} , denoted for each f by the magenta arrow. The flow profile has a representative form $(u_x, u_z) = (0, x)$. (b) Sketch of the phase space density at the origin at a slightly later time $t = t_0 + dt$. The portions of the phase space densities in (a) labeled 1 and 2 evolve to make up the portions of the phase space densities in (b) labeled 1 and 2, respectively. For this flow profile, there is a net displacement of particles away from the velocity space origin, implying an increase in thermal energy density.	98

3.4	Sketch illustrating the kinetic theory explanation of why (a) symmetric shear (pure straining motion) can lead to heating/cooling, while (b) anti-symmetric shear (rigid body rotation) cannot. In each sketch, the grid in x and z denotes physical positions in the environment of the origin $(x, z) = (0, 0)$. Each red and blue box denotes a phase space density f with a negative P_{xz} in the (v_x, v_z) plane at the location in question. The local bulk flow \mathbf{u} is denoted for each f with a magenta arrow. The flow profiles are (a) $(u_x, u_z) = (z, x)$ and (b) $(u_x, u_z) = (z, -x)$	101
4.1	Representative sketches of the eight sets of terms in the decomposition of the pressure-strain interaction in field-aligned coordinates. Black arrows represent the magnetic field \mathbf{B} . Green and blue arrows denote the curvature and binormal directions, respectively. Red arrows denote the bulk flow \mathbf{u} . The eight sketches represent (a) parallel flow compression $-PS_1$, (b) perpendicular flow compression $-PS_2$, (c) shear of parallel flow in the perpendicular direction $-PS_3$, (d) shear of perpendicular flow in the perpendicular and/or parallel directions $-PS_4$, (e) perpendicular geometrical compression $-PS_5$, (f) torsional geometrical compression $-PS_6$, (g) parallel geometrical shear $-PS_7$, and (h) torsional geometrical shear $-PS_8$	122
5.1	Two-dimensional profiles of the (a)-(f) six independent elements of the electron pressure tensor \mathbf{P} , (g)-(i) three components of bulk electron velocity \mathbf{u} , (j)-(l) three components of the magnetic field \mathbf{B} , and (m)-(r) six non-zero elements of the strain-rate tensor $\nabla\mathbf{u}$, as labeled in each panel. Representative magnetic field projections in the xy plane are in black. [Associated dataset available at http://dx.doi.org/10.5281/zenodo.7117619].	142
5.2	Pressure-strain interaction for electrons in a reconnection simulation. (a) The pressure-strain interaction $-\mathbf{P} : \mathbf{S}$. (b) Pressure dilatation $-\mathcal{P}(\nabla \cdot \mathbf{u})$ and (c) $\text{Pi} - \text{D}$, giving the compressible and incompressible parts. (d) PDU and (e) $\text{Pi} - \text{D}_{\text{shear}}$, giving the flow converging/diverging and flow shear parts. The dotted-line in (a) is the path along which 1D cuts are taken in Figs. 5.3 and 5.6. [Associated dataset available at http://dx.doi.org/10.5281/zenodo.7117619].	144
5.3	Pressure-strain interaction along the 1D path shown in Fig. 5.2(a). L_0 is the distance along the dotted path from the left. $-\mathbf{P} : \mathbf{S}$ is in black, PDU is in red, and $\text{Pi} - \text{D}_{\text{shear}}$ is in blue. The shading marks the regions of negative (blue) and positive (red) pressure-strain interaction. [Associated dataset available at http://dx.doi.org/10.5281/zenodo.7117619].	149

5.4	For the same data as in Fig. 5.1, 2D profiles of the (a)-(f) six independent elements of the electron pressure tensor \mathbf{P} and (g)-(i) three components of bulk electron velocity \mathbf{u} in field-aligned coordinates. The magnetic field \mathbf{B} is plotted again in (j)-(l) for convenience. Representative magnetic field projections in the xy plane are in black. [Associated dataset available at http://dx.doi.org/10.5281/zenodo.7117619].	151
5.5	Decomposition of the pressure-strain interaction $-(\mathbf{P} \cdot \nabla) \cdot \mathbf{u}$ for electrons in field-aligned coordinates classified according to their physical causes. Bulk flow compression in the (a) parallel $-PS_1$ and (b) perpendicular $-PS_2$ directions. Bulk flow shear for (c) parallel flow varying in the perpendicular direction $-PS_3$, (d) perpendicular flow varying in the perpendicular direction $-PS_{4,a}$, and (e) perpendicular flow varying in the parallel direction $-PS_{4,b}$. Geometrical compression terms due to (f) perpendicular flow $-PS_5$ and (g) torsion $-PS_6$. Geometrical shear terms due to (h) parallel flow $-PS_7$ and (i) torsion $-PS_8$. [Associated dataset available at http://dx.doi.org/10.5281/zenodo.7117619].	154
5.6	Pressure-strain interaction along the 1D cut shown as the dotted path in Fig. 5.2(a). L_0 is the distance from the left along the dotted path. In both panels, the pressure-strain interaction $-\mathbf{P} : \mathbf{S}$ is in black. (a) Contribution due to each $-PS_j$ term, with compression terms in red and shear terms in blue. (b) The pressure-strain interaction contribution $-\mathbf{P} : \mathbf{S}_{u_{\parallel}}$ dependent on u_{\parallel} (blue) and the pressure-strain interaction contribution $-\mathbf{P} : \mathbf{S}_{\mathbf{u}_{\perp}}$ dependent on u_{κ} and u_n (red). [Associated dataset available at http://dx.doi.org/10.5281/zenodo.7117619].	160
5.7	Sketch of the physical mechanisms contributing to the pressure-strain interaction in a magnetic reconnection region electron diffusion region (EDR) during the reconnection onset phase. In-plane projections of the magnetic field \mathbf{B} are in black and gray, and the in-plane electron bulk flow \mathbf{u}_e is in red. The green rectangle denotes the EDR. The ellipses in the red color palette denote regions of positive pressure-strain interaction (a contribution to heating), and the blue ellipses denote negative pressure-strain interaction (a contribution to cooling). The colored dashed arrows illustrate the physical mechanism causing the non-zero pressure-strain interaction in each location. . . .	164
6.1	Schematic showing energy conversion channels according to their impact on the phase space density f_{σ} . The initial f_{σ} is depicted as Maxwellian for illustrative purposes on the left. The final f_{σ} is to their right. The descriptions of the changes in f_{σ} are to their right. . .	179

6.2	Electron energy conversion in a PIC simulation of magnetic reconnection. (a) Out-of-plane current density J_z , with projections of magnetic field lines and segments of electron velocity streamlines overlaid in black and orange, respectively. (b) Electron entropy-based non-Maxwellianity $\bar{M}_{KP,e}$. Time rates of change per particle of (c) work $d\mathcal{W}_e/dt$, (d) internal energy $d\bar{\mathcal{E}}_{e,int}/dt$, and (e) relative energy $d\bar{\mathcal{E}}_{e,rel}/dt$. (f) $\log_{10}[(d\bar{\mathcal{E}}_{e,rel}/dt)/(d\bar{\mathcal{E}}_{e,int}/dt)]$. 1D cuts of the terms in panels (c)-(e) in the (g) x and (h) y directions. (i)-(l) Reduced electron phase space density $f_e(v_x, v_z)$ at locations denoted by the colored x's at the top left of the plots corresponding to the x's in panel (b) along a streamline.	181
6.3	Sketch illustrating energy conversion from Eq. (6.10). Arrows show conversion channels between work (blue), heat (pink), energy (orange), and collisions (green), with standard channels in black and relative channels in red. The light blue dashed arrow signifies how the relative terms couple to thermodynamic terms.	184
A.1	(a) Line plot of \mathcal{M} from Eq. (A.7) as a function of $r = v_{\perp 0}/v_{Th}$. (b) Contour plot of T_{\perp} from Eq. (A.10) as a function of r and v_{Th} for a ring population plus a Maxwellian core population assuming $n_M = n_r$ and $v_{Th,M} = v_{Th}$	228
A.2	rEVDFs in the $v_{\perp 1} - v_{\perp 2}$ plane (where velocities are given in units of the normalized Alfvén speed c_{A0}) for simulations with (a) - (e) varying $T_{TOT,up}$ and (f) - (j) varying n_{up} . The title of each panel gives its background temperature or density as appropriate, the position $x - x_0$ where the rEVDF is measured relative to the X-line, and the time t . For all panels, $z - z_0 = 0$	234
A.3	1D cuts of the rEVDF from Fig. A.2(f) for the simulation with $n_{up} = 0.2$ (black solid curve). The red solid curve is the best fit to three Maxwellians. The cuts are (a) $f(v_{\perp 1}, v_{\perp 2}=0)$ and (b) $f(v_{\perp 1}=0, v_{\perp 2})$	237
A.4	Ring distribution (a) and (c) major radius $v_{\perp,0}$ and (b) and (d) minor radius v_{Th} from simulations with varying (a) and (b) upstream temperature $T_{TOT,up}$ and (c) and (d) upstream density n_{up} . Data in black (with error bars) are from the simulations as given in Table A.2, and data in red are from the theoretical predictions in Eqs. (A.2) and (A.3). Note that the vertical axes of each panel have a different range.	240
A.5	Comparison between predicted electron temperatures $T_{e,\perp}, T_{e,\parallel}$ and $T_{e,eff}$ (red lines) and the simulation results (black lines with error bars). (a)-(c) are for the simulations with varying $T_{TOT,up}$, and (d)-(f) are for varying n_{up} . Note that the vertical axes of each panel has a different range.	242

A.6	Profiles of plasma parameters downstream of the reconnection site. (a) 2D plot of electron temperature $T_{e,\text{eff}}$ for the $T_{TOT,up} = 0.2$ simulation at $t = 38$. Horizontal cuts through the X-line as a function of $x - x_0$ of (b) perpendicular electron temperature $T_{e,\perp}$, (c) electron temperature anisotropy $A_{e,\perp}$, (d) reconnected magnetic field B_z , and (e) horizontal velocity V_{ex} for the simulations with varying $T_{TOT,up}$. Panels (g) to (j) repeat (b) to (e), but for the simulations with varying n_{up} . Panel (f) shows T_e for the $n_{up} = 0.2$ simulation at $t = 38$. The vertical blue lines highlight the shoulder in the reconnected magnetic field B_z for the $T_{TOT,up} = 0.2$ and $n_{up} = 0.2$ simulations.	244
A.7	(a) Ratio of the magnetic field radius of curvature R_c to the electron gyroradius ρ_{bfs} based on the bulk flow speed as a function of $x - x_0$ in a horizontal cut through the X-line for the $n_{up} = 0.2$ simulation at $t = 38$. The horizontal red dashed line at $R_c/\rho_{\text{bfs}} = 1$ is where electrons are expected to remagnetize. The vertical dashed red line marks the $x - x_0$ location where this condition is met. (b) ρ_{bfs} vs. $x - x_0$ for the same simulation, with the horizontal dashed line marking the value of ρ_{bfs} where electrons remagnetize.	249
B.1	Plot of the Kaufmann and Paterson non-Maxwellianity $\bar{M}_{KP,biM}$ for a bi-Maxwellian distribution function $f_{biM}(\vec{v})$ as a function of the ratio of perpendicular to parallel temperature T_{\perp}/T_{\parallel} . The black line uses a linear horizontal scale on the bottom axis, and the red line uses a logarithmic horizontal scale on the top axis over a wider range of T_{\perp}/T_{\parallel} to show that it diverges for small and large T_{\perp}/T_{\parallel}	272
B.2	Kinetic entropy density s_{Eg} and Kaufmann and Paterson non-Maxwellianity $\bar{M}_{KP,Eg}$ for an Egedal distribution function from Eq. (B.24) and Eq. (B.29) assuming $n/n_{\infty}=0.805$ and $T_{\infty} = 0.08 B_{\infty}^2/4\pi k_B n_{\infty}$. (a) and (d) are contour plots of s_{Eg} and $\bar{M}_{KP,Eg}$, respectively, as a function of $b = B/B_{\infty}$ and $\Phi = e\phi_{\parallel}/k_B T_{\infty}$. (b) and (e) are cuts of these as a function of b for five representative values of Φ . (c) and (f) are cuts of these as a function of Φ for five representative values of b . . .	276
B.3	Analogous to Fig. B.2, except plotted as a function of n/n_{∞} and $b = B/B_{\infty}$ upon inversion of Eq. (B.23). The shaded regions in (a) and (d) correspond to parameters for which the inversion gives values of Φ below 0 or above 80, and are removed from the plot.	277
C.1	Out of plane magnetic field B_M from simulations (a) with and (b) without an initial guide field of $B_g = -0.36 \text{ nT} = 0.03B_0$. The separatrices are thick black curves and the thick black line in (b) is our selected virtual spacecraft trajectory. [Associated dataset available at https://doi.org/10.5281/zenodo.5807744].	290

C.2	Comparison between MMS observations (left) and a PIC simulation (right) of a magnetotail EDR encounter. MMS observations are shown over an extended region to provide context and comparison to previous results (see text). The gold rectangle highlights the EDR and region of overlap with simulation. Comparisons are made between (a,b) electron density, (c,d) electron temperature anisotropy, (e,f) magnetic field, (g,h) electron bulk velocity, (i-n) electric field in the spacecraft and electron rest frame, (o,p) total and M-component of the rate of energy conversion between the electric field and the electrons. Simulation data is shown in real units (right-axis) on the same scale as MMS observations with the exception of panel (p), which is much smaller in magnitude. Overall, observations and simulations are in qualitative agreement. [Associated simulation dataset available at https://doi.org/10.5281/zenodo.5807744]	294
C.3	Kinetic entropy and non-Maxwellianity in an EDR and their relationship to structures in the distribution function. (a) 2D plot of electron non-Maxwellianity \bar{M}_e in the PIC simulation, the virtual satellite trajectory through the EDR, representative magnetic field lines, and the location of the EDR distribution in panel o, marked by an “x”. (b,f) Total and (c,g) velocity space kinetic entropy density for the measured (orange) and Maxwellianized (blue) distributions. (d,h) Kaufmann and Paterson non-Maxwellianity \bar{M}_{KP} using total (blue) and velocity space (green) entropy density. (e,i) Velocity space non-Maxwellianity \bar{M} (orange). For (b)-(i), MMS data is in the left column and simulation data is in the right column. (j,m) Upstream, (k,n) inflow, and (l,o) EDR electron distribution functions from MMS3 (j-l) and the PIC simulation (m-o). [Associated simulation dataset available at https://doi.org/10.5281/zenodo.5807744].	296

Chapter 1

Introduction

1.1 Motivation behind the work

As a dynamical system with a large number of constituents evolves during a physical process, it is important to understand the conversion of different forms of energy. For a system with its initial and final states in local thermodynamic equilibrium (LTE), the first law of thermodynamics describes the conversion between heat, work, and internal energy (Clausius, 1850). However, systems such as weakly collisional plasmas are often not in LTE and, in such cases, the first law of thermodynamics fails. Much research has gone into extending the first law of thermodynamics for systems near (Onsager, 1931; Chapman & Cowling, 1970; Jou et al., 2010) and far (Prigogine, 1978) from LTE, but systems far from LTE remain poorly understood.

A number of non-LTE extensions of thermodynamics have been previously developed. In (classical) irreversible thermodynamics, rates of non-equilibrium transport due to two or more mechanisms occurring simultaneously, such as conduction and diffusion, were shown to be related to each other (Onsager, 1931). Other extensions were based on the kinetic theory of gases, for which the fundamental variable, as we will discuss in Sec. 1.3, is the phase space density f_σ for a species σ . In Sec. 1.4.1, we will discuss how multiplying powers of velocity components by f_σ

and integrating over velocity space (called taking “moments”) yields an infinite set of fluid properties of the gas or plasma, including the density, bulk flow velocity, pressure tensor, heat flux tensor, etc. In the Chapman-Enskog expansion, the phase space density is expanded around LTE in powers of a dimensionless parameter related to a system’s collisionality, resulting in a derivation of non-LTE transport coefficients such as viscosity and thermal conductivity (Braginskii, 1965; Chapman & Cowling, 1970). In extended irreversible thermodynamics (EIT), additional non-LTE corrections to the first law of thermodynamics are systematically obtained using perturbation theory; EIT has proven useful for a wide variety of applications including microfluidics, nano-devices, polymer solutions, and cosmology (Jou et al., 2010). As these treatments are based on linear expansions around LTE, they are most valid for small departures from LTE. Less is known about thermodynamics in systems arbitrarily far from LTE (Jarzynski, 1997), but it is crucial for a number of research areas including condensed matter physics (Jaeger & Liu, 2010), plasma physics (Howes, 2017; Matthaeus et al., 2020), nano-machines and open quantum systems (Schaller, 2014), micro- and nano-scale gas and fluid flow for chemical and biological applications (Evans & Hoover, 1986), and numerous examples in chemistry (Popielawski & Gorecki, 1991).

Taking the second velocity moment of f_σ (which we will discuss in Sec. 1.4.2) provides the time evolution equation for internal (or thermal) energy density, where a term called the pressure-strain interaction emerges offering a non-LTE pathway through which internal energy can change via conversion from bulk kinetic energy. In recent years, pressure-strain interaction has garnered a lot of interest (Yang et al.,

2017a,b) as it is the only term that can change the internal energy of a closed collisionless system (Yang et al., 2022). The pressure-strain interaction is usually decomposed into two terms. The first term, called pressure dilatation accounts for compressible effects, while the second component, referred to as “Pi – D”, deals with incompressible effects and has been described as collisionless viscosity (Yang et al., 2017a,b). However, relating Pi – D to viscosity is confusing, as it can be locally negative, as observed in simulations of non-LTE systems (Yang et al., 2017a,b; Pezzi et al., 2019, 2021). A thorough understanding of the kinetic aspects of the pressure-strain interaction is crucial and we do this in Chapters 3-5.

However, the analysis of pressure-strain interaction and by extension the time evolution of internal energy still misses the fact that energy can be associated with changing the infinite number of moments of the phase space density f_σ , for systems not in LTE. In Chapter 6, to address this deficiency, we derive a first-principles generalization of the first law of thermodynamics that is valid arbitrarily far from LTE using the Boltzmann transport equation in kinetic theory that fully accounts for energy conversion into all moments of the phase space density, including both thermodynamic and non-thermodynamic degrees of freedom. The main result of Chapter 6 is that we arrive at what we dub “the first law of kinetic theory”, which captures all physics described by the internal energy evolution equation, as well as energy conversion to all higher order moments of the phase space density associated with changes to the shape of the phase space density that are not captured by the first law of thermodynamics. Though the first law of kinetic theory is a statement of conservation of energy, it follows from the evolution of kinetic entropy (Boltzmann,

1877). The result is important because it provides a first-principles analytical form for the energy going into or coming out of non-LTE moments. The theory identifies where and when all non-LTE effects occur, and quantifies their contribution to energy conversion. The present result and any further generalizations obtained by relaxing the assumptions used here will have far-reaching implications for physical, chemical, and biological systems that are not in LTE for which the phase space density can be measured experimentally and/or numerically, including solar, space, astrophysical, and laboratory plasmas (Howes, 2017; Matthaeus et al., 2020), many body astrophysics (Aarseth & Aarseth, 2003), micro- and nano-fluidics for chemical and biological applications (Karplus & Petsko, 1990), and quantum entanglement (Floerchinger & Haas, 2020).

The primary objective of this Chapter is to establish the fundamental concepts underlying the dissertation. To achieve this, we carefully examine the key terms mentioned in the title of the dissertation. We start by offering an overview of temperature, a quantity routinely associated with energy as defined in plasmas that are in and out of local thermodynamic equilibrium. Subsequently, we provide a brief introduction to kinetic theory, which is a theoretical framework used to describe the behavior of plasma statistically and their collective interactions. We focus on an inherently non-LTE plasma phenomenon of magnetic reconnection and also emphasize how magnetic reconnection serves as an ideal test-bed for studying this dissertation's central theme, *i.e.*, non-LTE energy conversion. Finally, we lay the foundational principles for better understanding non-LTE energy conversion as it is currently understood and relay the importance of the novel approach discussed

in this dissertation.

1.2 Temperature and thermodynamic equilibrium

Plasma is often referred to as the fourth state of matter and it is said that most of the visible matter in the universe is in the plasma state. Plasma is ionized gas, where “ionized” means the constituent atoms have lost one or more electrons, thereby turning the neutral atoms into positively charged ions in a sea of negatively charged electrons. A plasma needs to be sufficiently hot to deter electrons from recombining with the ions. Partial ionization and/or recombination can lead to neutral atoms being present; plasmas with no neutrals are called fully ionized plasmas and are the focus of subsequent material in this dissertation. Since the constituents of plasma are charged particles, they respond to and produce electric and magnetic fields, which in turn affect how these charged particles move, making a plasma a “non-linearly coupled system”.

To study plasmas, we take a statistical approach called kinetic theory that we describe in greater detail in a subsequent section. Here, for the purposes of understanding “temperature,” we present a basic explanation of a velocity distribution function. As the name suggests, it is a quantity that is a function of velocity and it arises from counting the particles in a system.

The most common distribution function in physics is called a Maxwell-Boltzmann distribution function (or a Maxwellian in short). It is ubiquitous because it describes particles of fluid or plasma that are in “thermodynamic equilibrium”. If the system

is in a “global” thermodynamic equilibrium (GTE), then enough time has passed that macroscopic quantities are uniform and unchanging with time. Mathematically, a Maxwellian distribution function for species σ in systems that are in GTE is represented as

$$f_{\sigma}(\mathbf{v}) = n_{\sigma} \left(\frac{m_{\sigma}}{2\pi k_B T_{\sigma}} \right)^{3/2} e^{-m_{\sigma}(\mathbf{v}-\mathbf{u}_{\sigma})^2/2k_B T_{\sigma}}, \quad (1.1)$$

where the bold \mathbf{v} is a short-hand describing the components of the velocity in an arbitrary coordinate system. A Maxwellian distribution function is shown in Fig. 1.1 for a one-dimensional case for simplicity, *i.e.*, f is a function of only one velocity component chosen here to be v . Here, n_{σ} is the number density which is equal to the area under the curve, k_B is the Boltzmann constant, and T_{σ} is related to the width of the distribution function elucidating that there are many particles inside the width moving with random velocities that are lower than the thermal speed $v_{th,\sigma} = \sqrt{2k_B T_{\sigma}/m_{\sigma}}$ and fewer particles with random velocities higher than the thermal speed. To reestablish a connection between temperature and energy, we illustrate a scenario in which the temperature increases, and thus the width of the distribution function increases, resulting in an increased number of particles exhibiting higher random velocities. Consequently, this reaffirms the intuitive understanding that a higher temperature corresponds to a greater proportion of particles with faster random motion. In our notation, \mathbf{u}_{σ} represents the offset of the peak of the distribution function in the \mathbf{v} coordinate from the origin, which carries the physical interpretation of the system’s bulk flow. Conceptually, this can be un-

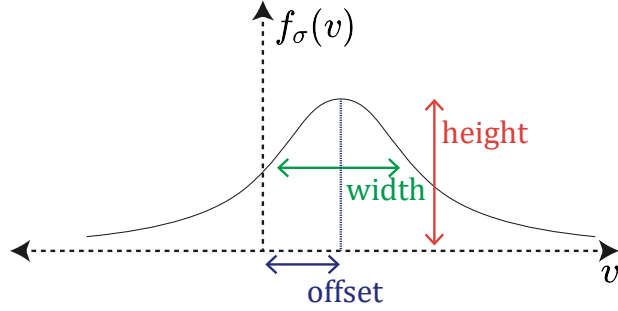


Figure 1.1: Sketch of a one-dimensional Maxwellian distribution function, where the black curve shows the distribution of particles as a function of velocity.

derstood as the statistical average velocity of the system. However, systems can be in “local” thermodynamic equilibrium (LTE) if small localized regions exist where thermodynamic equilibrium has been reached and where macroscopic quantities can be dependent on position space coordinate \mathbf{r} and time t (and we will discuss what they mean in the subsequent section). For LTE systems, a Maxwellian distribution function is represented as

$$f_{\sigma}(\mathbf{r}, \mathbf{v}, t) = n_{\sigma}(\mathbf{r}, t) \left(\frac{m_{\sigma}}{2\pi k_B T_{\sigma}(\mathbf{r}, t)} \right)^{3/2} e^{-m_{\sigma}(\mathbf{v} - \mathbf{u}_{\sigma}(\mathbf{r}, t))^2 / 2k_B T_{\sigma}(\mathbf{r}, t)}, \quad (1.2)$$

where n_{σ} , \mathbf{u}_{σ} , and T_{σ} are allowed to have dependencies on \mathbf{r} and t . Analogous to Eq. (1.1), Eq. (1.2) defines temperature for systems also in LTE, and the implication of linking temperature to LTE is that the temperature of a system not in LTE is ill-defined.

1.3 Kinetic theory - a brief primer

In this section, we provide an overview of kinetic theory, the statistical approach employed to study plasmas, which serves as the foundation for the theoretical developments and simulation results presented in this dissertation.

1.3.1 Phase space and its discretization for large N particles

In kinetic theory, a phase space plot provides a way to represent the positions and velocities of all the particles in a system at a given time. For a three-dimensional system, the phase space is a six-dimensional space, with three dimensions representing the positions \mathbf{r} of the particles along the three position-space coordinates and the other three dimensions representing the velocities \mathbf{v} of the particles along the three velocity-space coordinates. The position-space coordinate and velocity-space coordinate, along with time t , form the three independent variables. For simplicity, consider a system with a single particle. Then, at any given time, a single point in phase space denotes the position and velocity of the particle. Moreover, the dynamics of such a system can be studied by keeping track of this single point as it moves in this space.

In order to study the dynamics of N particles with $N \gg 1$, we can keep track of N points as they move in their orbits but this proposition becomes computationally hard for large N . Consider a 1-D system for simplicity, we discretize the phase space into small boxes of size Δx in each of the position-space coordinate and size Δv in each of the velocity-space coordinate. In 3-D, the three position-space bins need not

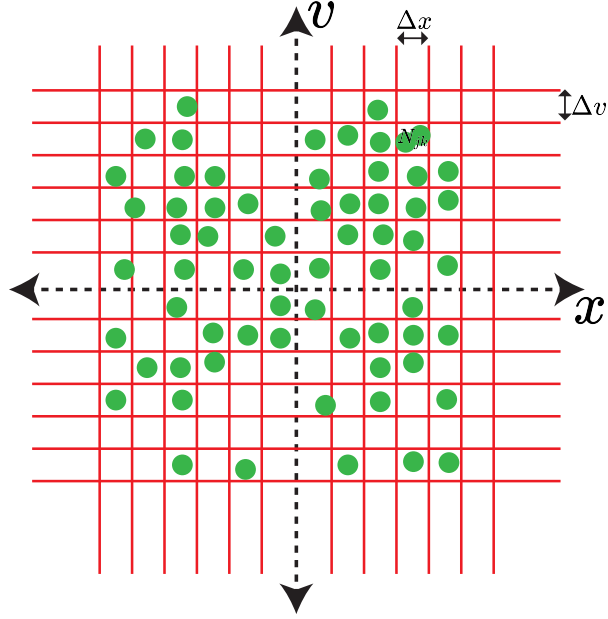


Figure 1.2: Sketch of a discretized phase space where the red lines show the uniformly spaced grid with phase space area $\Delta x \Delta v$ for a 2-D phase space. Green circles show the N particles populating this phase space. For illustrative purposes, there are phase space bins shown with few or no particles.

be equal and similarly, the three velocity-space bins need not be equal.

For simplicity of the discussion, we assume a 1-D dynamical system, and its phase space is shown in Fig. 1.2 that is populated by N particles. In Fig. 1.2, N_{jk} denotes the number of particles in the phase space area $\Delta x \Delta v$ with $x \in (x_j, x_j + \Delta x)$ in position-space and $v \in (v_k, v_k + \Delta v)$ in velocity-space, *i.e.*, the jk th bin of the phase space has N_{jk} particles in it. Note that in 3-D, the phase space volume is $\Delta^3 r \Delta^3 v$. Since there are N particles in total, summing the particles in each of the phase space bins gives N . Mathematically, $N = \sum_{j,k} N_{jk}$. We arrive at the fundamental meaning of a distribution function, *i.e.*, it is the number of particles

per unit phase space volume (or area in case of 1-D system). In 3-D,

$$f(\mathbf{r}_j, \mathbf{v}_k, t) = \frac{N_{jk}}{\Delta^3 r \Delta^3 v}. \quad (1.3)$$

This implies that f is a density in phase space, *i.e.*, it is a measure of the phase space density and it is non-negative with units of s^3/m^6 (in SI) or s^3/cm^6 (in CGS) in 3-D.

The discretization brings into question the size of the phase space bins and in Chapter 2, we will see it has important consequences for determining the position-space and velocity-space grid lengths in the particle-in-cell simulations. Δx should be big enough otherwise the statistical description of kinetic theory breaks down. In 3-D, $n \sim r^{-3} \implies r \sim n^{-1/3}$ where r is the average separation between particles with density n . Thus, $\Delta x \gg n^{-1/3}$. For plasmas collectively, a large number of particles is needed inside the Debye cube, *i.e.*, $n\lambda_{D\sigma}^3 \gg 1$, where $\lambda_{D\sigma} = \sqrt{k_B T_\sigma / (4\pi n_\sigma e^2)}$ (in CGS units). Thus the upper limit on Δx is set by $\lambda_{D\sigma}$. Suppressing the subscript σ , we have $n^{-1/3} \ll \Delta x \ll \lambda_D$. The velocity-space grid Δv is most appropriately determined relative to the thermal speed v_{th} , which sets the upper limit to ensure that the grid contains a sufficient number of particles for reliable statistical characterization. Thus, $\Delta v < v_{th}$. For appropriately small enough phase space volume, we turn the summation into integrals and rewrite Eq. (1.3) to give

$$N = \int f(\mathbf{r}, \mathbf{v}, t) d^3 r d^3 v. \quad (1.4)$$

For 3-D systems, \int is a shorthand notation for the integral over all position-space and all velocity-space.

Since $N = \int n(\mathbf{r}, t) d^3r$, using Eq. (1.4), we also obtain

$$n(\mathbf{r}, t) = \int f(\mathbf{r}, \mathbf{v}, t) d^3v. \quad (1.5)$$

Eq. (1.5) is an example of taking a moment which is multiplying f with powers of the velocity components and performing an integral over the whole velocity-space. n is thus the “zeroth-order” velocity moment. The “first-order” velocity moment of f is the bulk flow velocity determined as

$$\mathbf{u}(\mathbf{r}, t) = \frac{1}{n(\mathbf{r}, t)} \int \mathbf{v} f(\mathbf{r}, \mathbf{v}, t) d^3v, \quad (1.6)$$

which is the average velocity of the distribution and for a Maxwellian distribution function, it is presented as an offset in Fig. 1.1. The other moments used in the dissertation are as follows. The “second-order” moment of f is represented as \mathbf{P} which is a rank-2 tensor denoting the pressure tensor, with the jk th elements given by

$$P_{jk} = \int m v'_j v'_k f d^3v, \quad (1.7)$$

where $\mathbf{v}' = \mathbf{v} - \mathbf{u}$ is the random (also called peculiar or thermal) velocity. Note that taking moments of \mathbf{v}' is called taking “internal moments” of f . The temperature

tensor is defined as $\mathbf{T} = \mathbf{P}/(nk_B)$, with effective temperature given by

$$\mathcal{T} = \frac{\mathcal{P}}{nk_B} = \frac{2}{3nk_B} \int \frac{1}{2}mv'^2 f d^3v, \quad (1.8)$$

where \mathcal{P} is the effective pressure defined $\mathcal{P} = (1/3)\text{tr}[\mathbf{P}]$. The vector heat flux density is defined as

$$\mathbf{q} = \int \frac{1}{2}mv'^2 \mathbf{v}' f d^3v, \quad (1.9)$$

and it is a contraction of the rank-3 tensor that is the third-order internal moment of the distribution function. There are infinite moments of a general distribution function, however, for a Maxwellian distribution function, only the zeroth, first, and second moments can be non-zero. Moreover, the effective temperature can be thought of as the non-LTE generalization of temperature, *i.e.*, it defines a scalar temperature for distributions that are not Maxwellian.

We analyze distribution functions at particular position-space locations, and such distribution functions are called “velocity distribution functions”, an example of which was discussed in Sec. 1.2. By integrating out one (or more) velocity-space coordinates, we obtain “reduced velocity distribution functions”, and we show examples of reduced velocity distribution functions for electrons in Chapter 6 and in the appendices of the dissertation.

1.3.2 Time evolution of the distribution function

For large N particles, we discussed the statistical approach of kinetic theory to avoid examining the time evolution of each particle and developed the concept of distribution function $f(\mathbf{r}, \mathbf{v}, t)$. Here, we discuss the time evolution of the distribution function.

For simplicity, we again consider the case of a 2-D phase space for a 1-D system shown in Fig. 1.3 where particles of similar (x, v) move from the location given by (x, v) to $(x + \Delta x, v + \Delta v)$ in the phase space. As this motion happens, the distribution function cannot change if there are no physical processes that can locally (in phase space) change the distribution function. Such processes are collectively called “sources” and “sinks” of f , and they cause particles to suddenly appear or disappear from the phase space bins. Intra- and inter-species collisions change the distribution function in time, by causing particles to disappear and then reappear in different phase space bins. Ionization is a source of creating new charged species, while recombination is a sink and their presence changes species distribution functions in time.

We consider the absence of all other sources and sinks except for collisions $C[f]$. We omit the detailed derivation of the time evolution of the distribution function f which can be found in textbooks, *e.g.*, Bellan (2008), but discuss the result here. The time evolution of f_σ is given by the “Boltzmann equation” (Boltzmann, 1872)

$$\frac{\partial f_\sigma}{\partial t} + (\mathbf{v} \cdot \nabla) f_\sigma + \left(\frac{\mathbf{F}_\sigma}{m_\sigma} \cdot \nabla_v \right) f_\sigma = C[f]. \quad (1.10)$$

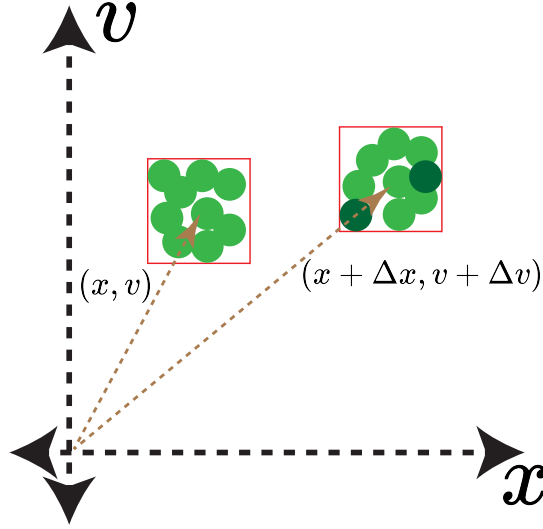


Figure 1.3: Sketch of a discretized phase space bin with particles (shown by green circles) moving in the phase space from location 1 denoted by (x, v) to location 2 denoted by $(x + \Delta x, v + \Delta v)$, with the phase space bin at location 2 losing some particles due to sinks (denoted by missing green-colored particles) and gaining few particles due to sources (denoted by dark green circles) that can abruptly change f .

Here we only consider the Lorentz force $\mathbf{F}_{\text{lor},\sigma} = q_\sigma(\mathbf{E} + \mathbf{v}/c \times \mathbf{B})$ (in CGS units) and inclusion of other forces, such as gravity is straight-forward. $\mathbf{E}(\mathbf{r}, t)$ and $\mathbf{B}(\mathbf{r}, t)$ denote the electric and magnetic fields, respectively, c is the speed of light and q_σ is the charge of species σ . We rewrite Eq. (1.10) to obtain

$$\frac{\partial f_\sigma}{\partial t} + (\mathbf{v} \cdot \nabla) f_\sigma + \frac{q_\sigma}{m_\sigma} \left(\mathbf{E} + \frac{\mathbf{v}}{c} \times \mathbf{B} \right) \cdot \nabla_v f_\sigma = C[f]. \quad (1.11)$$

We provide a brief overview (given the limited scope of this dissertation) of the collision operator. It should be noted that the plasmas considered throughout this dissertation consist of two species: electrons ($\sigma = e$) and ions ($\sigma = i$). The shorthand notation $C[f]$ in Eqs. (1.10) and (1.11) represents the combined effect of intra-species and inter-species collisions (we only consider binary collisions), de-

noted as $C_{\text{intra}}[f_\sigma]$ and $\sum_{\sigma'} C_{\text{inter}}[f_\sigma, f_{\sigma'}]$, respectively. For a collision operator to be physically meaningful, it needs to satisfy the following constraints which come from conservation laws. In the absence of sources and sinks, *e.g.*, ionization, recombination that can change the total number of particles thereby changing f_σ ,

1. collisions cannot change the number of particles. This is a statement of conservation of the number of particles and is mathematically given by

$$\int C_{\text{intra}}[f_\sigma] d^3v = 0 \quad (1.12)$$

and

$$\int \sum_{\sigma'} C_{\text{inter}}[f_\sigma, f_{\sigma'}] d^3v = 0, \quad (1.13)$$

2. collisions cannot change the total momentum of a species via intra-particle collisions but can transfer momentum between species via inter-species collisions. This is a statement of conservation of momentum, which for electron-ion plasma can be written mathematically as

$$\int m_\sigma \mathbf{v} C_{\text{intra}}[f_\sigma] d^3v = 0 \quad (1.14)$$

where $\sigma = i, e$ and

$$\int m_e \mathbf{v} C_{\text{inter}}[f_e, f_i] d^3v + \int m_i \mathbf{v} C_{\text{inter}}[f_i, f_e] d^3v = 0, \quad (1.15)$$

3. collisions cannot change the total energy of a species via intra-particle collisions

but can cause energy exchange between species via inter-species collisions. This is a statement of conservation of energy, which for electron-proton plasma can be written mathematically

$$\int \frac{1}{2} m_\sigma v^2 C_{\text{intra}}[f_\sigma] d^3v = 0, \quad (1.16)$$

where $\sigma = i, e$ and

$$\int \frac{1}{2} m_e v^2 C_{\text{inter}}[f_e, f_i] d^3v + \int \frac{1}{2} m_i v^2 C_{\text{inter}}[f_i, f_e] d^3v = 0. \quad (1.17)$$

1.3.3 Maxwell's Equations in kinetic theory

To complete the closure of the Boltzmann equation, Maxwell's equations are employed to determine the calculations of the electromagnetic fields. We reformulate the source terms of the electromagnetic fields, namely the charge density ρ and the current density \mathbf{J} , in terms of the distribution function f_σ and its moments. Thus,

$$\rho(\mathbf{r}, t) = \sum_\sigma q_\sigma n_\sigma(\mathbf{r}, t) \quad (1.18)$$

and

$$\mathbf{J}(\mathbf{r}, t) = \sum_\sigma q_\sigma n_\sigma(\mathbf{r}, t) \mathbf{u}_\sigma(\mathbf{r}, t) \quad (1.19)$$

are rewritten as

$$\rho(\mathbf{r}, t) = \sum_\sigma q_\sigma \int f_\sigma(\mathbf{r}, \mathbf{v}, t) d^3v \quad (1.20)$$

and

$$\mathbf{J}(\mathbf{r}, t) = \sum_{\sigma} q_{\sigma} \int \mathbf{v} f_{\sigma}(\mathbf{r}, \mathbf{v}, t) d^3v \quad (1.21)$$

by using Eq. (1.5) and Eq. (1.6). Thus, Maxwell's equations (in CGS units) become

$$\nabla \cdot \mathbf{E} = 4\pi\rho = 4\pi \sum_{\sigma} q_{\sigma} \int f_{\sigma}(\mathbf{r}, \mathbf{v}, t) d^3v, \quad (1.22a)$$

$$\nabla \cdot \mathbf{B} = 0, \quad (1.22b)$$

$$\nabla \times \mathbf{B} = \frac{4\pi}{c} \mathbf{J} + \frac{1}{c} \frac{\partial \mathbf{E}}{\partial t} = \frac{4\pi}{c} \sum_{\sigma} q_{\sigma} \int \mathbf{v} f_{\sigma}(\mathbf{r}, \mathbf{v}, t) d^3v + \frac{1}{c} \frac{\partial \mathbf{E}}{\partial t}, \quad (1.22c)$$

$$\nabla \times \mathbf{E} = -\frac{1}{c} \frac{\partial \mathbf{B}}{\partial t}. \quad (1.22d)$$

Eqs. (1.22a) - (1.22d) along with Eq. (1.11) are called the ‘‘Boltzmann-Maxwell equations’’.

We note that in the absence of any physical collisions $C[f] = 0$; this is a valid approximation for systems with low number density and/or due to the time scale of collisions being sufficiently lower than fundamental time scales of the plasma systems in question. An example of this is space plasma systems where the distance traveled between collisions can be as long as the system itself, *e.g.*, plasma that exists between the Sun and Earth at one astronomical unit. In such cases, Eq. (1.11) becomes the ‘‘Vlasov equation’’ (Vlasov, 1968) given by

$$\frac{\partial f_{\sigma}}{\partial t} + (\mathbf{v} \cdot \nabla) f_{\sigma} + \frac{q_{\sigma}}{m_{\sigma}} (\mathbf{E} + \frac{\mathbf{v}}{c} \times \mathbf{B}) \cdot \nabla_{\mathbf{v}} f_{\sigma} = 0. \quad (1.23)$$

and then along with Eqs. (1.22a) - (1.22d), they are called the “Vlasov-Maxwell equations”.

1.3.4 Entropy in kinetic theory

In anticipation of the forthcoming discussion on entropy in Chapter 6, here we provide a concise overview of these concepts, and readers are referred to previous literature (Bellan, 2008; Liang et al., 2019) for a comprehensive analysis.

Boltzmann described kinetic entropy (Boltzmann, 1877), for an isolated system, as

$$\mathcal{S}(t) = k_B \ln \Omega(t). \quad (1.24)$$

Ω is the total number of microstates which corresponds to a specific configuration of particles in the jk th phase space bin, *i.e.*, N_{jk} , that describes the macrostate of the system; here the macrostate is the macroscopic “observable” properties of the system. The N_{jk} particles are indistinguishable and the various ways they can be exchanged between phase space bins without changing the macrostate gives Ω . Mathematically, this statement is written as $\Omega = N! / \prod_{jk} N_{jk}!$. This simplifies Eq. (1.24) (and we suppress the t dependency) as

$$\mathcal{S} = k_B [\ln N! - \sum_{jk} \ln N_{jk!}]. \quad (1.25)$$

After application of Stirling’s approximation, *i.e.*, $\ln N_{jk}! \approx N_{jk} \ln N_{jk} - N_{jk}$ appli-

cable for $N_{jk} \gg 1$, Eq. (1.25) becomes

$$\mathcal{S} = k_B [N \ln N - \sum_{jk} N_{jk} \ln N_{jk}]. \quad (1.26)$$

We use Eq. (1.3) to rewrite Eq. (1.26) as

$$\mathcal{S} = k_B \left[N \ln \left(\frac{N}{\Delta^3 r \Delta^3 v} \right) - \sum_{jk} f(\mathbf{r}_j, \mathbf{v}_k) \Delta^3 r \Delta^3 v \ln [f(\mathbf{r}_j, \mathbf{v}_k)] \right]. \quad (1.27)$$

Under the assumption of appropriately small phase space volume as mentioned in sec 1.3.1, we turn summations into integrals, and get

$$\begin{aligned} S &= k_B \left[N \ln \left(\frac{N}{\Delta^3 r \Delta^3 v} \right) - \int f(\mathbf{r}, \mathbf{v}, t) \ln [f(\mathbf{r}, \mathbf{v}, t)] d^3 r d^3 v \right] \\ &= -k_B \int d^3 r d^3 v f(\mathbf{r}, \mathbf{v}, t) \ln \left[\frac{f(\mathbf{r}, \mathbf{v}, t) \Delta^3 r \Delta^3 v}{N} \right] \end{aligned} \quad (1.28)$$

$$= \int d^3 r s(\mathbf{r}, t) \quad (1.29)$$

where for Eq. (1.28), we employ the definition of $N = \int f(\mathbf{r}, \mathbf{v}) d^3 v d^3 r$. For Eq. (1.29), we define kinetic entropy density $s(\mathbf{r}, t)$ as

$$s(\mathbf{r}, t) = -k_B \int d^3 v f(\mathbf{r}, \mathbf{v}, t) \ln \left[\frac{f(\mathbf{r}, \mathbf{v}, t) \Delta^3 r \Delta^3 v}{N} \right]. \quad (1.30)$$

1.4 Fluid description of plasmas from kinetic theory

For a general $C[f]$ with properties as discussed in Sec. 1.3.2 and for the case of $C[f] = 0$, the derivation of the “fluid” equations from kinetic theory using the Boltz-

mann equation is straightforward and is available in plasma physics textbooks, *e.g.*, Bellan (2008). Below, we briefly discuss the results. We note that Braginskii (1965) provides the derivation of fluid equations (that Richardson (2019) calls “transport equations for a multispecies plasma”) for a particular collision operator $C[f]$ called the Landau collision operator (Landau, 1936) and by utilizing a Chapman-Enskog expansion (Chapman & Cowling, 1970) of the distribution function f .

1.4.1 Fluid equations

The fluid equations are

$$\frac{\partial n_\sigma}{\partial t} + \nabla \cdot (n_\sigma \mathbf{u}_\sigma) = 0, \quad (1.31)$$

$$m_\sigma n_\sigma \left[\frac{\partial \mathbf{u}_\sigma}{\partial t} + \mathbf{u}_\sigma \cdot \nabla \mathbf{u}_\sigma \right] = -\nabla \cdot \mathbf{P}_\sigma + q_\sigma n_\sigma \left(\mathbf{E} + \frac{\mathbf{u}_\sigma \times \mathbf{B}}{c} \right) + \mathbf{R}_\sigma, \quad (1.32)$$

$$\frac{3}{2} n_\sigma \left[\frac{\partial \mathcal{T}_\sigma}{\partial t} + \mathbf{u}_\sigma \cdot \nabla \mathcal{T}_\sigma \right] = -(\mathbf{P}_\sigma \cdot \nabla) \cdot \mathbf{u}_\sigma - \nabla \cdot \mathbf{q}_\sigma + \dot{Q}_{\sigma, \text{visc}, \text{coll}}. \quad (1.33)$$

Physically, Eq. (1.31) is the continuity equation describing how the number density changes with time. Eq. (1.32) is the force equation describing how the bulk flow velocity changes with time. Eq. (1.33) is the internal energy equation describing how effective temperature \mathcal{T}_σ changes with time.

\mathbf{R}_σ denotes the exchange of momentum between various plasma species due to collisions and is given by $\mathbf{R}_\sigma = \int m_\sigma \mathbf{v}'_\sigma \sum_{\sigma'} C_{\text{inter}}[f_\sigma, f_{\sigma'}] d^3v$. Finally, $\dot{Q}_{\sigma, \text{visc}, \text{coll}}$ denotes the volumetric heating rate from inter-species collisions and is given by $\dot{Q}_{\sigma, \text{visc}, \text{coll}} = \int (1/2) m_\sigma v_\sigma'^2 \sum_{\sigma'} C_{\text{inter}}[f_\sigma, f_{\sigma'}] d^3v$.

1.4.2 Energy time evolution equations

We define the internal or thermal energy density (which are used interchangeably in this dissertation) as $\mathcal{E}_{\sigma,th} = 3\mathcal{P}_\sigma/2 = 3n_\sigma k_B \mathcal{T}_\sigma/2$ and after some algebraic manipulations, we cast Eq. (1.33) into an equation for time evolution of internal energy density

$$\frac{\partial \mathcal{E}_{\sigma,th}}{\partial t} + \nabla \cdot (\mathcal{E}_{\sigma,th} \mathbf{u}_\sigma) = -(\mathbf{P}_\sigma \cdot \nabla) \cdot \mathbf{u}_\sigma - \nabla \cdot \mathbf{q}_\sigma + \dot{Q}_{\sigma,visc,coll}. \quad (1.34)$$

The time evolution of bulk kinetic energy density $\mathcal{E}_{\sigma,k} = 1/2 m_\sigma n_\sigma u_\sigma^2$, is obtained by taking a dot product of Eq. (1.32) with the bulk flow velocity \mathbf{u}_σ . After some algebraic manipulations and the usage of Eq. (1.31), it becomes

$$\frac{\partial \mathcal{E}_{\sigma,k}}{\partial t} + \nabla \cdot (\mathcal{E}_{\sigma,k} \mathbf{u}_\sigma) = -\nabla \cdot (\mathbf{u}_\sigma \cdot \mathbf{P}_\sigma) + (\mathbf{P}_\sigma \cdot \nabla) \cdot \mathbf{u}_\sigma + q_\sigma n_\sigma \mathbf{u}_\sigma \cdot \mathbf{E} + R_{\sigma,coll}. \quad (1.35)$$

Comparing Eqs. (1.34) and (1.35), we note $-(\mathbf{P}_\sigma \cdot \nabla) \cdot \mathbf{u}_\sigma$ term appears with a different sign in each equation. This indicates the $-(\mathbf{P}_\sigma \cdot \nabla) \cdot \mathbf{u}_\sigma$ term is the channel that facilitates conversion between bulk kinetic and thermal energy densities of the same species σ . We will briefly discuss the importance of this term in Sec. 1.6. The $q_\sigma n_\sigma \mathbf{u}_\sigma \cdot \mathbf{E}$ term can also be written as $n_\sigma \mathbf{u}_\sigma \cdot \mathbf{F}_\sigma$, with \mathbf{F}_σ being the Lorentz force given by $\mathbf{F}_\sigma = q_\sigma(\mathbf{E} + \mathbf{u}_\sigma \times \mathbf{B}/c)$. We note that in this form, it is straightforward to include other body forces. $R_{\sigma,coll} = \mathbf{u}_\sigma \cdot \mathbf{R}_\sigma$ denotes the inter-species collisional drag force power density.

We take the dot product of Eqs. (1.22c) with \mathbf{E} and (1.22d) with \mathbf{B} to attain a

time evolution equation for the electromagnetic energy density $\mathcal{E}_{EM} = (1/8\pi)(E^2 + B^2)$ (in CGS units) given by

$$\frac{\partial \mathcal{E}_{EM}}{\partial t} + \frac{c}{4\pi} \nabla \cdot (\mathbf{E} \times \mathbf{B}) = -\mathbf{J} \cdot \mathbf{E}, \quad (1.36)$$

where we notice that the $-\mathbf{J} \cdot \mathbf{E}$ term appears with an opposite sign as compared to $q_\sigma n_\sigma \mathbf{u}_\sigma \cdot \mathbf{E}$ in Eq. (1.35) which when summed over all species σ gives $\mathbf{J} \cdot \mathbf{E}$ using Eq. (1.21). This indicates that this term is the channel of conversion between bulk flow kinetic energy density (when all species are considered) and electromagnetic energy density. Yang et al. (2017a) shows these available channels of energy conversion pictorially (see their figure 1) efficiently when the system averages for a closed system (such as simulations considered in this dissertation) are considered.

A drawback of Eqs. (1.31) - (1.33) is that Eq. (1.33) specifically describes the time evolution of the effective temperature in time, but it relies on knowledge of the next (third-order) moment of f_σ . This presents what is referred to as the “closure problem”, which arises from the requirement of each moment’s time evolution equation to rely on the next higher-order moment. This issue becomes problematic since Eqs. (1.31) - (1.33) play a crucial role in understanding the energy evolution in dynamical plasma systems not in LTE. We will briefly touch on this issue in Sec. 1.6. In Chapter 6 of this dissertation, a novel approach is presented to overcome this closure problem and provide insights into the time evolution of energy that is not captured by Eqs. (1.34) - (1.36).

1.4.3 Magnetohydrodynamics (MHD) - a primer

The goal of this section is to find a single fluid equation for multispecies plasmas. The MHD approximation is valid for 1) length-scales of interest that are significantly larger than the characteristic length scales of electrons and ions, *i.e.*, their gyroradii, 2) the time-scales of interest that are much longer than the electron and ion time scales, *i.e.*, inverse of their plasma frequencies and cyclotron frequencies and 3) speeds involved to be much slower than the speed of light. Though the rest of the dissertation does not particularly use the MHD equations, they are pertinent in understanding the physics of reconnection discussed in the subsequent sections.

The derivation of single fluid equations can be found in many places in the literature, such as in MHD books and even in broader plasma physics books *e.g.*, Bellan (2008) and it involves manipulations of Eqs. (1.31) - (1.33) and implementing limits based on the scales of interest. Before we list the relevant equations, we first discuss the assumptions behind them. Ions are singly charged. The bulk flow of the plasma is a center of mass flow and is defined as $\mathbf{u} = (m_i\mathbf{u}_i + m_e\mathbf{u}_e)/(m_i + m_e)$, the current density is given by $\mathbf{J} = n_i e\mathbf{u}_i - n_e e\mathbf{u}_e$, and the mass density is given by $\rho_m = n_i m_i + n_e m_e$, where $i = \text{ions}$, and $e = \text{electrons}$. Under the assumption that $m_i \gg m_e$ and that of quasi-neutrality, *i.e.*, $n_i \approx n_e = n$, the first two can be solved to get \mathbf{u}_e and \mathbf{u}_i as $\mathbf{u}_e = \mathbf{u} - \mathbf{J}/(ne)$ and $\mathbf{u}_i = \mathbf{u}$, and the mass density becomes $\rho_m = nm_i$, which physically means that most of the mass density is coming from the heavier ions.

The MHD equations of mass continuity, force and pressure evolution are given as follows

$$\frac{\partial \rho_m}{\partial t} + \nabla \cdot (\rho_m \mathbf{u}) = 0 \quad (1.37)$$

$$\rho_m \left[\frac{\partial \mathbf{u}}{\partial t} + \mathbf{u} \cdot \nabla \mathbf{u} \right] = -\nabla P + \frac{\mathbf{J} \times \mathbf{B}}{c} \quad (1.38)$$

$$\frac{d}{dt} \left(\frac{P}{\rho_m^\gamma} \right) = 0 \quad (1.39)$$

where $P = P_i + P_e$, is the total scalar pressure and γ is the ratio of specific heat for the single fluid. Under the MHD limit, we also modify Maxwell's equations. The inductive electric field term in Eq. (1.22c) is neglected. The MHD limit of Maxwell's equations are

$$\nabla \cdot \mathbf{B} = 0, \quad (1.40a)$$

$$\nabla \times \mathbf{B} = \frac{4\pi}{c} \mathbf{J}, \quad (1.40b)$$

$$\nabla \times \mathbf{E} = -\frac{1}{c} \frac{\partial \mathbf{B}}{\partial t}. \quad (1.40c)$$

where we drop Gauss' law from Eq. (1.22a) since at MHD scales, ρ is negligible.

The two equivalent forms of the electron momentum equation, which when written in this particular way, are called the “generalized Ohm's law” are given by

$$\mathbf{E} + \frac{\mathbf{u}_i \times \mathbf{B}}{c} = \eta \mathbf{J} + \frac{\mathbf{J} \times \mathbf{B}}{nec} - \frac{\nabla \cdot \mathbf{P}_e}{ne} + \frac{m_e}{e^2} \frac{d}{dt} (\mathbf{J}/n), \quad (1.41a)$$

$$\mathbf{E} + \frac{\mathbf{u}_e \times \mathbf{B}}{c} = \eta \mathbf{J} - \frac{\nabla \cdot \mathbf{P}_e}{ne} + \frac{m_e}{e^2} \frac{d}{dt} (\mathbf{J}/n). \quad (1.41b)$$

Here, η is resistivity, and $\eta\mathbf{J}$ arises from \mathbf{R}_e from Eq. (1.32) for electrons, and it is given by $\eta = m_e\nu_{ei}/(ne^2)$ where ν_{ei} is the electron-ion collision frequency (Braginskii, 1965; Richardson, 2019). On the right-hand side of Eq. (1.41a), the first term is the resistive term, the second term is the Hall term, the third term is the electron pressure gradient term and the fourth term is the electron inertia term. In Eq. (1.41a), the left-hand side has the electric field and the ion bulk flow convective electric field, which together, can be thought of as the electric field in the frame of ion motion. Similarly, for Eq. (1.41b), the left-hand side has the electric field and the electron bulk flow convective electric field, which together, can be thought of as the electric field in the frame of electron motion, for which Hall term disappears in the right-hand side.

We use scaling analysis to evaluate the relative importance of each term on the right-hand side of Eq. (1.41a) in relation to the convective term on the left-hand side. This analysis allows us to ascertain the characteristic length scales at which each term on the right-hand side becomes significant.

For the resistive term, scaling gives

$$\frac{|\eta\mathbf{J}|}{\left|\frac{\mathbf{u}_i \times \mathbf{B}}{c}\right|} \sim \frac{\eta J}{uB/c} \sim \frac{\eta c B / l_{\delta, res}}{4\pi u B / c}, \quad (1.42)$$

where we use Eq. (1.40b) for the second scaling result. J denotes the typical scale value of \mathbf{J} and u is the typical scale value of \mathbf{u}_i . $l_{\delta, res}$ is the length over which \mathbf{B} changes if the resistive term is to be appreciable. Defining (Sweet, 1958; Parker, 1957) a resistive length $\lambda_\eta = \eta c^2 / (4\pi v_A)$ where $v_A = B / \sqrt{4\pi\rho_m}$ is the Alfvén speed,

we get,

$$\frac{|\eta \mathbf{J}|}{\left| \frac{\mathbf{u}_i \times \mathbf{B}}{c} \right|} \sim \frac{\lambda_\eta v_A}{ul_{\delta, res}}, \quad (1.43)$$

which shows that for the resistive term to be comparable to the convective term, $l_{\delta, res} \sim \lambda_\eta v_A / u$ (Vasyliunas, 1975) and if $u \sim v_A$, then $l_{\delta, res} \sim \lambda_\eta$.

For the Hall term, scaling gives

$$\frac{\left| \frac{\mathbf{J} \times \mathbf{B}}{nec} \right|}{\left| \frac{\mathbf{u}_i \times \mathbf{B}}{c} \right|} \sim \frac{JB/(nec)}{uB/c} \sim \frac{cB^2/(l_{\delta, H} nec)}{4\pi uB/c} \sim \frac{d_i^2 \Omega_{ci}}{ul_{\delta, H}} \sim \frac{d_i v_A}{ul_{\delta, H}}, \quad (1.44)$$

where $l_{\delta, H}$ is the length over which \mathbf{B} changes if the Hall term is to be appreciable. $\Omega_{ci} = eB/(m_i c)$ is the ion cyclotron or gyrofrequency, which is the frequency at which ions gyrate around the magnetic field. d_i is the ion skin depth or inertial length which is the length light travels over one ion plasma frequency interval, and hence is denoted by $d_i = c/\omega_{pi} = \sqrt{(c^2 m_i)/(4\pi n e^2)}$. Eq. (1.44) shows that for the Hall term to be comparable to the convective term, $l_{\delta, H} \sim d_i v_A / u$ and if $u \sim v_A$, then $l_{\delta, H} \sim d_i$.

For the electron pressure gradient term, we use Eq. (1.41b). Scaling gives

$$\frac{\left| \frac{\nabla \cdot \mathbf{P}_e}{ne} \right|}{\left| \frac{\mathbf{u}_e \times \mathbf{B}}{c} \right|} \sim \frac{P_e/(nel_{\delta, P})}{u_e B/c} \sim \frac{\beta_e B^2/(8\pi)}{neu_e B l_{\delta, P}/c} \sim \frac{d_e^2 \beta_e \Omega_{ce}}{u_e l_{\delta, P}} \sim \frac{d_e \beta_e v_{A, e}}{u_e l_{\delta, P}}, \quad (1.45)$$

where $l_{\delta, P}$ is the length over which \mathbf{B} changes if the pressure gradient term is to be appreciable, u_e is the characteristic value of \mathbf{u}_e , and P_e is the characteristic value of \mathbf{P}_e . For the second scaling result, we use electron plasma beta β_e defined as $\beta_e = P_e/(B^2/(8\pi))$; physically it describes the ratio of electron gas pressure and

magnetic pressure in a plasma. d_e is the electron skin depth or inertial length which is the length light travels over one electron plasma frequency interval and is given by $d_e = c/\omega_{pe} = \sqrt{(c^2 m_e)/(4\pi n e^2)}$. Eq. (1.45) shows that for the pressure gradient term to be comparable to the convective term, $l_{\delta,P} \sim \beta_e d_e v_{A,e}/u_e$ and if $u_e \sim c_{s,e}$, where $c_{s,e} = \sqrt{k_B T_e/m_e}$ is the electron sound speed, then $l_{\delta,P} \sim \beta_e^{1/2} d_e$.

For the electron inertia term, we again use Eq. (1.41b). Scaling gives

$$\frac{|\frac{m_e}{e^2} \frac{d}{dt} (\frac{\mathbf{J}}{n})|}{|\frac{\mathbf{u}_e \times \mathbf{B}}{c}|} \sim \frac{m_e J / (n e^2 l_{\delta,iner})}{B/c} \sim \frac{m_e c^2 / (4\pi n e^2)}{l_{\delta,iner}^2} \sim \frac{d_e^2}{l_{\delta,iner}^2}, \quad (1.46)$$

where $l_{\delta,iner}$ is the length over which \mathbf{B} changes if the electron inertia term is to be appreciable. In the last scaling result, we use the definition of d_e . Eq. (1.46) shows that for the electron inertia term to be comparable to convective term, $l_{\delta,iner} \sim d_e$.

1.5 Magnetic reconnection

Magnetic reconnection is perhaps one of the more ubiquitous processes occurring in the universe wherever there is magnetized plasma. In such environments, the close proximity of two regions with a component of the magnetic field that reverses direction can lead to the formation of a thin current sheet. These opposing magnetic fields can undergo cross-connections, *i.e.*, the magnetic fields break and reconnect, at what is termed the “X-line” in the current sheet. This change in the magnetic field configuration is referred to as a “change in magnetic field topology”. Since reconnection generates outflows, it becomes a process by which the electromagnetic energy of the regions with opposing magnetic fields is readily converted into the

kinetic energy of the outflows. Moreover, a portion of the electromagnetic energy is also channeled into heating the plasma, thereby changing the internal energy of the plasma. In the subsections that follow, we discuss how reconnection is essentially a small-scale process, but can affect the large-scale of the system.

1.5.1 Magnetic reconnection - where does it take place?

The history of magnetic reconnection can be traced back nearly eighty years to work done by Giovanelli (1947) to explain solar flares, which are explosive (10^{24} J) events that happen very fast (over a few minutes) (Priest & Forbes, 2002). What started with Giovanelli (1947) observing magnetic “neutral points” or “null points” occurring near solar flare locations has also been used to explain the production of ultra-high-energy cosmic rays from active galactic nuclei (AGNs) or gamma-ray bursts (GRBs) (Giannios, 2010) and astrophysical regions where the high-energy density requires taking special relativistic effects and even quantum electrodynamics (QED) effects into account (Uzdensky, 2011).

We focus on a limited segment of heliophysical (pertaining to the region around the Sun called the “heliosphere” where its magnetic field exerts influence), astrophysical (pertaining to regions beyond the heliosphere) systems, and terrestrial fusion experiments where magnetic reconnection is observed or theorized to occur.

1. Aurora is an indirect consequence of magnetic reconnection occurring in Earth’s magnetosphere, which represents the region influenced by Earth’s magnetic field. Reconnection takes place in the “magnetotail”, which refers to the side

of the magnetosphere facing away from the Sun, often referred to as the “night-side”. The occurrence of reconnection on the “dayside”, which is the side facing the Sun, has an impact on the magnetotail through the process dubbed the “Dungey cycle” (Dungey, 1953, 1958). Dungey coined the term “magnetic reconnection”.

2. In laboratory fusion experiments, reconnection has been used to elucidate the mechanism behind the “sawtooth instability.” This instability is characterized by a sawtooth-like pattern in the plasma parameters, such as temperature, when plotted against time. During a sawtooth event, there is a notable decrease in temperature accompanied by a sharp decline in the magnetic confinement of the plasma. As a result, the plasma expands and releases a burst of energy in the form of heat and particles (Kadomtsev, 1975; Yamada et al., 1994; Biskamp, 2000).
3. In turbulent systems, both observational (Phan et al., 2006; Retinò et al., 2007) and numerical studies (Matthaeus & Lamkin, 1986; Servidio et al., 2009) have revealed the occurrence of reconnection in thin (sub-ion and electron-scale) current sheets. The solar wind, consisting of energetic particles emitted by the Sun, exhibits turbulent behavior characterized by the presence of fluctuations in plasma parameters such as density, temperature, and electromagnetic fields.
4. Astrophysical plasma systems, such as astrophysical jets produced by AGNs (Uzdensky, 2011; Matsumoto et al., 2015), accretion disks around compact objects, *e.g.*, black holes, neutron stars, and magnetars which are a type of

neutron star with magnetic fields $\sim 10^{13} - 10^{15} G$ (Kaspi & Beloborodov, 2017), also possess magnetospheres and studies have proposed reconnection as the mechanism for producing highly energetic particles. Moreover, reconnection has been theorized to cause explosive stellar flares (Lyutikov, 2003, 2006) and for explaining the problem of stellar formation in accretion disks via transport of angular momentum across the different length-scales (Dal Pino et al., 2010).

1.5.2 Basic theory of magnetic reconnection

We motivate this discussion by looking at Eq. (1.41a) and imagining a situation when all the terms on the right-hand side are negligible. From our previous discussions in Sec. 1.4.3, we know this approximation is true if the length-scales of interest are larger than the characteristic length-scales of the terms on the right-hand side of Eq. (1.41a). This branch of MHD is called “ideal MHD” which, using $\mathbf{u}_i \approx \mathbf{u}$ from Sec. 1.4.3 gives,

$$\mathbf{E} + \frac{1}{c}(\mathbf{u} \times \mathbf{B}) = 0. \quad (1.47)$$

Eq. (1.47) has two profound implications, 1) an observer in the reference frame of plasma bulk flow moving at velocity \mathbf{u} does not see an electric field, 2) by manipulating Eq. (1.47) to give the plasma flow speed perpendicular to the local magnetic field, which comes out as

$$\mathbf{u}_\perp = \frac{c(\mathbf{E} \times \mathbf{B})}{B^2}, \quad (1.48)$$

and $\mathbf{u} \cdot \mathbf{B} = u_{\parallel}$ that denotes the plasma flow speed parallel to the local magnetic field. The right-hand side of Eq. (1.48) has the same form as the drift velocity experienced by single particles in crossed electric and magnetic field (Chen, 1974) and here it implies that the bulk of the plasma “drifts” along with the magnetic field, by forcing the plasma constituents to move at this velocity. This has been dubbed the “frozen-in” theorem (Axford, 1984) which essentially states that plasma is frozen into the magnetic field and is thus convected along with it. One can find its derivation in many of the plasma physics books (Chen, 1974; Bellan, 2008). An important implication of the frozen-in theorem is that it prohibits the process of reconnection from occurring. According to this theorem, plasma fluid elements are bound to the same magnetic field lines, while in regions of reconnection, there arises uncertainty regarding the “identity” of magnetic field lines. Consequently, if the frozen-in theorem were to be considered an inviolable “law” of nature, it would prevent any topological changes to the geometry of magnetic field lines. This implies that for reconnection to actually happen, the physics of the other terms from the right-hand side of Eq. (1.41a) must become important, which happens at their appropriate characteristic length-scales. That, in turn, allows the plasma to slip from the magnetic field and for the topology of the field line to change.

Nature is inherently spatially 3-D, but if the system is unvarying in one of the spatial directions called the “out-of-plane” direction, reconnection can be studied as a 2-D process, making it simpler to examine. Reconnection requires an oppositely directed magnetic field line geometry, an example of which is a Harris sheet (Harris, 1962) profile, which is a steady-state solution of the Vlasov equation (Eq. (1.23)).

The magnetic field follows a tanh profile given by $B_x(y) = B_0 \tanh(y/w_0)$, where B_0 is the asymptotic value at a far away distance and w_0 is the half-distance over which B_x changes direction. From Eq. (1.40b), there is a current density only along the out-of-plane direction given by $J_z(y) = -(cB_0/(4\pi w_0))\text{sech}^2(y/w_0)$. This thin current sheet is where the frozen-in theorem breaks down; the geometry is shown in Fig. 1.4. The light green colored box denotes the current sheet which separates the two regions along \hat{y} called “upstream” where we have oppositely directed magnetic field lines (shown by red and blue) and two regions along \hat{x} called “downstream” where we have newly reconnected magnetic field lines (shown by half red and half blue). For reconnection to begin, some dissipative mechanism, *i.e.*, one of the terms in the right-hand side of Eq. (1.41a) becomes appreciable, causing the magnetic field to break. In order to preserve Gauss’ law (Eq. (1.22b)), these broken magnetic field lines cross-connect or “reconnect” inside this “diffusion” or “dissipation” region shown by the light blue box in Fig. 1.4 at a location is called the “X-line” (shown by the black x). The newly reconnected field lines are bent and as they straighten out outside the diffusion region, they take the frozen-in plasma out, creating outflows (shown by thick green arrows). Here in the downstream regions, the stored magnetic energy gets converted to bulk flow kinetic energy. Plasma flowing outward from the diffusion region creates a dearth of mass, thus creating a low-pressure region and so plasma flows in from upstream (shown by thick red arrows) and doing so brings in magnetic field lines, turning reconnection into a self-sustaining process. The whole cycle repeats itself until the upstream magnetic flux is spent, and steady-state is achieved when the rate at which magnetic flux entering the diffusion region equals

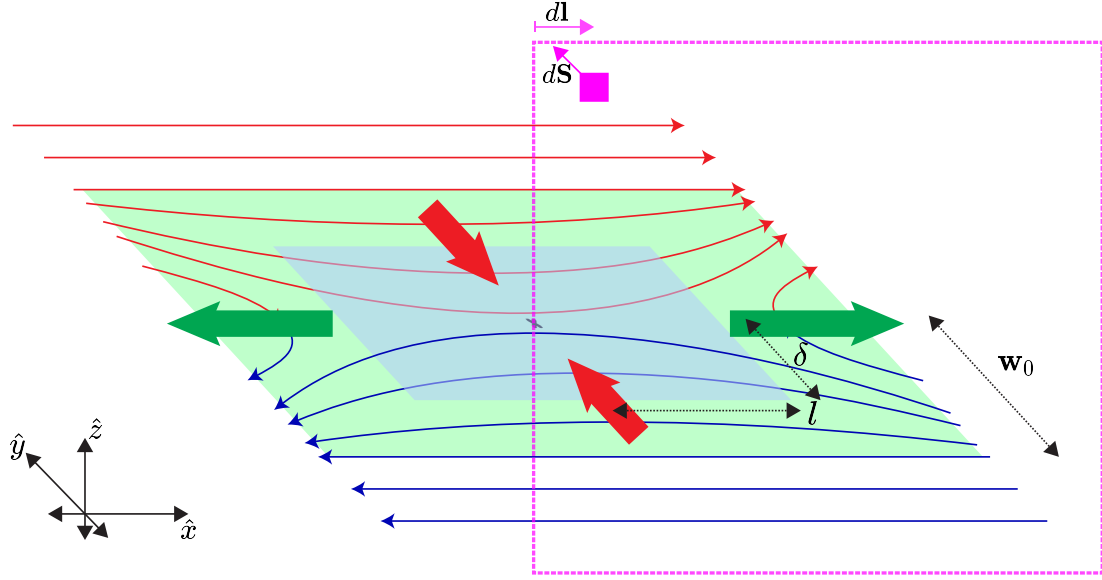


Figure 1.4: Sketch of the 2-D geometry of reconnection, tilted in the $x - y$ plane. Please refer to the text for a detailed description.

the magnetic flux exiting the diffusion region.

Magnetic flux is linked to reconnection and hence is a measure for quantifying the rate at reconnection proceeds. We define magnetic flux Φ as the flux of magnetic field \mathbf{B} through an area of interest \mathbf{S} illustrated by cyan loop in the $x - z$ plane in Fig. 1.4. $\Phi = \int_S \mathbf{B} \cdot d\mathbf{S}$ where $d\mathbf{S}$ is an infinitesimally small element shown by the small cyan box in Fig. 1.4. This $d\mathbf{S}$ is normal to the cyan loop. We use Faraday's law (Eq. (1.22d)), then dot it with $d\mathbf{S}$, integrate the flux over the whole surface and apply Stokes' theorem to convert the area integral into a line integral to obtain,

$$\frac{d\Phi}{dt} = -c \oint_C d\mathbf{l} \cdot \mathbf{E}, \quad (1.49)$$

where \oint_C denotes the integral along the perimeter of the cyan loop. The left-hand side of Eq. (1.49) describes the rate at which flux through the loop of interest changes

in time, and it is called the “reconnection rate”. The loop integral becomes

$$\begin{aligned} \frac{d\Phi}{dt} &= -c \oint_C d\mathbf{l} \cdot \mathbf{E} \\ &= -c [\mathbf{E} \cdot d\mathbf{l}|_{left} + \mathbf{E} \cdot d\mathbf{l}|_{up} + \mathbf{E} \cdot d\mathbf{l}|_{right} + \mathbf{E} \cdot d\mathbf{l}|_{down}] \end{aligned} \quad (1.50a)$$

$$\implies \frac{d\Phi}{dt} = -c (E_z l_z + E_x l_x - 0 l_z - E_x l_x) = -c E_z l_z. \quad (1.50b)$$

In Eq. (1.50a), the subscripts *left*, *right*, *up*, and *down* indicate the corresponding edges of the cyan loop perimeter: left, right, upper, and lower, respectively. For obtaining Eq. (1.50b), we assume that z -component of the electric field is only important at the X-line and not on the rightmost edge which we choose to be far away from the reconnection region, and that the x -component of the electric field has the same strength above and below the $x - y$ plane of reconnection because we assume it is a 2-D system. Eq. (1.50b) shows that the out-of-plane E_z becomes a metric of reconnection rate per unit out of plane length.

Since far from the diffusion region, plasma is frozen-in the magnetic field, ideal-MHD is an adequate model. We rewrite Eq. (1.38) as

$$\rho_m \left[\frac{\partial \mathbf{u}}{\partial t} + \mathbf{u} \cdot \nabla \mathbf{u} \right] = -\nabla \left[P + \frac{B^2}{8\pi} \right] + \frac{\mathbf{B} \cdot \nabla \mathbf{B}}{4\pi}, \quad (1.51)$$

where Eq. (1.40b) is utilized to replace \mathbf{J} in the second term on the right-hand side of Eq. (1.38). We note here that the force density due to a pressure gradient, *i.e.*, the ∇P term on the right-hand side of Eq. (1.51), is responsible for the motion of plasma into the diffusion region from upstream, as we discussed at the beginning of

this section. Moreover, the force density due to magnetic curvature, *i.e.*, $\mathbf{B} \cdot \nabla \mathbf{B} / (4\pi)$ on the right-hand side of Eq. (1.51) is responsible for plasma moving outward from the diffusion region with the newly reconnected bent magnetic field.

We use scaling analysis on relevant equations when the system is assumed to be in steady-state, *i.e.*, $\partial/\partial t \rightarrow 0$. From the mass continuity equation in MHD as shown in Sec. 1.4.3, *i.e.*, Eq. (1.37), we obtain $\nabla \cdot (\rho_m \mathbf{u}) = 0$. Doing a volume integral over the diffusion region, we get $\int_V dV \nabla \cdot (\rho_m \mathbf{u}) = \int_S d\mathbf{S} \cdot (\rho_m \mathbf{u}) = 0$, where dV is an infinitesimally small volume of the diffusion region, and $d\mathbf{S}$ is the corresponding surface, with out-of-plane length of Δz . We consider the surfaces on the upstream and downstream sides for scaling and obtain

$$\begin{aligned} \frac{\rho_m u_x}{2l\Delta z} &\sim \frac{\rho_m u_y}{2\delta\Delta z}, \\ \implies \frac{u_x}{l} &\sim \frac{u_y}{\delta} \\ \implies \frac{u_{in}}{u_{out}} &\sim \frac{\delta}{l}, \end{aligned} \tag{1.52}$$

where we assume that ρ_m is approximately uniform throughout the diffusion region and is dropped in the second relation. l is the half-length and δ is the half-width of the diffusion region, respectively. We also assume that the flow along \hat{y} is approximately uniform across the surface on the upstream side and $u_y \sim u_{in}$ where u_{in} is called the inflow speed. Similarly, the flow along \hat{x} is assumed to be approximately uniform across the surface on the downstream side and $u_x \sim u_{out}$ where u_{out} is called the outflow speed. Eq. (1.52) shows that for a diffusion region with $\delta \ll l$, the outflow speed is faster than the inflow speed. Using a similar

approach, we obtain a scaling result from Eq. (1.40a)

$$\frac{B_{down}}{B_{up}} \sim \frac{\delta}{l}. \quad (1.53)$$

Similar assumptions about the field strengths at the upstream and downstream sides of the diffusion region are made, *i.e.*, $B_x \sim B_{up}$ and $B_y \sim B_{down}$, where B_{up} and B_{down} denote the magnetic field at the upstream and downstream edges of the diffusion region, respectively. Eq. (1.53) implies that for a diffusion region with $\delta \ll l$, the downstream field strength is weaker than the upstream field strength. A scaling analysis of Eq. (1.51) during steady-state reveals that the curvature term balances the convective term under the assumption that the pressure gradient term balances the gradient of magnetic pressure, *i.e.*, $B^2/(8\pi)$, throughout the diffusion region. Therefore, we get $\rho_m \mathbf{u} \cdot \nabla \mathbf{u} \sim \mathbf{B} \cdot \nabla \mathbf{B}/(4\pi)$. Taking a dot product with \hat{x} , we obtain

$$\begin{aligned} \rho_m (u_x \partial_x u_x + u_y \partial_y u_x) &\sim \frac{1}{4\pi} (B_x \partial_x B_x + B_y \partial_y B_x) \\ \implies \rho_m \left(\frac{u_{out}}{l} + \frac{u_{in}}{\delta} \right) u_{out} &\sim \frac{1}{4\pi} \left(\frac{B_{up}}{l} + \frac{B_{down}}{\delta} \right) B_{up} \\ \implies \rho_m \frac{u_{out}^2}{l} &\sim \frac{1}{4\pi} \left(\frac{B_{up}^2}{l} \right) \\ \implies u_{out} &\sim \sqrt{\frac{B_{up}^2}{4\pi \rho_m}} = c_{A,up}. \end{aligned} \quad (1.54)$$

For the third scaling relation, we use Eqs. 1.52 and (1.53). Eq. (1.54) elucidates that the outflow speed of plasma exiting the diffusion region scales the Alfvén speed based on the upstream magnetic field $c_{A,up}$. Moreover, from Eq. (1.52), (1.53) and

(1.54), we also obtain that the inflow speed scales as the Alfvén speed based on the downstream magnetic field, *i.e.*, $u_{in} \sim c_{A,down}$.

Using ideal MHD, which is valid upstream of the diffusion region, we obtain a scaling result for the reconnection rate. We dot Eq. (1.47) with \hat{z} to get

$$E_z + \frac{1}{c} (u_x B_y - u_y B_x) = 0$$

$$\implies E_z \sim \frac{1}{c} B_{up} u_{in} \quad (1.55a)$$

$$\implies E_R \equiv \frac{c E_z}{u_{out} B_{up}} \sim \frac{\delta}{l}, \quad (1.55b)$$

where Eq. (1.55b) gives the normalized reconnection rate E_R , which is the out-of-plane electric field normalized to the outflow speed and upstream magnetic field strength.

We briefly discuss the resistive reconnection (Sweet, 1958; Parker, 1957) process, also eponymously called Sweet-Parker reconnection. It utilizes the resistive term (of Eq. (1.41a)) to break the frozen-in theorem and this limit of MHD is aptly called “resistive” MHD. In this model, previous work (Dungey, 1953; Sweet, 1958; Parker, 1957) has shown that the normalized reconnection rate scales as the square root of the resistivity η . However, η is small for many plasma systems of interest, *i.e.*, the solar corona, where the Sweet-Parker reconnection model was tried as a potential application for solar flares. Using values for ν_{ei} and n for the solar corona (Richardson, 2019), we get $\eta \approx 2.4 \times 10^{-16}$ s (in CGS), and this implies a very small reconnection rate and slow reconnection time-scales. This could not explain the time-scales of a few minutes observed in solar flares (Parker, 1963). The underlying

reason for the failure of the Sweet-Parker reconnection model can be attributed to mass conservation. In the Sweet-Parker model, the diffusion region where magnetic field lines reconnect is characterized by a long length and a narrow width. This aspect ratio leads to a slow reconnection process because plasma that enters the diffusion region from upstream is unable to escape quickly to the downstream region. Consequently, the limited outflow speed contributes to a slow reconnection process. Moreover, the resistive model fails to explain reconnection observed in plasma systems where collisions are infrequent, and thus the system is “collisionless” plasmas, which we discuss in the next section.

In concluding our discussion on collisional reconnection, it is noteworthy to comment on the thermodynamic aspects of the system. The frequent collisions occurring in a resistive plasma imply that the system is in local thermodynamic equilibrium (LTE). Previous work employing a volume control analysis of the Sweet-Parker model to examine the energy budget has shown that approximately 50% of the incoming Poynting flux, which represents the magnetic enthalpy, is converted to the bulk kinetic energy flux (Priest & Forbes, 2000; Birn et al., 2010; Shay et al., 2014). This implies approximately 50% is available for increasing the plasma temperature, *i.e.*, internal energy. However, for collisionless reconnection, the absence of collisions means that the system may not be in LTE and this partition of energy may not hold true.

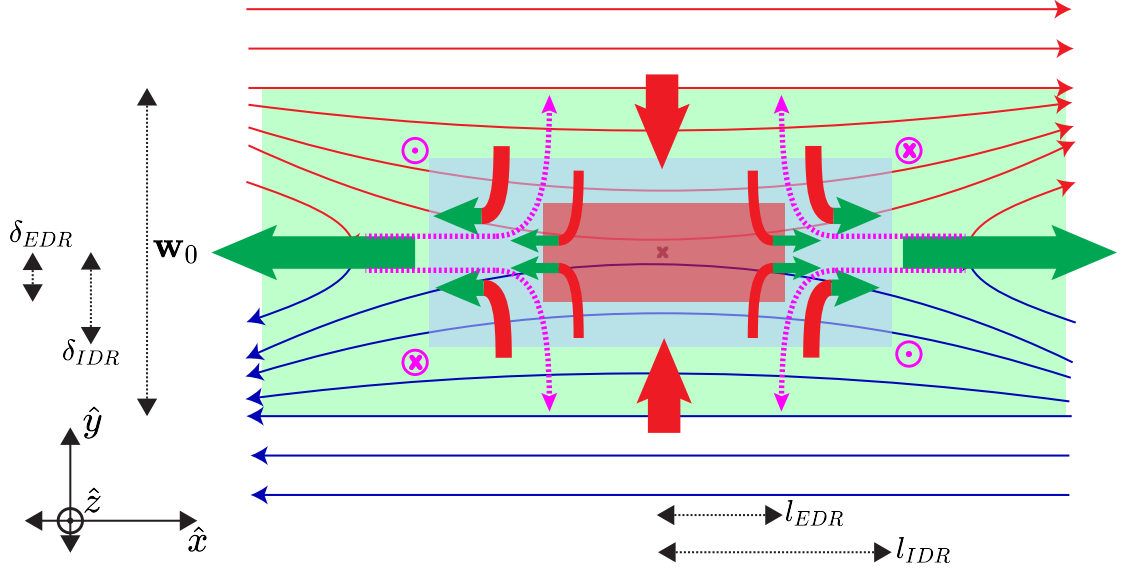


Figure 1.5: Sketch of the 2-D geometry of anti-parallel reconnection. Please refer to the text for a description.

1.5.3 Collisionless reconnection

We use the framework described in Sec.1.4.3 to motivate how reconnection can proceed in a collisionless plasma. In the absence of resistivity, the other terms in Eq. (1.41a) can cause dissipation at smaller scales which in turn leads to field lines breaking and reconnecting.

We first provide a description of the 2-D geometry of collisionless reconnection, where an out-of-plane external magnetic field (called a “guide field”) is absent before reconnection starts, thus giving us an “anti-parallel” configuration. Moreover, a simplistic case is when the two upstream regions have all the same plasma parameters, thus making the system “symmetric” as well. Such a system is shown in Fig. 1.5.

According to ideal-MHD, plasma is stuck to the same field line indefinitely due

to the frozen-in theorem. However, the finite gyroradii of these particles become important at length-scales at which when particles, while undergoing gyration, can get affected by the changes in the direction of the magnetic field \mathbf{B} within gyro-period. Then, particles “decouple” from the field line and begin to “meander” (Speiser, 1965). The distribution functions of such particles are not Maxwellian and they show sharp features, making the system not in LTE, which requires a theory beyond the first law of thermodynamics to properly account for the energy budget of the system.

In a two-species plasma such as the one examined in this dissertation, because ions are heavier than electrons, the former has larger gyroradii even if the two species have the same temperature (and the gyroradii are based on their thermal speeds). This implies that ions decouple first at a larger length-scale and then electrons decouple at a relatively smaller length-scale, giving rise to the two-scale structure, as shown in Fig. 1.5 (in contrast to resistive reconnection in Fig. 1.4) (Shay et al., 1998). The red box portrays the region where electrons are decoupled from the field, thus called the “electron” diffusion region (EDR). Since ions decouple at a larger length-scale, the EDR is embedded in the “ion” diffusion region (IDR), depicted by the blue box. The IDR itself can be embedded in a wider current sheet, illustrated by the green box (analogous to the green box shown in Fig. 1.4). We use the red thick arrows to illustrate flows into the diffusion regions, and in green are flows out of the diffusion regions. The thickest arrows indicate the bulk motion of plasma into and out of the diffusion regions when both electrons and ions are still coupled to the magnetic field while it is convecting into the diffusion region. Inside the IDR,

ion flows are shown by the thicker arrows. Similarly, electron flows are displayed by the least thick arrows.

We analyzed the different length scales associated with the terms in Eq. (1.41a) in relation to the spatial scale over which the magnetic field \mathbf{B} varies in Sec. 1.4.3. We utilize the generalized Ohm's law from Eq. (1.41b) to replace the electric field in Faraday's law from Eq. (1.40c) and obtain

$$\frac{\partial \mathbf{B}}{\partial t} = -c \nabla \times \left[-\frac{\mathbf{u}_e \times \mathbf{B}}{c} - \frac{\nabla \cdot \mathbf{P}_e}{ne} + \frac{m_e}{e^2} \frac{d}{dt} (\mathbf{J}/n) \right], \quad (1.56)$$

where we disregard the resistive term. At length-scales when the inertia term is unimportant and in the absence of off-diagonal electron pressure tensor elements, Eq. (1.56) reduces to

$$\frac{\partial \mathbf{B}}{\partial t} = \nabla \times [\mathbf{u}_e \times \mathbf{B}]. \quad (1.57)$$

Eq. (1.57) provides the mathematical foundation for understanding why electrons remain coupled to the magnetic field. This is because it shares the same form as the equation obtained when the ideal-MHD electric field, as shown in Eq. (1.47), is used to calculate the time derivative of \mathbf{B} . A key implication of Eq. (1.57) is that it implies that in order for electrons to decouple and reconnection to proceed, off-diagonal electron pressure tensor elements and/or electron inertia need to be non-negligible. Previous work, *e.g.*, Zenitani et al. (2011) has shown that for symmetric anti-parallel reconnection, it is the gradient of the off-diagonal electron pressure tensor that breaks the electron frozen-in condition.

An equivalent expression to Eq. (1.56) can be obtained by using the generalized Ohm's law from Eq. (1.41a) instead and we then find

$$\frac{\partial \mathbf{B}}{\partial t} = -c \nabla \times \left[-\frac{\mathbf{u}_i \times \mathbf{B}}{c} + \frac{\mathbf{J} \times \mathbf{B}}{nec} - \frac{\nabla \cdot \mathbf{P}_e}{ne} + \frac{m_e}{e^2} \frac{d}{dt} (\mathbf{J}/n) \right], \quad (1.58)$$

where we again ignore the resistive term. Eq. (1.58) can be simplified to give

$$\begin{aligned} \frac{\partial \mathbf{B}}{\partial t} = & -\mathbf{B}(\nabla \cdot \mathbf{u}_i) + (\mathbf{B} \cdot \nabla) \mathbf{u}_i - (\mathbf{u}_i \cdot \nabla) \mathbf{B} - \frac{cm_e}{e^2} \frac{d}{dt} \left(\nabla \times \frac{\mathbf{J}}{n} \right) \\ & + \frac{c \nabla \times (\nabla \cdot \mathbf{P}_e)}{ne} - \frac{(\mathbf{B} \cdot \nabla) \mathbf{J}}{ne} + \frac{(\mathbf{J} \cdot \nabla) \mathbf{B}}{ne}. \end{aligned} \quad (1.59)$$

In the right-hand side of Eq. (1.59), two terms appear that demonstrate the convection of magnetic field:

1. the third term $-(\mathbf{u}_i \cdot \nabla) \mathbf{B}$ denotes the convection of magnetic field with the bulk flow of ions,
2. the seventh term $(\mathbf{J} \cdot \nabla) \mathbf{B}/(ne)$ denotes the convection of magnetic field with the current, called the ‘‘Hall’’ current, and is portrayed by magenta dashed curves in Fig. 1.5.

Since the seventh term comes from the Hall term in Eq. (1.41a) and the third term from the convection term in Eq. (1.41a), their balance signifies the scale at which Hall term becomes important. Using the result obtained in Sec. 1.4.3, we obtain the thickness of the IDR is $\delta_{IDR} \sim d_i$. For the EDR where electrons decouple, we use the arguments from Sec. 1.4.3 to find the length-scales at which the electron inertia term balances the convective term in the electron frame. Doing so, we get

$\delta_{EDR} \sim d_e$. Numerical simulations (Shay et al., 1998; Birn et al., 2001; Hesse et al., 2002, 2011) have shown that these scaling results hold very well for symmetric anti-parallel reconnection. A simulation study of *in-situ* spacecraft observations of symmetric anti-parallel reconnection in Earth’s magnetosphere measured by NASA’s Magnetospheric Multiscale (MMS) mission (Burch et al., 2016a) has shown that the presence of off-diagonal electron pressure terms and thus their gradient indeed break the electron frozen-in theorem, and thus allow for reconnection to proceed (Egedal et al., 2019).

In order to determine the length of the diffusion regions, we turn to simulation studies of collisionless reconnection. Previous studies (Shay et al., 1999; Birn et al., 2001) demonstrate that the normalized reconnection rate E_R is not significantly affected by the specific non-ideal term in Eq. (1.41a) that facilitates the reconnection process and $E_R \sim 0.1$ implying $l_{IDR} \sim 10d_i$ and $l_{EDR} \sim 5 - 10d_e$.

The presence of the Hall current in two-species plasmas gives rise to the generation of an out-of-plane magnetic field. This magnetic field has a quadrupolar structure, which has been identified as a signature of collisionless Hall reconnection (Sonnerup, 1979; Mandt et al., 1994), and is a direct consequence of the two-scale structure. Studies of collisionless simulations for pair plasmas (where electron and ion inertial lengths are equal, hence no two-scale structure) have shown that the Hall term disappears, along with the quadrupolar out-of-plane magnetic field structure (Bessho & Bhattacharjee, 2005; Daughton & Karimabadi, 2007; Hesse & Zenitani, 2007). Even so, Bessho & Bhattacharjee (2005) finds an effective collisionless resistivity (Speiser, 1965) using which they find $E_R \sim 0.1$. The independence of the

normalized reconnection rate E_R on the specific dissipation mechanism has been a subject of confusion. In recent work, Liu et al. (2022) used geometrical arguments to claim a first-principles calculation of the 0.1 reconnection rate.

1.6 Motivation for studying non-LTE energy conversion in reconnection

Here, we motivate and justify our choice of employing reconnecting plasma systems for studying non-LTE energy conversion. In the preceding sections on reconnection, we have alluded to the inherent non-LTE nature of systems that reconnect with low or zero initial guide fields. Ions and electron distribution functions in the upstream regions, far away from the current sheet, are typically Maxwellian distributions, and numerical simulations are often initialized with such distributions, as elaborated upon in Chapter 2. Previous studies, both numerical (Egedal et al., 2013; Bessho et al., 2014; Shuster et al., 2014, 2015; Egedal et al., 2016; Barbhuiya et al., 2022) and observational (Burch et al., 2016b; Torbert et al., 2018; Nakamura et al., 2018, 2019; Egedal et al., 2019; Shi et al., 2022a,b), have demonstrated that plasmas exhibit highly structured and localized (in position-space) non-Maxwellian velocity distribution functions, which make applying the first law of thermodynamics as known for LTE systems, restrictive. Nonetheless, the partitioning of incoming magnetic energy into bulk flow energy and thermal energy of the plasma in reconnection systems is routinely investigated using the principles we developed in Sec. 1.4.1, specifically Eqs. (1.34) - (1.36) for thermal (internal) energy density, bulk flow energy

density, and electromagnetic energy density, respectively. This approach has been widely employed in first-principle theoretical studies (Liu et al., 2022), numerical studies (Shay et al., 2014; Haggerty et al., 2015), laboratory experiments (Yamada et al., 2014), as well as *in-situ* space satellite observation studies (Eastwood et al., 2013, 2020; Zhou et al., 2021).

We review the first law of thermodynamics for systems in LTE since it is among the core themes of the dissertation. One way to write the first law of thermodynamics is in terms of rates of energy conversion per particle in a small increment of time dt as

$$\frac{dQ}{dt} = \frac{dW}{dt} + \frac{d\bar{E}_{\text{int}}}{dt}. \quad (1.60)$$

This relates the increment in heat per particle dQ , work per particle dW done by the system, and increment in internal energy per particle $d\bar{E}_{\text{int}}$. In thermodynamics, these increments are parametrized as $dQ = TdS$ where T is the thermodynamic temperature and dS is the increment in entropy per particle, $dW = PdV$ where P is the thermodynamic pressure and dV is the change in volume per particle and $d\bar{E}_{\text{int}} = (3/2)k_B dT$ for a monatomic constituent.

As discussed and alluded to in Sec. 1.4.2, Eq. (1.34) is the non-LTE generalization of the first law of thermodynamics and it follows directly from kinetic theory. To obtain the internal energy evolution equation for a non-LTE system, we multiply Eq. 1.10 by the random energy $(1/2)m_\sigma v_\sigma^2$ and integrate over all velocity space

(Braginskii, 1965; Jou et al., 2010) to get

$$\frac{3}{2}n_{\sigma}k_B\frac{dT_{\sigma}}{dt} = -\nabla \cdot \mathbf{q}_{\sigma} - (\mathbf{P}_{\sigma} \cdot \nabla) \cdot \mathbf{u}_{\sigma} + n_{\sigma}\dot{Q}_{\sigma,\text{coll,inter}}, \quad (1.61)$$

which is yet another way of describing how effective temperature evolves in time, and is equivalent to Eq. (1.33) and Eq. (1.34). The pressure-strain interaction term, denoted as $-(\mathbf{P}_{\sigma} \cdot \nabla) \cdot \mathbf{u}_{\sigma}$ in Eq. 1.61 plays a crucial role in understanding non-LTE energy conversion. As discussed in Sec. 1.4.2, this term, along with its decomposition (discussed in the next paragraph), has been widely employed in plasma physics (Yang et al., 2017a,b; Pezzi et al., 2019, 2021) to elucidate the mechanisms responsible for temperature changes in such systems. However, several unanswered questions surround the pressure-strain interaction term, raising concerns about whether the conventional decomposition is always suitable for capturing the underlying physics of the system. Moreover, the system's geometry may necessitate the use of non-Cartesian coordinate systems, and to our knowledge, there is no existing study that investigates the pressure-strain interaction term and its decompositions using a non-Euclidean coordinate system. This dissertation aims to address these gaps and provide insights into these aspects and we do so in chapters 3 - 5.

To demonstrate that Eq. (1.61) is the non-LTE generalization of the first law of thermodynamics, we write it in a form analogous to Eq. (1.60) by using the known decomposition (Jou et al., 2010; Yang et al., 2017a) $(\mathbf{P}_{\sigma} \cdot \nabla) \cdot \mathbf{u}_{\sigma} = \mathcal{P}_{\sigma}(\nabla \cdot \mathbf{u}_{\sigma}) + \Pi_{\sigma,jk}\mathcal{D}_{\sigma,jk}$, where we use the Einstein summation convention on indices j and k , $\Pi_{\sigma,jk} = P_{\sigma,jk} - \mathcal{P}_{\sigma}\delta_{jk}$ are elements of the deviatoric pressure tensor $\mathbf{\Pi}$,

$\mathcal{D}_{\sigma,jk} = (1/2)(\partial u_{\sigma j}/\partial r_k + \partial u_{\sigma k}/\partial r_j) - (1/3)\delta_{jk}(\nabla \cdot \mathbf{u}_\sigma)$ are elements of the traceless symmetric strain rate tensor \mathcal{D} , and δ_{jk} is the Kroenecker delta. The continuity equation implies $\mathcal{P}_\sigma(\nabla \cdot \mathbf{u}_\sigma) = -(\mathcal{P}_\sigma/n_\sigma)dn_\sigma/dt = \mathcal{P}_\sigma n_\sigma d(1/n_\sigma)/dt = n_\sigma \mathcal{P}_\sigma dV_\sigma/dt = n_\sigma d\mathcal{W}_\sigma/dt$, where $V_\sigma = 1/n_\sigma$ is the volume per particle and $d\mathcal{W}_\sigma = \mathcal{P}_\sigma dV_\sigma$ is the non-LTE generalization of the work per particle done by the system. Dividing equation 1.61 by n_σ and rearranging gives

$$\frac{d\mathcal{W}_\sigma}{dt} + \frac{d\bar{\mathcal{E}}_{\sigma,\text{int}}}{dt} = \frac{d\mathcal{Q}_\sigma}{dt} + \dot{Q}_{\sigma,\text{coll,inter}}, \quad (1.62)$$

where we define $d\bar{\mathcal{E}}_{\sigma,\text{int}} = (3/2)k_B d\mathcal{T}_\sigma$ as the increment in internal energy per particle, $d\mathcal{Q}_\sigma$ as the increment in thermodynamic heat per particle, and $d\mathcal{Q}_\sigma/dt = -(\nabla \cdot \mathbf{q}_\sigma + \Pi_{\sigma,jk}\mathcal{D}_{\sigma,jk})/n_\sigma$. The non-LTE quantities in calligraphic font generalize the thermodynamic quantities in a standard font in Eq. (1.60). Thus, Eq. (1.62) is the non-LTE generalization of the first law of thermodynamics, which accounts for energy conversion between work, internal energy, and heat for systems not in LTE.

Though we described what effective temperature is early in this dissertation (see Sec. 1.2), its physical meaning warrants a small discussion. The effective temperature is the appropriate non-LTE generalization to the thermodynamic temperature. The thermodynamic temperature T is related to the average random kinetic energy in a thermodynamic system via $(3/2)k_B T = \langle (1/2)m_\sigma v_\sigma'^2 \rangle$, where the angular brackets denote the average over all constituent particles. For a non-LTE system, $(3/2)k_B \mathcal{T}_\sigma = \langle (1/2)m_\sigma v_\sigma'^2 \rangle$ as well, *i.e.*, it is the analogous measure of the average random kinetic energy of the particles in the distribution. The distinction

for systems not in LTE is that \mathcal{T}_σ only contains the average random kinetic energy; it importantly does not contain energy associated with other forms of random motion, such as $\langle m_\sigma v'_{\sigma j} v'_{\sigma k} \rangle$ where $j \neq k$, which are zero for systems in LTE but can be non-zero for systems out of LTE and captured in the deviatoric pressure tensor $\mathbf{\Pi}$. This fact underscores the necessity to account for random energy not captured by the non-LTE generalization of the first law of thermodynamics, and we do in Chapter 6.

1.7 Outline of the dissertation

We conclude by providing an outline of this dissertation, which is structured as follows:

1. Chapter 2 serves as a general introduction to the particle-in-cell code `p3d`, which is used for the numerical simulations of magnetic reconnection discussed in chapters 5 and 6. The Chapter also presents a comprehensive explanation of the new additions made to the kinetic entropy diagnostics and discusses methods for validating the quantities used in Chapter 6. Furthermore, it includes simulation material that is elaborated upon in appendices A and C,
2. chapters 3 to 5 consist of a series of published “Featured articles” in *Physics of Plasmas* (Cassak & Barbhuiya, 2022; Cassak et al., 2022; Barbhuiya & Cassak, 2022). These chapters focus on gaining a kinetic understanding of the pressure strain interaction term $-(\mathbf{P}_\sigma \cdot \nabla) \cdot \mathbf{u}_\sigma$ identified in Sec. 1.4.2, which describes the conversion between kinetic bulk energy and thermal energy densities. The

pressure-strain interaction term has garnered significant attention in recent years and the aforementioned chapters explore this term and its alternative decompositions in Cartesian coordinates and in a magnetic field-aligned coordinate system,

3. Chapter 6 features a published “Editor’s Suggestion” article in Physical Review Letters, where we discuss a novel approach for quantifying non-LTE energy conversion and how it originates from kinetic entropy (Cassak et al., 2023), and employ anti-parallel reconnection as a test case for our investigations,
4. Chapter 7 functions as the concluding chapter of the dissertation, where we summarize the main outcomes and their implications in the field. Additionally, we offer a roadmap for future research and also outline potential avenues that are being currently explored,
5. Appendix:
 - (a) A is a published article in the Journal of Geophysical Research Space Physics, where we discuss the formation of highly structured non-Maxwellian distributions which have torus shape in velocity-space. These “ring” distributions appear in the magnetic flux pile-up regions downstream of the EDR and lead to electron heating. We provide a theory of how the electron temperature of these ring distributions depends on upstream plasma conditions and make connections with observed electron temperatures in

dipolarization fronts in Earth’s magnetotail region and hypothesize how it could explain super-hot solar flares with temperature in the 10s of MK (Barbhuiya et al., 2022),

- (b) B is a portion of a published article in the Journal of Plasma Physics that provides the theoretical work where we analytically calculated the kinetic entropy density for commonly occurring non-Maxwellian distributions. An entropy-based non-Maxwellianity parameter called \bar{M}_{KP} is then calculated for said distributions (Liang et al., 2020a). Additionally, kinetic entropy density and different \bar{M}_{KP} for a ring distribution discussed in Appendix A is also provided.
- (c) C is a portion of a published article in Physics of Plasma with the first-ever MMS observation of kinetic entropy for electrons in a reconnection event followed by comparisons with 2-D simulation result showing good qualitative and quantitative agreement (Argall et al., 2022). We also discover that non-LTE features in the reduced velocity distributions agree well when comparing observations and simulation data.

Chapter 2

Numerical simulations

2.1 General description of the simulations

In order to examine the non-LTE plasma system we described in Chapter 1, *i.e.*, magnetic reconnection, we simulate antiparallel symmetric reconnection using a particle-in-cell code called `p3d` (Zeiler et al., 2002). It is a massively parallelized code capable of running on tens of thousands of processors, *e.g.*, the simulations used in this dissertation ran on 32,768 processors. It is important to note that all simulations conducted for this dissertation are 2.5-dimensional in position-space, which means there are no variations in quantities along one spatial direction that is the out-of-plane direction, while they are 3-dimensional in velocity-space. In `p3d`, the particles and electromagnetic fields are stepped forward in time using the relativistic Boris particle stepper (Birdsall & Langdon, 1991) and the trapezoidal leapfrog method (Guzdar et al., 1993), respectively. The particle time step is chosen to be twice that of the fields. In order to ensure the validity of Poisson's equation, the multigrid method (Trottenberg et al., 2000) is utilized to clean the electric field \mathbf{E} every 10 particle time steps. The simulation domain is bounded by periodic boundaries in both spatial directions.

2.2 Normalized units of simulated quantities

In Nature, quantities such as temperature and number density can have disparate orders of magnitude. For example, the number density in the solar corona is $\sim 10^9 \text{ cm}^{-3}$ whereas the temperature is $\sim 10^6 \text{ K}$ (Richardson, 2019). Simulating such quantities with varied magnitudes is computationally challenging. Hence, it is convenient in simulations to have all quantities in “code normalized units” which makes it so that all quantities have a similar order of magnitude in spite of being different variables. We now proceed to discuss the normalization in p3d.

2.2.1 Governing equations and normalization

At its core, the numerical code solves the four Maxwell’s equations (Eq. (2.1a)-(2.1d)) alongside the macroparticle equation of motion, with the subscript p denoting macroparticles (Eq. (2.1e)) and subscript σ denoting species, with the Lorentz force (Eq. (2.1f)) given by

$$\nabla \cdot \mathbf{E} = 4\pi\rho, \quad (2.1a)$$

$$\nabla \cdot \mathbf{B} = 0, \quad (2.1b)$$

$$\nabla \times \mathbf{B} = \frac{4\pi}{c}\mathbf{J} + \frac{1}{c}\frac{\partial \mathbf{E}}{\partial t}, \quad (2.1c)$$

$$\nabla \times \mathbf{E} = -\frac{1}{c}\frac{\partial \mathbf{B}}{\partial t}, \quad (2.1d)$$

$$\frac{d\mathbf{x}_{p,\sigma}}{dt} = \mathbf{v}_{p,\sigma}, \quad (2.1e)$$

$$m_{p,\sigma}\frac{d\mathbf{v}_{p,\sigma}}{dt} = q_{p,\sigma}\left(\mathbf{E} + \frac{\mathbf{v}_{p,\sigma} \times \mathbf{B}}{c}\right), \quad (2.1f)$$

where Eq. (2.1e) - (2.1f) are solved for ions and electrons separately. Macroparticles (or superparticles) correspond to a large number of actual particles, from which they are made, *i.e.*, the actual particles that make up a macroparticle have similar positions and velocities and thus can be regarded as chunks of phase space as discussed in Sec. 1.3. c is the speed of light. $\mathbf{x}_{p,\sigma}$ is the (macro)particle position of species σ , and $\mathbf{v}_{p,\sigma}$ is the (macro)particle velocity of species σ . We show the non-relativistic equations of motion in Eq. (2.1f) where $\mathbf{v}_{p,\sigma} \rightarrow \gamma \mathbf{v}_{p,\sigma}$ in the left-hand side for relativistic regimes, with $\gamma = (1 - v_{p,\sigma}^2/c^2)^{-1/2}$. Here, \mathbf{E} and \mathbf{B} are the electric and magnetic fields, respectively. $\rho = \sum_{\sigma} \sum_p q_{p,\sigma} n_{p,\sigma}$ is the charge density where $q_{p,\sigma}$ is the charge of the (macro)particle p of species σ and $n_{p,\sigma}$ is the number density of the (macro)particle p of species σ . $\mathbf{J} = \sum_{\sigma} \sum_p q_{p,\sigma} n_{p,\sigma} \mathbf{v}_{p,\sigma}$ is the current density..

For a detailed derivation of the normalization, which requires some algebraic manipulations, we refer readers to <https://terpconnect.umd.edu/~swisdak/p3d/> courtesy of Marc Swisdak. For brevity, we provide the normalized equations and normalization constants, also known as “dimensional constants” called as such since they contain the dimensional information. The normalized equations,

suppressing the p subscript, are as follows

$$\tilde{\nabla} \cdot \tilde{\mathbf{E}} = \frac{c^2}{v_0^2} \tilde{\rho}, \quad (2.2a)$$

$$\tilde{\nabla} \cdot \tilde{\mathbf{B}} = 0, \quad (2.2b)$$

$$\tilde{\nabla} \times \tilde{\mathbf{B}} = \tilde{\mathbf{J}} + \frac{v_0^2}{c^2} \frac{\partial \tilde{\mathbf{E}}}{\partial t}, \quad (2.2c)$$

$$\tilde{\nabla} \times \tilde{\mathbf{E}} = -\frac{\partial \tilde{\mathbf{B}}}{\partial t}, \quad (2.2d)$$

$$\frac{d\tilde{\mathbf{x}}}{dt} = \tilde{\mathbf{v}}, \quad (2.2e)$$

$$\frac{d\tilde{\mathbf{x}}_e}{dt} = \tilde{\mathbf{v}}_e, \quad (2.2f)$$

$$\frac{d\tilde{\mathbf{v}}}{dt} = \left(\tilde{\mathbf{E}} + \tilde{\mathbf{v}} \times \tilde{\mathbf{B}} \right), \quad (2.2g)$$

$$\tilde{m}_e \frac{d\tilde{\mathbf{v}}_e}{dt} = -\left(\tilde{\mathbf{E}} + \tilde{\mathbf{v}}_e \times \tilde{\mathbf{B}} \right), \quad (2.2h)$$

where $\tilde{}$ denote code normalized dimensionless variables. The dimensional constants are denoted by the “0” subscript and are as follows. For mass, $m_0 = m_i$, *i.e.*, the normalized ion mass is 1, for charge $q_0 = e$, *i.e.*, the normalized ion charge is 1. Eqs. (2.2e) and (2.2g) is for ions and we write Eqs. (2.2f) and (2.2h) separately for electrons. The normalization constants used are based on a reference density n_0 and a reference magnetic field B_0 . Doing so then defines the other dimensional constants which are as follows. For lengths, $L_0 = d_i$ which is ion skin depth based on n_0 . For times, $t_0 = \Omega_{ci0}^{-1} = [eB_0/(m_0c)]^{-1}$ which is the inverse of ion cyclotron frequency based on B_0 . Thus, for speeds, $v_0 = c_{Ai0}$ which is the ion Alfvén speed based on B_0 and n_0 . For electric fields, $E_0 = B_0 v_0/c$.

The dimensional constant for distribution functions f_0 can also be obtained.

We utilize Eq. (1.4) and $N = \int d^3rn$ to obtain $f_0 = n_0/v_0^3 = n_0c_{Ai0}^{-3}$. Thus, a reduced velocity distribution function is normalized to $n_0c_{Ai0}^{-2}$ if one velocity dimension is integrated out, and to $n_0c_{Ai0}^{-1}$ if two velocity dimensions are integrated out. The dimensional constant for temperatures is $T_0 = m_0v_0^2/k_B = m_ic_{Ai0}^2/k_B$ where k_B is Boltzmann's constant. This implies energy densities \mathcal{E} have a dimensional constant $\mathcal{E}_0 = m_0n_0v_0^2 = m_in_0c_{Ai0}^2$. Dimensional constants for other derived quantities can be similarly derived, *e.g.*, energy per particle $\bar{\mathcal{E}}$ is normalized to $\bar{\mathcal{E}} = \mathcal{E}_0/n_0 = m_0v_0^2 = m_ic_{Ai0}^2$.

We discussed kinetic entropy density in Sec. 1.3.4 in preparation for discussions done later in Chapter 6 where we will see that it is decomposed into position-space and velocity-space entropy densities (see Eqs. (6.4a) - (6.4b)). The dimensional constant for kinetic entropy density, position-space entropy density and velocity-space entropy density is k_Bn_0 . Dimensional constants for other derived quantities can be similarly calculated, *e.g.*, kinetic entropy density flux \mathcal{J}_σ given in Eq. (6.13) is $k_Bn_0c_{Ai0}$.

2.3 System setup

2.3.1 Plasma system at initialization

We note here that the initialization conditions used in the simulations in this dissertation are the same as that of Liang et al. (2019). The simulations are initialized with two current sheets, that are L_x in length and centered around $L_y/4$ and $3L_y/4$; here L_x and L_y are horizontal and vertical lengths of the simulation domain.

The simulation coordinates are such that the reconnection inflows are along $\pm\hat{y}$ and the outflows are along $\pm\hat{x}$. The out-of-plane direction $\hat{z} = \hat{x} \times \hat{y}$. At initialization, we employ a double tanh magnetic field profile for the \hat{x} component of the magnetic field, given by

$$B_x(y) = \tanh\left(\frac{y - L_y/4}{w_0}\right) - \tanh\left(\frac{y - 3L_y/4}{w_0}\right) - 1, \quad (2.3)$$

where w_0 is the width (also called the half thickness) over which B_x reverses directions across the current sheets (as desired in a reconnection simulation). Thus, the asymptotic value of B_x far upstream of the current sheet is ± 1 . We choose this asymptotic value as B_0 for code normalization. Initially, there is no out-of-plane (guide) magnetic field. At $t = 0$, plasma is neutral so $n_e = n_i = n$ and there is only one plasma population for each species with a number density profile given by

$$n(y) = \frac{1}{2(T_e + T_i)} \left[\operatorname{sech}^2\left(\frac{y - L_y/4}{w_0}\right) + \operatorname{sech}^2\left(\frac{y - 3L_y/4}{w_0}\right) \right] + n_{up}, \quad (2.4)$$

where T_e and T_i are electron and ion temperatures, respectively, that are uniform at $t = 0$, and n_{up} is the far upstream number density. The maximum of the number density minus the upstream number density at the center of the current sheet comes out to be $1/(2(T_e + T_i))$. We choose the total plasma temperature, *i.e.*, $T_e + T_i = 0.5$, thus making this maximum density equal 1, and we choose this as n_0 . At initialization, both electrons and ions have drifting Maxwellian distribution functions, given by Eq. (1.2). There is no electric field at initialization; using Eqs. (2.2c) and (2.3),

we find only out-of-plane current density exists (since $\partial/\partial z \rightarrow 0$) and it is given by

$$J_z(y) = -\frac{\partial B_x}{\partial y} = -\frac{1}{w_0} \left[\operatorname{sech}^2\left(\frac{y - L_y/4}{w_0}\right) - \operatorname{sech}^2\left(\frac{y - 3L_y/4}{w_0}\right) \right]. \quad (2.5)$$

This current density is sustained by the bulk flow of the plasma along the \hat{z} direction, which we discuss next.

It has been shown that a 1-D kinetic equilibrium current sheet solution to the Vlasov equation exists (Harris, 1962). A constraint relating temperature and bulk flow velocity of species in order to maintain charge neutrality of plasmas was later discovered (Biskamp, 2000). This condition is given by $\mathbf{u}_e/T_e = -\mathbf{u}_i/T_i$ where \mathbf{u}_e and \mathbf{u}_i are bulk flow velocities of electrons and ions, respectively. These velocities are only along \hat{z} direction at $t = 0$, thus giving $u_{e,z}/T_e = -u_{i,z}/T_i$. Since at $t = 0$, $J_z = n(u_{i,z} - u_{e,z})$, a quick derivation gives

$$u_{e,z} = -\frac{J_z(y)T_e}{n(y)(T_e + T_i)} \quad (2.6)$$

$$u_{i,z} = \frac{J_z(y)T_i}{n(y)(T_e + T_i)}. \quad (2.7)$$

We add a small magnetic perturbation (of the forms provided below) to initiate reconnection by seeding an X-O line pair in both upper and lower current sheets,

$$\delta B_x = -b_{x,pert} \sin \frac{2\pi x}{L_x} \sin \frac{4\pi y}{L_y}, \quad (2.8)$$

$$\delta B_y = b_{x,pert} \frac{L_y}{2L_x} \cos \frac{2\pi x}{L_x} \left[1 - \cos \frac{4\pi y}{L_y} \right]. \quad (2.9)$$

δ denotes the small perturbations, and $b_{x,pert}$ is a small (usually less than 10%) user-defined value. Associated additions to current densities and the bulk flows are thus small. Fig. 2.1 displays these perturbations for simulation parameters listed in Sec. 2.3.2.

2.3.2 Simulation parameters at initialization

We choose the speed of light c to be larger than the largest speed of the system, thus making the parameters non-relativistic (whilst p3d is relativistic) and $c = 15$ suffices for the simulations used in this dissertation. As we discussed in Sec. 2.2.1, electron mass \tilde{m}_e is user selected such that electron to ion mass ratio is 0.04 and it is sufficient for the study of the electron diffusion region (EDR). We select a small simulation domain of $L_x \times L_y = 12.8 \times 6.4$. We note here that the simulation domain is smaller than the smallest length required for full ion recoupling downstream of the X-line, *i.e.*, outflowing ions do not have the space needed to recouple back to the reconnected field, and thus reconnection proceeds in partial-ion recoupled regime (Sharma Pyakurel et al., 2019).

We choose the grid-length $\Delta = 0.0125$, which is smaller than the smallest length-scale of the system, *i.e.*, electron Debye length $\lambda_{De} = 0.0176$. The system has 1024×512 grid-cells. We choose the time-step $\Delta t = 0.001$ to be smaller than the smallest time-scale of the system, as set by the electron plasma oscillation time-scale $\omega_{pe}^{-1} = 0.012$. Each of the 1024×512 grid-cells is initialized with a (macro) particle per grid (PPG) of 25,600 that are also weighted. Using particle weights ensures

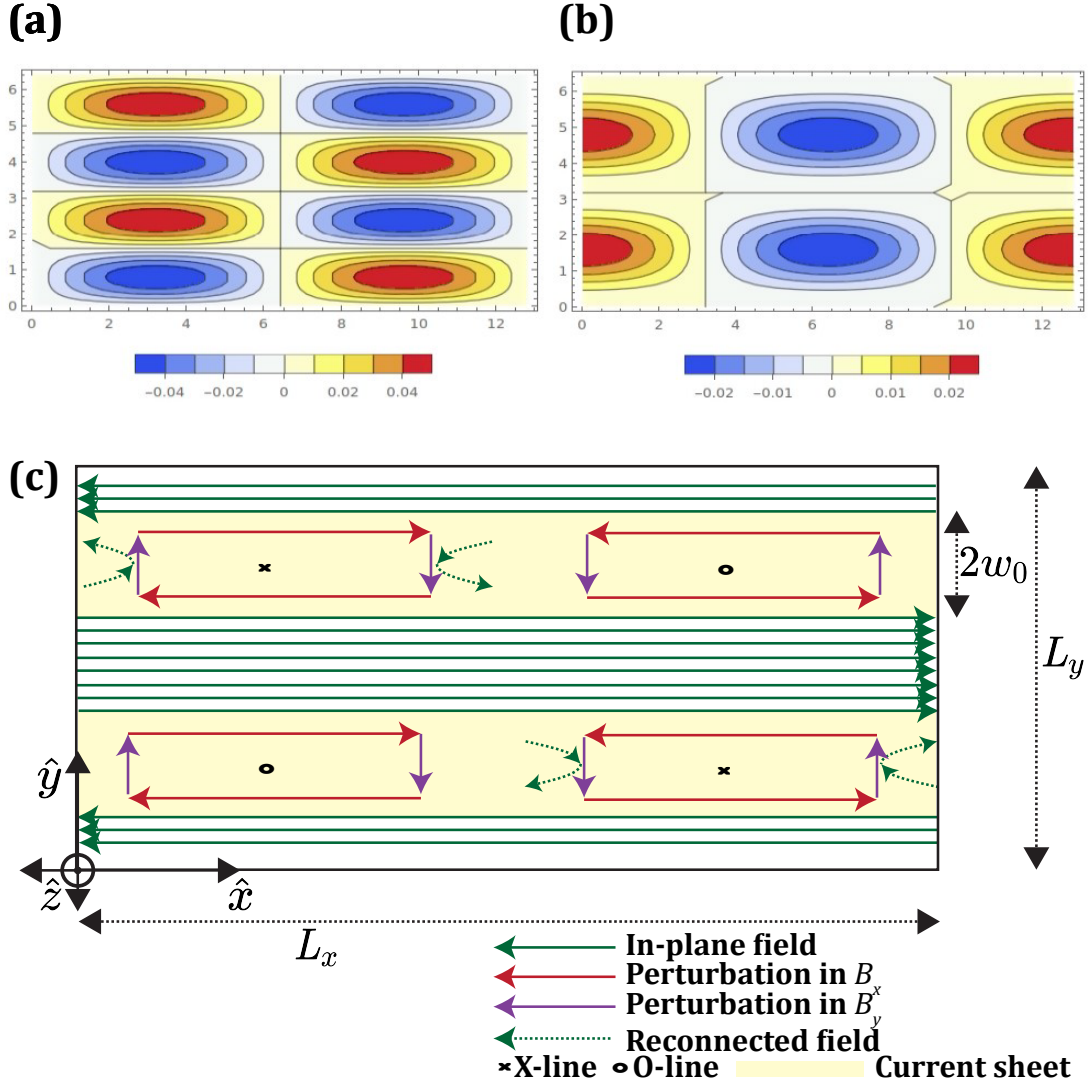


Figure 2.1: Plot of the magnetic field perturbation of the form given by Eq. (2.8) shown in panel (a) and Eq. (2.9) shown in panel (b) that seed an X-O line pair in lower current sheet at $(x, y) = (9.6, 1.6)$ and upper current sheet at $(x, y) = (3.2, 4.8)$ when simulation is initialized, shown by a sketch in panel (c).

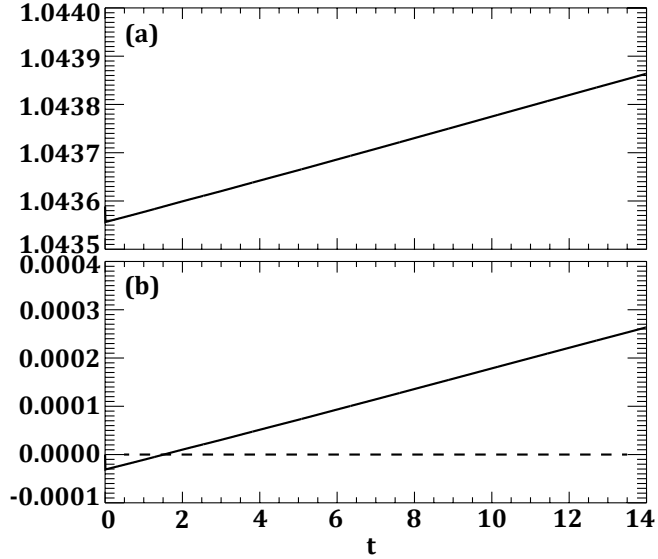


Figure 2.2: Plot of the total energy density (panel (a)) and change in total energy density (panel (b)), for the whole simulation domain, as a function of time.

good statistics since our system uses non-uniform densities at $t = 0$, Eq. (2.4). The choice of PPG makes the simulations computationally costly while ensuring excellent entropy statistics (Liang et al., 2019) by decreasing particle noise inherent to PIC codes. These numerical parameters lead to an energy change of 0.026% by $t = 14$ as shown in Fig. 2.2.

The initially uniform electron and ion temperatures are set to $T_e = 1/12$ and $T_i = 5/12$, giving the maximum density at the center of the current sheets minus n_{up} is 1.

This concludes the information necessary for simulations discussed in Chapter 5, and we next discuss code implementation of kinetic entropy-based quantities employed in Chapter 6 in detail.

2.4 Kinetic entropy-based quantities

Kinetic entropy calculations, which form the basis of calculating other quantities that are subsequently utilized in Chapter 6 for understanding energy conversion associated with changing the higher order velocity moments, have been previously implemented in Liang et al. (2019) to which readers are referred to for further details. This algorithm implemented by Liang et al. (2019) is a direct calculation of kinetic entropy. However, other methods exist, *e.g.*, discussed in Jara-Almonte & Ji (2021). We enhance Liang et al. (2019) implementation by introducing the capability to independently select the velocity-space grid scale Δv_σ for electrons and ions (Argall et al., 2022).

2.4.1 Velocity-space grid optimization

As discussed in previous work (Liang et al., 2020b), we first optimize the velocity-space grid by comparing kinetic entropy density (as defined in Eq. (1.30)) output from the code and known theoretical values at $t = 0$. As we employ a single population of drifting Maxwellian distribution (Eq. (1.2)), using Eq. (1.30) the kinetic entropy density for a Maxwellian distribution s_M can be exactly written as

$$s_M(\mathbf{r}, t) = \frac{3}{2}k_B n(\mathbf{r}, t) \left[1 + \ln \left(\frac{2\pi k_B T}{m[n(\mathbf{r}, t)]^{2/3}} \right) \right], \quad (2.10)$$

where we retain the dependencies on \mathbf{r} . This shows that since number density n is non-uniform, so is s_M , whose 1-D cut is taken at the lower X-line and shown in Fig. 2.3. We center the plot such that the origin is around the lower X-line,

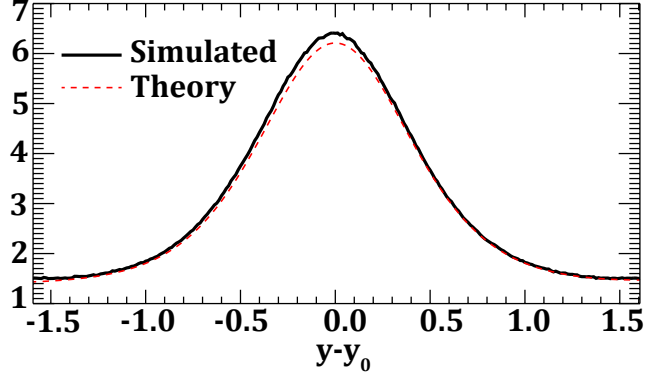


Figure 2.3: A 1-D cut (taken at the lower X-line) of the kinetic entropy density for electron s_e centered around the lower X-line at $t = 0$ displaying its profile. In black is shown the simulated s_e for $\Delta v_e = 1.33$, and in red dashed is shown the theoretical profile.

i.e., $(x_0, y_0) = (0, 0)$ denotes the lower X-line. Using various Δv_e and Δv_i , we test the agreement and then choose $\Delta v_e = 1.33$ and $\Delta v_i = 0.629$, where we note that ions are not the focus of the simulations. Our choice of optimal Δv_e leads to an agreement within $\pm 3\%$ at the center of current sheet and within $\pm 1\%$ at the asymptotic upstream as seen in Fig. 2.3.

2.4.2 Velocity-space kinetic entropy density flux

The kinetic entropy density flux \mathcal{J}_σ , with its subscript σ suppressed, which we will also see in Chapter 6 as Eq. (6.13), is

$$\mathcal{J} = \mathcal{J}_v - k_B \mathbf{u} n \ln \left(\frac{n \Delta^3 r}{N} \right). \quad (2.11)$$

Here, \mathcal{J}_v is the velocity-space kinetic entropy density flux given by

$$\mathcal{J}_v = -k_B \int \mathbf{v} f \ln \left(f \frac{\Delta^3 v}{n} \right) d^3 v. \quad (2.12)$$

We implement Eq. (2.12) in `p3d` since its validation against a known distribution function is simpler, which we explain next. For a single population drifting Maxwellian distribution, we calculate \mathcal{J}_v using Eqs. (1.2) and (2.12) to get

$$\mathcal{J}_{v,M}(\mathbf{r}) = \frac{3}{2} k_B \mathbf{u}(\mathbf{r}) n(\mathbf{r}) \left[1 + \ln \left(\frac{2\pi k_B T}{(\Delta^3 v)^{2/3} m} \right) \right]. \quad (2.13)$$

Here, the M subscript on $\mathcal{J}_{v,M}$ denotes the value for a Maxwellian distribution. Since the simulation is initialized with out-of-plane current sheets, u_z is non-zero at $t = 0$. (Note that the inclusion of magnetic field perturbation makes u_x and u_y also non-zero but very small and the effect is akin to what we discussed earlier in Sec. 2.3.1.) Fig. 2.4 shows a 1-D cut of the simulated $\mathcal{J}_{v,z}$ taken and centered around the lower X-line and it is compared with the theoretical prediction in Eq. (2.13). We observe that simulated $\mathcal{J}_{v,M,z}$ agrees well with the theory.

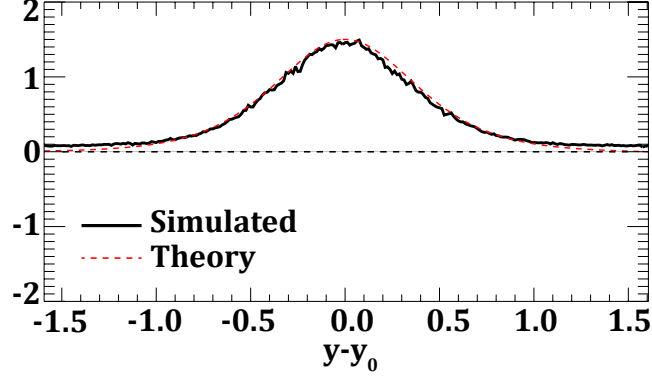


Figure 2.4: A 1-D cut (taken at the lower X-line) of the z -component of velocity-space kinetic entropy density flux $\mathcal{J}_{v,z}$ for electrons centered around the lower X-line at $t = 0$ displaying its profile. In black is shown the simulated curve and in red dashed is shown the theoretical profile, given by Eq. (2.13).

2.4.3 Velocity-space thermal kinetic entropy density flux

We use $\mathbf{v} = \mathbf{v}' + \mathbf{u}$ and rewrite Eq. (2.12), while again suppressing the subscript σ , as

$$\begin{aligned}\mathcal{J}_v &= -k_B \int (\mathbf{v}' + \mathbf{u}) f \ln \left(f \frac{\Delta^3 v}{n} \right) d^3 v \\ &= \mathcal{J}_{\text{th},v} + \mathbf{u} s_v,\end{aligned}\tag{2.14}$$

where $\mathcal{J}_{\text{th},v}$ is the velocity-space thermal entropy density flux given by

$$\mathcal{J}_{\text{th},v} = -k_B \int \mathbf{v}' f \ln \left(f \frac{\Delta^3 v}{n} \right) d^3 v.\tag{2.15}$$

In Eq. (2.14), s_v is the velocity-space kinetic entropy density, given by

$$s_v = -k_B \int f \ln \left(f \frac{\Delta^3 v}{n} \right) d^3 v,\tag{2.16}$$

which is also Eq. (6.4b), with σ subscript shown explicitly.

We implement $\mathcal{J}_{\text{th},v}$ in `p3d` which we discuss shortly. Before doing so, we note that $\mathcal{J}_{\text{th},v}$ is equivalent to \mathcal{J}_{th} utilized in Chapter 6. We observe this from Eq. (6.15) since

$$\begin{aligned}
\mathcal{J}_{\text{th}} &= -k_B \int \mathbf{v}' f \ln \left(\frac{f \Delta^3 r \Delta^3 v}{N} \right) d^3 v \\
&= -k_B \int \mathbf{v}' f \ln \left(\frac{f \Delta^3 v}{n} \right) d^3 v - k_B \int \mathbf{v}' f \ln \left(\frac{n \Delta^3 r}{N} \right) d^3 v \quad (2.17) \\
&= \mathcal{J}_{\text{th},v},
\end{aligned}$$

where the last term in Eq. (2.17) drops out since the argument in \ln is independent of \mathbf{v} , and thus can be brought out of the integral, leaving $\int \mathbf{v}' f d^3 v$ which vanishes, by definition.

We analytically calculate $\mathcal{J}_{\text{th},v}$ for a single population drifting Maxwellian distribution. After a few simple steps that involve using Eq. (2.10), we find that $\mathcal{J}_{\text{th},v}$ is identically zero. We compare $\mathcal{J}_{\text{th},v}$ from the simulation with the theoretical predictions and we also use the \mathcal{J}_v implementation and Eq. (2.14) to post-process $\mathcal{J}_{\text{th},v}$ for comparison with the code-output result. Fig. 2.5 shows a 1-D cut (taken and centered around the lower X-line) of the z -component of $\mathcal{J}_{\text{th},v}$, *i.e.*, $\mathcal{J}_{\text{th},v,z}$ in panel (a), with panel (b) showing the post-processed version and panel (c) showing their difference. We note the apparent mismatch between the theory predictions (red dashed line in panel (a) of Fig. 2.5) and simulated result in the current sheet, which can be reconciled by recalling that we use weighted macroparticles in the simulations. In the validation phase, we employ $\text{PPG} = 100$ simulations and we see

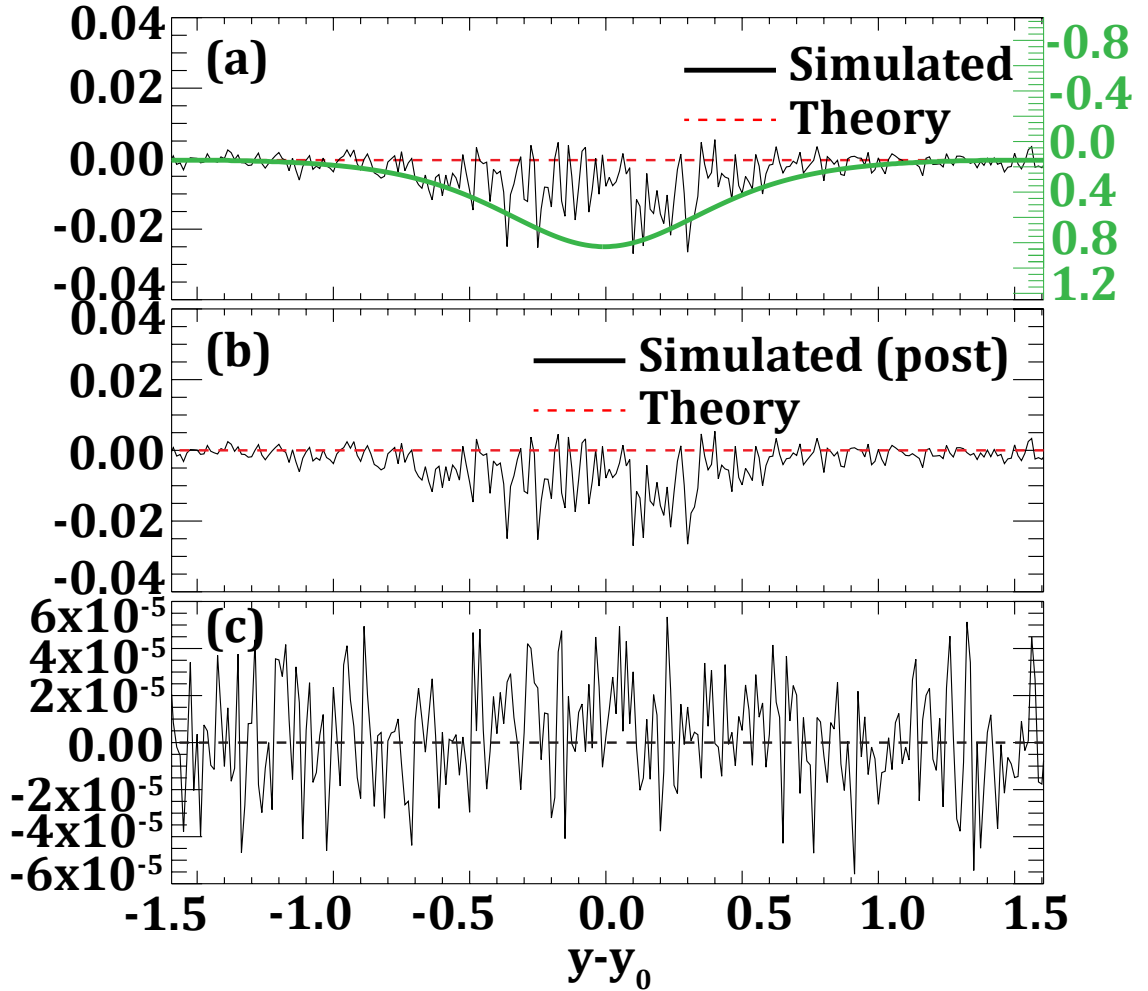


Figure 2.5: 1-D cut (taken and centered around the lower X-line) of the z -component of velocity-space thermal kinetic entropy density flux $\mathcal{J}_{\text{th},v,z}$ for electrons at $t = 0$. Panels (a) and (b) show $\mathcal{J}_{\text{th},v,z}$ simulated from our implementation in p3d and post-processed, respectively. The green curve in panel (a) shows the profile of the weight of the macroparticles, the red dashed line denotes the theoretical value and the black curves are the simulated values in panels (a) and (b). In panel (c), the difference between the simulated $\mathcal{J}_{\text{th},v,z}$ shown in panel (a) and (b) is plotted, where we observe less than a 1% error when comparing the two methods of obtaining $\mathcal{J}_{\text{th},v}$.

similar profiles for $\mathcal{J}_{\text{th},v}$ but the noise level in the upstream and current sheet regions (at $t = 0$) is approximately 16 times higher (not shown). Due to the extremely high PPG for the PPG=25,600 simulations used in this dissertation, we see the effects of the non-uniform weight assigned to the macroparticles, which manifests as simulated $\mathcal{J}_{\text{th},v,z}$ having a worse agreement with the theory in the current sheet region. To calculate weight W (a non-negative number), we utilize Eq. (B2) from Liang et al. (2019) that gives $W = N_{\text{cell}}/(PPG \times a)$, where N_{cell} is the number of actual particles in a spatial grid cell, which is $\sum_k N_{jk} = N_j$, N_{jk} is the actual number of particle in the jk th phase-space bin, and a is called “ a factor” and it is the ratio of actual particles per macroparticle which for the simulations used in this dissertation is $a = 1318.75$. (Readers are referred to Liang et al. (2019) for details on how “ a factor” is determined.) Doing so, we obtain the profile for W denoted by the green curve in Fig. 2.5 panel (a) where $W \approx 0.14$ in the upstream regions and $W \approx 0.83$ at the center of the current sheet. Here, we note a direct correlation between weight and quality of agreement between the simulated and theoretical values. The agreement is best when W is low, which is in the upstream regions. As W starts to increase, we observe that the agreement worsens. Thus, we can trace the disagreement seen in the current sheet region to the usage of non-uniform number density at initialization.

2.4.4 Relative entropy density

Prior to delving into the forthcoming discussion, we note that the implementation of relative entropy density in `p3d` that we are about to discuss is recent and was not utilized in the simulations examined in Chapter 6 of this dissertation. This implies the simulated results we will be addressing concerning relative entropy density and relative entropy per particle are from separate simulations that are not part of Chapter 6 of this dissertation. However, we think that this discussion will shed new light on the outcomes presented in Chapter 6.

2.4.4.1 Implementation in `p3d`

We now discuss the implementation and validation in `p3d` of relative entropy density $s_{v,\text{rel}}$ (with its σ subscript suppressed) that is defined as

$$s_{v,\text{rel}} = -k_B \int f \ln \left(\frac{f}{f_M} \right) d^3v. \quad (2.18)$$

We note that this equation is also seen in Chapter 6 as Eq. (6.6). Here f_M is the “Maxwellianized distribution function” (Grad, 1965) given by, with σ subscript suppressed,

$$f_M = n \left(\frac{m}{2\pi k_B \mathcal{T}} \right)^{3/2} e^{-m(\mathbf{v}-\mathbf{u})^2/2k_B \mathcal{T}}, \quad (2.19)$$

where n , \mathbf{u} , and \mathcal{T} are based on f . Eq. (2.19) also appears as Eq. (6.8) in Chapter 6. As the previously implemented subroutine from kinetic entropy density (Liang et al., 2019) creates f and f_M , we use them to implement the $s_{v,\text{rel}}$ calculation in

p3d according to Eq. (2.18).

For a single plasma population of drifting Maxwellian distribution we use at $t = 0$ in the simulations for this dissertation, Eq. (2.18) readily gives $s_{v,\text{rel}} = 0$. However, as in the case for $\mathcal{J}_{\text{th},v,z}$ seen in Fig. 2.5, a comparison of the simulated result with the theoretical prediction leads to interesting findings. In order to understand them, we first note that $s_{v,\text{rel}}$ for any arbitrary non-Maxwellian distribution is negative. Panel (a) of Fig. 2.6 shows a 1-D cut of $s_{v,\text{rel}}$ for electrons taken and centered at the lower X-line where we again overlay the non-uniform particle weight (shown in green). In doing so, we again notice that 1) the simulated signal is noisier in the current sheet where the weight is higher than in the background where the weight is lower, 2) the profile of the simulated quantity aligns well with that of the weight which implies that the cause of non-uniform simulated signal can be traced back to the non-uniform number density profile. However, looking at the 1-D cut of $s_{v,\text{rel}}/n$, *i.e.*, the relative entropy per particle shown in panel (b), we note that this issue with non-uniform number density disappears. However, we now clearly observe the mismatch between the theoretical prediction of $s_{v,\text{rel}}/n$ (red dashed line) and the simulated result. This disagreement originates from using a finite number of macroparticles in the simulations and is at the noise level inherent in PIC simulations. This is evident from panel (c) which is the PIC simulation of the same system but with $\text{PPG} = 6400$, implying an increase in PIC noise by a factor of 2 due to the reduction in PPG by a factor of 4. Moreover, in panel (d), we repeat the simulation with $\text{PPG} = 400$, *i.e.*, an increase in PIC noise by a factor of 8 due to the reduction in PPG by a factor of 64. We observe that going from $\text{PPG} = 400$ to $\text{PPG} = 6400$, $s_{v,\text{rel}}/n$

goes from ~ 0.08 to ~ 0.013 , implying a factor of ~ 6 decrease, which is close to $\sqrt{6400/400} = 4$. Similarly, we find that going from $\text{PPG} = 6400$ to $\text{PPG} = 25600$, $s_{v,\text{rel}}/n$ goes from ~ 0.013 to ~ 0.004 , implying a factor of ~ 3 decrease, which is close to $\sqrt{25600/6400} = 2$. This discussion indicates that the apparent mismatch seen in panel (b) is physical using the initial conditions employed in the PIC simulation and that it can be traced back to PIC simulations not creating f or its Maxwellianized distribution f_M to absolute precision. Additionally, the fact that the simulated $s_{v,\text{rel}}/n < 0$ indicates that the initial Maxwellian distribution f produced by p3d is not as precise as the Maxwellianized distribution f_M created by p3d.

2.4.4.2 Subtlety with relative entropy calculation

A subtlety arises in the computation of relative entropy, which becomes evident when comparing relative entropy per particle obtained directly from the simulation (utilizing the relative entropy implementation discussed in Sec. 2.4.4.1) and the post-processed relative entropy per particle obtained using the expression $s_{v,\text{rel}}/n = s_v/n - s_{v,\bar{\mathcal{E}}}/n$. Here, $s_{v,\bar{\mathcal{E}}}$ (with σ subscript suppressed) is

$$\frac{s_{v,\bar{\mathcal{E}}}}{n} = \frac{3}{2}k_B \left[1 + \ln \left(\frac{2\pi k_B \mathcal{T}}{m(\Delta^3 v)^{2/3}} \right) \right]. \quad (2.20)$$

This appears as Eq. (6.24) in Sec. 6.5.3. The post-processed $s_{v,\text{rel}}/n$ can then be readily obtained by simple subtraction.

We present a comparison of these quantities in Fig. 2.7 for electrons at time

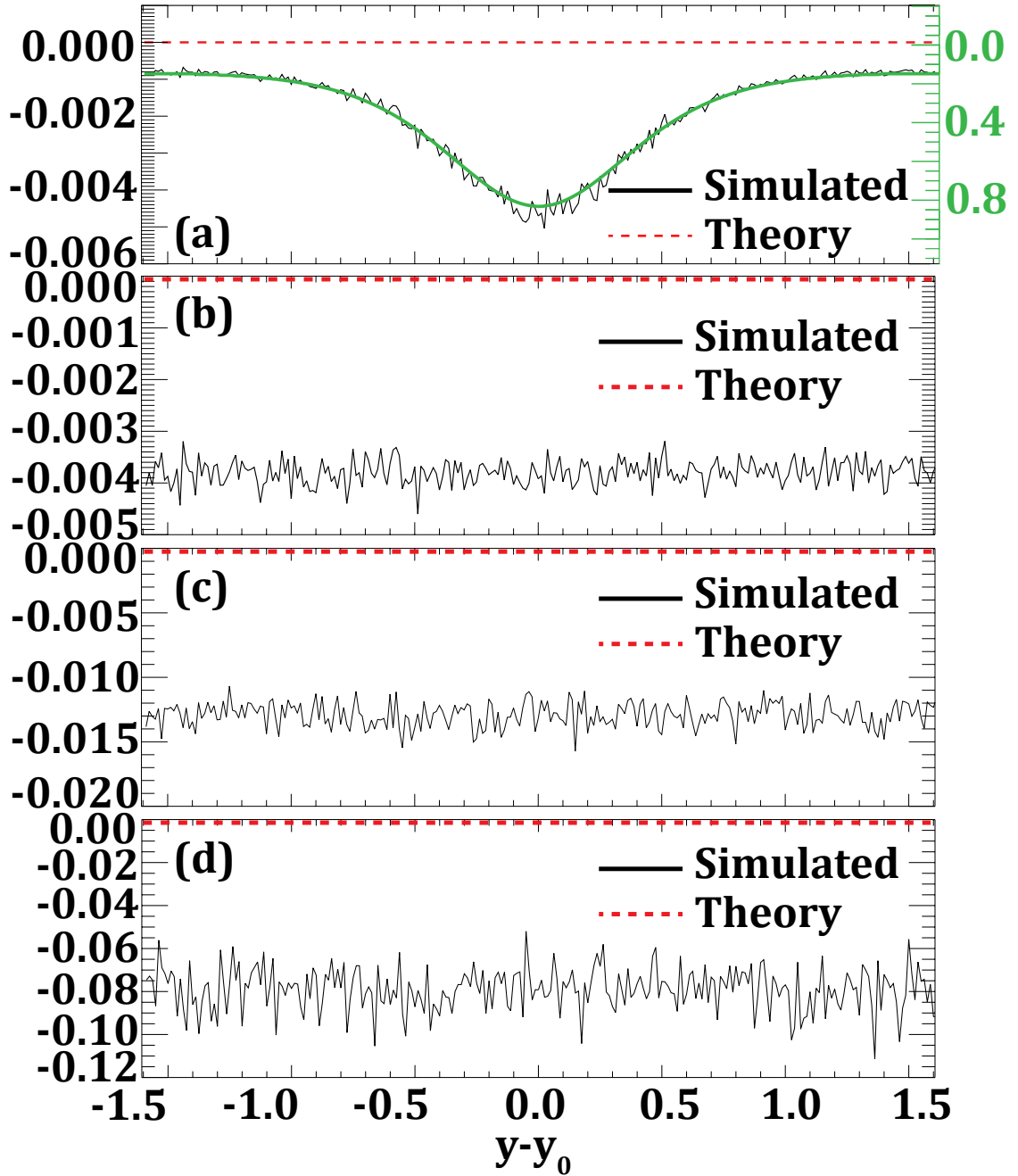


Figure 2.6: 1-D cut (taken and centered around the lower X-line) of relative entropy for electrons at $t = 0$ using $\text{PPG} = 25,600$. Panel (a) shows relative entropy density $s_{v,\text{rel}}$ and (b) shows relative entropy per particle $s_{v,\text{rel}}/n$ simulated from our implementation in `p3d`. The green curve in panel (a) shows the non-uniform macroparticles weight, red dashed line denotes the theoretical value and the black curves denote the simulated values in panels (a) and (b). Panels (c) and (d) repeat panel (b) but for $\text{PPG} = 6400$ and $\text{PPG} = 400$ simulations, respectively.

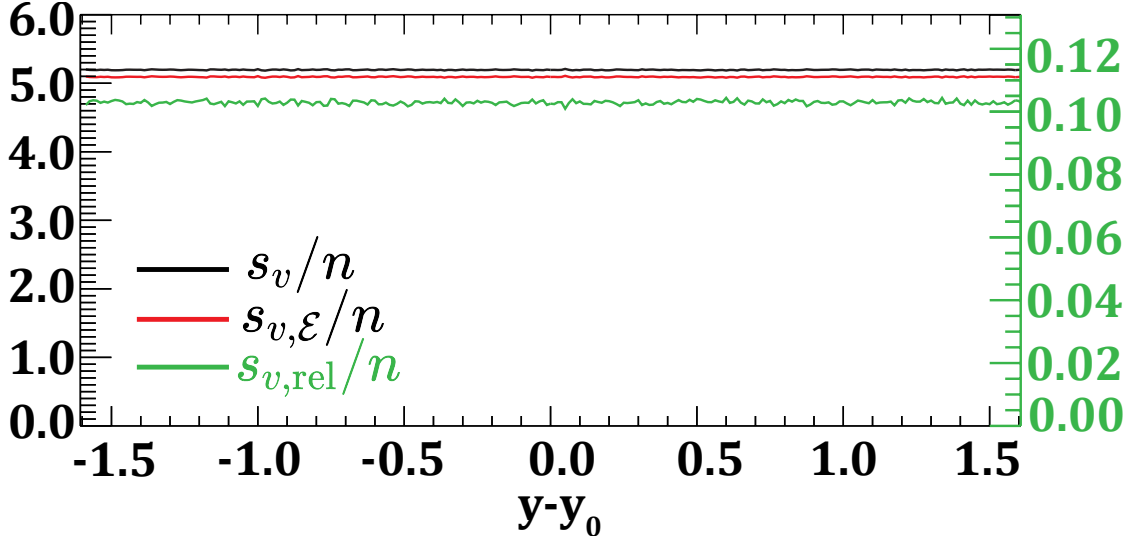


Figure 2.7: Plots of 1-D cuts (taken and centered around the lower X-line) for electrons at $t = 0$. In black, red, and green are simulated s_v/n , the simulated $s_{v,\epsilon}/n$, and the computed value of $s_{v,rel}/n$, respectively.

$t = 0$. We present 1-D cuts centered around the lower X-line. The simulated value of s_v/n is depicted with a black line, while the simulated value of $s_{v,\epsilon}/n$ is represented by a red line. Furthermore, we compute the value of $s_{v,rel}/n$ by subtracting the red line from the black line, and this result is visualized using a green line. Unlike the simulated $s_{v,rel}/n$ produced from `p3d` seen in panel (b) of Fig. 2.6, we note that $s_{v,rel}/n$ is instead positive, which is not surprising given that we observe $s_{v,\epsilon}/n < s_v/n$, which, according to the theory, should be equal at $t = 0$.

When we repeat this validation exercise for the $\text{PPG} = 6400$ simulation, with different Δv_e and $\text{PPG} = 400$ with the same Δv_e (plots not shown here), we obtain a post-processed $s_{v,rel}/n \sim 0.1$, with noisier data for lower PPG simulation. This indicates that the post-processed $s_{v,rel}/n$ is independent of Δv , which one can show analytically through straightforward algebraic analysis (which we omit here). An-

alytically, it can also be shown that the post-processed $s_{v,\text{rel}}/n$ relies solely on the parameters n , \mathcal{T} , and the kinetic entropy density. This, in turn, implies that the observed discrepancy in the post-processed $s_{v,\text{rel}}/n$ is due to the finite precision of PIC codes, which prevents the generation of an “ideal” Maxwellian distribution during initialization, with finite PPG as previously discussed in Sec. 2.4.4.1. This discussion underscores the value of directly computing $s_{v,\text{rel}}$ from the `p3d` code rather than relying on post-processing due to the sensitivity of $s_{v,\text{rel}}$ to both s_v and $s_{v,\mathcal{E}}$, which exhibit very similar signatures and are close in amplitudes. Nevertheless, as we will elaborate in the next section, the Lagrangian time derivative $d/dt = \partial/\partial t + \mathbf{u}_\sigma \cdot \nabla$, with \mathbf{u}_σ representing the bulk flow of the species σ , of relative entropy per particle obtained through post-processing, while not on par with the data derived directly from the code, can still provide valuable insights.

2.4.4.3 Lagrangian time derivative of relative entropy per particle

For the simulations used in Chapter 6, we require the Lagrangian time derivative of $s_{v,\text{rel}}$ and we obtain it via post-processing, *i.e.*, we subtract off the Lagrangian time derivative of $s_{v,\mathcal{E}}/n$ from the Lagrangian time derivative of s_v/n so that $d(s_{v,\text{rel}}/n)/dt = d(s_v/n)/dt - d(s_{v,\mathcal{E}}/n)/dt$. To examine if post-processing leads to numerical issues (due to what we discussed in Sec. 2.4.4.2), we compare $d(s_{v,\text{rel}})/dt$ obtained from $s_{v,\text{rel}}$ that is output from `p3d` using the relative entropy implementation discussed in Sec. 2.4.4.1 and a post-processed $d(s_{v,\text{rel}})/dt$. This is illustrated in Fig. 2.8 panel (a) and panel (b), respectively, for electrons at $t = 13$ from the PPG

= 6400 simulation. It demonstrates that the post-processing method of obtaining $d(s_{v,\text{rel}})/dt$, whilst not ideal, yields very similar results (the 2D structures are quite similar).

A careful examination of the 2D plots presented in Figure 2.8 reveals the presence of minor discrepancies between the two methods. They are further exemplified by the 1-D cuts (taken and centered at the lower X-line), and shown in panels (c) and (d) of Figure 2.8, displaying the horizontal cut and vertical cut, respectively. Both have black curves showing the result obtained from `p3d` and red curves showing the result obtained via post-processing. From both the 2D plots and 1-D cuts, we note that post-processing overestimates values everywhere, including the EDR region, which is $x - x_0 \in (-2, 2), y - y_0 \in (-0.35, 0.35)$. Quantifying this discrepancy, we find that, *e.g.*, at the lower X-line, post-processed data is $\approx 36\%$ higher relative to the `p3d` data.

2.5 Dynamics of the reconnecting system

Due to the choice of the simulation domain size, the reconnecting system never reaches steady-state and reconnection terminates when the island width becomes equal to half the width of the simulation domain. In Fig. 2.9, we show the reconnection rate in black, while its time rate of change is shown in red, as a function of time for the lower current sheet from the simulations used in Chapters 5 and 6. At $t = 13$, the reconnection rate increases most rapidly. Therefore, this particular time instant is expected to exhibit the most dynamic evolution of the system, making

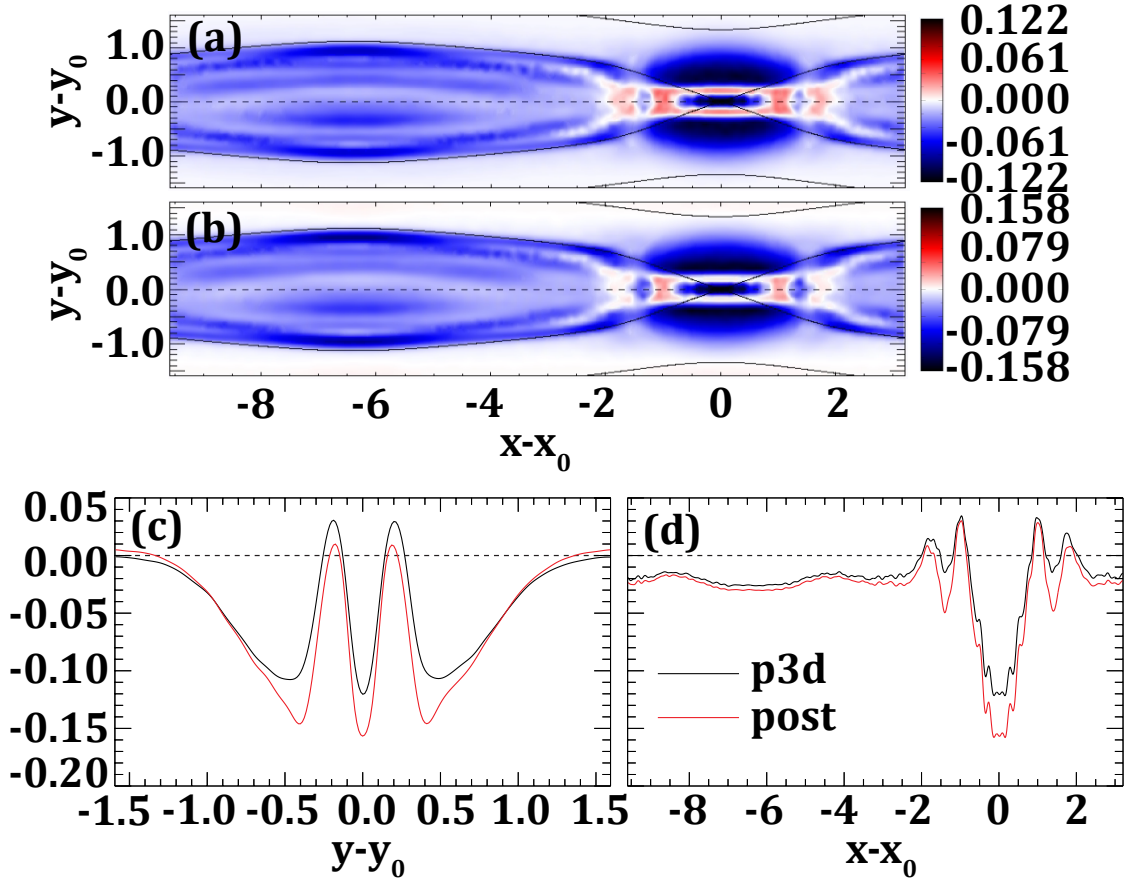


Figure 2.8: Plots of $d(s_{v,rel})/dt$ for electrons at $t = 13$ are shown. Panel (a) and (b) show 2D plots centered around the lower X-line, with the former displaying data from p3d implementation of relative entropy density and the latter data obtained via post-processing. Panel (c) and (d) show overplots of the 1-D cuts (taken and centered at the X-line) of data shown in panel (a) (in black color) and (b) (in red color), with former showing the horizontal cut and the latter showing the vertical cut.

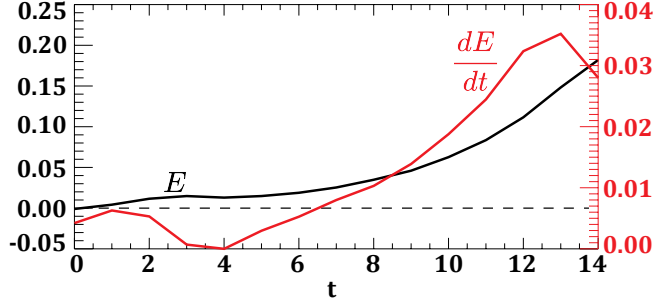


Figure 2.9: Plot of reconnection rate E and its instantaneous time rate of change dE/dt as a function of time in black and red, respectively, for the lower current sheet.

it an ideal choice for investigating energy conversion parameters such as pressure-strain interaction (as discussed in Chapter 5) and the Lagrangian time derivative of $d(s_{v,\text{rel}}/n)/dt$ (as explored in Chapter 6).

In Chapter 6, the Lagrangian (or total) time derivatives of various quantities are computed. To calculate the $\partial/\partial t$ term, we employ a central finite difference scheme utilizing data from $t = 12$ and $t = 14$. However, given our focus on electrons and considering that the aforementioned data are at ion time scales, we compare the obtained results with those derived from a finite difference between $t = 12.96$ and $t = 13.04$, which are time instances at the electron time scale and are obtained by rerunning the simulation with a higher cadence of data output. We observe that the results from the two approaches differ by less than 5%, which we consider to be negligible for the purposes of our study. Then, the $\mathbf{u}_\sigma \cdot \nabla$ term is calculated at $t = 13$ and added to the $\partial/\partial t$ term and we finally obtain the d/dt term.

We employ a smoothing procedure by using a built-in “smooth” function in IDL, that performs a boxcar average of the specified width (more on which can be found at <https://www.13harrisgeospatial.com/docs/SMOOTH.html>), to re-

cursively smooth the raw data output by the simulation four times over four cells. Afterward, we take the necessary spatial or temporal derivative. To ensure that the smoothing we perform is not excessive, we try different approaches to smoothing the data, including using a width of two cells for a varying number of iterations and a width of four cells for a varying number of iterations. We determine our smoothing approach by finding when we start to see clearer, sharper structures without over-smoothing. To confirm that oversmoothing is not occurring, we compare 1-D cuts of the unsmoothed data with the smoothed data. In Fig. 2.10, we show 1-D cuts of electron $\text{Pi} - \text{D} \equiv \Pi_{e,jk} \mathcal{D}_{e,jk}$ which we discussed in Sec. 1.6 and is the subject of analysis in Chapters 3 - 5, taken at the lower X-line. The black curve represents the raw data (a smoothing width of zero cells, iterated zero times). The other five curves give the result of smoothing over four cells for the given number of iterations. Our interpretation is that smoothing over four cells with two and four iterations is reasonably similar and captures the trend of the data while using six or more iterations results in oversmoothing, *i.e.*, the smoothed data is no longer representative of the raw data. We, therefore, opt to use four iterations over four cells, displayed in green curves in Fig. 2.10.

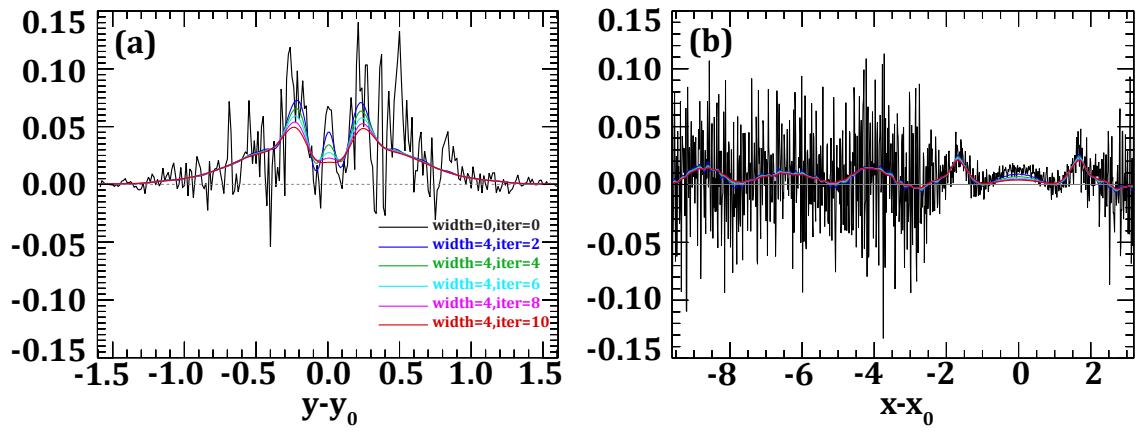


Figure 2.10: 1-D cuts of $\text{Pi} - \text{D}$ for electrons (taken and centered at the lower X-line), with panel (a) showing the horizontal cut and panel (b) showing the vertical cut. In both panels, various smoothing procedures are overplotted with the raw simulation data (black curves) and are color-coded as described in the legend.

Chapter 3

Pressure-Strain Interaction: I. On Compression, Deformation, and Implications For Pi-D

3.1 Introduction

Weakly collisional plasmas are important in many settings, from heliophysics to planetary magnetospheres to astrophysics (Howes, 2017). A host of plasma phenomena take place in such settings, including magnetic reconnection, plasma turbulence, and collisionless shocks. The dearth of collisions in many settings of interest implies that these plasmas can be far from local thermodynamic equilibrium (LTE). In the study of these physical phenomena, one of the forefront research questions is how energy is converted during each process, especially when non-LTE effects greatly affect the dynamics at the micro-, meso-, and even the macro-scale (Matthaeus et al., 2020).

We note here that unlike in the equations in Chapter 1, here we mostly suppress the subscript σ (that denotes species) for the sake of brevity. The same is applicable to quantities discussed in chapters 4 and 5.

A quantity contributing to non-LTE energy conversion that has received in-

Phys. Plasmas, 29, 122306 (2022)

Contributing authors: Paul A. Cassak, M. Hasan Barbhuiya

tense scrutiny over the last few years is the pressure-strain interaction, written as $-(\mathbf{P} \cdot \nabla) \cdot \mathbf{u}$, where \mathbf{P} is the pressure tensor of a species of a fluid or plasma and \mathbf{u} is its bulk flow velocity (Del Sarto et al., 2016; Yang et al., 2017a,b; Del Sarto & Pegoraro, 2018). In terms of the phase space density f (the number of particles per unit position space volume and velocity space volume), the bulk flow velocity is $\mathbf{u} = (1/n) \int d^3v \mathbf{v} f$, where \mathbf{v} is the velocity space coordinate, $n = \int d^3v f$ is the number density, and the integrals are over all velocity space, and the elements of the pressure tensor \mathbf{P} are (classically and non-relativistically) $P_{jk} = m \int v'_j v'_k f d^3v$, where j, k are indices for the spatial dimensions, m is the constituent particle mass, and $\mathbf{v}' = \mathbf{v} - \mathbf{u}$ is the peculiar (random) velocity.

To see why pressure-strain interaction is important for energy conversion, consider the thermal (internal) energy density $\mathcal{E}_{th} = 3\mathcal{P}/2 = \int (\frac{1}{2}mv'^2) f d^3v$, where $\mathcal{P} = (1/3)\text{tr}(\mathbf{P}) = (1/3)P_{jj}$ is the effective pressure, using the Einstein summation convention for repeated indices here and throughout. Its time evolution is described by (Braginskii, 1965)

$$\frac{\partial \mathcal{E}_{th}}{\partial t} + \nabla \cdot (\mathcal{E}_{th} \mathbf{u}) = -(\mathbf{P} \cdot \nabla) \cdot \mathbf{u} - \nabla \cdot \mathbf{q} + \dot{Q}_{\text{visc,coll}}, \quad (3.1)$$

where $\mathbf{q} = \int (1/2)mv'^2 \mathbf{v}' f d^3v$ is the vector heat flux density and $\dot{Q}_{\text{visc,coll}}$ is the volumetric viscous heating rate via collisions, where we use the word viscous regardless of the functional form of the collisional heating. The time evolution of the bulk

kinetic energy density $\mathcal{E}_k = (1/2)mnu^2$ is given by (Braginskii, 1965)

$$\frac{\partial \mathcal{E}_k}{\partial t} + \nabla \cdot (\mathbf{u}\mathcal{E}_k + \mathbf{u} \cdot \mathbf{P}) = (\mathbf{P} \cdot \nabla) \cdot \mathbf{u} + n\mathbf{u} \cdot \mathbf{F} + R_{\text{coll}}, \quad (3.2)$$

where \mathbf{F} is the net body force and R_{coll} is the inter-species collisional drag force power density. The pressure-strain interaction $-(\mathbf{P} \cdot \nabla) \cdot \mathbf{u}$ arises in each equation with opposite signs, so it describes the rate per unit volume that energy is converted between bulk flow and thermal. The minus sign is included in the definition so a positive value describes a contribution towards increasing thermal energy density. While these equations have been known for years, a watershed moment came recently when it was emphasized that the pressure-strain interaction is key to describing changes in thermal energy in plasmas (Del Sarto et al., 2016; Yang et al., 2017b,a; Del Sarto & Pegoraro, 2018).

The pressure-strain interaction can be simplified by defining the strain rate tensor $\nabla \mathbf{u}$, which can be decomposed (Batchelor, 2000; Del Sarto & Pegoraro, 2018) as $\nabla \mathbf{u} = \mathbf{S} + \mathbf{\Omega}$ into a symmetric (irrotational) strain rate tensor \mathbf{S} with elements $S_{jk} = (1/2)(\partial u_k / \partial r_j + \partial u_j / \partial r_k)$ and an anti-symmetric strain rate tensor $\mathbf{\Omega}$ with elements $\Omega_{jk} = (1/2)(\partial u_k / \partial r_j - \partial u_j / \partial r_k)$. A flow with non-zero \mathbf{S} but zero $\mathbf{\Omega}$ has “pure straining motion” (Batchelor, 2000); it strains a fluid element without rotating it. In contrast, a flow with non-zero $\mathbf{\Omega}$ but zero \mathbf{S} is “rigid body rotation” (Batchelor, 2000), which rotates a fluid element without changing its shape. A further decomposition of \mathbf{S} was introduced (Batchelor, 2000; Del Sarto et al., 2016; Yang et al., 2017b; Del Sarto & Pegoraro, 2018) by writing $\mathbf{S} = (1/3)\mathbf{I}(\nabla \cdot \mathbf{u}) + \mathcal{D}$,

i.e.,

$$S_{jk} = \frac{1}{3}\delta_{jk}(\nabla \cdot \mathbf{u}) + \mathcal{D}_{jk}, \quad (3.3)$$

where \mathbf{I} is the identity tensor, δ_{jk} is the Kroenecker delta and \mathcal{D} is the traceless strain rate tensor with elements

$$\mathcal{D}_{jk} = \frac{1}{2} \left(\frac{\partial u_j}{\partial r_k} + \frac{\partial u_k}{\partial r_j} \right) - \frac{1}{3}\delta_{jk}(\nabla \cdot \mathbf{u}). \quad (3.4)$$

Physically, $(1/3)\mathbf{I}(\nabla \cdot \mathbf{u})$ describes compression/expansion, while \mathcal{D} describes the incompressible deformation of a fluid element (Batchelor, 2000; Del Sarto & Pegoraro, 2018), which is a volume-preserving change of shape of the fluid element.

The pressure-strain interaction is then written in a number of equivalent ways. In terms of the strain rate tensor, $-(\mathbf{P} \cdot \nabla) \cdot \mathbf{u} = -\mathbf{P} : \nabla \mathbf{u} = -P_{jk}(\partial u_k / \partial r_j)$. Using $\nabla \mathbf{u} = \mathbf{S} + \mathbf{\Omega}$, it is immediately found that $\mathbf{P} : \mathbf{\Omega} = 0$ since \mathbf{P} is symmetric under interchange of indices, so rigid body rotation does not contribute to pressure-strain interaction (Del Sarto et al., 2016). Consequently, $-(\mathbf{P} \cdot \nabla) \cdot \mathbf{u} = -\mathbf{P} : \mathbf{S} = -P_{jk}S_{jk}$, *i.e.*, pressure-strain interaction only has contributions from the pure straining motion portion. Further, one decomposes the pressure tensor as

$$\mathbf{P} = \mathcal{P}\mathbf{I} + \mathbf{\Pi}, \quad (3.5)$$

where $\mathbf{\Pi}$ is the deviatoric pressure tensor that describes the non-isotropic part of the pressure tensor. While the diagonal elements of \mathbf{P} must be non-negative, all elements of $\mathbf{\Pi}$ can be either positive or negative. Using the decomposition of \mathbf{S} in

Eq. (3.3) with \mathcal{D} defined in Eq. (3.4) and the pressure decomposed in Eq. (3.5), one finds

$$-(\mathbf{P} \cdot \nabla) \cdot \mathbf{u} = -\mathcal{P}(\nabla \cdot \mathbf{u}) - \Pi_{jk} \mathcal{D}_{jk}, \quad (3.6)$$

where the cross-terms vanish because $\mathbf{\Pi}$ and \mathcal{D} are both traceless. The benefit of this decomposition is that the first term (including the minus sign), called pressure dilatation, describes the power density of heating due to bulk compression ($\nabla \cdot \mathbf{u} < 0$) or cooling due to bulk expansion ($\nabla \cdot \mathbf{u} > 0$). The second term (including the minus sign) has been called (Yang et al., 2017b) $\text{Pi} - \text{D}$, which is the power density due to incompressible deformation (Del Sarto & Pegoraro, 2018). $\text{Pi} - \text{D}$ was also called “collisionless viscosity” because it is analogous in form to collisional viscous heating (Yang et al., 2017a).

Much has been learned about the pressure-strain interaction and $\text{Pi} - \text{D}$ in the context of plasma physics. The pressure-strain interaction was studied in strongly magnetized plasmas (Hazeltine et al., 2013), including the recognition that the gyroviscous contribution to the pressure-strain interaction vanishes identically. The fluid description of the contributions to the pressure-strain interaction was studied for the case with zero heat flux density (Del Sarto et al., 2016; Del Sarto & Pegoraro, 2018). It was shown (Yang et al., 2017b) that for a periodic or closed domain in a purely collisionless system, the volume average of Eq. (3.1) implies that $\langle -(\mathbf{P} \cdot \nabla) \cdot \mathbf{u} \rangle$ is the only term that can change the total thermal energy $E_{th} = \int d^3r \mathcal{E}_{th}$ of the system, where angular brackets denote a volume average. Interestingly, the same study showed in simulations of plasma turbulence that $\text{Pi} - \text{D}$ could be locally positive or

negative (since elements of both $\mathbf{\Pi}$ and \mathcal{D} can be positive or negative).

Numerous studies have since investigated the pressure-strain interaction and $\text{Pi} - \text{D}$ using numerical simulations. $\text{Pi} - \text{D}$ is stronger in coherent structures (current sheets) than in the bulk in plasma turbulence (Yang et al., 2017a). The pressure-strain interaction was highest in regions with current sheets and high vorticity (Pezzi et al., 2019). $\text{Pi} - \text{D}$ was found to successfully identify regions of strong energy conversion in dipolarization fronts (Sitnov et al., 2018; Song et al., 2020). The pressure-strain interaction dominates other energy conversion metrics at small length scales (Yang et al., 2019b), and was shown to account for the net temperature increase in simulations of turbulence (Pezzi et al., 2019; Yang et al., 2022). A recent study compared the pressure-strain interaction during reconnection and turbulence, finding that pressure dilatation at current sheets was more important in turbulence than in reconnection (Pezzi et al., 2021). $\text{Pi} - \text{D}$ increases with plasma beta for ions, but the dependence is weak for electrons (Parashar et al., 2018). In island coalescence, pressure-strain interaction does not depend strongly on electron mass or system size (Du et al., 2018). It was suggested that pressure-strain interaction contributes to the break in the turbulent spectrum at ion (Hellinger et al., 2022) and electron (Arró, G. et al., 2022) scales, and therefore is a critical piece of the termination of the turbulent cascade (Matthaeus et al., 2020). Importantly, $\text{Pi} - \text{D}$ and the heat flux divergence have similar contributions in turbulence (Du et al., 2020), and the heat flux divergence can oppose the pressure-strain interaction (Fadanelli et al., 2021).

The pressure-strain interaction, including $\text{Pi} - \text{D}$, has also been studied observationally, facilitated greatly by the high resolution measurements afforded by

the Magnetospheric Multiscale (MMS) mission (Burch et al., 2016a). In the turbulent magnetosheath, it was found that pressure-dilatation contributed more to the pressure-strain interaction than $\text{Pi} - \text{D}$ (Chasapis et al., 2018), as would later be seen in simulations (Pezzi et al., 2021). A statistical study of $\text{Pi} - \text{D}$ in the turbulent magnetosheath found that it is spatially concentrated near current sheets as in the simulations, but is small within current sheets (Bandyopadhyay et al., 2020a), as would also later be reported in simulations (Pezzi et al., 2021). A study of magnetopause reconnection found that electrons were heated at a faster rate than ions and pressure-dilatation dominated $\text{Pi} - \text{D}$ (Bandyopadhyay et al., 2021). The same study measured negative $\text{Pi} - \text{D}$. In a statistical study of reconnection diffusion regions, it was common to see a negative $\text{Pi} - \text{D}$, and the pressure-strain interaction was positive in only about half of the events (Zhou et al., 2021). They also found that the gyrotropic portion of $\text{Pi} - \text{D}$ was more important than the non-gyrotropic part. In a study of 50 turbulent magnetosheath events, both positive and negative intervals were found for both pressure dilatation and $\text{Pi} - \text{D}$ (Wang et al., 2021). A statistical study of 122 dipolarization fronts suggested that $\text{Pi} - \text{D}$ is not a significant contributor to energy conversion (Zhong et al., 2019).

Despite great advances in our knowledge about pressure-strain interaction in general, and $\text{Pi} - \text{D}$ in particular, there are a number of puzzling aspects of its interpretation, especially $\text{Pi} - \text{D}$. For example, it is not understood how $\text{Pi} - \text{D}$ is effectively a collisionless viscosity but can be negative. This Chapter is the first in a three-part series on pressure-strain interaction. Here, we point out that the strain rate tensor contains both normal deformation and shear deformation, as is well

known in continuum mechanics, which therefore implies that $P_i - D$ contains power density due to both effects. This grouping of terms complicates the interpretation of $P_i - D$ because it mixes stresses from normal flows and sheared flows. Because pressure dilatation is also associated with normal flows, we suggest an alternate decomposition of the pressure-strain interaction that groups the normal deformation with the pressure dilatation instead of shear deformation. This separates the effects of converging/diverging flow from shear strain. We calculate the terms in this alternate decomposition analytically. We then develop a physical interpretation of the compression and normal and shear deformation using kinetic theory. This allows us to determine the physical mechanisms that can make $P_i - D$ negative, thereby clarifying how to interpret such measurements. In the next part of this series (Cassak et al., 2022) (Chapter 4), we write the pressure-strain interaction in magnetic field-aligned coordinates, which further elucidates the physical contributions to the pressure-strain interaction in a magnetized plasma. In the last part of this series (Barbhuiya & Cassak, 2022) (Chapter 5), we display the pressure-strain interaction and its Cartesian and magnetic field-aligned decompositions in simulations of reconnection. We determine the physical causes for the pressure-strain interaction during reconnection.

The layout of this Chapter is as follows. An alternate decomposition of the pressure-strain interaction is derived in Sec. 3.2. We then provide a kinetic theory interpretation of the pressure-strain interaction contributions in Sec. 3.3, and discuss the causes of $P_i - D$ and the normal deformation being negative using kinetic theory in Sec. 3.4. A discussion and conclusions are in Sec. 3.5.

3.2 An Alternate Decomposition of Pressure-Strain Interaction

From the expression in Eq. (3.4), we note the important general property, well known in continuum mechanics, that the diagonal elements of \mathcal{D} are associated with normal deformation while the off-diagonal elements are associated with shear deformation. To picture this, consider a cubic fluid element. Normal deformation of the fluid element results from flow parallel to the normal to the edges of the fluid element that vary, while shear deformation results from flow in the plane of the edges of the fluid element that vary. Thus, we decompose \mathcal{D} into a normal deformation tensor $\mathcal{D}_{\text{normal}}$ and a shear deformation tensor $\mathcal{D}_{\text{shear}}$, so that

$$\mathcal{D} = \mathcal{D}_{\text{normal}} + \mathcal{D}_{\text{shear}}. \quad (3.7)$$

Here, $\mathcal{D}_{\text{normal},jk} = [(\partial u_j / \partial r_j) - (1/3)(\nabla \cdot \mathbf{u})]\delta_{jk}$ (with no sum on j) has the same diagonal elements as \mathcal{D} with its off-diagonal elements equal to zero and isolates normal deformation. Similarly, $\mathcal{D}_{\text{shear},jk} = (1/2)(\partial u_j / \partial r_k + \partial u_k / \partial r_j)$ for $j \neq k$ and $\mathcal{D}_{\text{shear},jj} = 0$ (no sum on j) has its diagonal elements equal to zero and its off-diagonal elements equal to those of \mathcal{D} , which isolates shear deformation. (A related decomposition was discussed in Refs. (Du et al., 2018; Zhou et al., 2021), but we do not make any assumptions about gyrotropy.)

In terms of this decomposition of \mathcal{D} , we write $\text{Pi} - \text{D}$ as the sum of two terms,

$$\text{Pi} - \text{D} = \text{Pi} - \text{D}_{\text{normal}} + \text{Pi} - \text{D}_{\text{shear}}, \quad (3.8)$$

where $\text{Pi} - \text{D}_{\text{normal}} = -\boldsymbol{\Pi} : \boldsymbol{\mathcal{D}}_{\text{normal}}$ and $\text{Pi} - \text{D}_{\text{shear}} = -\boldsymbol{\Pi} : \boldsymbol{\mathcal{D}}_{\text{shear}}$. In Cartesian coordinates, a brief calculation reveals that these are

$$\begin{aligned} \text{Pi} - \text{D}_{\text{normal}} &= -(\Pi_{xx}\mathcal{D}_{xx} + \Pi_{yy}\mathcal{D}_{yy} + \Pi_{zz}\mathcal{D}_{zz}) \\ &= -\left(\Pi_{xx}\frac{\partial u_x}{\partial x} + \Pi_{yy}\frac{\partial u_y}{\partial y} + \Pi_{zz}\frac{\partial u_z}{\partial z}\right), \end{aligned} \quad (3.9a)$$

$$\begin{aligned} \text{Pi} - \text{D}_{\text{shear}} &= -(2\Pi_{xy}\mathcal{D}_{xy} + 2\Pi_{xz}\mathcal{D}_{xz} + 2\Pi_{yz}\mathcal{D}_{yz}) \\ &= -P_{xy}\left(\frac{\partial u_x}{\partial y} + \frac{\partial u_y}{\partial x}\right) - P_{xz}\left(\frac{\partial u_x}{\partial z} + \frac{\partial u_z}{\partial x}\right) \\ &\quad - P_{yz}\left(\frac{\partial u_y}{\partial z} + \frac{\partial u_z}{\partial y}\right). \end{aligned} \quad (3.9b)$$

The terms separate the contributions due to normal deformation and shear deformation, respectively.

Mirroring the decomposition of $\text{Pi} - \text{D}$, we revisit the pressure-strain interaction, which describes the full rate of conversion between bulk flow and thermal energy density. Following Eq. (3.3), we decompose the symmetric strain rate tensor \mathbf{S} as

$$\mathbf{S} = \frac{1}{3}\mathbf{I}(\boldsymbol{\nabla} \cdot \mathbf{u}) + \boldsymbol{\mathcal{D}}_{\text{normal}} + \boldsymbol{\mathcal{D}}_{\text{shear}}, \quad (3.10)$$

Then, the pressure-strain interaction is decomposed into three pieces,

$$-(\mathbf{P} \cdot \boldsymbol{\nabla}) \cdot \mathbf{u} = -\mathcal{P}(\boldsymbol{\nabla} \cdot \mathbf{u}) + \text{Pi} - \text{D}_{\text{normal}} + \text{Pi} - \text{D}_{\text{shear}}. \quad (3.11)$$

These three terms isolate the power density due to dilatation, normal deformation, and shear deformation, respectively. A key point is that the normal deformation

only depends on diagonal elements of \mathcal{D} , *i.e.*, on converging/diverging flow, as seen in Eq. (3.9a). We thus argue that it may be more natural for the normal deformation to be combined with the pressure dilatation, which also only depends on the diagonal elements of \mathcal{D} , than with $\text{Pi} - \text{D}_{\text{shear}}$. We therefore introduce the quantity PDU as

$$\text{PDU} = -\mathcal{P}(\nabla \cdot \mathbf{u}) + \text{Pi} - \text{D}_{\text{normal}} \quad (3.12a)$$

$$= -\left(P_{xx} \frac{\partial u_x}{\partial x} + P_{yy} \frac{\partial u_y}{\partial y} + P_{zz} \frac{\partial u_z}{\partial z} \right) \quad (3.12b)$$

so that

$$-(\mathbf{P} \cdot \nabla) \cdot \mathbf{u} = \text{PDU} + \text{Pi} - \text{D}_{\text{shear}}. \quad (3.13)$$

For an isotropic pressure with $P_{xx} = P_{yy} = P_{zz} \equiv P$, where P is the scalar pressure, Eq. (5.3a) reduces to $\text{PDU} = -P(\nabla \cdot \mathbf{u})$, the known pressure dilatation from fluid mechanics. For an arbitrary pressure tensor, PDU gives the power density due to converging and diverging flows, which contains both dilatation and normal deformation. Eq. (5.3a) is the reasonable generalization of pressure dilatation when isotropy is not valid, as it contains contributions from dilatation in each direction independently.

3.3 Physical Interpretation of Pressure-Strain Interaction

Here, we provide the physical interpretation of the pressure-strain interaction contributions in the fluid and kinetic descriptions. The fluid description has partially been addressed previously (Del Sarto et al., 2016; Del Sarto & Pegoraro, 2018). We

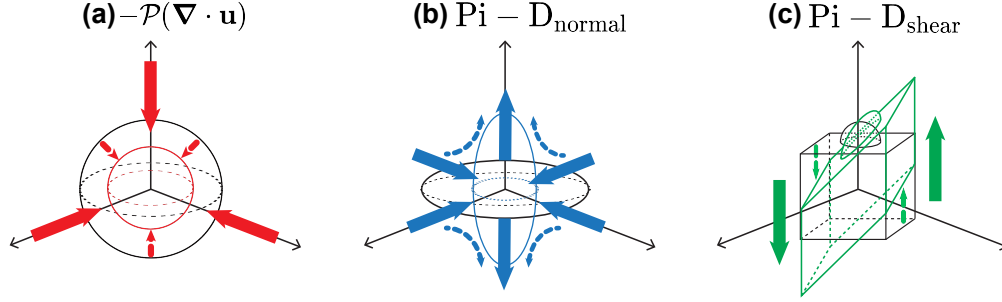


Figure 3.1: Sketch of representative contributions to the pressure-strain interaction in the fluid description. Black shapes are the initial fluid elements, and bold arrows show the bulk flow directions. The dashed arrows map the change between initial and final shapes of the fluid elements. (a) Pressure dilatation (red), showing compression, (b) normal deformation (blue), and (c) shear deformation (green). Panels (a) and (b) are essentially copies of Figure 1 from Ref. (Del Sarto & Pegoraro, 2018); panel (c) is new. Modified with permission from Figure 1 of “Shear-induced pressure anisotropization and correlation with fluid vorticity in a low collisionality plasma,” by Daniele Del Sarto and Francesco Pegoraro, *Monthly Notices of the Royal Astronomical Society*, **475**, 181 (2018).

provide simplified examples that allow for the physical interpretation to be made clear, with the idea that they can be used to motivate analogous processes for more general cases. While the fluid description is valid, both simulations and satellites now regularly measure the phase space density, measuring plasma properties at scales at and below the scales where treating a plasma as a fluid is no longer appropriate (Shuster et al., 2019, 2021). Thus, we argue it is important to develop a fully kinetic interpretation of the contributions to the pressure-strain interaction. As shown in Sec. 3.4, this understanding will provide insight into what it means to have a negative $\text{Pi} - \text{D}$.

3.3.1 Fluid Description of the Pressure-Strain Interaction

We begin with the physical interpretation of pressure-strain interaction in the fluid description. It was treated in the limit of vanishing vector heat flux density \mathbf{q} in Ref. (Del Sarto & Pegoraro, 2018), vividly conveyed in their Fig. 1 that contains valid sketches of the effects of dilatation (red) and normal deformation (blue). However, because their analysis did not contain a vector heat flux density, the shear deformation term in Eq. (5.3b) did not appear in their analysis. Thus, we extend their Fig. 1 in the general case in our Fig. 3.1.

Panel (a) exemplifies pressure dilatation $-\mathcal{P}(\nabla \cdot \mathbf{u})$, representing compression of the sketched spherical fluid element. Panel (b) exemplifies normal deformation $\text{Pi} - \text{D}_{\text{normal}}$, represented by the volume preserving change of shape of the sketched ellipsoidal fluid element. These two panels are modeled directly after Ref. (Del Sarto & Pegoraro, 2018). The initial fluid element is in black, the flow profile is in the large arrows, and the final fluid element is in color. The small colored arrows denote the action of the fluid element due to the flow.

Panel (c) exemplifies shear deformation $\text{Pi} - \text{D}_{\text{shear}}$, which is not present in Ref. (Del Sarto & Pegoraro, 2018). The sheared flow deforms the fluid element, as in the standard treatment of flow shear in a fluid, except that this effect is purely collisionless. A key point is that shear deformation requires a non-zero off-diagonal pressure tensor element in the plane of the varying bulk flow and its gradient for there to be a contribution to the pressure-strain interaction [see Eq. (5.3b)]. Thus, we draw a cubical fluid element in (c) with a feature sticking out of the box to

denote the need for the off-diagonal elements. Since the off-diagonal pressure tensor elements can be either positive or negative, shear deformation can lead to a positive or negative contribution to the pressure-strain interaction. Because the pressure-strain interaction is collisionless, any change in thermal energy due to it is formally reversible. In contrast, collisional viscous heating is unable to lead to a decrease in thermal energy and is irreversible.

3.3.2 Kinetic Description of PDU

Here we treat the kinetic theory interpretation of the pressure-strain interaction. We do this by investigating how a phase space density evolves in time when there is a non-zero pressure-strain interaction to illustrate kinetically why there is a change in the thermal energy density. We first emphasize that the pressure-strain interaction is local in space and time, and calculating it depends only on the local pressure tensor and the bulk flow velocity profile. Thus, instantaneously, determining if there is conversion between bulk flow and thermal energy density does not require knowledge of the presence of any body forces or collisions. In the treatment that follows, we ignore body forces and collisions. Although body forces and collisions are not needed to determine the local pressure-strain interaction, they do impact the motion of particles and the evolution of the phase space density, so these effects would have to be considered in addition to the phase space evolution considered here. We briefly return at the end to motivate how body forces change the pictures that follow.

In the force-free, collisionless limit, the Boltzmann/Vlasov equation becomes

$$\frac{\partial f}{\partial t} + \mathbf{v} \cdot \nabla f = 0. \quad (3.14)$$

As is well known, this is merely a linear convection equation in position space at every \mathbf{v} . We will use this in the examples that follow.

As an example which isolates PDU, consider a plasma with a drifting bi-Maxwellian phase space density f_{biM} aligned with a Cartesian coordinate system so that the pressure tensor \mathbf{P}_{biM} is uniform in space and its elements are given by $P_{xx} = P_{yy} = P_{\perp}$, $P_{zz} = P_{\parallel}$, and $P_{jk} = 0$ for $j \neq k$. The effective pressure is then $\mathcal{P}_{biM} = (2P_{\perp} + P_{\parallel})/3$, and Eq. (3.5) reveals that the deviatoric pressure tensor $\mathbf{\Pi}_{biM}$ is

$$\mathbf{\Pi}_{biM} = \mathbf{P}_{biM} - \mathcal{P}_{biM} \mathbf{I} = (P_{\perp} - P_{\parallel}) \begin{pmatrix} \frac{1}{3} & 0 & 0 \\ 0 & \frac{1}{3} & 0 \\ 0 & 0 & -\frac{2}{3} \end{pmatrix}. \quad (3.15)$$

Using Eq. (3.4), the associated $\text{Pi} - \text{D}_{biM}$ for an arbitrary bulk flow profile \mathbf{u} is

$$\text{Pi} - \text{D}_{biM} = -\Pi_{jk} \mathcal{D}_{jk} = -(P_{\perp} - P_{\parallel}) \left[\frac{1}{3} (\nabla \cdot \mathbf{u}) - \frac{\partial u_z}{\partial z} \right]. \quad (3.16)$$

As desired, this $\text{Pi} - \text{D}_{biM}$ does not depend on flow shear even if it is present. For definiteness, we consider $P_{\parallel} > P_{\perp}$. We first treat converging flow in the parallel direction, such that $\mathbf{u} = u_z(z) \hat{\mathbf{z}}$, and for simplicity we treat bulk flow towards $z = 0$.

A sketch of the system at initial time $t = t_0$ is in Fig. 3.2(a). The phase space

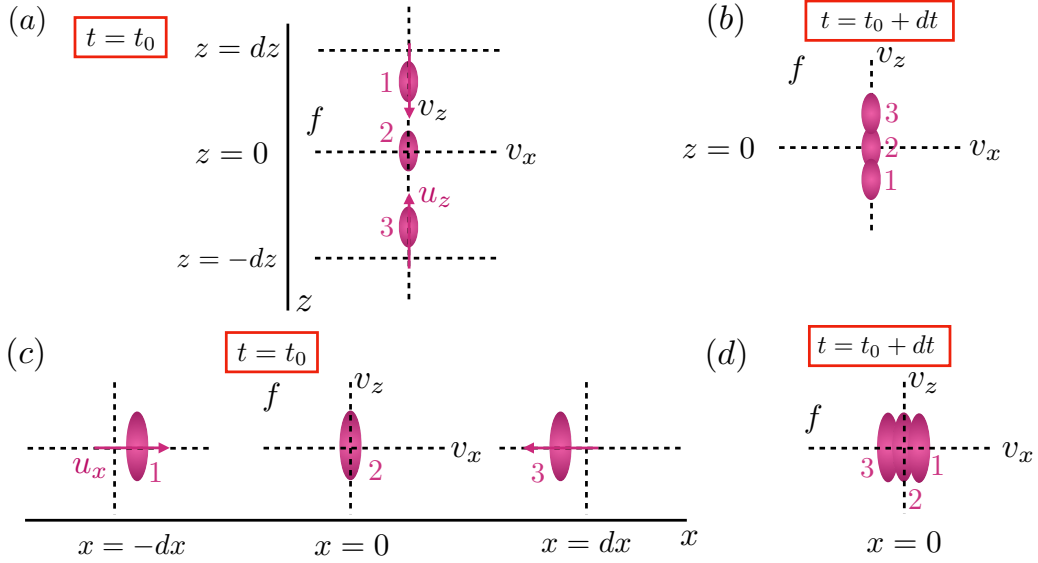


Figure 3.2: Sketches showing the physical interpretation of PDU, *i.e.*, heating via converging flow, in kinetic theory, ignoring body forces and collisions for simplicity. Magenta ellipses denote a 2D slice of the phase space density f in the (v_x, v_z) plane given by bi-Maxwellian distributions with $P_{\parallel} > P_{\perp}$, where x is a perpendicular direction and z is parallel. (a) Phase space densities at initial time $t = t_0$ at three locations at and near $z = 0$. The vertical bulk flow velocity u_z , denoted by the magenta arrows, is converging in the parallel direction. (b) The phase space density at $z = 0$ at a slightly later time $t = t_0 + dt$. The phase space densities labeled 1, 2, and 3 in panel (a) evolve to their associated positions labeled in panel (b). The phase space density at this time is broader in v_z , implying an increase in thermal energy density. Note, $\text{Pi} - \text{D}$ is positive for this case. (c) and (d) are analogous for the same phase space density except with converging bulk flow in x . There is an increase in the thermal energy density in the phase space density at $x = 0$ at $t = t_0 + dt$ in panel (d). Interestingly, $\text{Pi} - \text{D}$ is negative for this case.

density f_{biM} is sketched as the magenta ovals in the (v_x, v_z) plane at three different spatial locations, $z = dz, 0$, and $-dz$. The pressures are the same at each location, but the phase space densities are offset from the origin accordingly to impose that the bulk flow converges towards $z = 0$. A short time dt later, f_{biM} with $v_z < 0$ at $z > 0$ (labeled 1) convects down, f_{biM} with $v_z > 0$ at $z < 0$ (labeled 3) convects up, and f_{biM} near $v_z = 0$ at $z = 0$ (labeled 2) does not convect far, so the phase space density f at $z = 0$ at $t = t_0 + dt$ is qualitatively displayed in Fig. 3.2(b), with the same numbering scheme to show where the particles came from at $t = t_0$. (We acknowledge that the precise phase space density at time $t_0 + dt$ would be affected by particles from cells beyond those plotted and would smear out the final distribution, but we do not attempt to capture this effect in the sketch for simplicity.) Comparing the phase space densities f_{biM} and f at $z = 0$ at $t = t_0$ and at $t = t_0 + dt$, respectively, we note that the breadth of f in the perpendicular v_x direction is the same as in f_{biM} (there is no perpendicular heating), but f is broader in the parallel v_z direction than f_{biM} . Broadening a phase space density is the kinetic manifestation of heating, *i.e.*, increasing the thermal energy. This gives the kinetic interpretation of PDU, *i.e.*, heating via converging flow in the z direction, corresponding to $-P_{zz}(\partial u_z/\partial z)$ in Eq. (5.3a).

We now consider converging flow in the perpendicular direction for the same initial phase space density, so now $\mathbf{u} = u_x(x)\hat{\mathbf{x}}$, treating bulk flow converging towards $x = 0$ for simplicity. A sketch at the initial time $t = t_0$ is in Fig. 3.2(c), where the phase space density f_{biM} is sketched at $x = -dx, 0$, and dx . Since f_{biM} evolves in time according to the convection equation in Eq. (3.14) in the absence of body

forces and collisions, the phase space density f at $x = 0$ a short time dt later appears as sketched in Fig. 3.2(d). The phase space density f does not broaden in the parallel v_z direction, but does broaden in the v_x direction. This is the kinetic manifestation of heating from PDU via converging flow in the x direction, corresponding to $-P_{xx}(\partial u_x/\partial x)$ in Eq. (5.3a). In both examples, heating due to converging flow contains contributions from both dilatation and normal deformation, a key point we return to in the next section.

Finally, we return to the effect of the presence of a body force \mathbf{F} . As stated earlier, it is clear from the expression for pressure-strain interaction that a body force cannot contribute to it, even though the forces impact the motion of the particles. The sketches used here can still provide information for how to interpret the terms in the pressure-strain interaction when there is a body force present. First consider a uniform body force, *i.e.*, it is the same at every position. The body force \mathbf{F} changes the velocity of all particles of mass m at a given position by the same increment $d\mathbf{v} = \mathbf{F}dt/m$ in a small increment in time dt , so it merely translates the phase space density in velocity space. In the Lagrangian reference frame, this shift does not lead to a change in the thermal energy at the point in question beyond what is shown in the sketches in this section. If there is a force that is not uniform, a similar procedure happens except that the shift in velocity space of the particles is different at every location. In our example, the phase space density is uniform in space, so the result is unchanged. In the more general case for which the phase space density is also not uniform, it would require a detailed analysis to understand the evolution of the particles and the associated phase space densities, which is beyond the scope

of the present study. However, we know the result for an arbitrary force and initial phase space density must be that the body force does not alter the pressure-strain interaction in the Lagrangian reference frame.

3.3.3 Kinetic Description of $P_i - D_{\text{shear}}$

We next turn to the kinetic interpretation of heating via shear deformation. As noted in the introduction (Batchelor, 2000; Del Sarto et al., 2016; Del Sarto & Pegoraro, 2018), the symmetric strain rate tensor \mathbf{S} needs to be non-zero for the pressure-strain interaction to be non-zero, and the pressure-strain interaction is independent of the anti-symmetric strain rate tensor $\mathbf{\Omega}$. Moreover, from Eq. (5.3b), the pressure tensor must have a non-zero off-diagonal element in order for there to be heating via shear deformation. Consequently, we consider flow shear of a phase space density with non-zero off-diagonal pressure tensor elements.

Consider flow in the xz plane; dynamics in the other planes is analogous. Figure 3.3(a) contains sketches in a region near $(x, z) = 0$ at initial time $t = t_0$, with phase space densities sketched in (v_x, v_z) space at an array of spatial locations given by $x = dx, 0$, and $-dx$ and $z = dz, 0$, and $-dz$. In the kinetic picture, P_{xz} is non-zero if the phase space density lacks symmetry in both the v_x and v_z directions relative to the bulk flow speed (u_x, u_z) . One way a phase space density can have a positive P_{xz} is if it is elongated in the first and/or third quadrant in the (v_x, v_z) plane compared to the second and/or fourth quadrants; similarly a negative P_{xz} is elongated in the second and/or fourth quadrants in (v_x, v_z) space. Another is if f

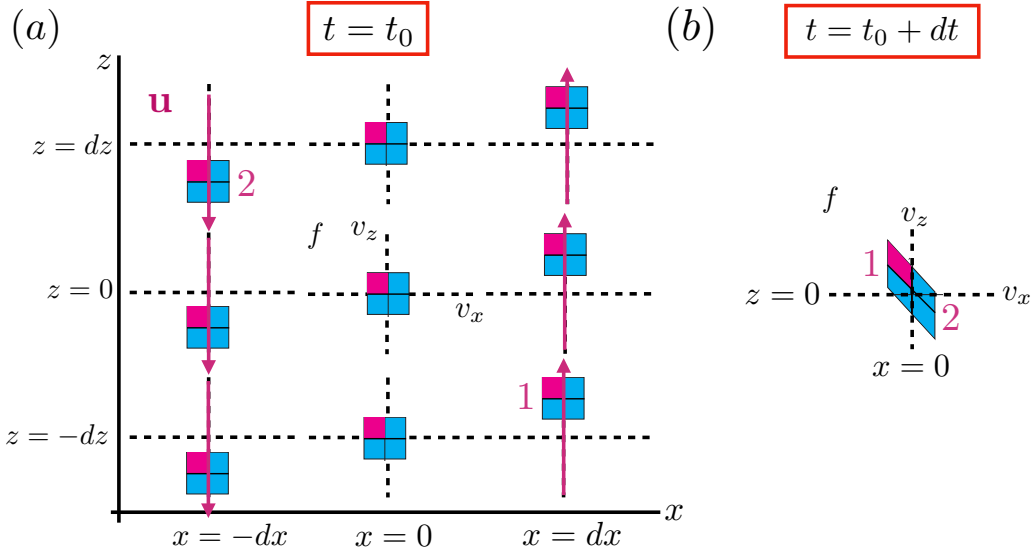


Figure 3.3: Sketch illustrating the kinetic theory explanation of why $\text{Pi} - \text{D}_{\text{shear}}$ leads to heating or cooling. (a) Array of sketches at locations in position space (x, z) near the origin at the initial time t_0 . Each sketch contains a phase space density f in the (v_x, v_z) plane in blue and red, where blue represents relatively low f and red represents relatively high f . Such phase space densities have $P_{xz} < 0$. The placement of the phase space density in each axis system reveals its bulk flow \mathbf{u} , denoted for each f by the magenta arrow. The flow profile has a representative form $(u_x, u_z) = (0, x)$. (b) Sketch of the phase space density at the origin at a slightly later time $t = t_0 + dt$. The portions of the phase space densities in (a) labeled 1 and 2 evolve to make up the portions of the phase space densities in (b) labeled 1 and 2, respectively. For this flow profile, there is a net displacement of particles away from the velocity space origin, implying an increase in thermal energy density.

weighted higher in the first and/or third quadrants than the second and/or fourth quadrants. Figure 3.3(a) includes a phase space density with $P_{xz} < 0$ due to the weighting of f that is uniform in space, displayed with red signifying larger f and blue signifying smaller f . To impose a bulk velocity shear, the phase space densities are shifted relative to the velocity space origin, with the bulk flow direction denoted by the magenta arrows. For this illustration, we assume a profile with $\mathbf{u} = u_z(x)\hat{\mathbf{z}}$, where u_z is positive for $x > 0$ and negative for $u_z < 0$.

In the next increment in time dt , particles with $v_x > 0, v_z < 0$ at $(-dx, dz)$ (labeled 2) move towards the origin (in the absence of body forces and collisions), appearing in the $v_x > 0, v_z < 0$ quadrant at the origin at $t = t_0 + dt$ (labeled 2) in Fig. 3.3(b). This portion of the phase space density is blue, meaning f is relatively low there. Similarly, in the phase space density at $(dx, -dz)$, particles in the left part of the distribution (labeled 1) have $v_x < 0, v_z > 0$, so they also move toward the origin. At $t = t_0 + dt$, they become the population in the $v_x < 0, v_z > 0$ portion of the phase space density (labeled 1) in Fig. 3.3(b). The red portion in Fig. 3.3(b) is the portion of the phase space density at $t = t_0 + dt$ with higher f values than elsewhere in the phase space density.

To interpret this result, we note the phase space density at the origin at $t = t_0 + dt$ effectively stretches away from the velocity space origin in the second and fourth quadrants relative to the phase space density at the origin at $t = t_0$, and moves closer to the velocity space origin in the first and third quadrants than at $t = t_0$. If f had begun at $t = t_0$ as symmetric in (v_x, v_z) space (*i.e.*, if P_{xz} had been 0), this would lead to no net heating at $t = t_0 + dt$, since there would be equal

numbers of particles brought closer to the velocity space origin as those brought further away. However, in this case, there are more particles in quadrant 2 than the other quadrants at $t = t_0 + dt$, so there are more particles further from the origin. This is the kinetic manifestation of heating. This example provides motivation for the kinetic theory of heating via pressure-strain interaction due to $\text{Pi} - \text{D}_{\text{shear}}$, with the same caveat as in the previous subsection that body forces and collisions can alter the particle trajectories and phase space density evolution, but cannot directly impact the pressure-strain interaction. We note that $P_{xz} < 0$ and $\partial u_z / \partial x > 0$ in this example, so the term $-P_{xz}(\partial u_z / \partial x)$ in Eq. (5.3b) is positive. This is associated with heating, consistent with the physical picture given here. A similar construction with the higher f region in the fourth quadrant (so that P_{xz} is again negative) also leads to heating. If the higher f region is in the first or third quadrant, it would lead to cooling because there are more particles closer to the velocity space origin than farther away from it. In this case P_{xz} is positive, and the $\text{Pi} - \text{D}_{\text{shear}}$ contribution to the pressure-strain interaction is negative, consistent with cooling. Thus, $\text{Pi} - \text{D}_{\text{shear}}$ can contribute to heating or cooling depending on the flow profile and the sign of the off-diagonal pressure-tensor elements, and it is in principle reversible.

We conclude this subsection with a kinetic theory interpretation of why pure straining motion leads to a contribution to the pressure-strain interaction, but rigid body rotation does not. Figure 3.4(a) is a sketch analogous to Fig. 3.3(a) of a hyperbolic bulk flow profile corresponding to pure straining motion with $\partial u_k / \partial r_j = \partial u_j / \partial r_k$, so $\mathbf{\Omega} = 0$. Analogous to Fig. 3.3(b), there is a flow of particles towards (and away from) the origin in the next small increment in time, which serves to increase

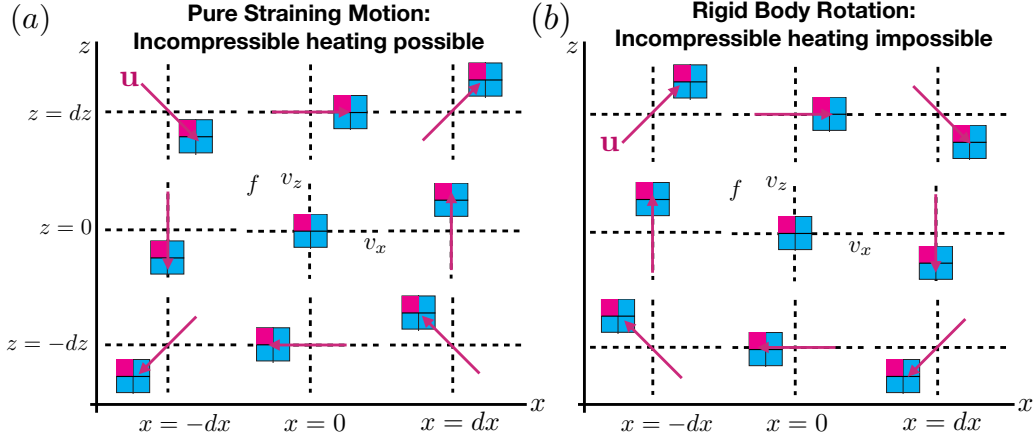


Figure 3.4: Sketch illustrating the kinetic theory explanation of why (a) symmetric shear (pure straining motion) can lead to heating/cooling, while (b) anti-symmetric shear (rigid body rotation) cannot. In each sketch, the grid in x and z denotes physical positions in the environment of the origin $(x, z) = (0, 0)$. Each red and blue box denotes a phase space density f with a negative P_{xz} in the (v_x, v_z) plane at the location in question. The local bulk flow \mathbf{u} is denoted for each f with a magenta arrow. The flow profiles are (a) $(u_x, u_z) = (z, x)$ and (b) $(u_x, u_z) = (z, -x)$.

the thermal energy density at the origin at $t = t_0 + dt$. In contrast, Fig. 3.4(b) shows a similar sketch, but for rigid body rotation for which $\partial u_k / \partial r_j = -\partial u_j / \partial r_k$, so $\mathbf{S} = 0$. In this case, the flow profile imposes that the particles in the phase space densities surrounding the origin predominantly go around the origin rather than changing the phase space density at the origin, leaving the thermal energy density at the origin unchanged. This is the kinetic explanation for why rigid body rotation does not contribute to the pressure-strain interaction.

3.4 Kinetic Interpretation of Normal Deformation and Implications for the Sign of $\text{Pi} - \text{D}$

It has been shown numerically and observationally that $\text{Pi} - \text{D}$, *i.e.*, collisionless viscous heating, can be positive or negative, which has been puzzling because collisional viscous heating must be non-negative. We use the present results to interpret the sign of $\text{Pi} - \text{D}$ within the kinetic description. We emphasized in Sec. 3.2 that $\text{Pi} - \text{D}$ contains both normal deformation and shear deformation. Consequently, it is not a well-posed question to ask what a negative value of $\text{Pi} - \text{D}$ means physically because it is ambiguous; it could have contributions from either term. The physics of $\text{Pi} - \text{D}_{\text{shear}}$ was discussed in Sec. 3.3.3, including what it means physically for it to be positive or negative. The example of heating due to converging flow in Sec. 3.3.2 explained the sign only for PDU , *i.e.*, the sum of the dilatation and normal deformation terms, so we reconsider the example given there to isolate the normal deformation and explain the kinetic interpretation of its sign.

Consider again the bi-Maxwellian distribution f_{biM} with $P_{xx} = P_{yy} = P_{\perp}$ and $P_{zz} = P_{\parallel}$ with $P_{\parallel} > P_{\perp}$ discussed in the previous section. For the two bulk flow profiles in Fig. 3.2, analytic expressions for $\text{Pi} - \text{D}_{\text{normal}}$ are readily calculated from Eq. (3.9a). For parallel converging flow $\mathbf{u} = u_z(z)\hat{\mathbf{z}}$, we get

$$\mathcal{D}_{\text{normal}} = \mathcal{D} = \frac{\partial u_z}{\partial z} \begin{pmatrix} -\frac{1}{3} & 0 & 0 \\ 0 & -\frac{1}{3} & 0 \\ 0 & 0 & \frac{2}{3} \end{pmatrix}, \quad (3.17)$$

so that

$$\text{Pi} - \text{D}_{\text{normal}} = \text{Pi} - \text{D} = \frac{2}{3} \frac{\partial u_z}{\partial z} (P_{\perp} - P_{\parallel}). \quad (3.18)$$

A similar derivation reveals that if $\mathbf{u} = u_x(x)\hat{\mathbf{x}}$ for perpendicular converging flow,

$$\text{Pi} - \text{D}_{\text{normal}} = \text{Pi} - \text{D} = -\frac{1}{3} \frac{\partial u_x}{\partial x} (P_{\perp} - P_{\parallel}). \quad (3.19)$$

Importantly, $\text{Pi} - \text{D}_{\text{normal}}$ for parallel and perpendicular converging flow have opposite signs.

For the flow profiles in Fig. 3.2, $\text{Pi} - \text{D}_{\text{normal}}$ is positive for parallel converging flow but negative for perpendicular converging flow. We know the net dilatation plus normal deformation due to converging flow leads to heating as quantified by PDU for converging flow in either direction. Thus, it may not be surprising that $\text{Pi} - \text{D}_{\text{normal}} > 0$ for parallel converging flow. However, it is counterintuitive that $\text{Pi} - \text{D}_{\text{normal}} < 0$ for perpendicular converging flow because negative $\text{Pi} - \text{D}$ has been referred to as “cooling.”

The resolution of this apparent paradox is to consider $\text{Pi} - \text{D}_{\text{normal}}$ in the context of pressure dilatation $-\mathcal{P}(\nabla \cdot \mathbf{u})$. For the perpendicular converging flow case,

$$-\mathcal{P}(\nabla \cdot \mathbf{u}) = -\mathcal{P} \frac{\partial u_x}{\partial x} = -\left(\frac{2P_{\perp} + P_{\parallel}}{3}\right) \frac{\partial u_x}{\partial x}. \quad (3.20)$$

This quantity is non-negative for converging flow, which reflects that there is heating.

The sum of dilatation and normal deformation from Eqs. (3.19) and (3.20) to get

PDU is

$$\text{PDU} = -P_{\perp} \frac{\partial u_x}{\partial x}, \quad (3.21)$$

as expected from Eq. (5.3a). This is positive for converging flow, corresponding to a net heating, as expected.

This simple example suggests the kinetic theory interpretation of $\text{Pi} - \text{D}_{\text{normal}}$. The quantity PDU describes the total volumetric heating rate due to converging flow. Pressure dilatation describes the volumetric rate of compressible heating if the system was in equilibrium with a (scalar) pressure \mathcal{P} since it has the form $-\mathcal{P}(\nabla \cdot \mathbf{u})$. Kinetically, pressure dilatation describes the heating that would take place if the phase space density f were replaced by a Maxwellian distribution f_M with the density $n = \int f d^3v$ and with its pressure P given by the effective pressure \mathcal{P} found from the local phase space density f . The phase space density f_M is known as the Maxwellianized distribution of f . The contribution from $\text{Pi} - \text{D}_{\text{normal}}$, then, describes the correction to the total of the volumetric heating rate due to converging flow due to the phase space density f not being the Maxwellianized distribution f_M .

In the example of the bi-Maxwellian distributions with $P_{\parallel} > P_{\perp}$ in Fig. 3.2(a), the Maxwellianized distribution f_M of the phase space density f_{biM} is round in velocity space, so it is cooler in the parallel direction and hotter in the perpendicular direction than f . Compression of f_M in the perpendicular x direction would heat the plasma, making the phase space density at $t = t_0 + dt$ broader in the v_x direction than it would be due to compression of f_{biM} . This means there would be a higher volumetric heating rate of f_M than there would be of f_{biM} since $P_{\parallel} > P_{\perp}$. Therefore,

$\text{Pi} - \text{D}_{\text{normal}}$ is negative in this example because it represents the correction to the volumetric heating rate of the actual phase space density f_{biM} because it is not the Maxwellianized distribution f_M ; in this case, the correction is negative. Thus, $\text{Pi} - \text{D}_{\text{normal}} < 0$ during converging flow does not represent physical cooling, because when combined with $-\mathcal{P}(\nabla \cdot \mathbf{u})$ to form PDU, the volumetric heating rate into thermal energy is positive, as is expected for converging flow. This is in contrast to $\text{Pi} - \text{D}_{\text{shear}}$, which necessarily contributes to cooling when it is negative.

Similar reasoning holds for parallel converging flow. As shown in Fig. 3.2(b), the result of converging parallel flow is to generate a phase space density at the origin that is even more elongated than f_{biM} at $t = 0$. In this case, pressure dilatation is again positive because there is converging flow, but here $\text{Pi} - \text{D}_{\text{normal}}$ is also positive. This is because the Maxwellianized distribution f_M is narrower in the parallel direction than f_{biM} , so the heating of f_M is less than the heating of f_{biM} . The contribution from $\text{Pi} - \text{D}_{\text{normal}}$ is positive to make up for the part of the heating omitted from the converging flow acting on f_M .

Thus, simply knowing that $\text{Pi} - \text{D}$ is negative is insufficient to know if it is caused by normal deformation or shear deformation, and it is insufficient to know if there is overall cooling via the pressure-strain interaction. If $\text{Pi} - \text{D} < 0$ and $\text{Pi} - \text{D}_{\text{shear}}$ dominates, there is a contribution towards cooling. However, if $\text{Pi} - \text{D} < 0$ and is dominated by $\text{Pi} - \text{D}_{\text{normal}}$, one cannot know if there is heating or cooling due to converging or diverging flow because $-\mathcal{P}(\nabla \cdot \mathbf{u})$ can have either sign depending on whether there is converging or diverging flow. It is PDU that must be measured to assess if heating/cooling due to converging/diverging flow is taking place.

3.5 Discussion and Conclusions

The pressure-strain interaction, including $\text{Pi} - \text{D}$, has undergone intense scrutiny in the past few years because it concisely describes the rate that energy density is converted between bulk flow and thermal. Pressure dilatation is the portion of pressure-strain interaction associated with compression and expansion, while $\text{Pi} - \text{D}$ is the portion associated with incompressible heating (Del Sarto & Pegoraro, 2018) and has been described as collisionless viscosity (Yang et al., 2017a). Despite the scrutiny, fundamental questions about the physical interpretation of the pressure-strain interaction and $\text{Pi} - \text{D}$ have persisted, including what it means for $\text{Pi} - \text{D}$ to be negative.

In this Chapter, we use the fact that $\text{Pi} - \text{D}$ contains both normal deformation and shear deformation to propose an alternate decomposition of the pressure-strain interaction with the PDU and $\text{Pi} - \text{D}_{\text{shear}}$ terms, which separate the pressure-strain interaction into the power densities associated with converging/diverging flow and flow shear, respectively. The PDU term is a combination of the dilatation and normal deformation terms, and gives the reasonable generalization of dilatation for systems not in local thermodynamic equilibrium. In the large magnetic field limit, it was shown (Hazeltine et al., 2013) that the $\text{Pi} - \text{D}_{\text{shear}}$ term ($-\boldsymbol{\pi}_{gv} : \boldsymbol{U}$ in their notation) vanishes to low order in the strong magnetic field expansion. This is because the magnetic field dominates all other collisionless physics in the limit in question, and the magnetic field itself does not directly contribute to the pressure-strain interaction [see Eq. (3.1) and Ref. (Del Sarto et al., 2016)]. Outside of this

limit, as shown here, $\text{Pi} - \text{D}_{\text{shear}}$ need not vanish.

Using these results, we provide a physical understanding of the contributions to the pressure-strain interaction both from a fluid perspective, with one modification from previous work on the subject that ignored the vector heat flux density (Del Sarto & Pegoraro, 2018), and fully in the kinetic picture at the phase space density-level. We use the results to explain kinetically why pure straining motion (a symmetric strain rate tensor) can lead to a change in thermal energy but rigid body rotation (an asymmetric strain rate tensor) cannot. We finally use these results to give the physical mechanisms that cause $\text{Pi} - \text{D}$, including giving a new kinetic theory interpretation for the normal deformation term. We further show the counterintuitive result that while converging flow must contribute to a positive pressure-strain interaction, it can contribute to a negative $\text{Pi} - \text{D}$ for systems not in LTE.

We emphasize a number of consequences of this study that may be of use to the field:

1. As has been recognized elsewhere (Yang et al., 2017b; Matthaeus et al., 2020; Yang et al., 2022), the pressure-strain interaction $-(\mathbf{P} \cdot \nabla) \cdot \mathbf{u}$ is the most relevant quantity to determine the rate of change of bulk flow energy density into thermal energy density (heating or cooling), rather than $\text{Pi} - \text{D}$ in isolation.
2. It is correct that the pressure dilatation $-\mathcal{P}(\nabla \cdot \mathbf{u})$ describes the volumetric rate of heating/cooling due to compression/expansion, but it is not the full description of energy conversion in converging or diverging flow. Similarly,

$\text{Pi} - \text{D}$ is the measure of incompressible heating, but contains both normal deformation and shear deformation. In contrast, PDU gives the effect of converging/diverging flows, and $\text{Pi} - \text{D}_{\text{shear}}$ gives the effect of flow shear. We believe both decompositions have merit for analyzing the energy conversion in physical processes and provide complementary information. We envision that keeping all three terms – pressure dilatation, $\text{Pi} - \text{D}_{\text{normal}}$, and $\text{Pi} - \text{D}_{\text{shear}}$ – may also prove useful in some circumstances.

3. A local measurement of a negative $\text{Pi} - \text{D}$ does not imply there is cooling. If $\text{Pi} - \text{D}$ is negative due to normal deformation, the net effect of normal deformation and dilatation in the total pressure-strain interaction is still positive if the flow is converging. Meanwhile, a negative $\text{Pi} - \text{D}$ could also be the result of shear deformation, so there is no way to unambiguously identify the key physical processes at play from the sign of $\text{Pi} - \text{D}$ alone.
4. The physical interpretation of the normal deformation portion of $\text{Pi} - \text{D}$ in kinetic theory is the difference between the rate of compressional heating and the rate of compressional heating of the same process were the phase space density replaced by a Maxwellian distribution of the same effective pressure.
5. The introduction of the traceless strain-rate tensor \mathcal{D} , which has been carried into plasma physics following a long history in the study of neutral fluids (Batchelor, 2000), is only advantageous to study the rate of heating/cooling that is compressible vs. incompressible. However, it is not useful for distinguishing the heating between converging/diverging flows and flow shear. While

the difference may be negligible in neutral fluids that are near local thermodynamic equilibrium, they can be very different in plasmas that are far from local thermodynamic equilibrium.

6. It bears noting that the pressure-strain interaction is rigorously the quantity that describes the rate of conversion between bulk flow and thermal energy density, but it is not the only term that determines the local thermal energy density. In particular, thermal energy density flux and/or heat flux can also change the local thermal energy density (Du et al., 2020; Song et al., 2020), even though these terms do not contribute to changes in the net thermal energy in a closed or isolated system (Yang et al., 2017b).

7. The thermal energy density describes the random energy in a phase space density, *i.e.*, $\int (1/2)mv^2 f d^3v$. However, other forms of energy such as $\int (1/2)mv'_x v'_y f d^3v$ or higher order moments are not contained in the thermal energy density, yet represent a possible energy channel during a physical process. We treat the energy going into channels beyond thermal energy density in a later Chapter (Chapter 6) (Cassak et al., 2023).

In Chapter 4, we derive the pressure-strain interaction in magnetic field-aligned coordinates. In Chapter 5, we display the pressure-strain interaction in Cartesian and magnetic field-aligned coordinates in PIC simulations and use the results to determine the mechanisms that contribute to the pressure-strain interaction during collisionless reconnection. For future work, it would be interesting to employ the decomposition of the pressure-strain interaction discussed here more broadly in

simulation data and observational data to separate converging/diverging flow effects from shear flow effects. Example systems where such studies would be interesting include collisionless reconnection, plasma turbulence, and collisionless shocks.

Also, we again point out from Eqs. (3.1) and (3.2), the presence of collisions and body forces such as electric, magnetic, or gravitational forces, enters directly into the bulk flow energy density equation but not directly into the pressure-strain interaction. Body forces are quantified by the $n\mathbf{u} \cdot \mathbf{F}$ term in Eq. (3.2), which for the electromagnetic force is $qn\mathbf{u} \cdot \mathbf{E}$ for a species of charge q . This quantity, including the version summed over species given by $\mathbf{J} \cdot \mathbf{E}$, has also been under intense scrutiny in the study for describing the conversion between bulk flow energy and electromagnetic energy (Zenitani et al., 2011; Klein & Howes, 2016; Burch et al., 2016b; Wilder et al., 2018; Chen et al., 2019; Afshari et al., 2021). A better understanding of how body forces impact thermal energy should remain a topic of future work (Howes, 2017).

Chapter 4

Pressure-Strain Interaction: II. Decomposition in Magnetic Field-Aligned Coordinates

4.1 Introduction

The pressure-strain interaction describes the rate of the direct conversion of energy between bulk flow and thermal (internal) energy density in neutral fluids or plasmas (Batchelor, 2000). It is written as $-(\mathbf{P} \cdot \nabla) \cdot \mathbf{u}$ (with the minus sign), where \mathbf{P} is the pressure tensor and \mathbf{u} is the bulk flow velocity. It was underutilized as a quantity of merit in plasma physics until recently (Del Sarto et al., 2016; Yang et al., 2017b,a; Del Sarto & Pegoraro, 2018). Since then, it has been the subject of intense scrutiny, primarily because it can be reliably measured using Magnetospheric Multiscale (MMS) mission (Burch et al., 2016a) satellites. This has made the observational study of energy conversion into thermal energy in systems out of local thermodynamic equilibrium accessible (Chasapis et al., 2018; Zhong et al., 2019; Bandyopadhyay et al., 2020a, 2021; Wang et al., 2021; Zhou et al., 2021). The pressure-strain interaction has also been studied in numerical simulations of magnetic reconnection (including magnetotail dipolarization fronts) and magnetized

Phys. Plasmas, 29, 122307 (2022)

Contributing authors: Paul A. Cassak, M. Hasan Barbhuiya, H. Arthur Weldon

plasma turbulence (Del Sarto et al., 2016; Sitnov et al., 2018; Del Sarto & Pegoraro, 2018; Du et al., 2018; Parashar et al., 2018; Pezzi et al., 2019; Yang et al., 2019b; Song et al., 2020; Du et al., 2020; Fadanelli et al., 2021; Arró, G. et al., 2022; Yang et al., 2022; Hellinger et al., 2022).

This Chapter is the second in a three-part series on the pressure-strain interaction. In Chapter 3, it was shown that while the commonly-used decomposition of the pressure-strain interaction into the pressure dilatation and the term known as $P_i - D$ separates the compressible and incompressible energy conversion (Batchelor, 2000), it does not separate the effects of converging/diverging flow from flow shear. A different decomposition was derived that does separate these effects. A kinetic description of the terms making up the pressure-strain interaction was provided.

In this Chapter, we present a decomposition of the pressure-strain interaction in a coordinate system with an axis aligned with the local magnetic field. The motivation is that the magnetic field often organizes the dynamics in magnetized plasmas, and therefore the magnetic field-aligned coordinate system can give a more direct indication of the physics at play (see also Ref. (Yuen & Lazarian, 2020)). The only other studies we are aware of that organized pressure-strain interaction relative to the magnetic field was a decomposition of the deviatoric pressure into a “gyrotropic” and “non-gyrotropic” part in MMS observations (Zhou et al., 2021) and studies on energy conversion in a strongly magnetized plasma (*e.g.*, Refs. (Hazeltine et al., 2013; Hazeltine & Waelbroeck, 2018)). The result of the present Chapter is eight sets of terms that can contribute to the pressure-strain interaction due to compression/expansion and flow shear, with the additional result that they can be

caused either by a direct strain of the bulk flow relative to the magnetic field or by a strain of the bulk flow caused by the geometry of the magnetic field. (We emphasize that the contribution to pressure-strain interaction due to the geometry of the magnetic field does not imply that the magnetic field itself is the direct cause of heating (Del Sarto et al., 2016)). We discuss the physical causes of each mechanism, which should be useful for interpreting measurements in simulations and satellite observations. (In what follows, we refrain from referring to a contribution to the pressure-strain interaction as “heating” or “cooling” because there are a number of effects beyond the pressure-strain interaction that can cause a change to the thermal energy density.) In Ref. (Barbhuiya & Cassak, 2022) (Chapter 5), we display the terms making up the pressure-strain interaction in both Cartesian and field-aligned coordinates for a particle-in-cell simulation of two-dimensional reconnection. We use the results to identify the physical causes of the conversion of bulk flow energy to thermal energy during the reconnection process.

The layout of this Chapter is as follows. A derivation of the pressure-strain interaction in magnetic field-aligned coordinates is provided in Sec. 4.2. The physical explanation of each term is provided in Sec. 4.3. Section 4.4 includes a discussion and conclusions.

4.2 Theory

4.2.1 Pressure-Strain Interaction in Magnetic Field-Aligned Coordinates

Consider a magnetized plasma with magnetic field \mathbf{B} . If the magnetic field is straight everywhere, the coordinate system can be chosen with a cardinal direction along the field, and the pressure-strain interaction can be decomposed in Cartesian coordinates as discussed in Chapter 3. If the magnetic field is not straight everywhere, we employ a local magnetic field-aligned orthonormal coordinate system, also used in Ref. (Yuen & Lazarian, 2020).

We define the unit vectors of the field-aligned coordinate system as the parallel direction $\hat{\mathbf{b}}$, the curvature direction $\hat{\boldsymbol{\kappa}}$, and the binormal direction $\hat{\mathbf{n}}$. (In differential geometry, these vectors are referred to as the tangent $\hat{\mathbf{t}}$, normal $\hat{\mathbf{n}}$, and binormal $\hat{\mathbf{b}}$ directions, respectively; our notation facilitates the identification of the magnetic field direction.) The parallel unit vector $\hat{\mathbf{b}} = \mathbf{B}/B$ is along the local magnetic field, where $B = |\mathbf{B}|$ is the magnitude of \mathbf{B} . The magnetic field curvature vector $\boldsymbol{\kappa} = (\hat{\mathbf{b}} \cdot \nabla)\hat{\mathbf{b}} = \nabla_{\parallel}\hat{\mathbf{b}}$ is defined in the standard way (Yang et al., 2019a), where $\nabla_{\parallel} = \hat{\mathbf{b}} \cdot \nabla$ is the gradient in the parallel direction. The unit vector $\hat{\boldsymbol{\kappa}}$ in the direction of the curvature is defined as $\hat{\boldsymbol{\kappa}} = \boldsymbol{\kappa}/\kappa$, where $\kappa = |\boldsymbol{\kappa}| = 1/R$ and R is the local radius of curvature of the magnetic field line. As is known, $\hat{\mathbf{b}} \cdot \hat{\boldsymbol{\kappa}} = 0$, which follows because $0 = \nabla_{\parallel}(\hat{\mathbf{b}} \cdot \hat{\mathbf{b}}) = 2\hat{\mathbf{b}} \cdot \nabla_{\parallel}\hat{\mathbf{b}} = 2\hat{\mathbf{b}} \cdot \boldsymbol{\kappa}$. The right-handed coordinate system is completed by defining $\hat{\mathbf{n}} = \hat{\mathbf{b}} \times \hat{\boldsymbol{\kappa}}$, which is normal to both the magnetic

field and the curvature.

We now calculate the pressure-strain interaction $-(\mathbf{P} \cdot \nabla) \cdot \mathbf{u}$ in field-aligned coordinates. We let Greek indices α, β, \dots refer to the b, κ, n directions, and we let \mathbf{e}_α be the unit vector in the α direction. The quantities in the pressure-strain interaction are written in terms of their elements in field-aligned coordinates as $\mathbf{P} = P_{\alpha\beta} \mathbf{e}_\alpha \mathbf{e}_\beta$, $\nabla = \mathbf{e}_\alpha \nabla_\alpha$, and $\mathbf{u} = \mathbf{e}_\beta u_\beta$. Then, the pressure-strain interaction (using the Einstein summation convention) is

$$-(\mathbf{P} \cdot \nabla) \cdot \mathbf{u} = -[(P_{\alpha\beta} \mathbf{e}_\alpha \mathbf{e}_\beta) \cdot (\mathbf{e}_\gamma \nabla_\gamma)] \cdot (\mathbf{e}_\delta u_\delta) \quad (4.1a)$$

$$= -P_{\alpha\beta} (\nabla_\alpha u_\beta) - P_{\alpha\beta} u_\delta [\mathbf{e}_\beta \cdot (\nabla_\alpha \mathbf{e}_\delta)] \quad (4.1b)$$

since $\mathbf{e}_\alpha \cdot \mathbf{e}_\beta = \delta_{\alpha\beta}$, where $\delta_{\alpha\beta}$ is the Kroenecker delta. The first term includes compression/expansion and shear in the standard sense of being related to gradients of the bulk flow with respect to the cardinal directions of the coordinate system, while the second term represents what we call geometrical compression/expansion and geometrical shear because they are caused by gradients of the bulk flow due to the geometry of the magnetic field. We discuss each in turn in what follows, grouping them into eight sets of terms we call $-PS_j$ (with the minus sign) for $j = 1, \dots, 8$.

For the first term $-P_{\alpha\beta} (\nabla_\alpha u_\beta)$, $\alpha = \beta$ and $\alpha \neq \beta$ are treated separately. There are three terms with $\alpha = \beta$, given by

$$-PS_1 = -P_{\parallel} (\nabla_{\parallel} u_{\parallel}), \quad (4.2)$$

where $P_{\parallel} = P_{bb} = \hat{\mathbf{b}} \cdot \mathbf{P} \cdot \hat{\mathbf{b}} = P_{kl}b_k b_l$ is the diagonal pressure element in the parallel direction and k and l are indices in Cartesian coordinates and $u_{\parallel} = u_b$, and

$$-PS_2 = -P_{\kappa\kappa}(\nabla_{\kappa}u_{\kappa}) - P_{nn}(\nabla_nu_n). \quad (4.3)$$

$-PS_1$ describes compression/expansion in the parallel direction, while $-PS_2$ describes compression/expansion in the plane normal to the parallel direction. For $\alpha \neq \beta$, we collect two of the six terms as

$$-PS_3 = -P_{\kappa b}(\nabla_{\kappa}u_{\parallel}) - P_{nb}(\nabla_nu_{\parallel}), \quad (4.4)$$

and the other four are

$$-PS_4 = -P_{b\kappa}(\nabla_{\parallel}u_{\kappa}) - P_{bn}(\nabla_{\parallel}u_n) - P_{\kappa n}(\nabla_{\kappa}u_n) - P_{n\kappa}(\nabla_nu_{\kappa}). \quad (4.5)$$

$-PS_3$ describes bulk flow velocity shear of the parallel flow in either perpendicular direction; $-PS_4$ describes bulk flow velocity shear of the flow perpendicular to the field that varies in either the parallel (first two terms) or perpendicular (last two terms) direction.

Finally, we need to simplify the geometric term in Eq. (4.1b), which depends on directional derivatives of unit vectors $\mathbf{e}_{\beta} \cdot (\nabla_{\alpha}\mathbf{e}_{\delta})$ and is related to the Christoffel symbol in differential geometry. We first consider parallel gradients of each of the unit vectors. These are given by the Frenet-Serret formulae from differential geometry (Struik, 1961; Patrikalakis & Maekawa, 2002; Yuen & Lazarian, 2020), which

in our notation are

$$\nabla_{\parallel} \hat{\mathbf{b}} = \kappa \hat{\boldsymbol{\kappa}}, \quad (4.6a)$$

$$\nabla_{\parallel} \hat{\boldsymbol{\kappa}} = \tau \hat{\mathbf{n}} - \kappa \hat{\mathbf{b}}, \quad (4.6b)$$

$$\nabla_{\parallel} \hat{\mathbf{n}} = -\tau \hat{\boldsymbol{\kappa}}, \quad (4.6c)$$

where $\tau = -\hat{\boldsymbol{\kappa}} \cdot \nabla_{\parallel} \hat{\mathbf{n}}$ is the torsion, which is a measure of the degree to which the magnetic field line is not confined to a plane. While κ is non-negative by definition, τ can be positive, negative, or zero. The first relation follows by definition of $\boldsymbol{\kappa}$. To get the form of the second, one notes $0 = \nabla_{\parallel}(\hat{\boldsymbol{\kappa}} \cdot \hat{\boldsymbol{\kappa}}) = 2\hat{\boldsymbol{\kappa}} \cdot \nabla_{\parallel} \hat{\boldsymbol{\kappa}}$, so $\nabla_{\parallel} \hat{\boldsymbol{\kappa}}$ can only have components in the $\hat{\mathbf{b}}$ and $\hat{\mathbf{n}}$ directions. The third then follows from writing $\nabla_{\parallel} \hat{\mathbf{n}} = \nabla_{\parallel}(\hat{\mathbf{b}} \times \hat{\boldsymbol{\kappa}}) = \hat{\mathbf{b}} \times \nabla_{\parallel} \hat{\boldsymbol{\kappa}}$ and using Eq. (4.6b). Finally, taking $\nabla_{\parallel} \hat{\boldsymbol{\kappa}} = \nabla_{\parallel}(\hat{\mathbf{n}} \times \hat{\mathbf{b}})$ and simplifying gives Eq. (4.6b). A key point is that the local geometry of the magnetic field is determined fully from the curvature κ and the torsion τ . Using the Frenet-Serret formulae provides all the directional derivatives in the parallel direction; the four non-zero ones are

$$\hat{\boldsymbol{\kappa}} \cdot \nabla_{\parallel} \hat{\mathbf{b}} = -\hat{\mathbf{b}} \cdot \nabla_{\parallel} \hat{\boldsymbol{\kappa}} = \kappa, \quad (4.7a)$$

$$\hat{\mathbf{n}} \cdot \nabla_{\parallel} \hat{\boldsymbol{\kappa}} = -\hat{\boldsymbol{\kappa}} \cdot \nabla_{\parallel} \hat{\mathbf{n}} = \tau, \quad (4.7b)$$

and the other five combinations all vanish.

We also need the directional derivatives in the direction of $\hat{\boldsymbol{\kappa}}$ and $\hat{\mathbf{n}}$. To find them, define the path length along the magnetic field line as s . Then, the coordinates

of the magnetic field line can be parametrized by $x(s)$, $y(s)$, and $z(s)$. The derivative of any function $f(s)$ of s in an arbitrary Cartesian direction is given by the chain rule as $\partial f(s)/\partial r_j = (\partial s/\partial r_j)(df/ds)$. This allows us to calculate the directional derivatives of $f(s)$ as

$$\nabla_{\parallel} f(s) = \hat{\mathbf{b}} \cdot \nabla f(s) = \frac{df(s)}{ds}, \quad (4.8a)$$

$$\nabla_{\kappa} f(s) = \hat{\boldsymbol{\kappa}} \cdot \nabla f(s) = (\hat{\boldsymbol{\kappa}} \cdot \nabla s) \frac{df(s)}{ds}, \quad (4.8b)$$

$$\nabla_n f(s) = \hat{\mathbf{n}} \cdot \nabla f(s) = (\hat{\mathbf{n}} \cdot \nabla s) \frac{df(s)}{ds}. \quad (4.8c)$$

Each is proportional to $df(s)/ds$, and its coefficient is purely geometrical depending on the trajectory of the magnetic field line. Defining the vector \mathbf{W} with components $W_b = \hat{\mathbf{b}} \cdot \nabla s = 1$, $W_{\kappa} = \hat{\boldsymbol{\kappa}} \cdot \nabla s$, and $W_n = \hat{\mathbf{n}} \cdot \nabla s$, we find the gradients in the curvature and binormal direction are

$$\nabla_{\kappa} = W_{\kappa} \nabla_{\parallel}, \quad (4.9a)$$

$$\nabla_n = W_n \nabla_{\parallel}. \quad (4.9b)$$

Using these results and the parallel derivatives given in Eqs. (4.7a) and (4.7b), all of the remaining directional derivatives $[\mathbf{e}_{\beta} \cdot (\nabla_{\alpha} \mathbf{e}_{\delta})]$ can be calculated in terms of the curvature κ and torsion τ . For example, $\hat{\boldsymbol{\kappa}} \cdot \nabla_{\kappa} \hat{\mathbf{b}} = \hat{\boldsymbol{\kappa}} \cdot W_{\kappa} \nabla_{\parallel} \hat{\mathbf{b}} = W_{\kappa} \kappa$ and $\hat{\boldsymbol{\kappa}} \cdot \nabla_n \hat{\mathbf{n}} = \hat{\boldsymbol{\kappa}} \cdot W_n \nabla_{\parallel} \hat{\mathbf{n}} = -W_n \tau$. Continuing in this manner for all the directional derivatives in the geometrical term in Eq. (4.1b), we group terms with like factors

of the components of \mathbf{u} and the geometrical factors κ or τ to give

$$-PS_5 = u_\kappa (P_{\parallel} + P_{\kappa b}W_\kappa + P_{nb}W_n) \kappa = u_\kappa P_{b\alpha}W_\alpha \kappa, \quad (4.10a)$$

$$-PS_6 = -u_\kappa (P_{bn} + P_{\kappa n}W_\kappa + P_{nn}W_n) \tau = -u_\kappa P_{n\alpha}W_\alpha \tau, \quad (4.10b)$$

$$-PS_7 = -u_{\parallel} (P_{b\kappa} + P_{\kappa\kappa}W_\kappa + P_{\kappa n}W_n) \kappa = -u_{\parallel} P_{\kappa\alpha}W_\alpha \kappa, \quad (4.10c)$$

$$-PS_8 = u_n (P_{b\kappa} + P_{\kappa\kappa}W_\kappa + P_{n\kappa}W_n) \tau = u_n P_{\kappa\alpha}W_\alpha \tau, \quad (4.10d)$$

where we consolidated terms using the vector $\mathbf{W} = \mathbf{e}_\alpha (\mathbf{e}_\alpha \cdot \nabla) s = (\hat{\mathbf{b}}\hat{\mathbf{b}} + \hat{\boldsymbol{\kappa}}\hat{\boldsymbol{\kappa}} + \hat{\mathbf{n}}\hat{\mathbf{n}}) \cdot \nabla s$.

We note that each of these terms depend on both diagonal and off-diagonal pressure tensor elements. We show in Sec. 4.3 that the terms proportional to u_κ ($-PS_5$ and $-PS_6$) represent geometrical compression/expansion, while the terms proportional to u_{\parallel} and u_n ($-PS_7$ and $-PS_8$) represent geometrical shear. We emphasize that the dependence on bulk velocity without a spatial derivative in these expressions does not imply a velocity gradient is not needed to have a non-zero pressure-strain interaction; rather, these terms contribute to the pressure-strain interaction because of the geometry of the magnetic field.

4.2.2 Example of Torsion for a Helical Magnetic Field

In preparation for explaining the physical manifestation of each term in the pressure-strain interaction, we present a simple example displaying the physical meaning of the torsion τ . Consider a circular helical magnetic field \mathbf{B}_H given in

Cartesian coordinates by

$$\mathbf{B}_H = -B_0 \frac{y}{\sqrt{x^2 + y^2}} \hat{\mathbf{x}} + B_0 \frac{x}{\sqrt{x^2 + y^2}} \hat{\mathbf{y}} + B_g \hat{\mathbf{z}}, \quad (4.11)$$

where $B_0 \geq 0$ is the magnitude of the in-plane magnetic field (which is uniform in this case) and B_g is the magnitude of the constant and uniform out-of-plane magnetic field. Then, $B = |\mathbf{B}_H| = (B_0^2 + B_g^2)^{1/2}$, and straight-forward calculations reveal the unit vectors are

$$\hat{\mathbf{b}} = -b_0 \frac{y\hat{\mathbf{x}} - x\hat{\mathbf{y}}}{\sqrt{x^2 + y^2}} + b_g \hat{\mathbf{z}}, \quad (4.12a)$$

$$\hat{\mathbf{k}} = \frac{-x\hat{\mathbf{x}} - y\hat{\mathbf{y}}}{\sqrt{x^2 + y^2}}, \quad (4.12b)$$

$$\hat{\mathbf{n}} = b_g \frac{y\hat{\mathbf{x}} - x\hat{\mathbf{y}}}{\sqrt{x^2 + y^2}} + b_0 \hat{\mathbf{z}}, \quad (4.12c)$$

where $b_0 = B_0/B$ and $b_g = B_g/B$. We note for future reference that the direction of the curvature is in the xy plane (radially in, $-\hat{\mathbf{r}}$) for this magnetic field, but the parallel and binormal directions have both an in-plane (azimuthal $\hat{\boldsymbol{\theta}}$) and out-of-plane ($\hat{\mathbf{z}}$) component.

A brief derivation reveals that the curvature and torsion for this magnetic field are $\kappa = b_0^2/r_\perp$ and $\tau = b_0 b_g/r_\perp$, where $r_\perp = \sqrt{x^2 + y^2}$ is the perpendicular distance from the z axis. This exemplifies that τ is positive for a right-handed helix ($B_g > 0$) and negative for a left-handed helix ($B_g < 0$). If $B_g = 0$, then $\tau = 0$, and the magnetic field lines are confined to planes. For this particular magnetic field, the torsion is proportional to the current helicity density through $\mathbf{B} \cdot \mathbf{J} = (cB^2/4\pi)\tau$ (in

cgs units), where $\mathbf{J} = (c/4\pi)\nabla \times \mathbf{B}$ is the current density, but this simple relation does not hold for general magnetic field profiles.

4.3 Physical Picture of the Pressure-Strain Interaction in Field-Aligned Coordinates

We now turn to the physical description of the contributions to the pressure-strain interaction in field-aligned coordinates. The analysis from the previous section showed that there are eight groups of terms. Sketches of representative examples of the general terms are given for each in Fig. 4.1. In each case, the magnetic field \mathbf{B} is sketched using black arrows, while the bulk flow \mathbf{u} is represented by red arrows. The curvature and binormal directions are depicted in green and blue, respectively. We treat each term in turn. The fluid description of the Cartesian analogue of the terms that arise in the absence of a heat flux was treated in Refs. (Del Sarto et al., 2016; Del Sarto & Pegoraro, 2018). We emphasize the kinetic description of each term, which complements the fluid description and makes no assumptions about the presence or absence of a heat flux. In so doing, when describing compression/expansion, we phrase it in terms of compression and analogous arguments can be used to describe expansion. We stress that the sketches are intended to give the simplest examples of the terms to illustrate the fundamental mechanism, while not intending to represent the general case.

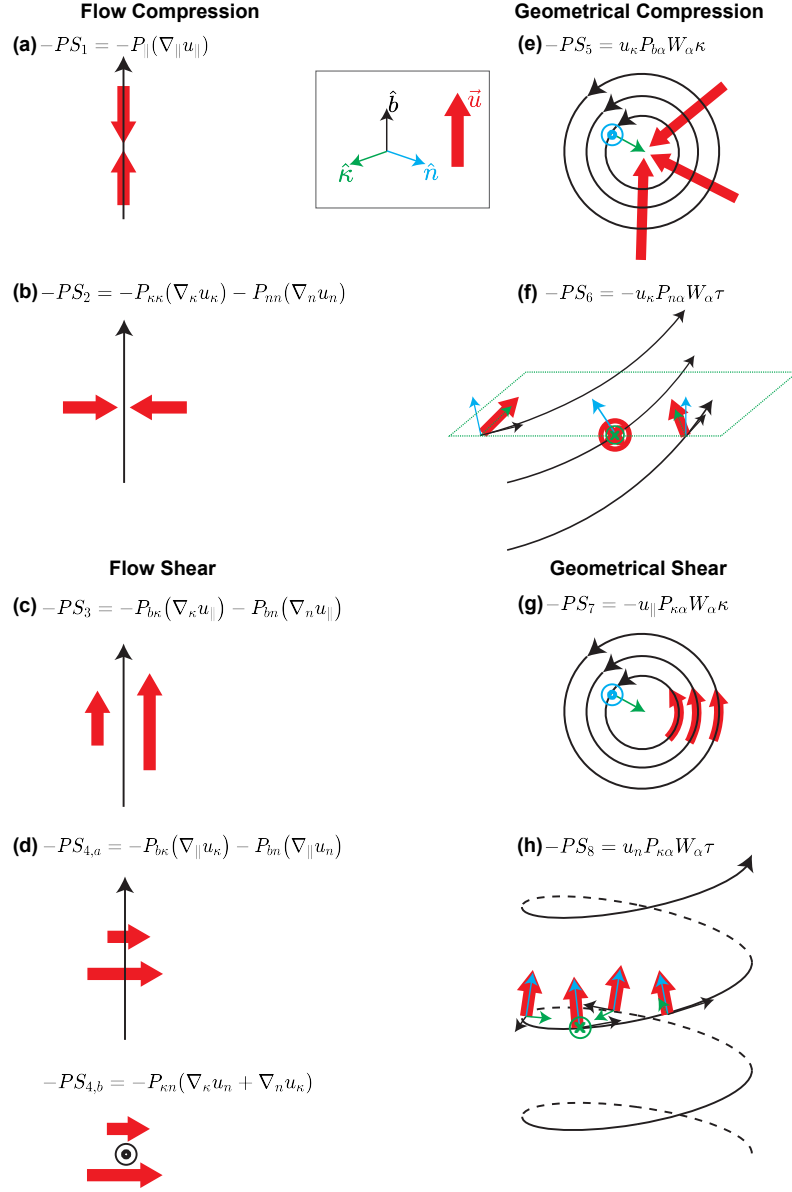


Figure 4.1: Representative sketches of the eight sets of terms in the decomposition of the pressure-strain interaction in field-aligned coordinates. Black arrows represent the magnetic field \mathbf{B} . Green and blue arrows denote the curvature and binormal directions, respectively. Red arrows denote the bulk flow \mathbf{u} . The eight sketches represent (a) parallel flow compression $-PS_1$, (b) perpendicular flow compression $-PS_2$, (c) shear of parallel flow in the perpendicular direction $-PS_3$, (d) shear of perpendicular flow in the perpendicular and/or parallel directions $-PS_4$, (e) perpendicular geometrical compression $-PS_5$, (f) torsional geometrical compression $-PS_6$, (g) parallel geometrical shear $-PS_7$, and (h) torsional geometrical shear $-PS_8$.

4.3.1 Parallel Flow Compression/Expansion: $-PS_1 = -P_{\parallel}(\nabla_{\parallel}u_{\parallel})$

For $-PS_1 = -P_{\parallel}(\nabla_{\parallel}u_{\parallel})$, the term describes compression due to a converging flow in the magnetic field direction $\hat{\mathbf{b}}$. A converging flow ($\nabla_{\parallel}u_{\parallel} < 0$) is associated with a positive contribution to the pressure-strain interaction, while a diverging flow ($\nabla_{\parallel}u_{\parallel} > 0$) is associated with a negative contribution. It is largely as expected from a fluid treatment, but the departure is that the term only depends on the parallel pressure P_{\parallel} . This is sketched in Fig. 4.1(a), showing it for a straight magnetic field line and oppositely directed converging flows. However, this mechanism operates even for curved magnetic field lines provided there are converging/diverging flows in the parallel direction. Also, converging/diverging flows can occur without a change of direction of the flow.

Kinetically, this term describes a fluid or plasma with an arbitrary phase space density, but only the parallel diagonal pressure element of its pressure contributes. The mechanism is analogous to parallel compressional heating in a Cartesian coordinate system, as displayed in Fig. 1(a) of Chapter 3. Briefly, the phase space density at a point where there is converging flow elongates in the parallel direction, which is the kinetic manifestation of heating, due to the offset of the nearby distributions from the bulk flow at the point of interest.

4.3.2 Perpendicular Flow Compression/Expansion: $-PS_2 = -P_{\kappa\kappa}$

$$(\nabla_{\kappa}u_{\kappa}) - P_{nn}(\nabla_nu_n)$$

For $-PS_2 = -P_{\kappa\kappa}(\nabla_{\kappa}u_{\kappa}) - P_{nn}(\nabla_nu_n)$, the two terms describe compression of the bulk flow in the plane perpendicular to the magnetic field. This again is as expected from a fluid treatment, but again shows that only the diagonal component of the pressure tensor parallel to the converging flow contributes. This is sketched in Fig. 4.1(b), showing it for a straight magnetic field line. This effect also occurs regardless of the shape of the magnetic field line provided there are converging flows across it. The flows need not go to zero at the field line; they only need to converge or diverge. This mechanism is analogous to perpendicular compressional heating in a Cartesian coordinate system, for which the kinetic interpretation was displayed in Fig. 1(b) of Chapter 3. As with parallel compression ($-PS_1$), diagonal elements of \mathbf{P} are non-negative, so compression necessarily has a positive contribution to the pressure-strain interaction and expansion necessarily has a negative contribution.

4.3.3 Parallel Flow Sheared in the Perpendicular Direction: $-PS_3 =$

$$-P_{b\kappa}(\nabla_{\kappa}u_{\parallel}) - P_{bn}(\nabla_nu_{\parallel})$$

For $-PS_3 = -P_{b\kappa}(\nabla_{\kappa}u_{\parallel}) - P_{bn}(\nabla_nu_{\parallel})$, these terms describe a parallel flow that varies in the plane normal to the magnetic field. A sketch exemplifying this term is given in Fig. 4.1(c). This mechanism does not require a curved magnetic field and depends on flow gradients, so it describes a bulk flow shear similar to expectations from a fluid picture. The key kinetic aspect is that this mechanism

is non-zero only if there is a non-zero off-diagonal pressure tensor element in the direction of the magnetic field. Kinetically, this effect is analogous to flow shear in a Cartesian coordinate system, as displayed in Fig. 2 of Chapter 3, *i.e.*, it is associated with collisionless viscosity, so it can be positive or negative and is in principle reversible. This figure explains why the necessary off-diagonal pressure tensor elements need a component along the magnetic field. In a weakly collisional or collisionless plasma, the off-diagonal pressure tensor elements can be positive or negative, which determines whether a given flow profile has a positive or negative contribution to the pressure-strain interaction.

4.3.4 Perpendicular Flow Shear: $-PS_4 = -P_{b\kappa} (\nabla_{\parallel} u_{\kappa}) - P_{bn} (\nabla_{\parallel} u_n) - P_{\kappa n} (\nabla_{\kappa} u_n + \nabla_n u_{\kappa})$

For $-PS_4 = -P_{b\kappa} (\nabla_{\parallel} u_{\kappa}) - P_{bn} (\nabla_{\parallel} u_n) - P_{\kappa n} (\nabla_{\kappa} u_n + \nabla_n u_{\kappa})$, the mechanisms are of two related varieties. They are similar to the heating mechanism in the previous subsection in that they do not rely on any curvature of the magnetic field, and as with $-PS_3$ they require a shear in the bulk flow velocity. The first two terms describe a bulk flow in the plane perpendicular to the magnetic field that varies in the parallel direction. A representative sketch is given in the top of Fig. 4.1(d). The second two terms describe a flow perpendicular to the magnetic field that varies in the orthogonal perpendicular direction, as sketched in Fig. 4.1(d) on the bottom.

As with $-PS_3$, these terms correspond to the kinetic notion of collisionless viscosity, requiring off-diagonal pressure tensor elements. In each case, the off-

diagonal pressure tensor element must have a component in the direction of the gradient of the flow. As with $-PS_3$, whether a given term leads to a positive or negative contribution to the pressure-strain interaction depends on the flow shear and the sign of the off-diagonal pressure tensor element in question. Kinetically, the heating mechanism is analogous to the Cartesian coordinate system result displayed in Fig. 2 of Chapter 3, which explains why the particular off-diagonal pressure-tensor elements in the expressions are needed for this term to be non-zero.

4.3.5 Perpendicular Geometrical Compression/Expansion: $-PS_5 =$

$$u_\kappa P_{b\alpha} W_\alpha \kappa$$

For $-PS_5 = u_\kappa P_{b\alpha} W_\alpha \kappa$, the contribution to the pressure-strain interaction requires a curved magnetic field (planar or not) and takes place in the plane of the curvature and the magnetic field. The bulk flow is in the direction of the curvature, which is perpendicular to the magnetic field lines. A simple example is shown in Fig. 4.1(f), with a positive u_κ that need not vary as one traverses along the magnetic field. This mechanism is a form of geometrical compression, which results from the red arrows denoting the flow converging in the direction of the curvature, which is the cause of compression in the fluid sense. Unlike the four terms discussed in the previous subsections, this mechanism does not require a gradient in the bulk velocity component in field-aligned coordinates; instead the flow shear arises due to the curvature of the magnetic field.

There is an important aspect of this mechanism: it requires at least one of the

pressure tensor elements in the $\hat{\mathbf{b}}$ direction to be non-zero since it is proportional to $P_{b\alpha}$. The reason for this is that if the plasma were perfectly cold in the $\hat{\mathbf{b}}$ direction, then all motion would be perpendicular to the magnetic field, so it would be in the direction of the flow. This would not cause any mixing in the direction normal to the flow, so there is no contribution to the pressure-strain interaction for such flow. If there is random particle motion in the $\hat{\mathbf{b}}$ direction, mixing can occur that spreads the phase space density in the $\hat{\mathbf{b}}$ direction, which is therefore associated with a non-zero contribution to the pressure-strain interaction. More specifically, particles with positive or negative v_{\parallel} and positive v_{κ} on the outer magnetic field line move inward to the middle field line in time, providing a population with non-zero $v_{\parallel} > 0$ and $v_{\kappa} > 0$. Particles on the inner magnetic field line with non-zero v_{\parallel} and negative v_{κ} move outward to the middle field line, providing a population with non-zero v_{\parallel} and $v_{\kappa} < 0$. This changes the spread in the distribution at the middle field line, which is the kinetic manifestation of a change to the thermal energy. This mechanism for geometrical compression can lead to a positive or negative contribution to the pressure-strain interaction depending on the phase space density of the plasma, in contrast to bulk flow compression $-PS_1$ or $-PS_2$ which necessarily makes a positive contribution to the pressure-strain interaction.

4.3.6 Torsional Geometrical Compression: $-PS_6 = -u_{\kappa}P_{n\alpha}W_{\alpha}\tau$

For $-PS_6 = -u_{\kappa}P_{n\alpha}W_{\alpha}\tau$, the mechanism is related to perpendicular geometrical compression discussed in the previous subsection, but it requires a non-planar

magnetic field, *i.e.*, a magnetic field with a non-zero torsion. The key is that in the absence of torsion, having a bulk flow in the curvature direction u_κ means that the flow converges in the plane of the curvature and magnetic field, as shown in Fig. 4.1(e) for $-PS_5$. Thus, all the plasma that is converging comes from the same plane initially.

As an example of this mechanism in a magnetic field that has non-zero torsion, consider the simple case of a helical right-handed torsional magnetic field of the type discussed in Sec. 4.2.2. The oblique view in Fig. 4.1(f) shows the magnetic field twisting out of the plane, with the dashed line representing the xy plane that contains the curvature vector κ . If the flow in the κ direction is converging, the particles in the xy plane that end up in the region of converging flow originate from regions of the magnetic field that are separated in the binormal $\hat{\mathbf{n}}$ direction. If the plasma is perfectly cold in the $\hat{\mathbf{n}}$ direction, the phase space density in the region of converging flow does not broaden and thus there is no contribution to the pressure-strain interaction due to shear [although there can be a contribution due to the $\hat{\mathbf{b}}$ direction from $-PS_5$, as sketched in Fig. 4.1(e)]. If, however, there are any particles with random velocity in the $\hat{\mathbf{n}}$ direction, there is mixing in that direction and a compressional effect gives a non-zero contribution to the pressure-strain interaction. This mechanism is purely due to the geometry of the magnetic field, so we call it torsional geometrical compression. This term is not positive definite as with the other geometrical terms, so it can be associated with positive or negative contributions to the pressure-strain interaction.

4.3.7 Parallel Geometrical Shear: $-PS_7 = -u_{\parallel}P_{\kappa\alpha}W_{\alpha\kappa}$

For $-PS_7 = -u_{\parallel}P_{\kappa\alpha}W_{\alpha\kappa}$, the mechanism requires a magnetic field line with curvature (planar or not) when there is a bulk flow with a component parallel or anti-parallel to the magnetic field. An example of this for a circular magnetic field line with $u_{\parallel} > 0$ is sketched in Fig. 4.1(g). In the fluid sense, this mechanism leads to shear because the inner field lines are shorter than the outer field lines, so a flow profile with uniform u_{\parallel} implies that there is a shear due to the plasma traversing the shorter curved field line further in azimuthal angle than along the longer field lines.

To understand this mechanism in kinetic theory, first suppose none of the particles have any velocity component in the $\hat{\kappa}$ direction, *i.e.*, the plasma is perfectly cold in the $\hat{\kappa}$ direction. This implies that all the motion of the particles is confined to the magnetic surfaces. In this case, in the next small increment in time, the particles remain confined to the magnetic surfaces. Therefore, there is no mixing of particles between different magnetic surfaces, and there is no contribution to pressure-strain interaction. This is why $-PS_7$ is proportional to $P_{\kappa\alpha}$, *i.e.*, why random motion in the $\hat{\kappa}$ direction is necessary for this mechanism to occur.

Now consider a phase space density such that there is a non-zero $P_{\kappa\kappa}$, which means that particles have some random motion in the direction perpendicular to the magnetic surfaces. Consider the time evolution of a phase space density at the middle of the three magnetic field lines in Fig. 4.1(g). As the particles go around the curve in the magnetic field lines, particles with negative velocity v_{κ} on the inner

field line in Fig. 4.1(g) move outward in the next increment in time, showing up as a positive v_κ population at the middle field line. Similarly, particles with positive v_κ on the outer field line move inward, showing up as a negative v_κ population at the middle field line. This broadens the phase space density at the middle field line in the $\hat{\kappa}$ direction, which is associated with an increase in thermal energy in the kinetic sense. This is an effective shear due to the geometry of the magnetic field, so we refer to it as parallel geometric shear. We note as an application that this mechanism is important for a plasma in a magnetic mirror configuration.

There are analogous mechanisms for distributions with non-zero $P_{b\kappa}$ and $P_{\kappa n}$. Since these off-diagonal pressure tensor elements can be positive or negative, shear due to field line geometry can contribute to a positive or negative contribution to the pressure-strain interaction.

4.3.8 Torsional Geometrical Shear: $-PS_8 = u_n P_{\kappa\alpha} W_\alpha \tau$

For $-PS_8 = u_n P_{\kappa\alpha} W_\alpha \tau$, the mechanism relies on the magnetic field having torsion, but the flow is in the binormal direction. We again appeal to the simple example of the right-handed circular helical field discussed in Sec. 4.2.2. To isolate the effect of the torsion, we consider a flow with uniform u_n . (If it were not uniform, there would be a perpendicular flow shear as in $-PS_4$ in addition to the geometrical shear.) A sketch of this is in Fig. 4.1(h). It was pointed out in Sec. 4.2.2 that the binormal direction $\hat{\mathbf{n}}$ has components both in the axial $\hat{\mathbf{z}}$ and azimuthal $\hat{\boldsymbol{\theta}}$ directions. This can be seen from the red arrows in the sketch. The component of the bulk

flow in the $\hat{\mathbf{z}}$ direction does not introduce shear because u_n is the same on all magnetic field lines in this configuration. Thus, the axial part is not associated with a contribution to the pressure-strain interaction.

However, the component in the $\hat{\boldsymbol{\theta}}$ direction describes flow in the azimuthal direction. As with $-PS_7$, the geometry of the curved magnetic field lines imposes that there is a shear effect on the plasma because fluid elements with the same u_θ on different magnetic surfaces traverse the circular cross-section of the magnetic surface more rapidly for smaller magnetic surfaces than larger magnetic surfaces. If the phase space densities are perfectly cold in the $\hat{\boldsymbol{\kappa}}$ direction, then all particles are confined to the magnetic surfaces, and therefore there is no mixing and no contribution to the pressure-strain interaction. If, however, there are particles with a random v_κ , particles on different magnetic surfaces mix according to a flow shear-like mechanism in the kinetic description, so there is a change to the thermal energy density. This is why $-PS_8$ is proportional to $P_{\kappa\alpha}$. We refer to this as torsional geometrical shear. It can be positive or negative depending on the torsion, pressure tensor elements, and the flow direction.

4.4 Discussion and Conclusions

In this study, we derive an expression for the pressure-strain interaction, the term describing the rate of conversion of energy between bulk flow and thermal energy density, in magnetic field-aligned coordinates for use in magnetized plasmas. As expected, there are contributions related to compression/expansion and bulk flow

shear. However, in field-aligned coordinates, each effect has contributions directly from the spatial dependence of the bulk velocity itself as well as contributions from velocity shear caused by the geometry imposed by the path of the magnetic field line. It is important to stress that the magnetic field itself and magnetic forces do not cause the pressure-strain interaction to be non-zero (Del Sarto et al., 2016), it is simply the flow pattern relative to the magnetic fields that contribute. The geometric compression/expansion and geometric shear are parametrized in terms of the magnetic field curvature κ and torsion τ . The former is well-known in plasma physics; the latter is borrowed from differential geometry and is much less employed in plasma physics (Yuen & Lazarian, 2020), and describes the extent to which the local magnetic field deviates from lying in a plane.

We provide a picture of the physical effects contributing to the pressure-strain interaction using the kinetic theory description for each of the sets of terms $-PS_1$ through $-PS_8$ that arise from the analysis. The fluid description for plasmas in the absence of a heat flux was previously provided (Del Sarto et al., 2016; Del Sarto & Pegoraro, 2018). We emphasize that the two descriptions complement each other and must agree with each other when the same approximations are made in both pictures. The kinetic approach discussed here makes no assumptions about the presence of a heat flux. The physical mechanism of the parallel and perpendicular compression/expansion $-PS_1$ and $-PS_2$, and the shear in the bulk flow $-PS_3$, $-PS_{4,a}$, and $-PS_{4,b}$ are analogous to compression/expansion and bulk velocity shear in Cartesian coordinates (Del Sarto & Pegoraro, 2018; Cassak & Barbhuiya, 2022). In the kinetic description, the physical mechanism for geometric compression and geomet-

ric shear is random motion in the direction perpendicular to the flow in $-PS_5$ through $-PS_8$, which causes mixing of particles that gives rise to a pressure-strain interaction contribution.

We expect these results, especially the simple sketches of the physical contributions to pressure-strain interaction in Fig. 4.1, will be useful in studying energy conversion in weakly collisional and collisionless magnetized plasmas. Physical systems where the pressure-strain interaction has been used to study energy conversion, and where the present results may be useful, include plasma turbulence and magnetic reconnection. We expect it to also be useful for the study of collisionless shocks. The quantities derived here can be readily calculated in kinetic simulations (particle-in-cell and Vlasov/Boltzmann in particular) of these phenomena. Moreover, recent observational studies (Cozzani et al., 2019; Qi et al., 2019; Bandyopadhyay et al., 2020b; Huang et al., 2020; Rogers et al., 2021) using the MMS satellites have directly measured the magnetic field curvature κ , so this quantity of importance for the present study is accessible to measurement. We are unaware of any calculations of the magnetic field line torsion τ using satellite data, but it is a simple extension of calculating the magnetic field and curvature directions, so it should be able to be calculated.

We make three important points about the present results. First, the pressure-strain interaction $-(\mathbf{P} \cdot \nabla) \cdot \mathbf{u}$ is a scalar quantity, meaning it is invariant in different coordinate systems. Thus, whether the pressure-strain interaction is calculated in Cartesian coordinates (Chapter 3) or field-aligned coordinates, it remains the same. However, there is mixing between compression/expansion and flow shear

when changing coordinate systems. Second, the results here rigorously provide the pressure-strain interaction contributions in field-aligned coordinates for applications to magnetized plasmas. However, we stress there are settings in magnetized plasmas where particles become demagnetized, and the direction of the magnetic field no longer organizes the dynamics (Servidio et al., 2012; Burch et al., 2016b; Egedal et al., 2018). Thus, caution is necessary to not assume the magnetic field direction is necessarily the direction that best organizes a general pressure tensor. Finally, the decomposition in field-aligned coordinates presented here does not use any properties of the magnetic field itself. Thus, if an application arises for which there is a different preferred direction other than the magnetic field, the analysis presented here remains valid with $\hat{\mathbf{b}}$ simply becoming the preferred direction. This underscores the key point that the magnetic field and magnetic forces themselves do not give rise to the pressure-strain interaction, it is only the bulk flow gradients relative to the geometry set up by the magnetic field that gives rise to the pressure-strain interaction.

In Chapter 5, we use the results obtained here and in Chapter 3 to analyze the mechanisms by which the pressure-strain interaction describes the conversion of bulk flow energy density to thermal energy density during magnetic reconnection using two-dimensional particle-in-cell simulations. For future work, it would be interesting to employ the decomposition of the pressure-strain interaction discussed here in observational data, especially using the MMS satellites. Applications of the results to plasma turbulence and collisionless shocks, as well as other manifestations of reconnection including three-dimensional systems, would also be very interesting.

Chapter 5

Pressure-Strain Interaction: III. Particle-in-Cell Simulations of Magnetic Reconnection

5.1 Introduction

The pressure-strain interaction has garnered significant attention in the past few years because it describes the rate of conversion between bulk flow and thermal energy density [see Ref. (Cassak & Barbhuiya, 2022) and references therein]. The pressure-strain interaction is written equivalently as

$$-(\mathbf{P} \cdot \nabla) \cdot \mathbf{u} = -\mathbf{P} : \mathbf{S}, \quad (5.1)$$

where \mathbf{P} is the pressure tensor, \mathbf{u} is the bulk flow velocity, \mathbf{S} is the symmetric strain rate tensor, and the minus sign is included so that a positive value denotes a contribution to increasing the thermal energy density. The symmetric strain rate tensor can be decomposed into the bulk flow divergence $(1/3)\mathbf{I}(\nabla \cdot \mathbf{u})$ describing compression and \mathcal{D} describing incompressible flow (Del Sarto & Pegoraro, 2018), where \mathbf{I} is the identity tensor and \mathcal{D} is the traceless strain rate tensor with elements

Phys. Plasmas, 29, 122308 (2022)

Contributing authors: M. Hasan Barbhuiya, Paul A. Cassak

$\mathcal{D}_{jk} = (1/2)(\partial u_j/\partial r_k + \partial u_k/\partial r_j) - (1/3)\delta_{jk}(\nabla \cdot \mathbf{u})$, where δ_{jk} is the Kroenecker delta.

The pressure-strain interaction is then decomposed as (Del Sarto et al., 2016; Yang et al., 2017b,a; Del Sarto & Pegoraro, 2018)

$$-(\mathbf{P} \cdot \nabla) \cdot \mathbf{u} = -\mathcal{P}(\nabla \cdot \mathbf{u}) - \mathbf{\Pi} : \mathcal{D}, \quad (5.2)$$

where $\mathcal{P} = (1/3)P_{jj}$ is the effective pressure and $\mathbf{\Pi} = \mathbf{P} - \mathcal{P}\mathbf{I}$ is the deviatoric pressure tensor. The first and second terms in Eq. (5.2), including the minus signs, are the pressure dilatation and the term dubbed Pi – D, respectively (Yang et al., 2017b). Pi – D is the collisionless analogue of the viscous heating rate (Yang et al., 2017a).

In the first part of a three part series (Cassak & Barbhuiya, 2022) (Chapter 3), we introduced an alternate decomposition to Eq. (5.2). Rather than isolating compressible and incompressible heating/cooling, it isolates the effect of flow convergence/divergence in a term we call PDU and flow shear in a term we call Pi – D_{shear}. Analytically, $-\mathbf{P} : \mathbf{S} = \text{PDU} + \text{Pi} - \text{D}_{\text{shear}}$, where (in Cartesian coordinates)

$$\text{PDU} = - \left(P_{xx} \frac{\partial u_x}{\partial x} + P_{yy} \frac{\partial u_y}{\partial y} + P_{zz} \frac{\partial u_z}{\partial z} \right), \quad (5.3a)$$

$$\begin{aligned} \text{Pi} - \text{D}_{\text{shear}} = & - P_{xy} \left(\frac{\partial u_x}{\partial y} + \frac{\partial u_y}{\partial x} \right) - P_{xz} \left(\frac{\partial u_x}{\partial z} + \frac{\partial u_z}{\partial x} \right) \\ & - P_{yz} \left(\frac{\partial u_y}{\partial z} + \frac{\partial u_z}{\partial y} \right). \end{aligned} \quad (5.3b)$$

Equation (5.3a) is a sum of pressure dilatation (compression/expansion) and normal deformation (the part of Pi-D coming from the diagonal elements of \mathcal{D}

describing an incompressible change of shape of a fluid element), while Eq. (5.3b) is the part of $\text{Pi} - \text{D}$ coming from the off-diagonal elements of \mathbf{D} related to bulk flow shear.

In the second part in the series (Cassak et al., 2022) (Chapter 4), we calculated the decomposition of the pressure-strain interaction in magnetic field-aligned coordinates, finding eight sets of terms:

$$-PS_1 = -P_{\parallel}(\nabla_{\parallel}u_{\parallel}), \quad (5.4a)$$

$$-PS_2 = -P_{\kappa\kappa}(\nabla_{\kappa}u_{\kappa}) - P_{nn}(\nabla_nu_n), \quad (5.4b)$$

$$-PS_3 = -P_{\kappa b}(\nabla_{\kappa}u_{\parallel}) - P_{nb}(\nabla_nu_{\parallel}), \quad (5.4c)$$

$$-PS_4 = -P_{b\kappa}(\nabla_{\parallel}u_{\kappa}) - P_{bn}(\nabla_{\parallel}u_n) - P_{\kappa n}(\nabla_{\kappa}u_n) - P_{n\kappa}(\nabla_nu_{\kappa}), \quad (5.4d)$$

$$-PS_5 = u_{\kappa}(P_{\parallel} + P_{b\kappa}W_{\kappa} + P_{bn}W_n)\kappa = u_{\kappa}P_{b\alpha}W_{\alpha}\kappa \quad (5.4e)$$

$$-PS_6 = -u_{\kappa}(P_{bn} + P_{\kappa n}W_{\kappa} + P_{nn}W_n)\tau = -u_{\kappa}P_{n\alpha}W_{\alpha}\tau \quad (5.4f)$$

$$-PS_7 = -u_{\parallel}(P_{b\kappa} + P_{\kappa\kappa}W_{\kappa} + P_{\kappa n}W_n)\kappa = -u_{\parallel}P_{\kappa\alpha}W_{\alpha}\kappa \quad (5.4g)$$

$$-PS_8 = u_n(P_{b\kappa} + P_{\kappa\kappa}W_{\kappa} + P_{n\kappa}W_n)\tau = u_nP_{\kappa\alpha}W_{\alpha}\tau, \quad (5.4h)$$

where the b and \parallel subscripts denote the component parallel to the magnetic field \mathbf{B} , the κ subscript denotes the component in the direction of the magnetic field line curvature $\boldsymbol{\kappa} = \hat{\mathbf{b}} \cdot \nabla \hat{\mathbf{b}}$, where $\hat{\mathbf{b}} = \mathbf{B}/|\mathbf{B}|$, and the n subscript denotes the component in the binormal direction $\hat{\mathbf{n}} = \hat{\mathbf{b}} \times \hat{\boldsymbol{\kappa}}$, where $\hat{\boldsymbol{\kappa}} = \boldsymbol{\kappa}/|\boldsymbol{\kappa}|$. The quantities $\kappa = |\boldsymbol{\kappa}| = |\hat{\mathbf{b}} \cdot \nabla \hat{\mathbf{b}}|$ and $\tau = -\hat{\boldsymbol{\kappa}} \cdot \nabla_{\parallel} \hat{\mathbf{n}}$ are the magnetic field line curvature and torsion, respectively. The quantity \mathbf{W} is a vector with components $W_b = 1, W_{\kappa} = (\hat{\boldsymbol{\kappa}} \cdot \nabla_{\kappa} \hat{\mathbf{b}})/\kappa$, and

$W_n = -(\hat{\boldsymbol{\kappa}} \cdot \nabla_n \hat{\mathbf{n}})/\tau$. These components are the prefactors linking gradients in the curvature and binormal directions to the parallel direction such that $\nabla_\kappa = W_\kappa \nabla_\parallel$, and $\nabla_n = W_n \nabla_\parallel$. It was shown in Ref. (Cassak et al., 2022) that these eight terms correspond physically to parallel flow compression ($-PS_1$), perpendicular flow compression ($-PS_2$), shear of parallel flow in the perpendicular direction ($-PS_3$), shear of perpendicular flow in the parallel and/or perpendicular directions ($-PS_4$), perpendicular geometrical compression ($-PS_5$), torsional geometrical compression ($-PS_6$), parallel geometrical shear ($-PS_7$), and torsional geometrical shear ($-PS_8$). Here and in what follows, we simplify the wording by using compression to mean positive (compression) or negative (expansion) effects.

In this Chapter, we calculate the terms in the decomposition of the pressure-strain interaction in Cartesian and magnetic field-aligned coordinates in two-dimensional particle-in-cell (PIC) simulations of anti-parallel symmetric magnetic reconnection. The purposes for this Chapter are two-fold. First, we demonstrate a roadmap for using the analytical results in Chapters 3 and 4 to study the pressure-strain interaction in weakly collisional or collisionless plasmas, using magnetic reconnection as an example. Second, understanding the rate of conversion between bulk flow and thermal energy density during reconnection is of intrinsic interest, and has been the subject of numerical and observational studies (Sitnov et al., 2018; Chasapis et al., 2018; Bandyopadhyay et al., 2021; Pezzi et al., 2021). An outcome of the present Chapter is a map of an electron diffusion region identifying where energy conversion via pressure-strain interaction occurs and the physical causes of it in each location. Since Pi – D has been a significant topic of research, including the realization that it

can be negative (Yang et al., 2017b; Zhou et al., 2021), we also identify its physical cause during reconnection.

The layout of this Chapter is as follows. Section 5.2 gives the details of the numerical simulation setup. Sections 5.3 and 5.4 give the numerical results in Cartesian and magnetic field-aligned coordinates, respectively. Section 5.5 includes a discussion and conclusions.

5.2 Numerical Simulation Setup

To calculate the contributions to the pressure-strain interaction in a numerical simulation, we use the particle-in-cell code `p3d` (Zeiler et al., 2002) to simulate symmetric anti-parallel magnetic reconnection. The simulations are 2.5D in position space and 3D in velocity-space. The particles are stepped forward in time using the relativistic Boris particle stepper (Birdsall & Langdon, 1991), while electromagnetic fields are stepped forward using the trapezoidal leapfrog (Guzdar et al., 1993). The time step for the fields is half the time step for the particles. The multigrid method (Trottenberg et al., 2000) is used to clean the electric field \mathbf{E} every 10 particle time-steps to enforce Poisson’s equation. The boundary conditions are periodic in both spatial directions.

Quantities produced by the simulation are in normalized units. The initial asymptotic reconnecting magnetic field strength is B_0 , and n_0 is the plasma number density at the center of the current sheet minus the ambient background plasma density. Lengths, velocities, times, and temperatures are normalized to the ion

inertial scale $d_{i0} = c/\omega_{pi0}$, the Alfvén speed $c_{A0} = B_0/(4\pi m_i n_0)^{1/2}$, the inverse ion cyclotron frequency $\Omega_{ci0}^{-1} = (eB_0/m_i c)^{-1}$, and $m_i c_{A0}^2/k_B$, respectively, where $\omega_{pi0} = (4\pi n_0 e^2/m_i)^{1/2}$ is the ion plasma frequency, e is the ion charge, m_i is the ion mass, and c is the speed of light. Consequently, power densities making up the pressure-strain interaction are in units of $\Omega_{ci0}(B_0^2/4\pi)$.

The speed of light is $c = 15$, which is sufficient for the purposes of the present study. The electron to ion mass ratio is $m_e/m_i = 0.04$, which is relatively high. We expect this choice could influence the amplitude and spatial size of structures in the electron diffusion region (Ricci et al., 2002; Jun & Quan-Ming, 2007), but we do not expect it to affect the qualitative structure (Du et al., 2018). The scaling of the results with electron mass is discussed further in Secs. 5.4.3 and 5.5. The simulation domain size is $L_x \times L_y = 12.8 \times 6.4$. We use 1024×512 grid cells, and initially use 25,600 weighted particles per grid. The grid scale is $\Delta = 0.0125$, smaller than the smallest length-scale of the system, the electron Debye length $\lambda_{De} = 0.0176$. The time-step is $\Delta t = 0.001$, smaller than the smallest time-scale of the system, the inverse electron plasma frequency $\omega_{pe}^{-1} = 0.012$.

The initial conditions are a standard double tanh magnetic field. The initial magnetic field profile is

$$B_x(y) = \tanh\left(\frac{y - L_y/4}{w_0}\right) - \tanh\left(\frac{y - 3L_y/4}{w_0}\right) - 1, \quad (5.5)$$

where $w_0 = 0.5$ is the initial half-thickness of the current sheet. There is no initial out-of-plane (guide) magnetic field. The electrons and ions are initially drifting

Maxwellian distributions with density profiles given by

$$n(y) = \frac{1}{2(T_e + T_i)} \left[\operatorname{sech}^2 \left(\frac{y - L_y/4}{w_0} \right) + \operatorname{sech}^2 \left(\frac{y - 3L_y/4}{w_0} \right) \right] + n_{up}, \quad (5.6)$$

where $n_{up} = 0.2$ is the initial plasma density far from the current sheet. The temperature of the background plasma is initially uniform, with electron temperature $T_e = 1/12$ and ion temperature $T_i = 5/12$. A magnetic perturbation $\tilde{\mathbf{B}} = -\hat{\mathbf{z}} \times \nabla \tilde{\psi}$ is used to initiate reconnection, where

$$\tilde{\psi} = -\frac{\tilde{B}L_y}{4\pi} \sin \left(\frac{2\pi x}{L_x} \right) \left[1 - \cos \left(\frac{4\pi y}{L_y} \right) \right], \quad (5.7)$$

and the perturbation amplitude is $\tilde{B} = 0.05$.

All simulation data are shown from the lower current sheet at $t = 13$, when the reconnection rate is most rapidly increasing from zero to its maximum value, *i.e.*, it is not in the steady state. To reduce PIC noise, we recursively smooth the raw simulation quantities four times over a width of four cells, then we take the necessary spatial derivatives, and finally the results are recursively smoothed four times over four cells again. This level of smoothing is decided on by trying a number of different options for the number of cells and how many recursions, while confirming that smoothing does not greatly alter the signal structure. We focus on the electrons for this study; in what follows, the e subscript denoting electrons is suppressed for simplicity except where needed for clarity.

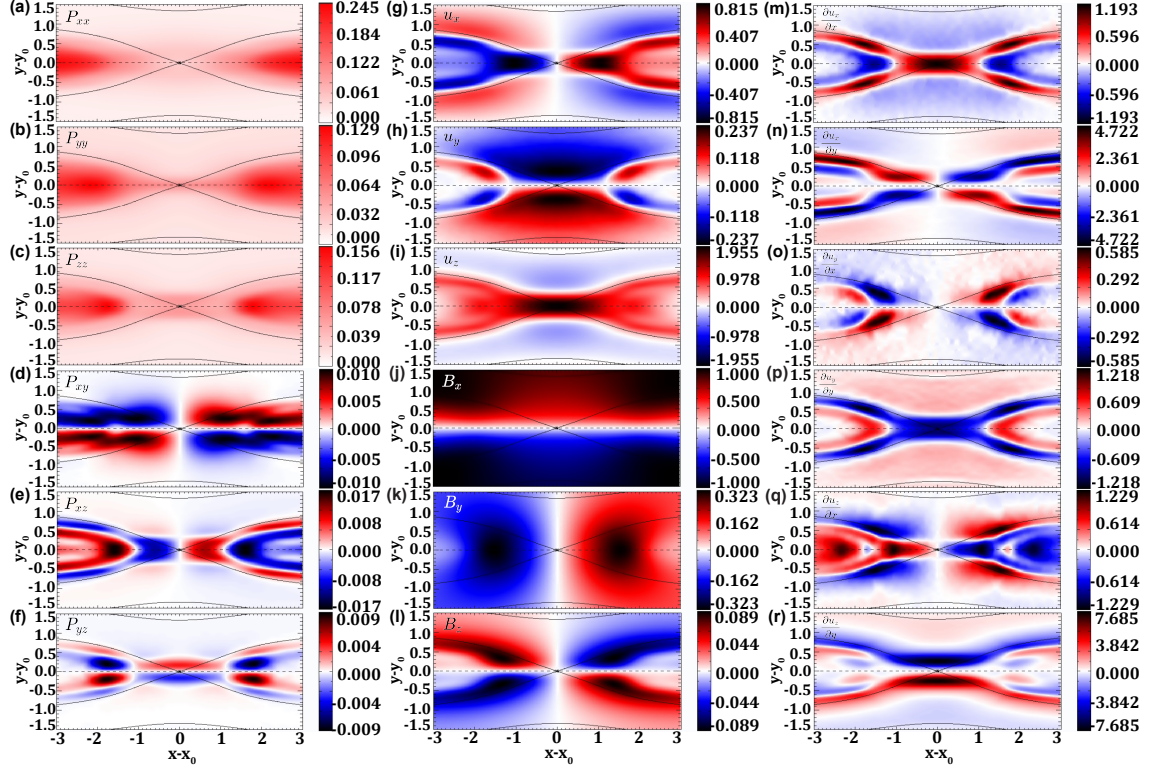


Figure 5.1: Two-dimensional profiles of the (a)-(f) six independent elements of the electron pressure tensor \mathbf{P} , (g)-(i) three components of bulk electron velocity \mathbf{u} , (j)-(l) three components of the magnetic field \mathbf{B} , and (m)-(r) six non-zero elements of the strain-rate tensor $\nabla\mathbf{u}$, as labeled in each panel. Representative magnetic field projections in the xy plane are in black. [Associated dataset available at <http://dx.doi.org/10.5281/zenodo.7117619>].

5.3 Simulation results - Cartesian Coordinates

5.3.1 Overview

The 2D profiles of the quantities that go into the calculation of the pressure-strain interaction in Cartesian coordinates and the magnetic field are provided in Fig. 5.1. It contains the (a)-(f) six independent elements of the electron pressure tensor \mathbf{P} , (g)-(i) three components of bulk electron velocity \mathbf{u} , (j)-(l) three components of the magnetic field \mathbf{B} , and (m)-(r) six non-zero elements of strain rate

tensor $\nabla \mathbf{u}$ (since $\partial/\partial z = 0$ for this 2D simulation). Representative magnetic field projections in the xy plane are included in black for perspective. The plots represent only a portion of the computational domain centered at the X-line location (x_0, y_0) from $|x - x_0| < 3$ and $|y - y_0| < 1.5$. This encompasses the electron diffusion region (EDR) which is approximately $|x - x_0| < 2, |y - y_0| < 0.35$.

5.3.2 Decomposition of Pressure-Strain Interaction in Cartesian Coordinates

The pressure-strain interaction and two decompositions in Cartesian coordinates are shown in Fig. 5.2. The color bars have red values for positive and blue for negative, and their ranges are different for the different plots. In this subsection, we largely focus on a qualitative comparison of the pressure-strain interaction and the decompositions in question. In the subsequent one, we extract the physical causes. The pressure-strain interaction $-\mathbf{P} : \mathbf{S}$ is shown in Fig. 5.2(a). The pressure-strain interaction at the X-line is negative, *i.e.*, in isolation it would lead to a decrease in thermal energy. We reiterate that although the thermal energy flux and heat flux must integrate to zero over the whole periodic domain, they are not necessarily zero locally. Thus, one cannot conclude that there is a net decrease in thermal energy at the X-line simply because $-\mathbf{P} : \mathbf{S}$ is negative, only that the pressure-strain interaction by itself would lead to a decrease in thermal energy. (Indeed, in Chapter 6, we show that the thermal energy at the X-line is increasing at the time shown.) The edges of the EDR indicate a net positive pressure-strain interaction. The down-

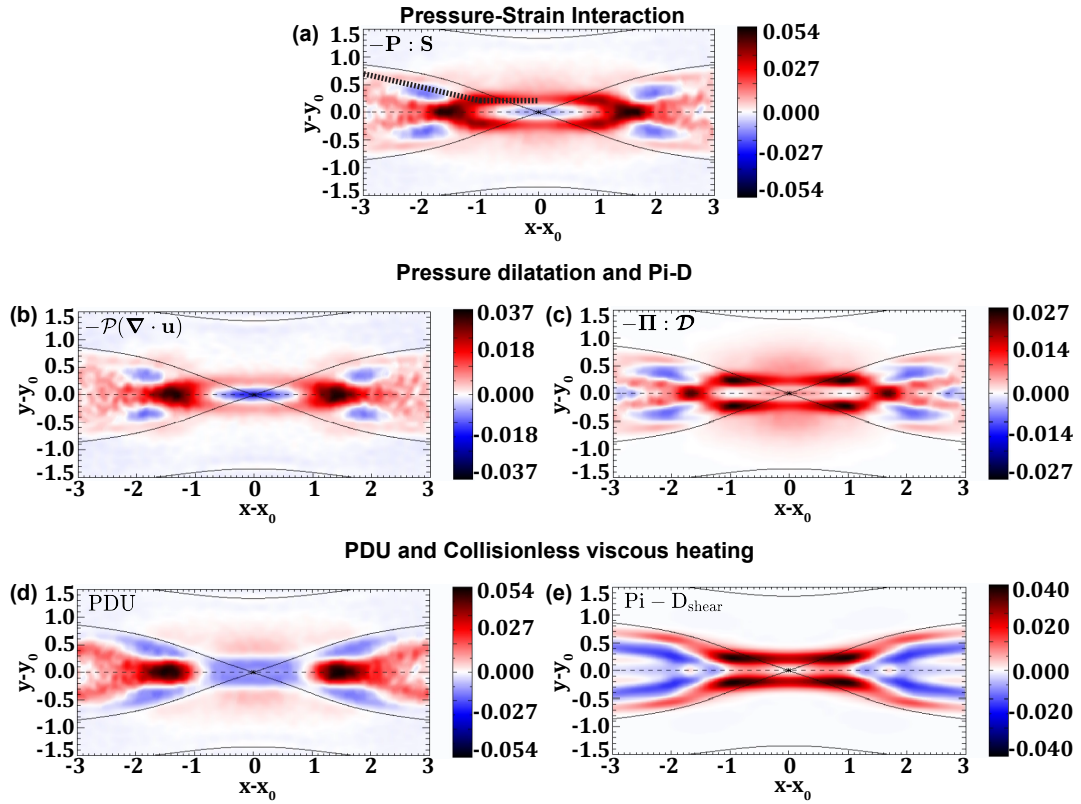


Figure 5.2: Pressure-strain interaction for electrons in a reconnection simulation. (a) The pressure-strain interaction $-\mathbf{P} : \mathbf{S}$. (b) Pressure dilatation $-\mathcal{P}(\nabla \cdot \mathbf{u})$ and (c) $\Pi - \mathcal{D}$, giving the compressible and incompressible parts. (d) PDU and (e) $\Pi - D_{\text{shear}}$, giving the flow converging/diverging and flow shear parts. The dotted-line in (a) is the path along which 1D cuts are taken in Figs. 5.3 and 5.6. [Associated dataset available at <http://dx.doi.org/10.5281/zenodo.7117619>].

stream region $|x - x_0| \simeq 2$ reveals a positive pressure-strain interaction near the neutral line $y = y_0$, immediately surrounded by a region of negative pressure-strain interaction out to about $|y - y_0| \simeq 0.5$.

The pressure dilatation $-\mathcal{P}(\nabla \cdot \mathbf{u})$ and $\text{Pi} - \text{D}$ are shown in Figs. 5.2(b) and (c), respectively. The pressure dilatation gives the contribution due to compression/expansion, while $\text{Pi} - \text{D}$ is due to incompressible effects. They have previously been plotted in 2D simulations of reconnection (Pezzi et al., 2021) (see their Fig. 2). We believe the present data look sharper because it is zoomed in closer, we employ more particles per grid and smoothing, and our data is plotted during the phase when the reconnection rate is increasing most rapidly rather than after the reconnection rate reaches its maximum value. We see a coherent region of negative $-\mathcal{P}(\nabla \cdot \mathbf{u})$ and $\text{Pi} - \text{D}$ near the downstream edge of the EDR at $|x - x_0| \simeq 2$, $|y - y_0| \simeq 0.35$, not seen in Ref. (Pezzi et al., 2021), as will be discussed further in the next subsection.

The decomposition of $-\mathbf{P} : \mathbf{S}$ into PDU and $\text{Pi} - \text{D}_{\text{shear}}$, defined in Eqs. (5.3a) and (5.3b), respectively, are plotted in Figs. 5.2(d) and (e). While the pressure dilatation and $\text{Pi} - \text{D}$ each have similar overall structure to $-\mathbf{P} : \mathbf{S}$, we find PDU and $\text{Pi} - \text{D}_{\text{shear}}$ have qualitative dissimilarities compared to the structure of $-\mathbf{P} : \mathbf{S}$. In PDU, the entire inner part of the EDR is negative, as opposed to only a small region near the X-line in $-\mathbf{P} : \mathbf{S}$. Perhaps most importantly, the region of highest pressure-strain interaction, the downstream edge of the EDR, shows up entirely in PDU, and it is essentially zero in $\text{Pi} - \text{D}_{\text{shear}}$. This shows the contribution to positive pressure-strain interaction is due entirely to the converging flows at the edge of the EDR. The decomposition given by pressure-dilatation and $\text{Pi} - \text{D}$ reveal that

the converging flow is associated with both compression and incompressible deformation. A similar example is in the upstream region, where there is weak positive pressure-strain interaction. Similar structure is seen in PDU, while $\text{Pi} - \text{D}_{\text{shear}}$ is nearly zero everywhere upstream of the EDR. Since $\text{Pi} - \text{D}$ is non-zero upstream of the EDR, we can conclude that incompressible normal deformation is the cause of this contribution to the pressure-strain interaction. We similarly note that there is a relatively strong positive pressure-strain interaction at the upstream edges of the EDR (the horizontal red bands), and it is caused nearly completely by flow shear. The cause of this positive pressure-strain interaction is more ambiguous in the pressure dilatation and $\text{Pi} - \text{D}$ decomposition, where both compressible and incompressible effects contribute. These three examples imply that PDU and $\text{Pi} - \text{D}_{\text{shear}}$ can be useful to help separate out the key physical cause of the pressure-strain interaction in these three regions of interest. In summary, both decompositions provide useful information about the causes of the pressure-strain interaction, and using the different decompositions together can help identify the key physical causes of the pressure-strain interaction.

5.3.3 Largest Contributions to Pressure-Strain Interaction in Cartesian Coordinates

Here, we discuss the regions of most significant contributions to the pressure-strain interaction and use the decompositions to understand their physical causes. The region of the highest contribution to the pressure-strain interaction is the down-

stream edge of the EDR, $1 < |x - x_0| < 2$ and $|y - y_0| < 0.3$, as seen in Fig. 5.2(a). As discussed briefly in the previous subsection, the cause of this is the converging flow when the electron jet from the EDR impacts the magnetic island [see Figs. 5.1(a) and (m) and Fig. 5.2(d)]. Both compression and (incompressible) normal deformation are taking place in this region, which is why both pressure-dilatation and $\text{Pi} - \text{D}$ are non-zero in this region [Fig. 5.2(b) and (c)].

In the ion diffusion region (IDR) significantly upstream of the EDR $|x - x_0| < 1$, $0.35 < |y - y_0| < 2.24$, electrons decouple from the ions at the upstream edge of the IDR and then accelerate towards the X-line due to the Hall electric field. This leads to expansion, associated with cooling. This shows up as the weakly blue region in $-\mathcal{P}(\nabla \cdot \mathbf{u})$ and PDU outside $|y - y_0| \simeq 0.8$, with the inflow gradient profile in Fig. 5.1(p). Then, the electrons slow down upon reaching the upstream edge of the EDR, $|y - y_0| < 0.35$ [Fig. 5.1(p)], which causes compression and is associated with heating. This shows up in PDU but not $\text{Pi} - \text{D}_{\text{shear}}$, meaning both compression and normal deformation are taking place. The normal deformation describes the change of shape of the phase space density, which are known to elongate in the parallel direction due to electron trapping (Egedal et al., 2013). This is to be contrasted with the decomposition in terms of the pressure dilatation and $\text{Pi} - \text{D}$, where this effect shows up in $\text{Pi} - \text{D}$ because normal deformation is one of the two terms within $\text{Pi} - \text{D}$.

Surrounding the X-line at $|x - x_0| < 0.7$, $|y - y_0| < 0.2$, there is a region of negative pressure-strain interaction [Fig. 5.2(a)]. This is caused by the acceleration of electrons into the exhaust jet; the u_x flow increases in magnitude away from the

X-line [Fig. 5.1(m)], which is an expansion of the plasma. This shows up as the negative region near the origin in $-\mathcal{P}(\nabla \cdot \mathbf{u})$ and PDU. Since $\text{Pi} - \text{D}$ is small near the X-line, we immediately conclude that compression is the most important effect here.

There are two other regions of significant pressure-strain interaction [Fig. 5.2(a)], namely the positive region at the upstream edge of the EDR ($|x - x_0| < 1.5, 0.2 < |y - y_0| < 0.35$), and the negative region at the downstream edge of the EDR just inside the separatrices ($1 < |x - x_0| < 2, |y - y_0| \simeq 0.5$). For the positive region at the upstream edge of the EDR, $\text{Pi} - \text{D}_{\text{shear}}$ provides the physical cause. As there is no comparable signal in PDU, we conclude it is caused solely by flow shear. The plots of $-\mathcal{P}(\nabla \cdot \mathbf{u})$ and $\text{Pi} - \text{D}$ both show signals in this region, which implies that both compression and normal deformation are playing a role but are actually nearly canceling out. Two effects lead to the bulk flow shear that leads to this positive pressure-strain interaction. First, the rapid drop-off of the out-of-plane flow u_z in the inflow direction [Fig. 5.1(i)] gives rise to a significant bipolar $\partial u_z / \partial y$ [Fig. 5.1(r)]. This is in the same location as a bipolar pressure anisotropy P_{yz} [Fig. 5.1(f)], which conspires with the flow shear to give a positive $\text{Pi} - \text{D}_{\text{shear}}$ in the region $|x - x_0| < 1$. In addition, the outflow u_x [Fig. 5.1(g)] rapidly changes in the inflow direction, leading to a quadrupolar $\partial u_x / \partial y$ [Fig. 5.1(n)]. There is a quadrupolar P_{xy} [Fig. 5.1(d)], which conspires with the flow to give a positive $\text{Pi} - \text{D}_{\text{shear}}$ in the region $0.5 < |x - x_0| < 1.5$.

To see the contributions more clearly, we plot the profiles of the pressure-strain interaction $-\mathbf{P} : \mathbf{S}$ (black), PDU (red), and $\text{Pi} - \text{D}_{\text{shear}}$ (blue) in Fig. 5.3 along the

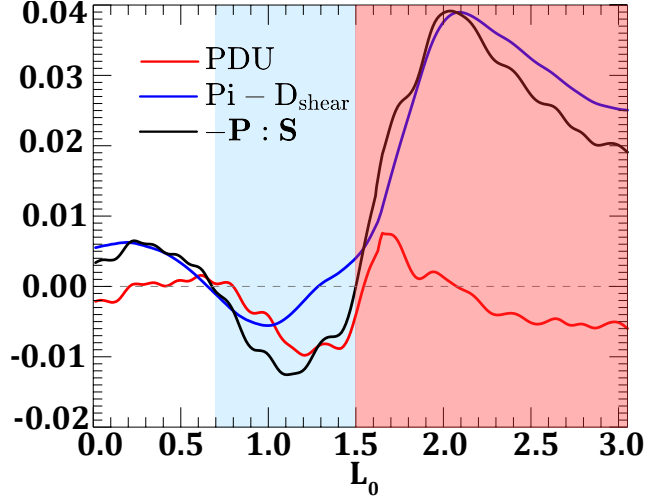


Figure 5.3: Pressure-strain interaction along the 1D path shown in Fig. 5.2(a). L_0 is the distance along the dotted path from the left. $-\mathbf{P} : \mathbf{S}$ is in black, PDU is in red, and $\text{Pi} - \text{D}_{\text{shear}}$ is in blue. The shading marks the regions of negative (blue) and positive (red) pressure-strain interaction. [Associated dataset available at <http://dx.doi.org/10.5281/zenodo.7117619>].

cut displayed as the black dotted path in Fig. 5.2(a). This path goes through the region of negative pressure-strain interaction in the exhaust and positive pressure-strain interaction along the upstream edge of the EDR. The distance along the path starting from the left is L_0 . The plot shows that the region of positive pressure-strain interaction at the upstream edge of the EDR, shaded in red, is due to $\text{Pi} - \text{D}_{\text{shear}}$, as inferred from the 2D plots in Fig. 5.2.

Finally, for the region of negative pressure-strain interaction shaded in blue, closer to the X-line the dominant contribution is diverging flow (PDU), which occurs as the electron exhaust gets deflected around the island and accelerates away from the neutral line. Further from the X-line, bulk flow shear due to the localized electron beam going around the island becomes equally important. This region of negative pressure-strain interaction is not seen in the simulations in Ref. (Pezzi et al.,

2021). It is possibly due to the expansion caused by the separatrix opening out in time as reconnection onsets in our simulations, which would not have been seen in Ref. (Pezzi et al., 2021) because their data were from a time after the maximum in the reconnection rate. Further work would be necessary to confirm or refute this possibility.

Since the negativity of $\text{Pi} - \text{D}$ has been an important topic of consideration in the recent literature, we also discuss it here. By taking cuts of the deformation and shear parts of $\text{Pi} - \text{D}$ along the same black dotted path in Fig. 5.2(a) (not shown), we find that the region of negative $\text{Pi} - \text{D}$ in the downstream region (centered around $|x - x_0| \approx 2, |y - y_0| \approx 0.3$) is due to flow shear rather than normal deformation.

5.4 Simulation Results - Magnetic Field-Aligned Coordinates

5.4.1 Overview

Figure 5.4 displays 2D profiles of the plasma quantities, analogous to those in panels Fig. 5.1(a)-(l) except the electron pressure tensor \mathbf{P} [panels (a)-(f)] and the electron bulk flow velocity \mathbf{u} [panels (g)-(i)] are in field-aligned coordinates with subscripts b, κ , and n . The magnetic field components [panels (j)-(l)] are repeated from Fig. 5.1 for convenience.

The curvature direction is mostly in the $\pm x$ direction along $y = y_0$ and the $\pm y$ direction along $x = x_0$. There is an abrupt change in the direction of $\hat{\mathbf{k}}$ in the upstream region where the direction of the curvature of the magnetic field lines flips, which is particularly evident in Figs. 5.4(h) and (i). The magnetic field curvature κ

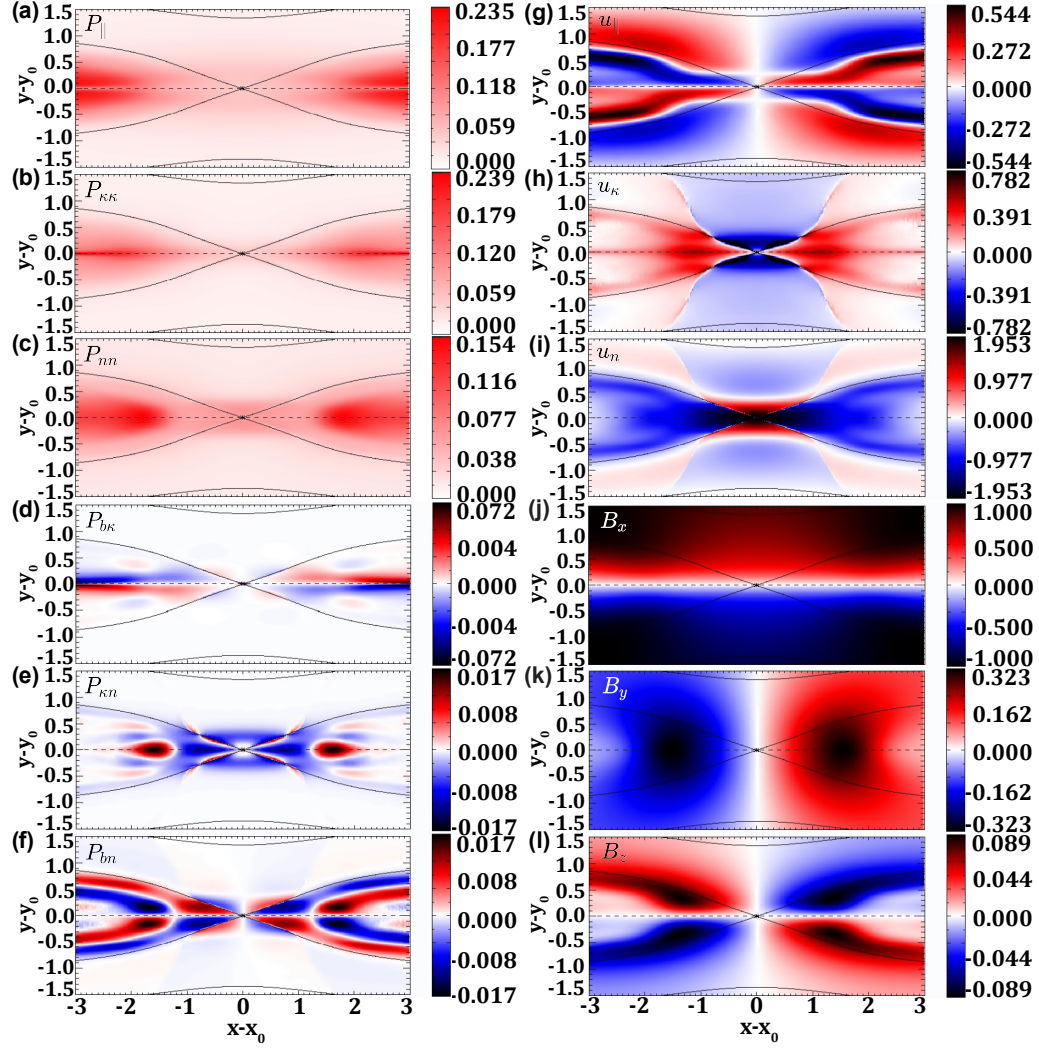


Figure 5.4: For the same data as in Fig. 5.1, 2D profiles of the (a)-(f) six independent elements of the electron pressure tensor \mathbf{P} and (g)-(i) three components of bulk electron velocity \mathbf{u} in field-aligned coordinates. The magnetic field \mathbf{B} is plotted again in (j)-(l) for convenience. Representative magnetic field projections in the xy plane are in black. [Associated dataset available at <http://dx.doi.org/10.5281/zenodo.7117619>].

is highest in the exhaust region near $y = y_0$ due to the curvature of the reconnected field lines. The binormal direction is mostly in the $\pm z$ direction except in the region of the out-of-plane Hall magnetic field where $\hat{\mathbf{n}}$ develops an in-plane component because the Hall effect bends the reconnecting magnetic field out of the reconnection plane within the diffusion region (Sonnerup, 1979; Mandt et al., 1994), as seen in Fig. 5.4(1). (There would be torsion in the upstream region if there was an initial out-of-plane guide magnetic field.) There is also a strong torsion where $\hat{\mathbf{k}}$ abruptly switches signs in the upstream region, since this causes an abrupt change in the $\hat{\mathbf{n}}$ direction and $\tau = -\hat{\mathbf{k}} \cdot \nabla_{\parallel} \hat{\mathbf{n}}$. However, the contribution to the pressure-strain interaction associated with this strong τ in the upstream region is weak. The torsion due to the Hall magnetic field has the same sign in the first and third quadrants relative to the X-line, and the opposite sign in the second and fourth quadrants. In our simulations, it is negative in the first quadrant close to the X-line ($x - x_0 < 0.2$), then becomes positive from $0.2 < x - x_0 \lesssim 0.6$, and negative again further out in the EDR.

For the spatial structure of the plasma properties in field-aligned coordinates, the diagonal elements of the electron pressure tensor broadly have similarities in the Cartesian and field-aligned coordinate system, but the off-diagonal elements look very different. The bulk flow profiles are largely as expected. The parallel bulk flow u_{\parallel} [Fig. 5.4(g)] is field aligned or anti-field aligned in the exhaust between the separatrices due to the change of direction of the magnetic field [Fig. 5.4(j)], with a similar pattern with reversed polarity due to the inflow outside the separatrix. This gives rise to an overall octupolar structure around the X-line. The flow in

the direction of the curvature u_κ is negative in the upstream region where the flow opposes the magnetic field curvature and positive in the exhaust where it is along the curvature [Fig. 5.4(h)]. The out-of-plane velocity u_z [Fig. 5.1(i)] is slightly negative in the IDR and mostly positive in the EDR, so the sign flips within those regions in the binormal component of the velocity u_n [Fig. 5.4(i)] are due to the changing direction of $\hat{\mathbf{n}}$.

5.4.2 Decomposition of Pressure-Strain Interaction in Field-Aligned Coordinates

We plot the contributions to the pressure-strain interaction in field-aligned coordinates in Fig. 5.5. We briefly discuss each term in turn and relate their most significant structures to the physics of the reconnection process as an example of the utility of the method.

We start with bulk flow compression. Parallel flow compression [$-PS_1$, panel (a)], is largest along $y = y_0$. There, electrons are accelerated in the exhaust and obtain a component of flow parallel to the reconnected magnetic field that is positive in the first and third quadrants and negative in the second and fourth. At $y = y_0$, the magnetic field is mostly in the y direction, so this abrupt change in u_{\parallel} getting faster in the direction of the flow is expansion, so this is associated with a negative contribution to the pressure-strain interaction. Perpendicular flow compression [$-PS_2$, panel (b)] is extremely large along a portion of the separatrix within a localized region near the X-line. This arises because the magnetic field lines are strongly

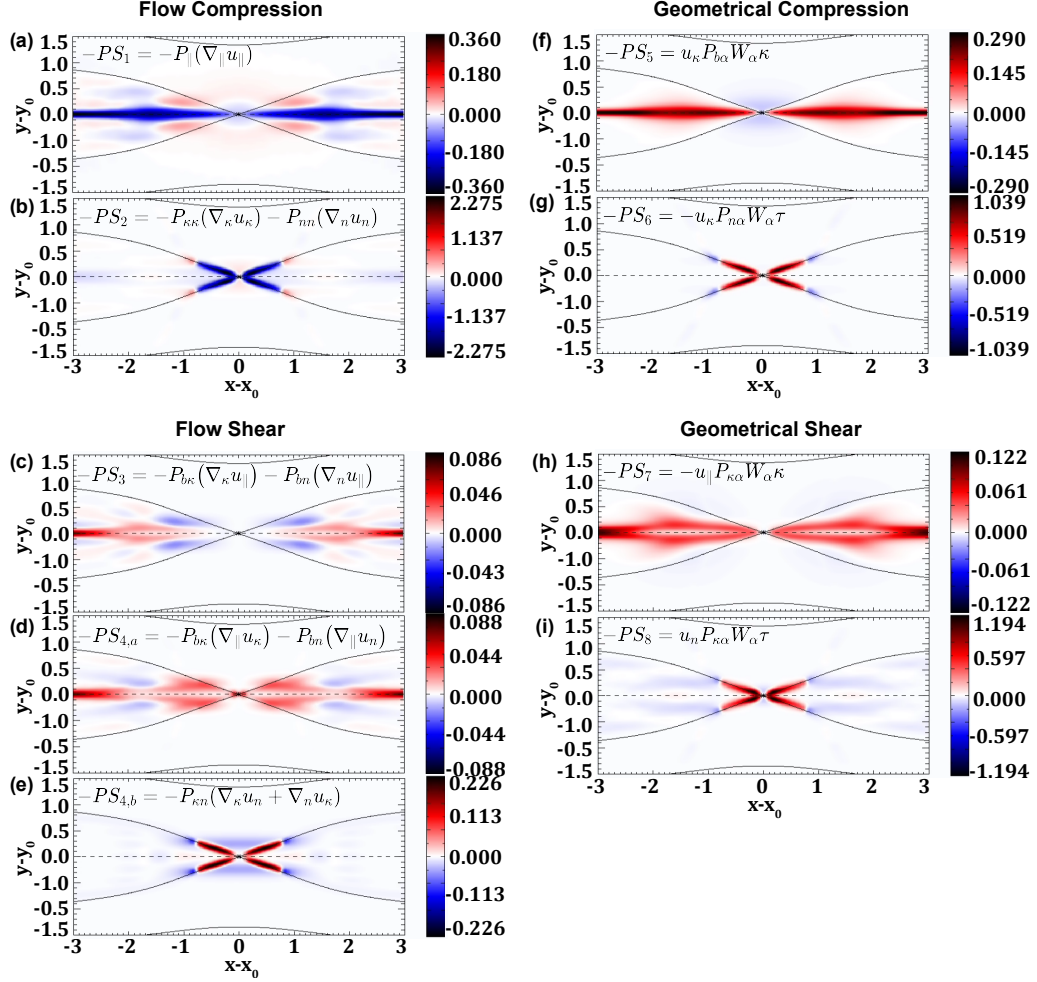


Figure 5.5: Decomposition of the pressure-strain interaction $-(\mathbf{P} \cdot \nabla) \cdot \mathbf{u}$ for electrons in field-aligned coordinates classified according to their physical causes. Bulk flow compression in the (a) parallel $-PS_1$ and (b) perpendicular $-PS_2$ directions. Bulk flow shear for (c) parallel flow varying in the perpendicular direction $-PS_3$, (d) perpendicular flow varying in the perpendicular direction $-PS_{4,a}$, and (e) perpendicular flow varying in the parallel direction $-PS_{4,b}$. Geometrical compression terms due to (f) perpendicular flow $-PS_5$ and (g) torsion $-PS_6$. Geometrical shear terms due to (h) parallel flow $-PS_7$ and (i) torsion $-PS_8$. [Associated dataset available at <http://dx.doi.org/10.5281/zenodo.7117619>].

kinked at the separatrices, accelerating electrons into the outflow jet normal to the magnetic field. This expansion is associated with a negative contribution to the pressure-strain interaction.

Next, we treat the bulk flow shear. The shear of the parallel flow in the perpendicular directions [$-PS_3$, panel (c)] is relatively weak within the EDR. It is most significant downstream of the exhaust at $y - y_0 \simeq 0$, where the jet enters the larger magnetic island. Within the EDR but near the downstream edge, there is parallel flow in the $\pm y$ direction, that slows down with distance away from the X-line in the $\hat{\kappa} \simeq \pm \hat{x}$ direction. Due to the structure of $P_{b\kappa}$ [Fig. 5.4(d)] this term contributes to relatively weak positive pressure-strain interaction. Within the EDR but closer to the separatrices in the exhaust, the same parallel flow speeds up in the $\hat{\kappa}$ direction, which is expansion. Since $P_{b\kappa}$ has the same sign in this region as the downstream EDR edge, this contributes to very weak negative pressure-strain interaction. Parallel shear of the perpendicular flow [$-PS_{4,a}$, panel (d)] is strongest in the EDR region in the exhausts just inside the separatrices. This is caused by u_n , which has a component in the outflow direction because of the bending of the reconnected field by the Hall effect, that changes along the magnetic field in a region of non-zero P_{bn} . This contribution to pressure-strain interaction is rather weak; there is stronger heating downstream of the EDR near $y = y_0$. Perpendicular shear of the perpendicular flow [$-PS_{4,b}$, panel (e)] is strongest in the separatrix region near the X-line, where the terms due to the outflow mostly in u_κ and the current sheet flow mostly in u_n contribute a comparable amount. This leads to a contribution towards positive pressure-strain interaction. Also, at the upstream

edge of the EDR, u_n is predominantly in the out-of-plane ($\hat{\mathbf{z}}$) direction and varies in the inflow ($\pm\hat{\mathbf{y}}$) direction, which is opposite to the curvature direction in this region. This conspires with the negative $P_{\kappa n}$ to give a negative contribution to the pressure-strain interaction.

Turning to the geometrical terms, perpendicular geometrical compression [$-PS_5$, panel (f)] has its dominant signal near $y = y_0$, where the strongly curved field lines drive the outflow jet in the direction of the magnetic curvature, *i.e.*, the bulk flow in the exhaust has a strong positive perpendicular component u_κ [Fig. 5.4(h)]. Predominantly due to the diagonal element P_{\parallel} [see Fig. 1(e) in Chapter 4], this gives a positive contribution to the pressure-strain interaction. As emphasized in Chapter 4, no contribution to the pressure-strain interaction is due to direct heating by the magnetic field; rather the flows relative to the curve of the magnetic field line in this case are convergent, leading to geometrical compression. In the regions upstream of the X-line within the EDR, the bulk flow is in the opposite direction to the curvature, so it contributes towards negative pressure-strain interaction but much more weakly than in the exhaust. Torsional geometrical compression [$-PS_6$, panel (g)] has a significant contribution towards positive pressure-strain interaction at the separatrix near the X-line, which is due to the torsion generated by the in-plane magnetic field lines being dragged out of the page due to the Hall effect. It is strongest at the separatrices where the inflow is initially accelerated into the outflow, generating a positive u_κ [see Fig. 5.4(h)]. The P_{nn} term leads to the strongest contribution to positive pressure-strain interaction. Next is parallel geometrical shear [$-PS_7$, panel (h)]. It is strongest downstream of the EDR, but also has positive signal inside the

EDR in the outflow edges confined within the separatrices and away from $y = y_0$. This occurs because there is a diagonal pressure tensor element $P_{\kappa\kappa}$ coinciding with a parallel velocity u_{\parallel} in the curved magnetic fields of the exhaust, and this leads to a contribution towards positive pressure-strain interaction [see Fig. 1(g) of Chapter 4]. Finally, torsional geometrical shear [$-PS_8$, panel (i)] describes a positive contribution to pressure-strain interaction localized to the separatrix near the X-line, as with the other torsional geometrical term $-PS_6$ [panel (g)]. This occurs because there is a flow due the projection of the out-of-plane electron flow in the binormal direction, which conspires with $P_{\kappa\kappa}$ to contribute to give a positive contribution to the pressure-strain interaction.

5.4.3 Largest Contributions to the Pressure-Strain Interaction in Field-Aligned Coordinates

Having treated the terms individually, now we discuss the terms that dominate the regions where we see the most important features of the pressure-strain interaction. Consider first the region immediately surrounding the X-line, where Fig. 5.2(a) shows that there is a local negative contribution at the X-line that extends in the outflow direction. The physical cause of this feature is that the outflow $u_{e,out}$ accelerates from rest to the peak outflow speed over a distance L_e in the outflow direction. Thus, the perpendicular flow u_{κ} [see Fig. 5.4(h)] is expanding in the direction it is pointing, which is associated with cooling from $-PS_2$.

We perform a scaling analysis of this term to estimate its contribution quanti-

tatively. The κ term of $-PS_2$, namely $-P_{\kappa\kappa}(\nabla_{\kappa}u_{\kappa})$, scales like $-PS_2 \sim -P_{\kappa\kappa}(u_{e,out}/L_e)$. For $P_{\kappa\kappa}$, this is P_{xx} in the EDR, and for scaling purposes we take this to be the upstream electron pressure $P_{e,up}$ [which is justified by Fig. 5.4(b)]. For the outflow speed, we expect that during steady state reconnection, it scales as the electron Alfvén speed $c_{Ae,up}$ based on the magnetic field strength $B_{e,up}$ upstream of the EDR. For the length of the EDR in the outflow direction, it scales as approximately $5 d_e$, where d_e is the electron inertial scale. Putting these together and using $c_{Ae,up}/d_e = \Omega_{ce,up}$, the electron cyclotron frequency based on $B_{e,up}$, we get $-PS_2 \sim -0.2P_{e,up}\Omega_{ce}$. We expect this to hold in the steady state, but our simulation data is taken during the onset phase instead. To test the scaling, we therefore use the empirically measured $u_{e,out} \simeq u_{\kappa} \simeq 0.8$ from Fig. 5.4(h). With simulation parameters $P_{e,up} = n_e T_{e,up} = 0.017$ and $L_e = 5 d_e = 2.2$, we get $-PS_2 \simeq -0.006$. This is in reasonable agreement with the simulated value of 0.009 for $-(\mathbf{P} \cdot \nabla) \cdot \mathbf{u}$ at the X-line in Fig. 5.2(a).

Further away from the X-line in the outflow direction along $y - y_0 = 0$ line, the pressure-strain interaction becomes strongly positive. In field-aligned coordinates, this happens because the outflow jet has a significant component parallel to the curvature direction leading to perpendicular geometrical compression $-PS_5$. The associated contribution scales as $-PS_5 \simeq u_{\kappa} P_{\parallel} \kappa \sim u_{e,out} P_{e,up} / d_e \sim P_{e,up} \Omega_{ce,up}$. The gradient scale in this case is d_e , the thickness of the EDR in the y direction, since that is the gradient that comes into the calculation of the curvature κ , and we similarly take $P_{\parallel} \sim P_{e,up}$. This heating rate is 5 times higher than the cooling rate near the X-line discussed in the previous paragraph. For the simulations, this gives

$-PS_5 \simeq 0.03$. This is in good agreement with the measured value of $-(\mathbf{P} \cdot \nabla) \cdot \mathbf{u}$ in this region of 0.05, as seen in Fig. 5.2(a).

The other main regions of non-zero pressure strain are the upstream edges of the EDR and the region of cooling at $1.5 < |x - x_0| < 2.5$ and $|y - y_0| \simeq 0.35$. To investigate the dominant terms, we take a cut along the dotted path in Fig. 5.2(a), the same path used to make Fig. 5.3. The result is shown in Fig. 5.6, with panel (a) showing the pressure-strain interaction in black, and the nine terms $-PS_j$ (with separate lines for $-PS_{4,a}$ and $-PS_{4,b}$) in red (compression terms) and blue (shear terms) lines. Panel (b) again shows the pressure-strain interaction in black, but here the sum of all of the terms dependent on u_{\parallel} are given in blue, while the sum of all the terms dependent on u_{κ} and u_n are given in red. We consider three different regions on this plot: immediately upstream of the X-line ($2.7 < L_0 < 3.0$, shaded pink), between this region and the separatrix in the upstream region ($1.5 < L_0 < 2.7$, shaded red), and the region of negative pressure-strain interaction ($0.7 < L_0 < 1.5$, shaded blue).

Immediately upstream of the X-line (or more appropriately for the present purposes, the stagnation point), the contribution to positive pressure-strain interaction is caused by electrons slowing down from their inflow speed to a speed of 0 at the stagnation point, which is a convergent (compressional) perpendicular flow. Thus, $-PS_2$ is the dominant contributor to the observed pressure-strain interaction, appearing as the red region near $x = x_0$ in Fig. 5.5(b), and showing up as the dominant contribution in the range $2.7 < L_0 < 3.0$ as the dashed red line in Fig. 5.6(a). We find that the dominant contribution to $-PS_2$ is $-P_{nn}(\nabla_n u_n)$ (not

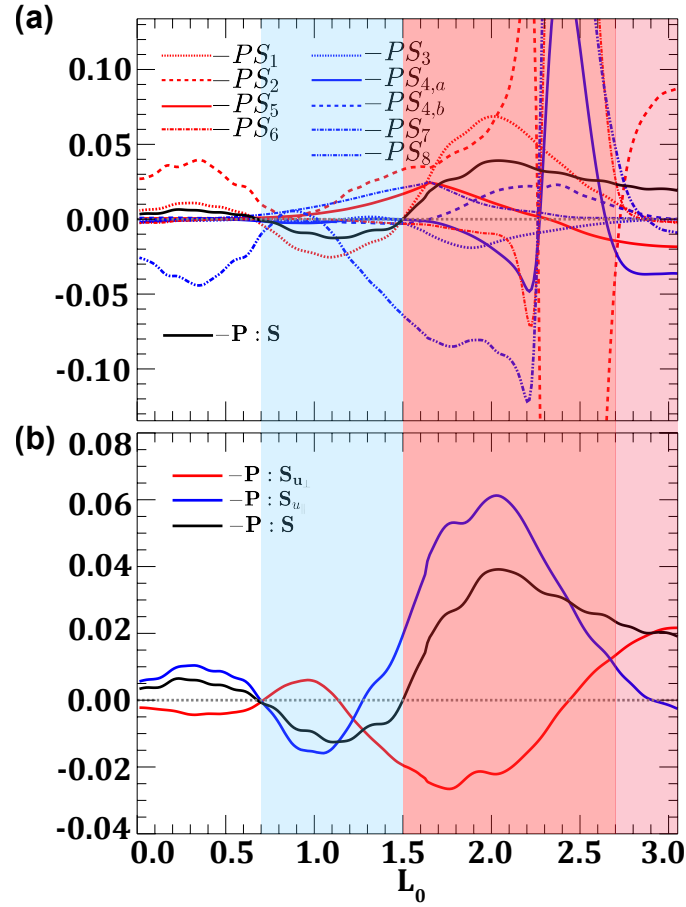


Figure 5.6: Pressure-strain interaction along the 1D cut shown as the dotted path in Fig. 5.2(a). L_0 is the distance from the left along the dotted path. In both panels, the pressure-strain interaction $-\mathbf{P} : \mathbf{S}$ is in black. (a) Contribution due to each $-PS_j$ term, with compression terms in red and shear terms in blue. (b) The pressure-strain interaction contribution $-\mathbf{P} : \mathbf{S}_{u_{\parallel}}$ dependent on u_{\parallel} (blue) and the pressure-strain interaction contribution $-\mathbf{P} : \mathbf{S}_{u_{\perp}}$ dependent on u_{κ} and u_n (red). [Associated dataset available at <http://dx.doi.org/10.5281/zenodo.7117619>].

shown). To estimate this term with a scaling analysis, we again take $P_{nn} \sim P_{e,up}$, so $-PS_2 \sim P_{e,up}u_n/L_n$, where u_n is the characteristic binormal speed and L_n is the gradient scale in the n direction. In this region, the magnetic fields bend out of the plane because of the Hall effect (Sonnerup, 1979; Mandt et al., 1994), so the $\hat{\mathbf{n}}$ direction has components in the $\hat{\mathbf{z}}$ and the $\pm\hat{\mathbf{y}}$ directions. Since the Hall B_z field strength scales as (Mandt et al., 1994) the reconnecting field strength B_x , the angle θ that $\hat{\mathbf{n}}$ makes with the reconnection plane scales as 45° . Then, we estimate u_n knowing that the dominant bulk flow in this region is the current sheet flow in the $\hat{\mathbf{z}}$ direction. A scaling analysis using Ampère’s law gives (in cgs units) $u_z \sim c(\partial B_x/\partial y)/4\pi en_e \sim cB_{e,up}/4\pi en_e d_e \sim c_{Ae,up}$. Projecting this into the n direction gives $u_n \sim u_z \cos\theta \sim c_{Ae,up} \cos\theta$. Similarly, we estimate L_n by noting the primary direction of variation is y . This gives $L_n \sim L_y \cos\theta \sim d_e \cos\theta$. Putting it all together, we get $-PS_2 \sim P_{e,up}\Omega_{ce,up} \cos^2\theta$. With $\theta \sim 45^\circ$, this term scales as approximately half the value of $-PS_5$ in the exhaust. For the simulations, we use the empirically determined $u_z \simeq 2$ to get a scaling prediction of $-PS_2 \sim P_{e,up}(u_z/d_e) \cos^2\theta \simeq 0.04$. This is a factor of two lower compared to the heating rate of 0.09 given by the dashed red line at $L_0 = 3.0$ in Fig. 5.6(a), which reflects the significant assumptions made in our estimates.

In the region of positive pressure-strain interaction $1.5 < L_0 < 2.7$ leading up to the separatrix, Fig. 5.6(a) reveals that a complicated mixture of terms play a role, with significant cancellation in parts. Figure 5.6(b) makes an assessment of the contributions more transparent, showing that the terms associated with the parallel flow are the main contributors. In the region of interest, a positive pressure-

strain interaction occurs due to $-PS_1$ because the parallel velocity of the inflowing electrons changes direction at the upstream edge of the EDR [Fig. 5.4(g)] which is a flow convergence and is therefore contributes to positive pressure-strain interaction. To quantify this with a scaling analysis, $-PS_1 \simeq P_{\parallel} \Delta u_{e,in\parallel} / L_{\parallel}$, where $\Delta u_{e,in\parallel}$ is the change in parallel inflow speed at the upstream edge of the EDR, and L_{\parallel} is the length-scale over which $u_{e,in\parallel}$ changes directions. It is difficult to estimate the change in flow and the gradient scale in terms of the upstream parameters, so we use values empirically determined from the simulations. Using $L_{\parallel} \sim d_e \sim 0.45$ and $\Delta u_{e,in\parallel} \simeq 0.4$ from Fig. 5.4(g), and $P_{\parallel} \sim P_{e,up} \sim 0.017$, we get $-PS_1 \simeq 0.015$. This is in reasonable agreement with the values of $-PS_1$ in the region of interest in Fig. 5.6(a), where the dotted red curve varies from 0 to $\simeq 0.07$ with an average of $\simeq 0.03$. This is less than the heating rate due to $-PS_5$ in the exhaust, and we expect it would also be smaller than $-PS_5$ for a realistic system.

Finally, at the location where the pressure-strain interaction is negative ($0.7 < L_0 < 1.5$), we see from both panels of Fig. 5.6 that parallel flow compression $-PS_1$ is the dominant term. This is consistent with the hypothesis in Sec. 5.3.3 that this negative pressure-strain interaction is caused by the separatrix opening out while reconnection is getting faster during its onset phase. To estimate the amplitude via a scaling analysis, it is $-PS_1 \sim P_{\parallel} \Delta u_{e,out\parallel} / L_{out,\parallel}$, where $\Delta u_{e,out\parallel}$ is the parallel speed in the exhaust region at the location of interest and $L_{out,\parallel}$ is the length scale over which it changes, *i.e.*, the distance to the X-line. This is again difficult to estimate in terms of the upstream parameters, but the empirical simulation results are $u_{e,out\parallel} \simeq -0.5$ and $L_{out,\parallel} \simeq 2$, so $-PS_1 \simeq -0.004$. Fig. 5.6(a) gives a value

of -0.025, about a factor of 6 higher, which again reflects the roughness of the estimation.

5.5 Discussion and Conclusions

This Chapter concerns using the pressure-strain interaction to study the rate of conversion between bulk flow and thermal energy density during magnetic reconnection. Using two-dimensional particle-in-cell simulations of anti-parallel symmetric reconnection and the analyses in Chapters 3 and 4, we calculate decompositions of the pressure-strain interaction in Cartesian and magnetic field-aligned coordinates in and around the EDR.

One purpose of this Chapter is to demonstrate how to use the results of Chapters 3 and 4 to analyze a physical system. In so doing, we plot the decomposition of the pressure-strain interaction in terms of the pressure dilatation and $Pi - D$ (compressible and incompressible contributions, respectively), and compare it to the decomposition from Chapter 3 with PDU and $Pi - D_{\text{shear}}$ terms (flow convergence/divergence and flow shear, respectively). We find their structure is noticeably different. Both decompositions have their merit in isolating particular physical effects. For the present study of reconnection, we find that a number of features of the most prominent contributions to the pressure-strain interaction are better isolated by employing PDU and $Pi - D_{\text{shear}}$, and significant insights are gained by using the two decompositions in tandem. We similarly calculate the decomposition of pressure-strain interaction in magnetic field-aligned coordinates. As desired, this

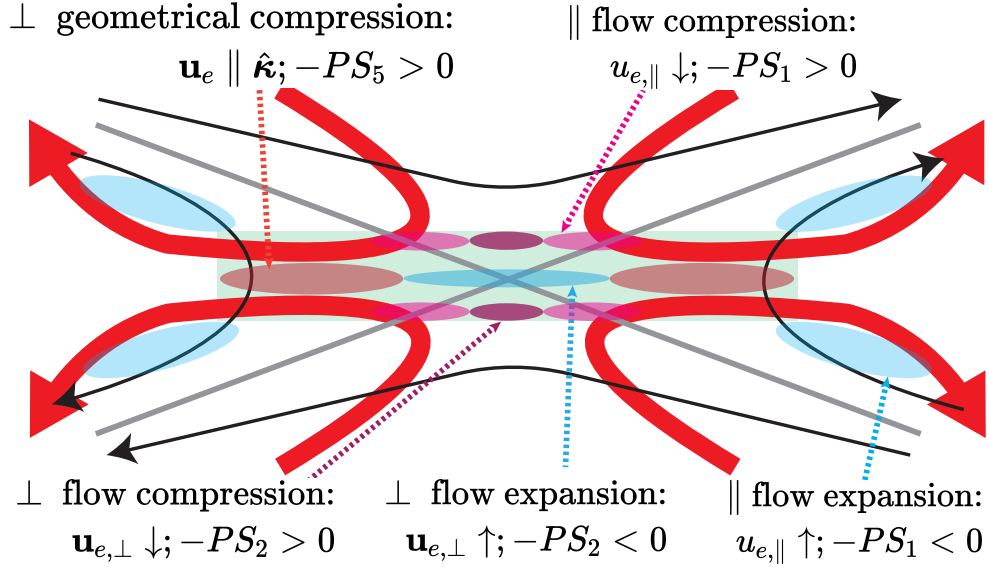


Figure 5.7: Sketch of the physical mechanisms contributing to the pressure-strain interaction in a magnetic reconnection region electron diffusion region (EDR) during the reconnection onset phase. In-plane projections of the magnetic field \mathbf{B} are in black and gray, and the in-plane electron bulk flow \mathbf{u}_e is in red. The green rectangle denotes the EDR. The ellipses in the red color palette denote regions of positive pressure-strain interaction (a contribution to heating), and the blue ellipses denote negative pressure-strain interaction (a contribution to cooling). The colored dashed arrows illustrate the physical mechanism causing the non-zero pressure-strain interaction in each location.

decomposition facilitates a physical interpretation of the mechanisms for heating relative to the ambient magnetic field, and allows for quantitative estimates of the energy density conversion rate from scaling analyses.

A second purpose of this Chapter is to better understand the conversion of energy between bulk flow and thermal energy density during magnetic reconnection. The result of this analysis is summarized by a map in Fig. 5.7 of where the different effects are most important near the EDR in our simulations during the onset phase of reconnection. It contains a sketch of a region around a reconnection X-line, with projections of the magnetic field in the reconnection plane in black, electron flow

lines in red, and the EDR shaded green. Ellipses denote regions for which the pressure-strain interaction is most appreciable, with colors in the red color palette denoting a contribution to positive pressure-strain interaction and blue denoting negative pressure-strain interaction. Each set of regions has an arrow pointing to it describing the physical mechanism causing the positive or negative pressure-strain interaction as a result of the analysis in Sec. 5.4.3:

1. $-PS_2$ causes positive pressure-strain interaction at the upstream edges of the EDR above and below the X-line due to perpendicular compression as the electron inflow slows down.
2. $-PS_1$ causes positive pressure-strain interaction at the upstream edge of the EDR out to the separatrices due to parallel compression as the inflow of electrons slow down as they approach the EDR.
3. $-PS_2$ causes negative pressure-strain interaction at and in the near vicinity of the X-line because electrons experience expansion as they are accelerated in the outflow direction.
4. $-PS_5$ causes positive pressure-strain interaction at the downstream edge of the EDR due to perpendicular geometrical compression since the outflow has a component in the direction of the magnetic curvature.
5. $-PS_1$ causes negative pressure-strain interaction in the downstream region due to expansion of the parallel flow, which is presumably associated the outflow jets being redirected in the vertical direction and speeding up while

the separatrix opens out during the onset phase.

It bears repeating that, in isolation, positive and negative pressure-strain interaction would be associated with a local increase and decrease in thermal energy density, respectively, *i.e.*, heating and cooling, but there are other terms that can locally change the thermal energy density so one cannot conclude there is local heating or cooling just from the sign of the pressure-strain interaction. Also, as a reminder, the present simulations were carried out with relatively high electron mass; we expect the structures would look qualitatively similar for a more realistic mass ratio, but likely with sharper features and higher amplitudes. This should be tested in future work.

To apply these results to steady-state reconnection, we expect that mechanisms #1-4 carry over relatively unchanged from the results here during reconnection onset. However, the downstream negative pressure-strain interaction in #5 is not likely to occur close to the EDR in steady-state reconnection. Instead, we expect it would occur in natural systems far downstream where the magnetic island grows. This is consistent with the absence of a coherent negative pressure-strain interaction in Fig. 2 of Ref. (Pezzi et al., 2021) for steady-state reconnection. This raises the possibility that the presence of negative pressure-strain interaction near the downstream edge of the EDR could be used as a signal of reconnection being amidst its onset phase, but it would take further work beyond a single simulation to confirm or refute this possibility.

A key result of the present Chapter is quantifying the expected scale of pressure-

strain interaction in the EDR during magnetic reconnection. A simple scaling analysis reveals that the natural scale that describes heating via the pressure-strain interaction $-(\mathbf{P} \cdot \nabla) \cdot \mathbf{u}$ in an anti-parallel reconnection EDR is $\pm P_{e,up} c_{Ae,up} / (1 - 5d_e)$ during the steady-state reconnection phase. In writing this, we use that the pressure in the EDR scales with the electron pressure $P_{e,up}$ upstream of the diffusion region, the bulk flow velocity scales with the electron Alfvén speed $c_{Ae,up}$ based on the magnetic field $B_{e,up}$ at the upstream edge of the EDR, and the gradient scale is either 1 or $5d_e$, depending on if the gradient is in the inflow or outflow direction, since $5d_e$ is an expected relevant scale for the length of the EDR in the outflow direction. This implies

$$-\mathbf{P} : \mathbf{S}_e \sim \pm(0.2 - 1)P_{e,up}\Omega_{ce,up}, \quad (5.8)$$

where $\Omega_{ce,up} = c_{Ae,up}/d_e$ is the electron cyclotron frequency based on $B_{e,up}$.

This prediction should be useful for quantitative comparisons of the pressure-strain interaction during magnetic reconnection in space and the laboratory. We treat a single case study as an example. The pressure-strain interaction was studied (Bandyopadhyay et al., 2021) during a magnetosheath reconnection event (Wilder et al., 2018). Using plasma parameters of $B_{i,up} \simeq 40$ nT for the asymptotic (ion scale) reconnecting magnetic field, $n \simeq 10$ cm⁻³ for the electron number density, and $T_{e,up} \simeq 70$ eV for the upstream electron temperature, and assuming the magnetic field at the electron layer scales as (Liu et al., 2022) $B_{e,up} \simeq (m_e/m_i)^{1/4}B_{i,up}$, we find $P_{e,up} \simeq 0.112$ nPa, $\Omega_{ce,up} \simeq 1.07 \times 10^3$ rad/s, and therefore $(0.2 - 1)P_{e,up}\Omega_{ce,up} \simeq 24 - 120$ nW/m³. We expect a similar scaling relation as Eq. (5.8) to hold for ions

except that the length scale in the outflow direction scales as $10 d_i$, so we expect

$$-\mathbf{P} : \mathbf{S}_i \sim \pm(0.1 - 1)P_{i,up}\Omega_{ci,up}. \quad (5.9)$$

For the same event (Wilder et al., 2018), $T_{i,up} \simeq 800$ eV and $n_i \simeq n_e$, so $P_{i,up} \simeq 1.28$ nPa and $\Omega_{ci,up} \simeq 3.8$ rad/s which implies $(0.1-1)P_{i,up}\Omega_{ci,up} \simeq (0.49-4.9)$ nW/m³. The measured pressure-strain interaction terms for electrons and ions peaked in the 30-40 nW/m³ range and just above 2 nW/m³, respectively (Bandyopadhyay et al., 2021). The ratio of the electron heating rate to the ion heating rate scales as $(T_{e,up}/T_{i,up})(B_{e,up}/B_{i,up})(m_i/m_e) \sim (T_{e,up}/T_{i,up})(m_i/m_e)^{3/4}$. For the MMS event, this is $\simeq 25$, compared to the measured ratio of about 20. Thus, the present scaling predictions are in good agreement with the observations of this event, both for the absolute scale for electrons and ions, and for the ratio between the electron and ion heating rates.

The research presented here reveals some important insights. The pressure-strain interaction is independent of the coordinate system in use, whether in a Cartesian coordinate system or one in which the coordinate system is curved. We have confirmed this for the simulations presented here (not shown).

However, the contributions to the pressure-strain interaction from compression/expansion and bulk flow shear are strongly dependent on the coordinate system, as anticipated in Chapter 4. Thus, the physical mechanism leading to the dominant pressure-strain interaction need not be the same in different coordinate systems. This is vividly seen for the example of magnetic reconnection treated here,

with the plots shown in Figs. 5.3 and 5.6 in Cartesian coordinates and field-aligned coordinates, respectively. We find in the region $0.7 < L_0 < 1.5$ that the negative pressure-strain interaction has contributions in Cartesian coordinates from both PDU and $\text{Pi} - \text{D}_{\text{shear}}$, with PDU being the dominant contributor; the mechanism in magnetic field-aligned coordinates is parallel flow expansion. This is the same physical mechanism, although it is not possible to identify from the Cartesian decomposition that the expansion is largely in the parallel direction. (This also illustrates one benefit of employing the magnetic field-aligned coordinate system.) However, for the positive pressure-strain interaction contribution ($1.5 < L_0 < 2.7$), it was found in Cartesian coordinates that the dominant contribution is $\text{Pi} - \text{D}_{\text{shear}}$, *i.e.*, bulk flow shear, while the magnetic field-aligned coordinate result is parallel flow compression. This exposes a potential pitfall in analyzing decompositions of the pressure-strain interaction contributions: the physical mechanisms in a Cartesian coordinate system may be different in a magnetic field-aligned coordinate system.

A second pitfall could arise in determining the dominant contribution to the pressure-strain interaction. If one wants to find the term in the decomposition that leads to the highest values, one might find the $-PS_j$ terms that are the largest and identify them as the most important. If we were to do that in the present study of reconnection, we would find that $-PS_2$ [Fig. 5.5(b)] is the largest due to its contribution at the separatrix region near the X-line. However, in this region the perpendicular flow shear [$-PS_{4,b}$, Fig. 5.5(e)], torsional geometrical compression [$-PS_6$, Figs. 5.5(g)], and torsional geometrical shear [$-PS_8$, Figs. 5.5(i)] are also important. By comparing amplitudes individually and with the pressure-strain

interaction $[-(\mathbf{P} \cdot \nabla) \cdot \mathbf{u}$, panel (a)], we see that perpendicular flow compression is more than 40 times larger the maximum value of the pressure-strain interaction. Moreover, the pressure-strain interaction does not display a feature at the separatrices near the X-line where these signals are strongest. This implies that the four terms cancel each other nearly completely in this region, leaving relatively weak pressure-strain interaction at the EDR separatrix. Thus, the decomposition of pressure-strain interaction in may lead to individual terms that are much larger than the total. Instead, finding the dominant term should be carried out by finding the pressure-strain interaction first, then finding which terms contribute most strongly in the region of interest.

There is a physical reason that the terms in the decomposition in field-aligned coordinates can be significantly larger than the pressure-strain interaction itself, with significant cancellation between terms. Field-aligned coordinates follow magnetic field lines. At the separatrices the flow lines are strongly kinked. The strong kink leads to a huge velocity shear, which contributes to positive pressure-strain interaction. But the plasma is strongly accelerated as well, leading to negative pressure-strain interaction through expansion. For both, the gradient length scale is set by the scale over which the flow profile changes. As seen in Fig. 5.4, the gradient in the flow can occur on scales far below the electron inertial scale. In our simulations, the gradient scale could be as low as the electron Debye scale or the grid scale, both less than 0.02 in normalized units. This is about 20-40 times smaller than d_e , which explains why the terms mentioned in the previous paragraph can be 20-40 times the pressure-strain interaction in total. We do not attempt in

this study to ascertain whether the Debye scale or grid scale sets the gradient scale and instead leave that for future work; it can be easily studied by varying the two scales relative to each other.

Finally, it bears repeating that the pressure-strain interaction is a local measure of the rate of energy conversion between bulk flow and thermal energy density, but it is not the full local measure of heating or cooling. It remains true that in an infinite or closed and isolated system, the global energy conversion is governed by the pressure-strain interaction (Yang et al., 2017b, 2022), but thermal energy flux, heat flux, and enthalpy flux can also change the local thermal energy density (Du et al., 2020; Song et al., 2020). Moreover, there are other metrics for the rate of other kinds of energy conversion in plasma processes, such as $\mathbf{J} \cdot \mathbf{E}$ (Zenitani et al., 2011) and its kinetic counterpart, the field-particle correlation (Klein & Howes, 2016), which have received a lot of attention (Burch et al., 2016b; Wilder et al., 2018; Chen et al., 2019; Afshari et al., 2021) because they describe the volumetric rate of conversion between the bulk flow energy and the energy in the electromagnetic fields. There have been studies comparing these other metrics with the pressure-strain interaction (Pezzi et al., 2021); it would be interesting to revisit such studies in light of the results of the present series of Chapters. A second important point is that thermal energy is merely one form of energy in a plasma not in local thermodynamic equilibrium. The pressure-strain interaction does not provide information about energy conversion into other forms of energy, such as $\int (1/2)mv'_xv'_y f d^3v$ or higher order moments. A measure of the energy conversion associated with moments of the phase space density other than the thermal energy density is treated in Chapter 6.

Chapter 6

Quantifying Energy Conversion in Higher Order Phase Space

Density Moments in Plasmas

6.1 Introduction

Energy conversion is largely well understood for systems with initial and final states in or near local thermodynamic equilibrium (LTE) (Chapman & Cowling, 1970; Jou et al., 2010). However, energy conversion in systems far from LTE, such as weakly collisional or collisionless plasmas endemic to many space and astrophysical environments, remains a forefront research area (Howes, 2017; Matthaeus et al., 2020).

For a species σ not in LTE, internal moments of the phase space density f_σ are defined as f_σ multiplied by powers of components of \mathbf{v}'_σ and integrated over all velocity space. Here, the random velocity is $\mathbf{v}'_\sigma = \mathbf{v} - \mathbf{u}_\sigma$, velocity space coordinate is \mathbf{v} , bulk flow velocity is $\mathbf{u}_\sigma = (1/n_\sigma) \int f_\sigma \mathbf{v} d^3v$, and number density is $n_\sigma = \int f_\sigma d^3v$. A standard approach to study energy conversion in plasmas (Yang et al., 2017b; Chasapis et al., 2018; Zhong et al., 2019; Bandyopadhyay et al., 2020a, 2021; Wang

Phys. Rev. Lett. 130, 085201 (2023)

Contributing authors: Paul A. Cassak, M. Hasan Barbhuiya, Haoming Liang, Matthew R. Argall

et al., 2021; Zhou et al., 2021; Del Sarto et al., 2016; Sitnov et al., 2018; Del Sarto & Pegoraro, 2018; Du et al., 2018; Parashar et al., 2018; Pezzi et al., 2019; Yang et al., 2019b; Song et al., 2020; Du et al., 2020; Fadanelli et al., 2021; Arró, G. et al., 2022; Yang et al., 2022; Hellinger et al., 2022; Cassak & Barbhuiya, 2022; Cassak et al., 2022; Barbhuiya & Cassak, 2022) centers on the first few internal moments. Compressional work describes changes to n_σ , *i.e.*, the zeroth internal moment of f_σ , described by the continuity equation (Yang et al., 2017b; Braginskii, 1965). The internal energy per particle $\bar{\mathcal{E}}_{\sigma,\text{int}} = (3/2)k_B\mathcal{T}_\sigma$, *i.e.*, the second internal moment of f_σ divided by n_σ , can change due to compressional heating by work $-\mathcal{P}_\sigma(\nabla \cdot \mathbf{u}_\sigma)$, incompressional heating via the remainder of the pressure-strain interaction (called Pi-D (Yang et al., 2017b)), heat flux, or collisions, according to (Braginskii, 1965; Jou et al., 2010; Yang et al., 2017b)

$$\frac{3}{2}n_\sigma k_B \frac{d\mathcal{T}_\sigma}{dt} = -(\mathbf{P}_\sigma \cdot \nabla) \cdot \mathbf{u}_\sigma - \nabla \cdot \mathbf{q}_\sigma + n_\sigma \dot{Q}_{\sigma,\text{coll,inter}}. \quad (6.1)$$

Here, the elements of the pressure tensor \mathbf{P}_σ are $P_{\sigma,jk} = m_\sigma \int v'_j v'_k f_\sigma d^3v$, temperature tensor is $\mathbf{T}_\sigma = \mathbf{P}_\sigma/n_\sigma k_B$, effective pressure is $\mathcal{P}_\sigma = (1/3)\text{tr}[\mathbf{P}_\sigma]$, effective temperature is $\mathcal{T}_\sigma = \mathcal{P}_\sigma/n_\sigma k_B = (m_\sigma/3n_\sigma k_B) \int v_\sigma'^2 f_\sigma d^3v$, vector heat flux density is $\mathbf{q}_\sigma = \int (1/2)m_\sigma v_\sigma'^2 \mathbf{v}'_\sigma f_\sigma d^3v$, and volumetric heating rate per particle due to inter-species collisions is $\dot{Q}_{\sigma,\text{coll,inter}} = (1/n_\sigma) \int (1/2)m_\sigma v_\sigma'^2 \sum_{\sigma'} C_{\text{inter}}[f_\sigma, f_{\sigma'}] d^3v$, where the inter-species collision operator is $C_{\text{inter}}[f_\sigma, f_{\sigma'}]$, k_B is Boltzmann's constant, m_σ is the constituent mass, and $d/dt = \partial/\partial t + \mathbf{u}_\sigma \cdot \nabla$ is the convective derivative.

There is an energy conversion channel beyond those discussed thus far. f_σ has

an infinite number of internal moments that are all treated on equal footing. While Eq. (6.1) includes the impact of off-diagonal pressure tensor elements and heat flux on $\bar{\mathcal{E}}_{\sigma,\text{int}}$, any energy conversion associated with time evolution of all other internal moments themselves is not contained in the continuity equation or Eq. (6.1).

Studies have addressed time evolution of other moments and their contribution to energy conversion. The evolution of non-isotropic pressures has been studied (Kuznetsova et al., 1998; Yin & Winske, 2003; Brackbill, 2011; Greco et al., 2012; Servidio et al., 2012; Egedal et al., 2013; Wang et al., 2015; Swisdak, 2016; Del Sarto et al., 2016; Del Sarto & Pegoraro, 2018). Other approaches capture the effect of all moments of f_σ . Linearizing f_σ around its equilibrium in kinetic theory and gyrokinetics reveals the so-called free energy (Hallatschek, 2004; Howes et al., 2006; Schekochihin et al., 2009), which quantifies non-LTE energy conversion into mechanical or magnetic energy (Hallatschek, 2004). It is associated with the phase space cascade of entropy which can lead to dissipation (Tatsuno et al., 2009). The velocity space cascade has been studied without linearizing f_σ (Servidio et al., 2017; Pezzi et al., 2018; Cerri et al., 2018; Pezzi et al., 2019). In another approach, changes to bulk kinetic energy are quantified kinetically using field-particle correlations (Klein & Howes, 2016; Howes et al., 2017; Klein et al., 2017; Klein, 2017; Chen et al., 2019; Li et al., 2019; Klein et al., 2020; Juno et al., 2021; Verniero et al., 2021; Montag & Howes, 2022).

In this Chapter, we use a first-principles theory to quantify energy conversion associated with all internal moments. We show this energy conversion is physically associated with changing the velocity space shape of f_σ . There are three important

ingredients. First, the key quantity is kinetic entropy (Boltzmann, 1877; Eu, 1995; Chan Eu, 2006; Jou et al., 2010; Eyink, 2018) rather than energy. Second, we employ the decomposition of kinetic entropy into position and velocity space kinetic entropy (Mouhot & Villani, 2011; Liang et al., 2019). Third, we employ the so-called relative entropy (Grad, 1965; Eu, 1995; Chan Eu, 2006). Our analysis was performed independently, but we found it is similar to treatments in chemical physics of dilute gases (Eu, 1995) and quantum statistical mechanics (Floerchinger & Haas, 2020). The novelty of our analysis stems from using the decomposition of kinetic entropy and significant differences in interpretation than in previous work. We employ a particle-in-cell (PIC) simulation of collisionless magnetic reconnection, revealing energy conversion associated with higher order moments can be locally significant.

6.2 Theory

We first derive an expression for the rate of energy conversion associated with non-LTE internal moments of f_σ , emphasizing departures from the treatment in Ref. (Eu, 1995). We assume a classical (non-relativistic, non-quantum) three-dimensional (3D) system of infinite volume or in a thermally insulated domain with a fixed number N_σ of monatomic particles. The kinetic entropy density s_σ associated with f_σ is (Boltzmann, 1872)

$$s_\sigma = -k_B \int f_\sigma \ln \left(\frac{f_\sigma \Delta^3 r_\sigma \Delta^3 v_\sigma}{N_\sigma} \right) d^3 v, \quad (6.2)$$

where the integral is over all velocity space, and $\Delta^3 r_\sigma$ and $\Delta^3 v_\sigma$ are position space and velocity space volume elements in phase space, respectively (Liang et al., 2019, 2020a; Argall et al., 2022). In the comoving (Lagrangian) frame, s_σ evolves according to ((Eu, 1995) and Supplemental Material 6.5.1)

$$\frac{d}{dt} \left(\frac{s_\sigma}{n_\sigma} \right) + \frac{\nabla \cdot \mathcal{J}_{\sigma,\text{th}}}{n_\sigma} = \frac{\dot{s}_{\sigma,\text{coll}}}{n_\sigma}, \quad (6.3)$$

where $\mathcal{J}_{\sigma,\text{th}}$ is thermal kinetic entropy density flux and $\dot{s}_{\sigma,\text{coll}}$ is local time rate of change of kinetic entropy density through collisions, defined in Eqs. (6.14) and (6.13), respectively. We note that Eq. (6.3) has no explicit dependence on body forces including gravitational and electromagnetic forces, which implies they do not directly change internal moments of f_σ . Eq. (6.1) exemplifies this for the special case of internal energy.

In a key departure from Ref. (Eu, 1995), we decompose kinetic entropy density s_σ into a position space kinetic entropy density $s_{\sigma p}$ and velocity space kinetic entropy density $s_{\sigma v}$, with $s_\sigma = s_{\sigma p} + s_{\sigma v}$, as (Mouhot & Villani, 2011; Liang et al., 2019)

$$s_{\sigma p} = -k_B n_\sigma \ln \left(\frac{n_\sigma \Delta^3 r_\sigma}{N_\sigma} \right), \quad (6.4a)$$

$$s_{\sigma v} = -k_B \int f_\sigma \ln \left(\frac{f_\sigma \Delta^3 v_\sigma}{n_\sigma} \right) d^3 v. \quad (6.4b)$$

A direct calculation (see Supplemental Material 6.5.2-6.5.4) of the terms on the left

side of Eq. (6.3) using Eqs. (6.4a) and (6.4b) gives

$$\frac{d}{dt} \left(\frac{s_{\sigma p}}{n_\sigma} \right) = \frac{1}{\mathcal{T}_\sigma} \frac{d\mathcal{W}_\sigma}{dt}, \quad (6.5a)$$

$$\frac{d}{dt} \left(\frac{s_{\sigma v}}{n_\sigma} \right) = \frac{1}{\mathcal{T}_\sigma} \frac{d\bar{\mathcal{E}}_{\sigma, \text{int}}}{dt} + \frac{d}{dt} \left(\frac{s_{\sigma v, \text{rel}}}{n_\sigma} \right), \quad (6.5b)$$

$$\frac{\nabla \cdot \mathcal{J}_{\sigma, \text{th}}}{n_\sigma} = -\frac{1}{\mathcal{T}_\sigma} \frac{d\mathcal{Q}_\sigma}{dt} + \frac{(\nabla \cdot \mathcal{J}_{\sigma, \text{th}})_{\text{rel}}}{n_\sigma}, \quad (6.5c)$$

where $d\mathcal{W}_\sigma = \mathcal{P}_\sigma d(1/n_\sigma)$ is the compressional work per particle done by the system, $d\bar{\mathcal{E}}_{\sigma, \text{int}} = (3/2)k_B d\mathcal{T}_\sigma$ is the increment in internal energy per particle, and $d\mathcal{Q}_\sigma/dt = [-\nabla \cdot \mathbf{q}_\sigma - (\mathbf{P}_\sigma \cdot \nabla) \cdot \mathbf{u}_\sigma + \mathcal{P}_\sigma(\nabla \cdot \mathbf{u}_\sigma)]/n_\sigma$ is the (thermodynamic) heating rate per particle from sources other than compression that can change the effective temperature [see Eq. (6.1)]. Lastly, $s_{\sigma v, \text{rel}}$ is the relative entropy density and $(\nabla \cdot \mathcal{J}_{\sigma, \text{th}})_{\text{rel}}$ is the thermal relative entropy density flux divergence, given by

$$s_{\sigma v, \text{rel}} = -k_B \int f_\sigma \ln \left(\frac{f_\sigma}{f_{\sigma M}} \right) d^3v, \quad (6.6)$$

$$(\nabla \cdot \mathcal{J}_{\sigma, \text{th}})_{\text{rel}} = -k_B \int \left[\nabla \cdot (\mathbf{v}'_\sigma f_\sigma) \right] \ln \left(\frac{f_\sigma}{f_{\sigma M}} \right) d^3v, \quad (6.7)$$

and the ‘‘Maxwellianized’’ phase space density $f_{\sigma M}$ associated with f_σ is (Grad, 1965)

$$f_{\sigma M} = n_\sigma \left(\frac{m_\sigma}{2\pi k_B \mathcal{T}_\sigma} \right)^{3/2} e^{-m_\sigma(\mathbf{v}-\mathbf{u}_\sigma)^2/2k_B \mathcal{T}_\sigma}, \quad (6.8)$$

where n_σ , \mathbf{u}_σ , and \mathcal{T}_σ are based on f_σ . (Ref. (Eu, 1995) used a more general reference phase space density than $f_{\sigma M}$, so our choice is a special case of theirs.)

Equations (6.5a)-(6.5c) have important implications, and our interpretation

greatly departs from Ref. (Eu, 1995). Ignoring the relative terms in Eqs. (6.5b) and (6.5c), we see Eq. (6.3) (scaled by the effective temperature) inherently contains information about work, internal energy, and thermodynamic heat as captured by the continuity equation and Eq. (6.1). This suggests the relative terms describe energy conversion associated with all internal moments beyond the second moment.

We therefore define increments of relative energy per particle $d\bar{\mathcal{E}}_{\sigma,\text{rel}}$ and relative heat per particle $d\mathcal{Q}_{\sigma,\text{rel}}$ by

$$\frac{d\bar{\mathcal{E}}_{\sigma,\text{rel}}}{dt} = \mathcal{T}_{\sigma} \frac{d(s_{\sigma v,\text{rel}}/n_{\sigma})}{dt}, \quad (6.9a)$$

$$\frac{d\mathcal{Q}_{\sigma,\text{rel}}}{dt} = -\mathcal{T}_{\sigma} \frac{(\nabla \cdot \mathcal{J}_{\sigma,\text{th}})_{\text{rel}}}{n_{\sigma}}. \quad (6.9b)$$

Further defining energy increments per particle in all internal moments at and above the second moment as $d\bar{\mathcal{E}}_{\sigma,\text{gen}} = d\bar{\mathcal{E}}_{\sigma,\text{int}} + d\bar{\mathcal{E}}_{\sigma,\text{rel}}$ and generalized heat per particle as $d\mathcal{Q}_{\sigma,\text{gen}} = d\mathcal{Q}_{\sigma} + d\mathcal{Q}_{\sigma,\text{rel}}$, Eqs. (6.3) - (6.5c), (6.9a) and (6.9b) take on the simple form

$$\frac{d\mathcal{W}_{\sigma}}{dt} + \frac{d\bar{\mathcal{E}}_{\sigma,\text{gen}}}{dt} = \frac{d\mathcal{Q}_{\sigma,\text{gen}}}{dt} + \dot{\mathcal{Q}}_{\sigma,\text{coll}}. \quad (6.10)$$

Equation (6.10) generalizes Eq. (6.1), which contains energy conversion associated with only density and effective temperature, as opposed to all internal moments of f_{σ} . This interpretation is a significant departure from Ref. (Eu, 1995).

We now provide a physical interpretation, which requires understanding energy conversion via its impact on f_{σ} . Work per particle $d\mathcal{W}_{\sigma} = \mathcal{P}_{\sigma}d(1/n_{\sigma})$ changes the zeroth moment of f_{σ} . This is depicted graphically in Fig. 6.1, where two ve-

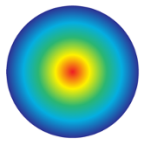
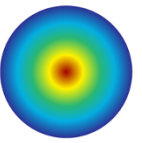
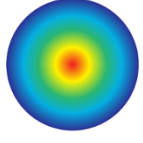
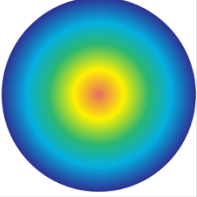
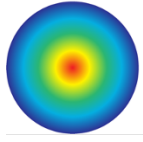
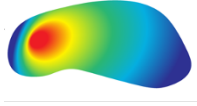
Initial f_σ	Final f_σ	Physics	
		Change of Density (Work)	$\frac{d\mathcal{W}_\sigma}{dt}$
		Change of Temperature (Internal Energy)	$\frac{d\bar{\mathcal{E}}_{\sigma,\text{int}}}{dt}$
		Change of Shape of f_σ (Relative Energy)	$\frac{d\bar{\mathcal{E}}_{\sigma,\text{rel}}}{dt}$

Figure 6.1: Schematic showing energy conversion channels according to their impact on the phase space density f_σ . The initial f_σ is depicted as Maxwellian for illustrative purposes on the left. The final f_σ is to their right. The descriptions of the changes in f_σ are to their right.

locity space dimensions of f_σ are sketched. The top row shows a process taking a Maxwellianized f_σ from an initial to final state. The intensification of colors denote a change in f_σ , and therefore n_σ . Similarly, $d\bar{\mathcal{E}}_{\sigma,\text{int}}$ is associated with changes to the second internal moment of f_σ , depicted in the second row of Fig. 6.1 for a process that increases $\bar{\mathcal{E}}_{\sigma,\text{int}}$, *i.e.*, the Maxwellianized f_σ spreads in velocity space.

To interpret $d\bar{\mathcal{E}}_{\sigma,\text{rel}}$, Eq. (6.6) shows $s_{\sigma v,\text{rel}}$ vanishes if f_σ is a Maxwellian ($f_\sigma = f_{\sigma M}$) (Grad, 1965). Thus, $d\bar{\mathcal{E}}_{\sigma,\text{rel}}$ describes non-LTE physics. Since a Maxwellian is the highest kinetic entropy state for a fixed N_σ and $\bar{\mathcal{E}}_{\sigma,\text{int}}$ (Boltzmann, 1877), $d(s_{\sigma v,\text{rel}}/n_\sigma)/dt > 0$ implies f_σ evolves towards Maxwellianity in the comoving frame, associated with $d\bar{\mathcal{E}}_{\sigma,\text{rel}} > 0$, while $d(s_{\sigma v,\text{rel}}/n_\sigma)/dt < 0$ implies f_σ evolves away from

Maxwellianity and $d\bar{\mathcal{E}}_{\sigma,\text{rel}} < 0$. A process changing the shape of f_σ is depicted in the third row of Fig. 6.1, where f_σ is initially Maxwellian and finally it is not.

A concrete example showing that $d\bar{\mathcal{E}}_{\sigma,\text{rel}}$ is associated with f_σ changing shape is provided in Supplemental Material 6.5.5. $d\bar{\mathcal{E}}_{\sigma,\text{rel}}$ is calculated analytically for a bi-Maxwellian distribution with converging flow. It is shown that the evolution of f_σ is consistent with the interpretation in the previous paragraph.

Collisions directly change the shape of f_σ , so $d\bar{\mathcal{E}}_{\sigma,\text{rel}}$ includes irreversible contributions if collisions are present. However, since f_σ can change shape even in the perfectly collisionless limit, $d\bar{\mathcal{E}}_{\sigma,\text{rel}}$ also contains reversible effects. Thus, the term is not purely irreversible as previously suggested (Eu, 1995).

$d\mathcal{Q}_\sigma$ describes non-Maxwellian features of f_σ that cause a flux of energy per particle that changes \mathcal{T}_σ [see Eq. (6.1)]. $d\mathcal{Q}_{\sigma,\text{rel}}$ is analogous: non-Maxwellian features in higher order internal moments produce a flux that modifies internal moments of f_σ other than n_σ and \mathcal{T}_σ . $\dot{Q}_{\sigma,\text{coll}}$ describes both intra- and inter-species collisions, as opposed to solely inter-species arising in Eq. (6.1). This is because both collision types can change higher order internal moments of f_σ , while elastic intra-species collisions conserve energy.

6.3 Simulation Results

We demonstrate key results of the theory using simulations of reconnection. Data are from the simulation in Chapter 5. The code and numerical aspects are discussed there and in Supplemental Material 6.5.6. The out-of-plane current density

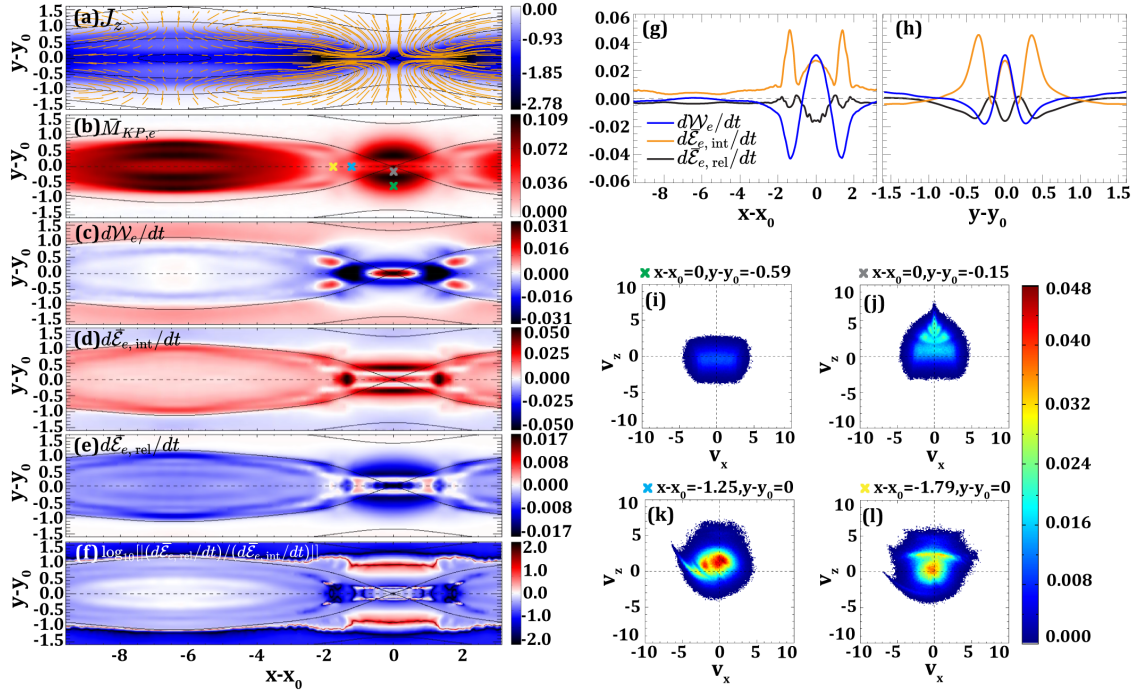


Figure 6.2: Electron energy conversion in a PIC simulation of magnetic reconnection. (a) Out-of-plane current density J_z , with projections of magnetic field lines and segments of electron velocity streamlines overlotted in black and orange, respectively. (b) Electron entropy-based non-Maxwellianity $\bar{M}_{KP,e}$. Time rates of change per particle of (c) work $d\mathcal{W}_e/dt$, (d) internal energy $d\bar{\mathcal{E}}_{e,int}/dt$, and (e) relative energy $d\bar{\mathcal{E}}_{e,rel}/dt$. (f) $\log_{10}[(d\bar{\mathcal{E}}_{e,rel}/dt)/(d\bar{\mathcal{E}}_{e,int}/dt)]$. 1D cuts of the terms in panels (c)-(e) in the (g) x and (h) y directions. (i)-(l) Reduced electron phase space density $f_e(v_x, v_z)$ at locations denoted by the colored x's at the top left of the plots corresponding to the x's in panel (b) along a streamline.

J_z around a reconnection X-line at (x_0, y_0) is in Fig. 6.2(a), with reversing magnetic field lines in black and electron streamline segments in orange, revealing typical profiles.

We first confirm relative energy changes are related to f_σ evolving towards or away from LTE. Figure 6.2(b) shows the electron entropy-based Kaufmann and Paterson non-Maxwellianity $\bar{M}_{e,KP} = (s_{eM} - s_e)/[(3/2)k_B n_e]$ (Kaufmann & Paterson, 2009; Liang et al., 2020a), where s_e comes from Eq. (6.2) based on f_e , while s_{eM}

comes from Eq. (6.2) based on f_{eM} in Eq. (6.8). It is a measure of the temporally and spatially local departure from LTE. Figure 6.2(e) is the rate of relative energy per particle $d\bar{\mathcal{E}}_{e,\text{rel}}/dt$. Figure 6.2(i)-(l) are reduced electron phase space densities $f_e(v_x, v_z)$ at the four color-coded x's along a streamline in Fig. 6.2(b).

$\bar{M}_{e,KP}$ and $d\bar{\mathcal{E}}_{e,\text{rel}}/dt$ together reveal whether f_σ is locally in LTE [panel (b)] and whether it is evolving towards or away from LTE [(e)]. Just upstream of the electron diffusion region (EDR) ($|x - x_0| < 1, 0.45 < |y - y_0| < 1$), electrons get trapped by the upstream magnetic field (Egedal et al., 2013), so f_e becomes non-Maxwellian [dark red in (b)], with f_e elongated in the parallel direction [(i)]. Thus, in the comoving frame, as a fluid element convects towards the X-line from upstream, f_e evolves away from Maxwellianity, consistent with (e) where $d\bar{\mathcal{E}}_{e,\text{rel}}/dt < 0$. Continuing towards the X-line, f_e develops striations [(j)] due to electrons becoming demagnetized in the reversed magnetic field (Speiser, 1965; Ng et al., 2011). This is associated with evolution away from LTE [blue in (e)]. Downstream of the X-line, there is a red patch in (e) at $|x - x_0| \simeq 1.25, |y - y_0| \simeq 0$ where electrons thermalize (Maxwellianize) (Shuster et al., 2014; Wang et al., 2016), which is seen in f_e [(k)]. Just downstream from there ($|x - x_0| \simeq 1.8$), f_e evolves away from LTE where electrons begin to remagnetize at the downstream edge of the EDR (Shuster et al., 2014; Barbhuiya et al., 2022) [(l)]. These results confirm the sign of $d\bar{\mathcal{E}}_{\sigma,\text{rel}}$ identifies whether f_σ changes shape towards or away from LTE in the comoving frame.

Next, we demonstrate the quantitative importance of relative energy. Rates of work and internal energy per particle are shown in Figs. 6.2(c) and (d), respectively. Cuts of these quantities through the X-line in the horizontal and vertical directions,

along with $d\bar{\mathcal{E}}_{e,\text{rel}}/dt$, are plotted in Figs. 6.2(g) and (h), respectively. At the X-line, the values are 0.031, 0.027, and -0.016 , respectively, in normalized code units. Their sum, 0.042, is the total rate of energy per particle going into internal moments of electrons. To see that relative energy is important, the standard approach using Eq. (6.1) would say the energy rate going into changing n_e and \mathcal{T}_e is $0.031 + 0.027 = 0.058$, 38% higher than the total rate when relative energy is included, which is a significant difference.

To assess its importance in other locations, Fig. 6.2(f) shows $\log_{10}[|(d\bar{\mathcal{E}}_{e,\text{rel}}/dt)/(d\bar{\mathcal{E}}_{e,\text{int}}/dt)|]$, with a color bar saturated at ± 2 to better reveal details. Regions where internal and relative energy changes are comparable are white. Locations where $|d\bar{\mathcal{E}}_{e,\text{rel}}|$ exceeds $|d\bar{\mathcal{E}}_{e,\text{int}}|$ are red, especially just upstream of the EDR. In the deep blue regions, $|d\bar{\mathcal{E}}_{e,\text{rel}}| \ll |d\bar{\mathcal{E}}_{e,\text{int}}|$. In the light blue regions, including much of the EDR and island, $|d\bar{\mathcal{E}}_{e,\text{rel}}|$ is at least 20% of the magnitude of $|d\bar{\mathcal{E}}_{e,\text{int}}|$. Thus, energy conversion associated with non-LTE internal moments in reconnection is broadly non-negligible and can be locally significant or even dominant.

6.4 Discussion

We conclude with implications of the present results. First, the theory applies for systems arbitrarily far from LTE, so it could lead to significant advances compared to manifestly perturbative theories (Jou et al., 2010; Chapman & Cowling, 1970; Schekochihin et al., 2009). An extensive comparison to previous work is in Supplemental Material 6.5.7. For a physical process that changes both inter-

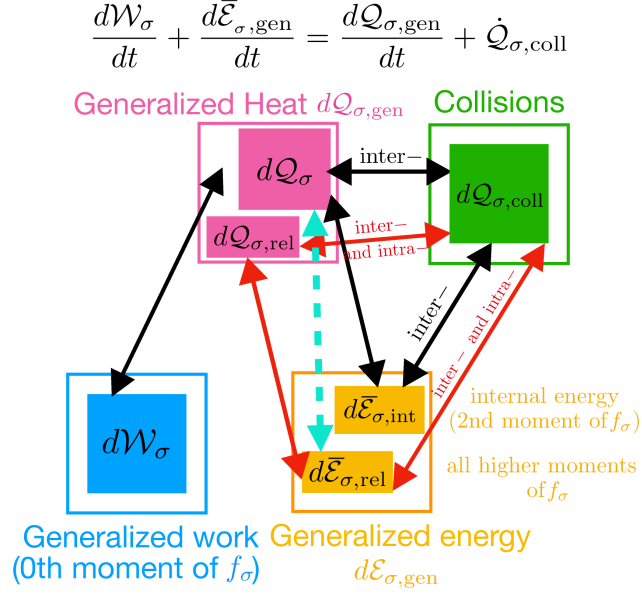


Figure 6.3: Sketch illustrating energy conversion from Eq. (6.10). Arrows show conversion channels between work (blue), heat (pink), energy (orange), and collisions (green), with standard channels in black and relative channels in red. The light blue dashed arrow signifies how the relative terms couple to thermodynamic terms.

nal energy and higher order moments, the theory captures both and allows each to be calculated separately. Since the theory contains all internal moments of f_σ , it overcomes the closure problem.

It is important to note that internal energy per particle $\bar{\mathcal{E}}_{\sigma,\text{int}}$ is a state variable, meaning it is history independent, but relative energy per particle $\bar{\mathcal{E}}_{\sigma,\text{rel}}$ is not. Only in special cases can relative energy per particle $\bar{\mathcal{E}}_{\sigma,\text{rel}}$ be calculated from f_σ at a particular time. Rather, only the increment $d\bar{\mathcal{E}}_{\sigma,\text{rel}}$ has an instantaneous physical meaning. This was pointed out in Ref. (Eu, 1995), and used as motivation to not employ relative entropy per particle because they sought a thermodynamic theory of irreversible processes. Our interpretation is distinctly different; we argue relative energy per particle not being a state variable reflects the physical consequence that

changing the shape of f_σ is typically history dependent. Thus, a description retaining this history dependence is crucial for quantifying energy conversion into non-LTE internal moments.

Our results reveal that the standard treatment of energy conversion in Eq. (6.1) needs to be expanded to accurately describe energy conservation when not in LTE. Since Eq. (6.1) is equivalent to the first law of thermodynamics, we argue Eq. (6.10) is its kinetic theory generalization, which we dub “the first law of kinetic theory”.

A flow chart depicting energy conversion in non-LTE systems is in Fig. 6.3. Black arrows denote energy conversion contained in thermodynamics, namely conversion between heat, work, and internal energy, plus collisions. Red arrows are for relative energy and heat associated with non-LTE internal moments of f_σ . The dashed light blue arrow denotes coupling between relative energy and thermodynamic heat through the vector heat flux density and Pi-D.

We expect the results to be useful when f_σ is reliably measured, such as PIC and Vlasov/Boltzmann plasma simulations and satellite observations (Burch et al., 2016a; Pollock et al., 2016). Satellites measure f_σ with spatio-temporal resolution sufficient to take gradients (Shuster et al., 2019, 2021) and compute kinetic entropy (Argall et al., 2022). The theory may advance efforts using machine learning to parametrize kinetic corrections to transport terms in fluid models (Laperre et al., 2022). Generalizations of the present result may be useful beyond plasma physics, such as many body astrophysics (Aarseth & Aarseth, 2003), micro- and nano-fluidics (Karplus & Petsko, 1990; Schaller, 2014), and quantum entanglement (Floerchinger & Haas, 2020).

There are limitations of the present work. Each restriction to the theory before Eq. (6.2) could be relaxed. Relative energy describes energy conversion associated with all non-LTE internal moments, but does not identify which of the individual non-LTE internal moments contribute; it would be interesting to address this in future work, likely in context of recent theories of the velocity space cascade (Servidio et al., 2017) and/or Casimir invariants (Zhdankin, 2022a). There are settings for which $f_{\sigma M}$ is not the appropriate reference for f_σ (Lynden-Bell, 1967; Livadiotis, 2018); Ref. (Eu, 1995) employs a more general reference f_σ than we use here; it would be interesting to generalize the results for more general plasma-relevant forms.

6.5 Supplemental Material for *Quantifying Energy Conversion in Higher Order Phase Space Density Moments in Plasmas*

6.5.1 Derivation of Kinetic Entropy Evolution Equation

The evolution equation for the kinetic entropy density s_σ defined in Eq. (6.2) is obtained by taking its partial time derivative and eliminating $\partial f_\sigma / \partial t$ using the Boltzmann equation (Boltzmann, 1872),

$$\frac{\partial f_\sigma}{\partial t} + \mathbf{v} \cdot \nabla f_\sigma + \frac{\mathbf{F}_\sigma}{m_\sigma} \cdot \nabla_v f_\sigma = C[f], \quad (6.11)$$

where \mathbf{F}_σ is the sum of any body forces, ∇_v is the velocity space gradient operator, and $C[f]$ is the inter- and intra-species collision operator, yielding (Eu, 1995; Jou

et al., 2010; Eyink, 2018)

$$\frac{\partial s_\sigma}{\partial t} + \nabla \cdot \mathcal{J}_\sigma = \dot{s}_{\sigma,\text{coll}}, \quad (6.12)$$

where \mathcal{J}_σ is the kinetic entropy density flux

$$\mathcal{J}_\sigma = -k_B \int \mathbf{v} f_\sigma \ln \left(\frac{f_\sigma \Delta^3 r_\sigma \Delta^3 v_\sigma}{N_\sigma} \right) d^3 v \quad (6.13)$$

and $\dot{s}_{\sigma,\text{coll}}$ is the local time rate of change of kinetic entropy density through collisions,

$$\dot{s}_{\sigma,\text{coll}} = -k_B \int C[f] \ln \left(\frac{f_\sigma \Delta^3 r_\sigma \Delta^3 v_\sigma}{N_\sigma} \right) d^3 v. \quad (6.14)$$

Note, there is no term containing body forces such as the electric and magnetic forces in Eq. (6.12) because the force term in Eq. (6.11) identically vanishes in deriving Eq. (6.12). An equivalent form of Eq. (6.12) comes from writing $\mathbf{v} = \mathbf{u}_\sigma + \mathbf{v}'_\sigma$ in Eq. (6.13), which implies $\mathcal{J}_\sigma = s_\sigma \mathbf{u}_\sigma + \mathcal{J}_{\sigma,\text{th}}$, where the thermal kinetic entropy density flux $\mathcal{J}_{\sigma,\text{th}}$ is defined as

$$\mathcal{J}_{\sigma,\text{th}} = -k_B \int \mathbf{v}'_\sigma f_\sigma \ln \left(\frac{f_\sigma \Delta^3 r_\sigma \Delta^3 v_\sigma}{N_\sigma} \right) d^3 v. \quad (6.15)$$

Then, Eq. (6.12) becomes (Jou et al., 2010)

$$\frac{\partial s_\sigma}{\partial t} + \nabla \cdot (s_\sigma \mathbf{u}_\sigma + \mathcal{J}_{\sigma,\text{th}}) = \dot{s}_{\sigma,\text{coll}}. \quad (6.16)$$

This equation is in the stationary (Eulerian) reference frame.

Here, we manipulate Eq. (6.16) to derive an evolution equation for kinetic entropy per particle s_σ/n_σ in a comoving (Lagrangian) frame [Eq. (6.3)]. Using the convective derivative $d/dt = \partial/\partial t + \mathbf{u}_\sigma \cdot \nabla$ and dividing Eq. (6.16) by the density n_σ gives

$$\frac{1}{n_\sigma} \frac{ds_\sigma}{dt} + \frac{s_\sigma}{n_\sigma} (\nabla \cdot \mathbf{u}_\sigma) + \frac{\nabla \cdot \mathcal{J}_{\sigma,\text{th}}}{n_\sigma} = \frac{\dot{s}_{\sigma,\text{coll}}}{n_\sigma}. \quad (6.17)$$

Using the continuity equation $dn_\sigma/dt = -n_\sigma \nabla \cdot \mathbf{u}_\sigma$ (since N_σ is assumed constant), we get

$$\frac{1}{n_\sigma} \frac{ds_\sigma}{dt} - \frac{s_\sigma}{n_\sigma^2} \frac{dn_\sigma}{dt} + \frac{\nabla \cdot \mathcal{J}_{\sigma,\text{th}}}{n_\sigma} = \frac{\dot{s}_{\sigma,\text{coll}}}{n_\sigma}. \quad (6.18)$$

Finally, the two terms on the left are equal to $d(s_\sigma/n_\sigma)/dt$, which completes the derivation of Eq. (6.3).

We conclude this section with two important notes. First, Eq. (6.2) is the ‘‘Boltzmann’’ form of kinetic entropy density s_σ . For collisionless systems, any function of f_σ is conserved, so other entropies could be defined (Zhdankin, 2022a). We choose the Boltzmann entropy because it reduces to the ideal fluid entropy density for a system in LTE and, for collisional systems, the total Boltzmann entropy $S_\sigma = \int s_\sigma d^3r$ obeys an H-theorem (S_σ is non-decreasing in time) for a reasonably defined collision operator (Boltzmann, 1877). Neither need be the case for other entropies. The present analysis may be redone for other entropies for future work.

Second, the approach we use remains valid even if there is an entropy source in the Boltzmann equation beyond collisions, such as due to boundaries of a finite domain. Such sources can lead to non-conservation of total kinetic entropy $S_\sigma = \int s_\sigma d^3r$ even in collisionless systems (Grandy, 2004), but s_σ is local in space and

time and therefore remains well-defined.

6.5.2 Derivation of Generalized Work Term

Here, we derive Eq. (6.5a). Dividing both sides of Eq. (6.4a) by n_σ and taking its total time derivative gives

$$\frac{d}{dt} \left(\frac{s_{\sigma p}}{n_\sigma} \right) = -\frac{k_B}{n_\sigma} \frac{dn_\sigma}{dt}. \quad (6.19)$$

A brief derivation reveals this is equivalent to

$$\frac{d}{dt} \left(\frac{s_{\sigma p}}{n_\sigma} \right) = k_B n_\sigma \frac{d(1/n_\sigma)}{dt}. \quad (6.20)$$

Defining $V_\sigma = 1/n_\sigma$ as the volume per particle, and using $\mathcal{P}_\sigma = n_\sigma k_B \mathcal{T}_\sigma$, the previous equation is equivalent to

$$\frac{d}{dt} \left(\frac{s_{\sigma p}}{n_\sigma} \right) = \frac{1}{\mathcal{T}_\sigma} \frac{d\mathcal{W}_\sigma}{dt}, \quad (6.21)$$

where $d\mathcal{W}_\sigma = \mathcal{P}_\sigma dV_\sigma = \mathcal{P}_\sigma d(1/n_\sigma)$ is the non-LTE generalization of the work per particle done by the system.

To physically interpret this, note $s_{\sigma p}$ is associated with the number of permutations of particles in position space that produce the same macrostate without concern for their velocity (Liang et al., 2019). The argument of the natural logarithm in $s_{\sigma p}/n_\sigma = -k_B \ln(n_\sigma \Delta^3 r_\sigma / N_\sigma)$ is always between 0 and 1, so $s_{\sigma p}/n_\sigma$ is non-negative and is a strictly decreasing function of n_σ . Thus, local compression ($d\mathcal{W}_\sigma = \mathcal{P}_\sigma dV_\sigma < 0$) increases n_σ and decreases $s_{\sigma p}/n_\sigma$ [*i.e.*, $d(s_{\sigma p}/n_\sigma)/dt < 0$],

while local expansion ($d\mathcal{W}_\sigma = \mathcal{P}_\sigma dV_\sigma > 0$) decreases n_σ and increases $s_{\sigma p}/n_\sigma$ [*i.e.*, $d(s_{\sigma p}/n)/dt > 0$].

6.5.3 Derivation of Generalized Energy Term

We next derive Eq. (6.5b). We decompose the velocity space kinetic entropy density $s_{\sigma v}$ in Eq. (6.4b) as $s_{\sigma v} = s_{\sigma v, \bar{\mathcal{E}}} + s_{\sigma v, \text{rel}}$, where

$$s_{\sigma v, \bar{\mathcal{E}}} = -k_B \int f_\sigma \ln \left(\frac{f_{\sigma M} \Delta^3 v_\sigma}{n_\sigma} \right) d^3 v, \quad (6.22)$$

$$s_{\sigma v, \text{rel}} = -k_B \int f_\sigma \ln \left(\frac{f_\sigma}{f_{\sigma M}} \right) d^3 v, \quad (6.23)$$

where $f_{\sigma M}$ is the Maxwellianized distribution of f_σ defined in Eq. (6.8). The relative entropy is related to the Kullback-Leibler divergence (Kullback & Leibler, 1951) from information theory which is a measure of the statistical difference between a two probability distributions, and has been extensively used in a variety of fields, such as statistical mechanics, applied mathematics, chemistry, biology, quantum information theory, and economics (Jaynes, 1963; Grad, 1965; Diperna, 1979; Dafermos, 1979; Eu, 1995; Vedral, 2002; Robertson et al., 2005; Tzavaras, 2005; Shell, 2008; Berthelin et al., 2009; Baez & Pollard, 2016). Substituting Eq. (6.8) into Eq. (6.22) and carrying out straight-forward manipulations gives

$$\frac{s_{\sigma v, \bar{\mathcal{E}}}}{n_\sigma} = \frac{3}{2} k_B \left[1 + \ln \left(\frac{2\pi k_B \mathcal{T}_\sigma}{m_\sigma (\Delta^3 v_\sigma)^{2/3}} \right) \right]. \quad (6.24)$$

Its Lagrangian time derivative immediately gives

$$\frac{d}{dt} \left(\frac{s_{\sigma v, \bar{\mathcal{E}}}}{n_\sigma} \right) = \frac{1}{\mathcal{T}_\sigma} \frac{d\bar{\mathcal{E}}_{\sigma, \text{int}}}{dt}, \quad (6.25)$$

where $d\bar{\mathcal{E}}_{\sigma, \text{int}} = (3/2)k_B d\mathcal{T}_\sigma$ is the increment in internal energy per particle. This reproduces Eq. (6.5b). Thus, $d(s_{\sigma v, \bar{\mathcal{E}}}/n_\sigma)/dt > 0$ implies the effective temperature increases, while $d(s_{\sigma v, \bar{\mathcal{E}}}/n_\sigma)/dt < 0$ implies the effective temperature decreases. Physically, $s_{\sigma v}$ is associated with the number of permutations of particles of different velocities in a given position in phase space that produces the same macrostate (Liang et al., 2019).

6.5.4 Derivation of Generalized Heat Term

We now derive Eq. (6.5c). We find it is advantageous to decompose $\nabla \cdot \mathcal{J}_{\sigma, \text{th}}$ using Eq. (6.15) as

$$\nabla \cdot \mathcal{J}_{\sigma, \text{th}} = (\nabla \cdot \mathcal{J}_{\sigma, \text{th}})_{\mathcal{W}} + (\nabla \cdot \mathcal{J}_{\sigma, \text{th}})_{\bar{\mathcal{E}}} + (\nabla \cdot \mathcal{J}_{\sigma, \text{th}})_{\text{rel}}, \quad (6.26)$$

where

$$\begin{aligned} (\nabla \cdot \mathcal{J}_{\sigma, \text{th}})_{\mathcal{W}} &= -k_B \int (f_\sigma \mathbf{v}'_\sigma) \cdot \\ &\quad \nabla \left[\ln \left(\frac{f_\sigma \Delta^3 r_\sigma \Delta^3 v_\sigma}{N_\sigma} \right) \right] d^3 v, \end{aligned} \quad (6.27a)$$

$$\begin{aligned} (\nabla \cdot \mathcal{J}_{\sigma, \text{th}})_{\bar{\mathcal{E}}} &= -k_B \int \left[\nabla \cdot (\mathbf{v}'_\sigma f_\sigma) \right] \\ &\quad \ln \left(\frac{f_\sigma M \Delta^3 r_\sigma \Delta^3 v_\sigma}{N_\sigma} \right) d^3 v, \end{aligned} \quad (6.27b)$$

and $(\nabla \cdot \mathcal{J}_{\sigma,\text{th}})_{\text{rel}}$ is defined in Eq. (6.7). The latter has equivalent forms of

$$\begin{aligned}
(\nabla \cdot \mathcal{J}_{\sigma,\text{th}})_{\text{rel}} &= -\nabla \cdot (\mathbf{u}_\sigma s_{\sigma v,\text{rel}}) \\
&\quad -k_B \int \nabla \cdot (\mathbf{v} f_\sigma) \ln \left(\frac{f_\sigma}{f_{\sigma M}} \right) d^3v, \\
&= -s_{\sigma v,\text{rel}} (\nabla \cdot \mathbf{u}_\sigma) \\
&\quad -k_B \int (\mathbf{v}'_\sigma \cdot \nabla f_\sigma) \ln \left(\frac{f_\sigma}{f_{\sigma M}} \right) d^3v,
\end{aligned}$$

which may be useful in applications depending on which quantities are easiest to measure in a given system.

We first treat $(\nabla \cdot \mathcal{J}_{\sigma,\text{th}})_{\mathcal{W}}/n_\sigma$. The gradient of the term in brackets in Eq. (6.27a) is $(1/f_\sigma)\nabla f_\sigma$. Using $\mathbf{v}'_\sigma = \mathbf{v} - \mathbf{u}_\sigma$, straight-forward manipulations give

$$\frac{(\nabla \cdot \mathcal{J}_{\sigma,\text{th}})_{\mathcal{W}}}{n_\sigma} = -k_B \nabla \cdot \mathbf{u}_\sigma = -k_B n_\sigma \frac{d(1/n_\sigma)}{dt}, \quad (6.28)$$

where we use the continuity equation to eliminate $\nabla \cdot \mathbf{u}_\sigma$. Therefore, this term describes the non-LTE generalization of heating associated with compression or expansion, with the same form as $d(s_{\sigma p}/n_\sigma)/dt$ in Eq. (6.20) but with the opposite sign. This motivates our use of the \mathcal{W} subscript.

Turning to $(\nabla \cdot \mathcal{J}_{\sigma,\text{th}})_{\bar{\mathcal{E}}}/n_\sigma$, we use Eq. (8) to write Eq. (6.27b) as

$$\begin{aligned}
\frac{(\nabla \cdot \mathcal{J}_{\sigma,\text{th}})_{\bar{\mathcal{E}}}}{n_\sigma} &= -\frac{k_B}{n_\sigma} \int \nabla \cdot (\mathbf{v}'_\sigma f_\sigma) \\
&\quad \left\{ \ln \left[\left(\frac{n_\sigma \Delta^3 r_\sigma \Delta^3 v_\sigma}{N_\sigma} \right) \left(\frac{m_\sigma}{2\pi k_B \mathcal{T}_\sigma} \right)^{3/2} \right] - \frac{m_\sigma v_\sigma'^2}{2k_B \mathcal{T}_\sigma} \right\} d^3v.
\end{aligned}$$

The term in square brackets is independent of \mathbf{v} and hence comes out of the integral, and the remaining part of that integral is $\int \nabla \cdot (\mathbf{v}'_{\sigma} f_{\sigma}) d^3v = 0$. Manipulations of the remaining term after integration by parts gives

$$\frac{(\nabla \cdot \mathcal{J}_{\sigma, \text{th}})_{\bar{\mathcal{E}}}}{n_{\sigma}} = \frac{\nabla \cdot (\mathbf{q}_{\sigma} / \mathcal{T}_{\sigma})}{n_{\sigma}} - \frac{m_{\sigma}}{2n_{\sigma}} \int f_{\sigma} \mathbf{v}'_{\sigma} \cdot \left[\frac{\nabla v'_{\sigma}{}^2}{\mathcal{T}_{\sigma}} - \frac{v'_{\sigma}{}^2 \nabla \mathcal{T}_{\sigma}}{\mathcal{T}_{\sigma}^2} \right] d^3v, \quad (6.29)$$

where \mathbf{q}_{σ} is the vector heat flux density defined after Eq. (6.1). Using index notation and the Einstein summation convention,

$$\mathbf{v}'_{\sigma} \cdot \nabla v'_{\sigma}{}^2 = v'_{\sigma j} \frac{\partial (v'_{\sigma k} v'_{\sigma k})}{\partial r_j} = 2v'_{\sigma j} v'_{\sigma k} \frac{\partial v'_{\sigma k}}{\partial r_j} = -2v'_{\sigma j} v'_{\sigma k} \frac{\partial u_{\sigma k}}{\partial r_j},$$

where we use $\partial v'_{\sigma k} / \partial r_j = \partial (v_k - u_{\sigma k}) / \partial r_j = -\partial u_{\sigma k} / \partial r_j$ in the last equality. Carrying out the remaining integrals and simplifying gives

$$\frac{(\nabla \cdot \mathcal{J}_{\sigma, \text{th}})_{\bar{\mathcal{E}}}}{n_{\sigma}} = \frac{\nabla \cdot \mathbf{q}_{\sigma}}{n_{\sigma} \mathcal{T}_{\sigma}} + \frac{(\mathbf{P}_{\sigma} \cdot \nabla) \cdot \mathbf{u}_{\sigma}}{n_{\sigma} \mathcal{T}_{\sigma}}. \quad (6.30)$$

Comparing the right hand side of Eq. (6.30) with Eq. (6.1), we see both terms appear directly in the internal energy equation with the opposite sign, motivating the choice of the subscript $\bar{\mathcal{E}}$. This term describes heat per particle that changes only the effective temperature. A negative value of $(\nabla \cdot \mathcal{J}_{\sigma, \text{th}})_{\bar{\mathcal{E}}} / n_{\sigma}$ drives increasing \mathcal{T}_{σ} , and a positive value drives decreasing \mathcal{T}_{σ} .

A consequence of Eq. (6.28) is that $(\nabla \cdot \mathcal{J}_{\sigma,\text{th}})_{\mathcal{W}}/n_{\sigma} = -(\mathcal{P}_{\sigma}/n_{\sigma}\mathcal{T}_{\sigma})\nabla \cdot \mathbf{u}_{\sigma}$, so

$$\begin{aligned} \frac{(\nabla \cdot \mathcal{J}_{\sigma,\text{th}})_{\mathcal{W}}}{n_{\sigma}} + \frac{(\nabla \cdot \mathcal{J}_{\sigma,\text{th}})_{\bar{\mathcal{E}}}}{n_{\sigma}} &= \frac{\nabla \cdot \mathbf{q}_{\sigma}}{n_{\sigma}\mathcal{T}_{\sigma}} + \frac{\Pi_{\sigma,jk}\mathcal{D}_{\sigma,jk}}{n_{\sigma}\mathcal{T}_{\sigma}} \\ &= -\frac{1}{\mathcal{T}_{\sigma}}\frac{d\mathcal{Q}_{\sigma}}{dt}, \end{aligned} \quad (6.31)$$

where we use the known decomposition $(\mathbf{P}_{\sigma} \cdot \nabla) \cdot \mathbf{u}_{\sigma} = \mathcal{P}_{\sigma}(\nabla \cdot \mathbf{u}_{\sigma}) + \Pi_{\sigma,jk}\mathcal{D}_{\sigma,jk}$, with $\Pi_{\sigma,jk} = P_{\sigma,jk} - \mathcal{P}_{\sigma}\delta_{jk}$ being elements of the deviatoric pressure tensor $\mathbf{\Pi}$, $\mathcal{D}_{\sigma,jk} = (1/2)(\partial u_{\sigma j}/\partial r_k + \partial u_{\sigma k}/\partial r_j) - (1/3)\delta_{jk}(\nabla \cdot \mathbf{u}_{\sigma})$ being elements of the traceless symmetric strain rate tensor \mathcal{D} , and δ_{jk} being the Kroenecker delta (Jou et al., 2010; Yang et al., 2017b). This derivation provides the expression given in Eq. (6.5c).

6.5.5 Derivation of Relative Energy Per Particle Rate for a Bi-Maxwellian Plasma

Here we derive the rate of relative energy per particle change $d\bar{\mathcal{E}}_{\sigma,\text{rel}}/dt$ for a bi-Maxwellian initial phase space density. Consider a purely collisionless system in which the initial f_{σ} is bi-Maxwellian with a converging bulk flow $\mathbf{u}(\mathbf{r}, t)$. We define z as the parallel direction \parallel , x and y as perpendicular \perp directions, and T_{\perp} and T_{\parallel} as the uniform temperatures in the \perp and \parallel directions. The initial phase space density is

$$\begin{aligned} f_{biM} &= n \left(\frac{m}{2\pi k_B T_{\perp}} \right) \left(\frac{m}{2\pi k_B T_{\parallel}} \right)^{1/2} \\ &\quad e^{-m[(v_x - u_x)^2 + (v_y - u_y)^2]/2k_B T_{\perp}} e^{-m(v_z - u_z)^2/2k_B T_{\parallel}}, \end{aligned} \quad (6.32)$$

where n is the initial number density and the constituent mass is m . The Maxwellianized distribution for this system has the form of Eq. (6.8) with effective temperature $\mathcal{T} = (2T_{\perp} + T_{\parallel})/3$. Then,

$$\ln\left(\frac{f_{biM}}{f_M}\right) = \ln\left(\frac{\mathcal{T}^{3/2}}{T_{\perp}T_{\parallel}^{1/2}}\right) - \frac{m(v_x'^2 + v_y'^2)}{2k_B} \left[\frac{T_{\parallel} - T_{\perp}}{T_{\perp}(2T_{\perp} + T_{\parallel})}\right] - \frac{mv_z'^2}{2k_B} \left[\frac{2(T_{\perp} - T_{\parallel})}{T_{\parallel}(2T_{\perp} + T_{\parallel})}\right],$$

and a straight-forward derivation using Eq. (6.6) yields

$$\frac{s_{v,\text{rel}}}{n} = -\frac{3}{2}k_B \ln\left[\frac{2}{3}\left(\frac{T_{\perp}}{T_{\parallel}}\right)^{1/3} + \frac{1}{3}\left(\frac{T_{\parallel}}{T_{\perp}}\right)^{2/3}\right]. \quad (6.33)$$

The Lagrangian time derivative of this equation, after some algebra, gives

$$\frac{d}{dt}\left(\frac{s_{v,\text{rel}}}{n}\right) = k_B \left(\frac{T_{\parallel} - T_{\perp}}{2T_{\perp} + T_{\parallel}}\right) \left(\frac{1}{T_{\perp}} \frac{dT_{\perp}}{dt} - \frac{1}{T_{\parallel}} \frac{dT_{\parallel}}{dt}\right). \quad (6.34)$$

The thermal evolution equations in a collisionless gyrotropic system, which follow directly from the second parallel and perpendicular moments of the collisionless Boltzmann equation, are written in terms of parallel and perpendicular pressures as (Chew et al., 1956; Hesse & Birn, 1992)

$$\frac{dP_{\parallel}}{dt} + P_{\parallel} \nabla \cdot \mathbf{u} + 2P_{\parallel} [\hat{\mathbf{z}} (\hat{\mathbf{z}} \cdot \nabla)] \cdot \mathbf{u} = 0, \quad (6.35a)$$

$$\frac{dP_{\perp}}{dt} + 2P_{\perp} \nabla \cdot \mathbf{u} - P_{\perp} [\hat{\mathbf{z}} (\hat{\mathbf{z}} \cdot \nabla)] \cdot \mathbf{u} = 0, \quad (6.35b)$$

where $P_{\perp} = nk_B T_{\perp}$ and $P_{\parallel} = nk_B T_{\parallel}$. Substituting these into Eq. (6.34) gives

$$\frac{d}{dt} \left(\frac{s_{v,\text{rel}}}{n} \right) = k_B \left(\frac{T_{\parallel} - T_{\perp}}{2T_{\perp} + T_{\parallel}} \right) \left(-\nabla_{\perp} \cdot \mathbf{u}_{\perp} + 2 \frac{\partial u_z}{\partial z} \right), \quad (6.36)$$

where $\mathbf{u}_{\perp} = \mathbf{u} - \hat{\mathbf{z}}u_z$. Finally, using Eq. (9a) to relate this to $d\bar{\mathcal{E}}_{\sigma,\text{rel}}/dt$ gives

$$\frac{d\bar{\mathcal{E}}_{\sigma,\text{rel}}}{dt} = \frac{1}{3} k_B (T_{\parallel} - T_{\perp}) \left(-\nabla_{\perp} \cdot \mathbf{u}_{\perp} + 2 \frac{\partial u_z}{\partial z} \right). \quad (6.37)$$

To interpret this result physically, suppose $T_{\parallel} > T_{\perp}$. First consider a bulk flow profile $\mathbf{u} = \mathbf{u}_{\perp}$ that is isotropically converging in the xy plane. Compression leads to heating, but only in the perpendicular direction (Cassak & Barbhuiya, 2022). Thus, f_{σ} becomes more Maxwellian. From Eq. (6.37), both $T_{\parallel} - T_{\perp}$ and the bulk velocity term are positive, so $d\bar{\mathcal{E}}_{\sigma,\text{rel}}/dt > 0$, consistent with energy going into higher order moments making f_{σ} more Maxwellian. Now consider converging bulk flow in the z direction. The compression heats the distribution in the parallel direction, so f_{σ} becomes more elongated in the parallel direction, *i.e.*, less Maxwellian. From Eq. (6.37), $T_{\parallel} - T_{\perp}$ is positive but the bulk velocity term is negative, so this evolution away from Maxwellianity is consistent with $d\bar{\mathcal{E}}_{\sigma,\text{rel}}/dt$ being negative. This example illustrates general features: $d\bar{\mathcal{E}}_{\sigma,\text{rel}}/dt > 0$ is associated with energy conversion making higher moments of f_{σ} evolve to become more Maxwellian, and vice-versa.

6.5.6 Numerical Simulation Methodology

Details of the simulation in addition to what follows are available in Ref. (Barbhuiya & Cassak, 2022). We use the massively parallel particle-in-cell code `p3d` (Zeiler et al., 2002) to perform simulations that are 3D in velocity-space and 2.5D in position-space. Periodic boundary conditions are used in both spatial directions. The code uses the relativistic Boris particle stepper (Birdsall & Langdon, 1991) for stepping particles forward in time, while the trapezoidal leapfrog method (Guzdar et al., 1993) is utilized for stepping electromagnetic fields forward in time. The fields have a time-step half of that of the particles. The multigrid method (Trottenberg et al., 2000) is used to clean the electric field \mathbf{E} to enforce Poisson's equation every 10 particle time-steps.

Simulation results are presented in normalized units. The reference magnetic field B_0 is the initial asymptotic magnetic field strength. The reference number density n_0 is the peak current sheet number density minus the asymptotic background number density. Length scales are normalized to the ion inertial scale $d_{i0} = c/\omega_{pi0}$, where $\omega_{pi0} = (4\pi n_0 q_i^2/m_i)^{1/2}$ is the ion plasma frequency (in cgs units), q_i is the ion charge, m_i is the ion mass, and c is the speed of light. Velocities are normalized to the Alfvén speed $c_{A0} = B_0/(4\pi m_i n_0)^{1/2}$. Times are normalized to the inverse ion cyclotron frequency $\Omega_{ci0}^{-1} = (q_i B_0/m_i c)^{-1}$. Temperatures are normalized to $m_i c_{A0}^2/k_B$. Current densities are normalized to $cB_0/4\pi d_{i0}$. Reduced phase space densities, with one velocity dimension integrated out, are normalized to n_0/c_{A0}^2 . Energy per particle conversion rates are given in units of $\Omega_{ci0} B_0^2/4\pi n_0$.

The initial condition has two oppositely directed current sheets with drifting Maxwellian initial distributions. The magnetic field profile is a double tanh with no initial out-of-plane (guide) magnetic field. The current sheet thickness is $w_0 = 0.5$, the background density is $n_{up} = 0.2$, and the electron and ion temperatures are $1/12$ and $5/12$, respectively. A magnetic perturbation of amplitude 0.05 seeds an X-line/O-line pair in each of the two current sheets. The simulation system size is $L_x \times L_y = 12.8 \times 6.4$, where x and y are the outflow and inflow directions, respectively. The speed of light c is 15 and the electron-to-ion mass ratio is $m_e/m_i = 0.04$. There are 1024×512 grid cells initialized with 25,600 weighted particles per grid (PPG), which is chosen to be very large to decrease particle noise. The grid-length Δ in both directions is 0.0125, which is smaller than the smallest length scale which is the electron Debye length of 0.0176. The time-step Δt is 0.001, which is smaller than the smallest time scale which is the inverse of electron plasma frequency of 0.012. Our choice of these numerical parameters results in a total energy increase by only 0.026% by $t = 14$. (Note that this number was erroneously given as 0.022 % in Cassak et al. (2023).)

All plots display data from only the lower current sheet at time $t = 13$, when the rate of reconnection is increasing most rapidly in time. To reduce PIC noise for all quantities plotted other than phase space densities, the raw quantities are recursively smoothed four times over a width of four cells, then any temporal or spatial derivatives are carried out, and then the results are again smoothed recursively four times over four cells. For temporal derivatives, the presented data is calculated from a finite difference between $t = 12$ and 14 (on ion cyclotron time scales). The

results are compared to those obtained from a finite difference between $t = 12.96$ and 13.04 (electron time scales), and the results are found to differ by less than 5%; this change is deemed inconsequential for the present purposes.

Kinetic entropy is calculated in the simulations employing the implementation from Ref. (Argall et al., 2022). Optimization of the velocity-space grid (Liang et al., 2020b) is done by checking the agreement between the kinetic entropy density for electrons s_e calculated by the simulation for various Δv_e and the theoretical value at $t = 0$. We find an optimal Δv_e of 1.33 which leads to an initial agreement to within $\pm 1\%$ in the upstream region and $\pm 3\%$ at the center of the current sheet. For plots of reduced electron phase space densities, we use a domain of size 0.0625×0.0625 centered at the location of interest. Particles are binned with a velocity space bin of size 0.1 in all velocity directions.

6.5.7 Additional Comments on the Relation to Previous Work

Here, we put our result in context of previous work on related topics.

- **Energy Conversion in δf_σ Kinetic Theory and Gyrokinetics:** We first compare the present work with previous work on energy conversion in linearized kinetic theory and gyrokinetics (Hallatschek, 2004; Howes et al., 2006; Schekochihin et al., 2009; Tatsuno et al., 2009). Consider a linear expansion of the phase space density about its Maxwellianized distribution, so that $f_\sigma = f_{\sigma M} + \delta f_\sigma$, and $\delta f_\sigma \ll f_{\sigma M}$. A straight-forward calculation using

Eq. (6.23) reveals that the linearized relative entropy $\delta s_{\sigma v, \text{rel}}$ is

$$\delta s_{\sigma v, \text{rel}} \simeq -k_B \int \frac{(\delta f_\sigma)^2}{2f_{\sigma M}} d^3v. \quad (6.38)$$

Here, we assume that $\int d^3v \delta f = \delta(\int d^3v f) = \delta n = 0$ which is true because $f_{\sigma M}$ is the Maxwellianized distribution of f_σ and thus, by definition, has the density identical to the density associated with f_σ . This assumption need not be true if the perturbation changes n , \mathbf{u}_σ or \mathcal{T}_σ from the equilibrium. In linear theory, the density and temperature in $f_{\sigma M}$ are their equilibrium values, which we call $n_{\sigma 0}$ and $T_{\sigma 0}$, respectively. Then, the linearized equation describing the relative energy increment using Eq. 6.9a) is

$$\frac{d\bar{\mathcal{E}}_{\sigma, \text{rel}}}{dt} \simeq T_{\sigma 0} \frac{d(s_{\sigma v, \text{rel}}/n_{\sigma 0})}{dt}. \quad (6.39)$$

Since the equilibrium temperature does not change to low order in linear theory, $n_{\sigma 0}$ and $T_{\sigma 0}$ are constant in time, so integrating Eq. (6.39) in time gives

$$\begin{aligned} \delta \bar{\mathcal{E}}_{\sigma, \text{rel}} &\simeq \frac{T_{\sigma 0}}{n_{\sigma 0}} \delta s_{\sigma v, \text{rel}} \\ &\simeq -\frac{k_B T_{\sigma 0}}{n_{\sigma 0}} \int \frac{(\delta f_\sigma)^2}{2f_{\sigma M}} d^3v, \end{aligned} \quad (6.40)$$

where we use Eq. (6.38).

In comparison, the free energy in a δf_σ linearized thermodynamic approach

(Hallatschek, 2004) [κ_{int} in their Eq. (7)] was derived to be

$$\kappa_{\text{int}} = k_B T_0 \int \frac{(\delta f)^2}{2f_{\sigma M}} d^3 v \quad (6.41)$$

and in a gyrokinetic analysis of energy conversion (Howes et al., 2006; Schekochihin et al., 2009), the comparable term from the free energy {the first term of W in Eq. (74) from Ref. (Schekochihin et al., 2009)} is

$$W = \int d^3 r \sum_{\sigma} \int k_B T_{0\sigma} \frac{(\delta f)^2}{2f_{\sigma M}} d^3 v. \quad (6.42)$$

Clearly, the linearized relative energy per particle $\delta \bar{\mathcal{E}}_{\sigma, \text{rel}}$ in Eq. (6.40) is related to the free energy in the δf_{σ} thermodynamic and the gyrokinetic approaches when the aforementioned assumptions hold true. In particular, $\kappa_{\text{int}} = -n_{\sigma 0} \delta \bar{\mathcal{E}}_{\sigma, \text{rel}}$ and $W = -\int d^3 r \sum_{\sigma} n_{\sigma 0} \delta \bar{\mathcal{E}}_{\sigma, \text{rel}}$. [Note, the relative entropy term differs from the nonlinear term used in Ref. (Cerri et al., 2018) that reproduces Eq. (6.41) when linearized; theirs is related to \bar{M}_{KP} rather than the relative energy term.] The sign difference is a result of $\delta \bar{\mathcal{E}}_{\sigma, \text{rel}}$ measuring the energy going into the random energy of the particles, while κ_{int} and W describe energy going into the bulk flow energy and magnetic fields from the particles. Thus, the present work is consistent with previous work, and generalizes these linear approaches for phase space densities when changes to its lowest moments can be dropped.

- **Previous Schematics of Energy Conversion:** We now put the sketch of

energy conversion in Fig. 3 in the context of previous sketches about energy conversion in plasmas. It is similar to Fig. 1 in Ref. (Yang et al., 2017b), except theirs is averaged over a closed or periodic domain so the heat flux does not contribute, theirs includes conversion into bulk kinetic energy and electromagnetic energy which are omitted from the present treatment for simplicity, and ours includes collisions. The key difference is the additional energy conversion channel associated with relative energy and heat that arise from our analysis as another possible energy conversion channel.

Another related sketch is Fig. 4 in Ref. (Howes et al., 2018), which describes energy conversion in weakly collisional turbulent plasmas. There, electromagnetic fields play a key role in converting energy to non-thermal (non-LTE) energy in the plasma, which ultimately produce irreversible dissipation through the collisions. The present work treats only internal moments of the phase space density, which formally has only indirect input from body forces [which, for example, do not appear in Eq. (6.1)]. Thus, our result is in many ways complementary to the research done on the field-particle correlation (Klein & Howes, 2016). It would be interesting and important to unite the two approaches in future work.

- **The Velocity Space Cascade and Hermite Expansions of f_σ :** An important approach that has previously been used to study non-LTE energy conversion is to take a local phase space density and expand the velocity space part in Hermite polynomials (Servidio et al., 2017; Pezzi et al., 2018,

2019). The coefficients in the expansion provide information about how non-Maxwellian the system is at that location in space and time. In a weakly collisional or collisionless system, many phase space densities develop sharp structures in velocity space, which shows up as a cascade of power into the higher order coefficients in the expansion.

It would be tempting to associate the power in non-LTE modes, called the enstrophy in Ref. (Servidio et al., 2017), with the relative energy per particle in the present analysis, but this association is not possible. The reason is that the enstrophy is a local quantity that can be calculated for any phase space density, but the relative energy per particle is history dependent, so only changes to it can be uniquely determined from the local phase space density at a particular time. A phase space density becoming more non-Maxwellian has an increase in enstrophy, while it corresponds to a decrease in the relative energy per particle because the Maxwellian is the maximum entropy state. While associating the two approaches in this manner is therefore not possible, we do believe there are links between the two approaches which will be pursued in future studies.

- **Energy Conversion Using Other Entropies:** Recent work quantified non-LTE effects using non-Boltzmann entropies for collisionless plasmas (Zhdankin, 2022a,b). In Ref. (Zhdankin, 2022a), energy conversion was parametrized by moments of integer powers of f_σ , which are invariants in collisionless systems. In Ref. (Zhdankin, 2022b), it was shown that power law entropies are

well-suited for describing power law tails during non-thermal particle acceleration. As pointed out there, these terms provide information about the shape of the phase space density, so there are some similarities about the aims of the two studies despite their different approaches.

The formulation here using the Boltzmann entropy is related to these invariants, as an expansion of the natural logarithm in powers of f_σ inside the kinetic entropy density $s_\sigma = -k_B \int f_\sigma \ln(f_\sigma \Delta^3 r_\sigma \Delta^3 v_\sigma / N_\sigma) d^3 v$ yields integrals over all integer powers of f_σ , as done in Ref. (Zhdankin, 2022a). Consequently, the form derived here based on Boltzmann entropy without expanding the natural logarithm automatically contains the information about all of the power law invariants for collisionless systems. Ref. (Zhdankin, 2022a) is important for identifying how the energy is contained in different individual invariants, which is not possible in the present formulation. However, our results can readily be used for collisional systems even though powers of f_σ are no longer invariants.

- **Extended Irreversible Thermodynamics (EIT):** EIT begins with the kinetic entropy evolution equation [Eq. (6.12)] and employs a perturbative expansion of f_σ , and the terms of higher order represent corrections to the first law of thermodynamics. This is very important because the corrections are in terms of fluid moments of f_σ , so a direct measurement of f_σ is not necessary. The advantage of the present analysis is that all internal moments are retained, so there is no need to be near LTE.

We also point out that the phase space density f_σ inside the natural logarithm in the general expression for $\mathcal{J}_{\sigma,\text{th}}$ [Eq. (6.15)] is expanded about the Maxwellianized distribution $f_{\sigma M}$ in EIT. The lowest order term in this expansion is (Jou et al., 2010)

$$\mathcal{J}_{\sigma,q} = -k_B \int \mathbf{v}'_\sigma f_\sigma \ln \left(\frac{f_{\sigma M} \Delta^3 r_\sigma \Delta^3 v_\sigma}{N_\sigma} \right) d^3 v. \quad (6.43)$$

A brief derivation using Eq. (6.8) reveals that $\mathcal{J}_{\sigma,q} = \mathbf{q}_\sigma / \mathcal{T}_\sigma$. In the present Chapter, instead of decomposing f_σ inside $\mathcal{J}_{\sigma,\text{th}}$, we decompose f_σ inside $\nabla \cdot \mathcal{J}_{\sigma,\text{th}}$ as Eq. (6.26). The difference here is that $\mathcal{J}_{\sigma,q} = \mathbf{q}_\sigma / \mathcal{T}_\sigma$ from Eq. (6.43), so $\nabla \cdot \mathcal{J}_{\sigma,q}$ contains both a $(\nabla \cdot \mathbf{q}_\sigma) / \mathcal{T}_\sigma$ term and a $-(\mathbf{q}_\sigma \cdot \nabla \mathcal{T}_\sigma) / \mathcal{T}_\sigma^2$ term. The latter term is included as an entropy source term in the fluid form of EIT (Jou et al., 2010). Eq. (6.30) reveals that $-(\mathbf{q}_\sigma \cdot \nabla \mathcal{T}_\sigma) / \mathcal{T}_\sigma^2$ vanishes exactly when all orders of non-LTE terms are retained so that it should not be retained.

- **Quantum Statistical Mechanics:** There are similarities and differences of our results with a recent independent analysis showing that the quantum first law of thermodynamics can be obtained from the quantum relative entropy (Floerchinger & Haas, 2020). In the classical limit, the density matrix ρ is analogous to the distribution function f_σ / n_σ (Sakurai, 1994). The maximally mixed state σ_m , which has the highest entropy, is analogous to the Maxwellianized distribution function $f_{\sigma M} / n_\sigma$. The von Neumann entropy $S(\rho) = -\text{tr}[\rho \ln \rho]$ (Von Neumann, 1927) is decomposed as $S(\rho) = S_{\text{cross}}(\rho) - S_{\text{rel}}(\rho)$, where $S_{\text{cross}}(\rho) = -\text{tr}[\rho \ln \sigma_m]$ is the cross-entropy

and $S_{\text{rel}} = \text{tr}[\rho \ln \rho - \rho \ln \sigma_m] = -S(\rho) + S_{\text{cross}}(\rho)$ is the relative entropy (Floerchinger & Haas, 2020). This is similar to the decomposition done here for the velocity space kinetic entropy per particle, so $S_{\text{cross}}(\rho)$ is analogous to $s_{\sigma v, \bar{\epsilon}}/n_\sigma$ [Eq. (6.22)] and $S_{\text{rel}}(\rho)$ is analogous to $-s_{\sigma v, \text{rel}}/n_\sigma$ [Eq. (6.6)]. In Ref. (Floerchinger & Haas, 2020), the volume of the system was kept fixed for simplicity, so there was no term analogous to the position space entropy term in our analysis. Including this term, which gives rise to work in the classical case, is very straight-forward; indeed, it appears automatically when the phase space density f_σ is employed instead of the distribution function f_σ/n_σ . Undoubtedly the quantum statistical mechanical approach can be generalized to include work done on the system using open quantum mechanics (Lidar, 2020).

For the classical case presented here, the physical interpretation of the terms are able to be clearly ascertained. This allows us to help elucidate the physical interpretation of the terms in the quantum statistical mechanics treatment (Floerchinger & Haas, 2020). The time rate of change of the relative quantum entropy is a measure of whether a system is evolving towards or away from the maximally mixed state and the rate at which it does so. Scaling it by the temperature of the state described by σ_m gives the time rate of change in the energy associated with non-equilibrium terms.

Chapter 7

Conclusion

7.1 Summary and discussion

In this dissertation, we discussed the non-LTE generalization of the first law of thermodynamics, otherwise known as the time evolution equation of effective temperature (Braginskii, 1965; Jou et al., 2010; Yang et al., 2017a). We motivated that this equation generalizes first law of thermodynamics for applications to plasma systems inherently out of local thermodynamic equilibrium (LTE), yet it remains incomplete. This is so because it ignores energy associated with cross terms of peculiar (or random/thermal) velocity, *i.e.*, $\int d^3v f m v'_j v'_k$ where $j \neq k$. Thus, while random energy associated with $j = k$, *i.e.*, internal (thermal) energy, is considered by the non-LTE generalization of the first law, other random energies are not. We also discussed in Chapter 1 how one such ubiquitous plasma phenomenon called magnetic reconnection can be inherently in non-LTE, thus making the examination of its energetics challenging. We motivated our choice of studying energy conversion in reconnection where non-Maxwellian velocity distribution functions are routinely observed (Egedal et al., 2013; Bessho et al., 2014; Shuster et al., 2014, 2015; Egedal et al., 2016; Barbhuiya et al., 2022; Torbert et al., 2018; Nakamura et al., 2018, 2019; Egedal et al., 2019). The presence of non-Maxwellianity, which by definition indicates not being in LTE, has been used for analyzing reconnection and turbulence

(Pezzi et al., 2021).

In spite of the past few years of rigorous work around examining the pressure-strain interaction which facilitates conversion between kinetic and thermal energy densities and its decomposition into pressure dilatation (which is associated with compression and expansion) and $\text{Pi} - \text{D}$ (which is associated with incompressible heating (Del Sarto & Pegoraro, 2018) and that has been called collisionless viscosity (Yang et al., 2017a)), a kinetic understanding of these terms has been missing. As we motivated, a kinetic picture is required for a fundamental understanding of energy conversion in plasma systems that are not in LTE since non-Maxwellian distributions lead to non-zero $\text{Pi} - \text{D}$ which act as part of heat per particle in the non-LTE generalization of the first law of thermodynamics. In Chapter 3, we propose an alternate decomposition of the pressure-strain interaction into the PDU and $\text{Pi} - \text{D}_{\text{shear}}$ terms, that capture converging/diverging flow and flow shear physics, respectively. We also show that the PDU term is a valid generalization of dilatation for systems not in local thermodynamic equilibrium (LTE). We provide a physical understanding of the contributions to the pressure-strain interaction both from a fluid and a kinetic perspective. We use these results to provide the underlying physical mechanisms that cause $\text{Pi} - \text{D}$ to be non-zero, and also provide a new kinetic theory interpretation for the normal deformation term, *i.e.* $\text{Pi} - \text{D}_{\text{normal}}$. We also show how converging flow, while contributing to a positive pressure-strain interaction, can have a negative $\text{Pi} - \text{D}$ for non-LTE systems. Depending on the situation, both decompositions may provide valuable information about the system, in addition to a third decomposition where we write pressure-strain interaction as the sum

of the pressure dilatation, $Pi - D_{\text{normal}}$, and $Pi - D_{\text{shear}}$. Moreover, as $Pi - D$ itself can be decomposed into two terms that denote different physics, there is no way to unambiguously identify the key physical processes at play from the sign of $Pi - D$ alone. In Chapter 4, by using magnetic field-aligned coordinates to decompose the pressure-strain interaction, we find that there exist contributions from compression/expansion and bulk flow shear, as we expect. However, there are contributions from velocity compression and shear caused by the geometry imposed by the path of the magnetic field line. The magnetic field itself and magnetic forces do not cause the pressure-strain interaction to be non-zero (Del Sarto et al., 2016), but the flow pattern relative to the magnetic fields lead to these geometrical compression and shear effects. These are parametrized in terms of the magnetic field curvature κ and torsion τ , where the latter is a measure of how much the local magnetic field is 3-D. As with Chapter 3, we start with providing a picture of the physical effects contributing to the pressure-strain interaction using the kinetic theory description for each of the sets of terms $-PS_1$ through $-PS_8$ that arise from the analysis. The physical mechanism of the parallel and perpendicular compression/expansion $-PS_1$ and $-PS_2$, and the shear in the bulk flow $-PS_3$, $-PS_{4,a}$, and $-PS_{4,b}$ are analogous to compression/expansion and bulk velocity shear in Cartesian coordinates (Del Sarto & Pegoraro, 2018; Cassak & Barbhuiya, 2022). From a kinetic perspective, we find that the mixing of particles and the pressure-strain interaction is caused by the particle random motion in the direction perpendicular to the flow in $-PS_5$ through $-PS_8$. Since $-(\mathbf{P} \cdot \nabla) \cdot \mathbf{u}$ is a scalar quantity, it is invariant in different coordinate systems and should be the same whether it is calculated in Cartesian co-

ordinates (Chapter 3) or field-aligned coordinates (Chapter 4). However, we observe mixing between compression/expansion and flow shear when changing coordinate systems. In magnetized plasmas where particles become demagnetized and the direction of the magnetic field no longer organizes the dynamics (Servidio et al., 2012; Burch et al., 2016b; Egedal et al., 2018), caution is necessary to not assume the magnetic field direction is necessarily the direction that best organizes a general pressure tensor. The decomposition in field-aligned coordinates presented in Chapter 4 is general because there is nothing special about $\hat{\mathbf{b}}$ and it can be some other preferred direction determined by a particular plasma system. This furthers the key point that the magnetic field and magnetic forces themselves do not give rise to the pressure-strain interaction, it is only the bulk flow gradients relative to the geometry set up by the magnetic field that gives rise to the pressure-strain interaction.

In Chapter 5, we employ the newly formulated decompositions of the pressure-strain interaction to calculate the two formulations in Cartesian coordinates and all eight terms in magnetic field-aligned coordinates in and around the electron diffusion region (EDR) of a 2-D antiparallel symmetric reconnection simulation using the particle-in-cell code `p3d`. We first demonstrate how to use the results of Chapters 3 and 4 to analyze a reconnecting system. In so doing, we plot the decomposition of the pressure-strain interaction in terms of the pressure dilatation and $\text{Pi} - \text{D}$ (compressible and incompressible contributions, respectively), and compare it to the decomposition from Chapter 3 with PDU and $\text{Pi} - \text{D}_{\text{shear}}$ terms (flow convergence/divergence and flow shear, respectively). We find their structure is noticeably different and they each have their merits in isolating particular physical

effects. For the present study of reconnection, we find that a number of features of the most prominent contributions to the pressure-strain interaction are better isolated by employing PDU and $P_i - D_{\text{shear}}$, and significant insights are gained by using the two decompositions in tandem. We similarly calculate the decomposition of pressure-strain interaction in magnetic field-aligned coordinates. As desired, this decomposition facilitates a physical interpretation of the mechanisms for heating relative to the ambient magnetic field, and allows for quantitative estimates of the energy density conversion rate from scaling analyses. We summarize the result of thorough analysis of determining the largest contributions to pressure-strain interaction, which in turn contributes to changing the thermal energy density, by a map in Fig. 5.7. Figure 5.7 illustrates the region surrounding the EDR, where various physically distinct effects play significant roles in the simulations at $t = 13$. This particular time represents a phase where reconnection is occurring at its most rapid rate. The figure demonstrates how these effects contribute to the generation of positive or negative pressure-strain interaction. We find that the underlying physics of the dominant term match with known reconnection physics. $-PS_2$ causes positive pressure-strain interaction at the upstream edges of the EDR in the inflow regions due to perpendicular compression as the electron inflow slows down. $-PS_1$ causes positive pressure-strain interaction at the upstream edge of the EDR out to the separatrices due to parallel compression as the inflow of electrons slows down as they approach the EDR. $-PS_2$ causes negative pressure-strain interaction at and in the near vicinity of the X-line because electrons experience expansion as they are accelerated in the outflow direction. $-PS_5$ causes positive pressure-strain interaction

at the downstream edge of the EDR due to perpendicular geometrical compression since the outflow has a component in the direction of the magnetic curvature. $-PS_1$ causes negative pressure-strain interaction in the downstream region due to the expansion of the parallel flow, which is presumably associated with the outflow jets being redirected in the vertical direction and speeding up while the separatrix opens out during the onset phase. We find a key result here that leads to obtaining an expected scale of pressure-strain interaction in the EDR during magnetic reconnection. A simple scaling analysis reveals that the natural scale that describes heating via the pressure-strain interaction in an anti-parallel reconnection EDR is $\pm P_{e,up} c_{Ae,up} / (1 - 5d_e) = (0.2 - 1) P_{e,up} \Omega_{ce,up}$ during the steady-state reconnection phase. Here, $P_{e,up}$ is the electron pressure upstream of the diffusion region, $c_{Ae,up}$ is the bulk flow velocity that scales with the electron Alfvén speed based on the magnetic field $B_{e,up}$ at the upstream edge of the EDR, the gradient scale is either 1 or $5 d_e$ (depending on if the gradient is in the inflow or outflow direction), and finally $\Omega_{ce,up} = c_{Ae,up} / d_e$ is the electron cyclotron frequency based on $B_{e,up}$. This prediction should be useful for quantitative comparisons of the pressure-strain interaction during magnetic reconnection in space and the laboratory. The present scaling predictions are in good agreement with the observations (Bandyopadhyay et al., 2021) of a magnetosheath event by MMS (Wilder et al., 2018), both for the absolute scale for electrons and ions, and for the ratio between the electron and ion heating rates. In this dissertation, we also confirmed that the pressure-strain interaction remains independent of the coordinate system employed through the simulations conducted.

In Chapter 6, we transition from examining physical processes that can change

the second internal velocity moment, *i.e.*, the internal (thermal) energy, to developing a first-principles theory of energy conversion associated with all the higher order internal moments. We find that this theory is applicable to systems arbitrarily far from LTE. Unlike what has been used previously, for a physical process that changes both internal energy and higher order moments, this theory captures both and allows each to be calculated separately. Since the theory contains all internal moments of f_σ , it overcomes the closure problem. We, thus, dub Eq. (6.10) “the first law of kinetic theory”, since it has the same form as the first law of thermodynamics and is its kinetic theory generalization. Using the same simulations employed in Chapter 5, we measure the relative energy term in 2D anti-parallel reconnection simulation and find that there are regions where the change relative energy can be a significant fraction of, or even greater than the change in internal energy. We expect the results to be readily useful in the study of plasma systems using Vlasov/Boltzmann simulations and satellite observations (Burch et al., 2016a; Pollock et al., 2016). Beyond plasma physics, we anticipate that the present analysis may be generalized to be useful in other branches of sciences which utilize Boltzmann transport-type equations, such as many body astrophysics (Aarseth & Aarseth, 2003), micro- and nano-fluidics (Karplus & Petsko, 1990; Schaller, 2014), and quantum entanglement (Floerchinger & Haas, 2020).

7.2 Future work and concluding remarks

We investigate the pressure-strain interaction (and its various decompositions) and while this term quantifies the conversion rate between bulk flow and thermal energy densities, it is not the only quantity that is responsible for changes in thermal energy density. Heat flux density, which does not contribute to changes in the net thermal energy in a closed or isolated system (Yang et al., 2017b), can still locally modify the thermal energy density (Du et al., 2020; Song et al., 2020). The influence of heat flux density on thermal energy density is currently the subject of ongoing research.

It is worth noting that the influence of collisions and body forces, such as electric, magnetic, or gravitational forces, directly affects the bulk flow energy density equation but not the pressure-strain interaction. The electromagnetic force, represented by $qn\mathbf{u} \cdot \mathbf{E}$ for a species with charge q , or $\mathbf{J} \cdot \mathbf{E}$ when summed over species σ , has received significant attention in studying the conversion between bulk flow energy and electromagnetic energy (Zenitani et al., 2011; Klein & Howes, 2016; Burch et al., 2016b; Wilder et al., 2018; Chen et al., 2019; Afshari et al., 2021). However, the understanding of how body forces impact thermal energy is still limited and is an area that we plan to explore in future research.

For this present dissertation work, we conduct simulations of anti-parallel magnetic reconnection using small simulation domains that do not reach a steady state. For future work, we are actively pursuing simulations with larger domains where steady-state reconnection can be achieved. These simulations allow us to investi-

gate the time evolution of the pressure-strain interaction and its decompositions, as well as the divergence of heat flux density. Notably, we are examining the links between these quantities and the reconnection phase. Furthermore, we are conducting a detailed analysis of the time evolution of other terms in the thermal energy equation to understand how their contributions to changes in the effective temperature vary over time, particularly during different phases of reconnection. Additionally, our research involves the investigation of the time evolution of $\mathbf{J} \cdot \mathbf{E}$ and its decomposition into $\mathbf{J}_e \cdot \mathbf{E}$ and $\mathbf{J}_i \cdot \mathbf{E}$, for electrons and ions, respectively. We are currently studying how their 2D structures and amplitudes change over time, as well as how the contributions from electrons and ions to $\mathbf{J} \cdot \mathbf{E}$ evolve over time.

We are actively pursuing the development of a term that captures the time rate of change of relative energy and has units of power density, which will quantify the volumetric time rate of change of energy due to changing higher order moments and will be a better tool for comparison with the pressure-strain interaction, divergence of heat flux density, aforementioned $\mathbf{J} \cdot \mathbf{E}$ and its kinetic counterpart, the field-particle correlation (Klein & Howes, 2016), since these also have the dimensions of power density. There have been previous studies comparing these other metrics with the pressure-strain interaction (Pezzi et al., 2021) and it will be interesting to revisit such studies in light of the results of this dissertation.

A limitation of the work conducted in Chapter 6 is that the existing formulation of the “first law of kinetic theory” does not account for changes in the first velocity moment, specifically bulk flow, and thus by extension bulk flow energy. We are currently exploring a first-principles theory that addresses this limitation.

Currently, relative energy serves as the mechanism for energy conversion associated with all non-LTE internal moments. However, it does not distinguish between the significant and negligible contributions of individual non-LTE internal moments. Investigating this aspect would be an intriguing direction for future studies.

By employing simulations with a high particle per grid (PPG) in this dissertation, we can account for all the terms in the time evolution equations of thermal, bulk flow, and electromagnetic energy densities (Eqs. (1.34) - (1.36)). Through this comprehensive analysis accounting of the energetics of the system, we can infer the local and temporal behavior of the collisional terms, which, in the case of p3d, originate solely from numerical effects that is called “numerical dissipation”. Furthermore, by utilizing the continuity equation for kinetic entropy density (see Eq. (6.3)), we can establish a connection between numerical dissipation and the observed increase in the total entropy of the simulation domain. These concepts are currently being actively investigated.

In this dissertation, we use simulations with a relatively high electron mass. Similar structures in the pressure-strain interaction, its decomposition, and relative energy are expected for more realistic mass ratios, albeit with sharper features and higher amplitudes. Further studies are needed to validate this hypothesis and expand our investigations to include ions. We are also actively exploring the energy evolution equations and the behavior of relative energy in other non-LTE systems such as electron-only reconnection (Sharma Pyakurel et al., 2019), and decaying kinetic turbulence using high PPG simulations.

Appendix A

Scaling of electron heating by magnetization during reconnection and applications to dipolarization fronts and super-hot solar flares

A.1 Introduction

Energy conversion by magnetic reconnection, and its after effects, are of significant importance in numerous magnetospheric and solar processes (Birn & Priest, 2007; Gonzalez & Parker, 2016). Two examples are solar flares, which are energetic eruptions in the solar corona caused by reconnection (Priest & Forbes, 2002), and geomagnetic storms and substorms, during which energy from the interplanetary magnetic field gets stored and released via reconnection in Earth's magnetotail (Angelopoulos et al., 2008). Some of the magnetic energy released during reconnection appears as bulk flow energy of a plasma jet. In Earth's magnetotail, the energy in the jet is ultimately injected into the inner magnetosphere where it can greatly impact magnetospheric dynamics and has important space weather implications (McPherron, 1979; Pulkkinen, 2007). Analogous dynamics takes place in magnetospheres of other planets (Smith et al., 2018; Xu et al., 2021) and in sunward jets

Journal of Geophysical Research: Space Physics, 127 (2022)

Contributing authors: M. Hasan Barbhuiya, Paul A. Cassak, M.A. Shay, Vadim Roytershteyn, M. Swisdak, Amir Caspi, Andrei Runov, Haoming Liang

that occur during solar flares (Reeves et al., 2008).

In Earth’s magnetotail, the reconnected magnetic field on the Earthward side of the reconnection site dipolarizes as it releases its stored energy (Fu et al., 2020). The Earthward reconnection jet impinges on the pre-existing and relatively dense plasma sheet, which acts as an obstacle to the jet (Hesse & Birn, 1991). The jet’s kinetic energy compresses the reconnecting magnetic field, producing a dipolarization front (DF) (Ohtani et al., 2004; Runov et al., 2009; Sitnov et al., 2009; Runov et al., 2010, 2011; Sitnov & Swisdak, 2011; Hwang et al., 2011; Schmid et al., 2011; Runov et al., 2013; Fu et al., 2012a, 2013; Sitnov et al., 2013). (It has been argued that a more appropriate name for DFs is “reconnection jet fronts,” but we retain the name dipolarization fronts to conform to the majority of the literature.) Characteristic properties of DFs at the Earthward jet include a steep increase in the magnetic field component B_z normal to the plasma sheet and a steep decrease in plasma density as one goes in the tailward direction. Here, we use Geocentric Solar Magnetospheric (GSM) coordinates, for which x is Sunward, y is the duskward direction normal to x and Earth’s magnetic dipole, and z completes the right-handed coordinate system in the northward direction. DFs have been seen in the mid-tail plasma sheets associated with bursty bulk flows (BBFs) (Angelopoulos et al., 1992). Energy in the compressed magnetic field in DFs has been observed to convert into particle kinetic energy (Angelopoulos et al., 2013) and particle heating (Runov et al., 2015) while the DFs move Earthward.

One of the many consequences of DFs, and the focus of this Appendix, is that electrons are significantly heated near the fronts. An electron temperature T_e close

to 1.8 keV was observed in a DF event by Time History of Events and Macroscale Interactions during Substorms (THEMIS), a factor of ~ 3 higher than the electron temperature before the spacecraft crossed the DF, with a small perpendicular temperature anisotropy $T_{e,\perp} > T_{e,\parallel}$, where \perp and \parallel denote the directions perpendicular and parallel to the local magnetic field \vec{B} (Runov et al., 2010). Later observations revealed electron temperatures in the DFs in the range of 1–4 keV (Runov et al., 2015). Observational studies (Fu et al., 2011; Pan et al., 2012; Ashour-Abdalla et al., 2011; Liu & Fu, 2019) attributed such heating to adiabatic processes such as Fermi and betatron acceleration. Moreover, observations of electron velocity distribution functions in DFs reveal various non-isotropic electron pitch-angle distributions (PADs) (Wu et al., 2006; Fu et al., 2012b; Tang et al., 2021). So-called pancake PADs have a perpendicular temperature anisotropy (Wu et al., 2013). They were attributed to betatron acceleration in the compressed magnetic field of the DF (Xu et al., 2018). Also observed are so-called rolling pin PADs, which are a combination of a cigar PAD (with particles moving parallel and antiparallel to the local magnetic field, generated by Fermi acceleration in the bent magnetic field (Wang et al., 2014)) and a pancake PAD (Liu et al., 2017b). Analytical theory suggests particle distributions with a perpendicular temperature anisotropy are unstable to wave generation, including whistler waves (Gary & Madland, 1985). Whistler waves have been detected near DFs using satellite observations and cause non-adiabatic electron heating through wave-particle interactions (Le Contel et al., 2009; Deng et al., 2010; Viberg et al., 2014; Li et al., 2015; Yoo et al., 2019). A later observational study (Grigorenko et al., 2020) revealed that whistler waves heat electrons to

1–5 keV in rolling pin PADs.

Electron dynamics in DFs have also been studied extensively in numerical simulations. Motivated by observations, particle-in-cell (PIC) simulations have been used to study two broad classes of DFs: (i) flux rope (FR) type DFs with multiple X-lines, and (ii) flux bundle (FB) type DFs with a single transient X-line (Divin et al., 2007; Sitnov et al., 2009; Lu et al., 2016). The energization mechanism for electrons in FR-type DFs was found to be repeated reflections between the double peaked B_z structure present when there are two X-lines, and is betatron acceleration caused by the compressed B_z in FB-type DFs (Birn et al., 2013; Lu et al., 2016). A strong electron temperature anisotropy with $T_{e,\perp} > T_{e,\parallel}$ appears in the magnetic flux pile-up region of FR-type DFs in their PIC simulations and this anisotropy was shown to generate whistler waves (Fujimoto & Sydora, 2008). Electron velocity distribution functions in the electron diffusion region (EDR) and the downstream region were systematically investigated using PIC simulations (Shuster et al., 2014; Bessho et al., 2014). It was shown that the perpendicular temperature anisotropy is associated with electron ring distributions, *i.e.*, distributions that are toroidal in velocity space. They suggested the ring distributions form when electron outflow jets from reconnection get remagnetized by the stronger normal magnetic field B_z in the DF. In subsequent studies (Shuster et al., 2015; Wang et al., 2016), it was argued that this magnetization by the reconnected magnetic field heats the electrons downstream of the EDR. In another PIC simulation study (Egedal et al., 2016), electron ring distributions were found to grow in size when moving downstream from the X-line as a result of betatron heating. Recent PIC simulations (Huang

et al., 2021) suggest that as the DF moves downstream, first pancake PADs appear (as a result of betatron acceleration), followed by rolling pin PADs (when particles undergo Fermi reflections along with betatron acceleration), and culminating with cigar PAD (when Fermi acceleration becomes the dominating heating mechanism). Thus, electron ring distribution functions are associated with elevated temperatures, wave generation, and subsequent heating via wave-particle interactions in the region of DFs in Earth’s magnetotail.

In the solar corona, reconnection during solar flares produces sunward jets (“reconnection outflows”) that have some similarities to DFs (Reeves et al., 2008). These jets are associated with both particle acceleration and plasma heating. Solar flares routinely exhibit temperatures of $\sim 10\text{--}25$ MK ($\sim 0.9\text{--}2.2$ keV), generally thought to result from collisional energy transfer by particles accelerated to tens or hundreds of keV in or near the reconnection region impacting the dense chromosphere and heating the ambient plasma, whereupon it expands to fill the newly-reconnected flare loop in a process called chromospheric evaporation (Holman et al., 2011). However, a growing body of evidence suggests that the hottest plasmas in the flare thermal distribution are heated directly in the corona (Fletcher et al., 2011; Cheung et al., 2019). While this likely occurs to some extent in flares of all intensities (Warmuth & Mann, 2016), it appears most pronounced for so-called “super-hot” flares, where peak temperatures exceed 30 MK (~ 2.6 keV), significantly hotter than the component heated by chromospheric evaporation. Spectroscopic imaging analyses show that the super-hot plasma appears earlier and higher in the flare loop/arcade than the evaporative component (Caspi & Lin, 2010; Caspi et al., 2015). The densities of

the super-hot component are ~ 10 times smaller than the evaporative component, but ~ 10 times larger than the background coronal plasma (Caspi & Lin, 2010), suggestive of significant plasma compression. Such super-hot temperatures also appear to be associated exclusively with strong coronal magnetic fields exceeding 100 G (Caspi et al., 2014) and have a quasi-impulsive time profile, suggesting the mechanism for the heating of the super-hot plasma is directly connected to the magnetic reconnection process itself (Caspi & Lin, 2010). Many super-hot plasma heating mechanisms have been suggested, including Ohmic pre-heating coupled followed by Fermi and betatron acceleration from collapsing magnetic traps (Caspi, 2010), gas dynamic shock heating from relaxation of the reconnected magnetic loop (Longcope & Guidoni, 2011; Longcope et al., 2016), Fokker-Planck collisions (Allred et al., 2020), and others [(Warmuth & Mann, 2016) and references therein], but there is not yet a widely-accepted model.

We are not aware of any studies which give a first-principles prediction of the temperatures of the hot electrons downstream of reconnection exhausts as a function of the upstream plasma conditions, *i.e.*, the upstream (lobe) magnetic field, electron temperature and density. Such a prediction requires an understanding of the processes causing the complex electron distribution functions in reconnection exhausts. In this Appendix, for reasons justified in what follows, we focus on electron ring distributions in the region of the dipolarization front. Our starting point is the suggestion (Shuster et al., 2014; Bessho et al., 2014) that electron ring distributions are formed by the remagnetization of electron jets from reconnection. We quantitatively predict the major and minor radii of the ring distributions solely in

terms of plasma parameters in the region upstream of the reconnecting region. In particular, if the ring distributions are formed by the magnetization of electron jets, the major radius is governed by the electron Alfvén speed of the electron outflow jet, and the minor radius is governed by the electron thermal speed. To test the predictions, we perform a parametric study using two-dimensional (2D) PIC simulations in which the upstream density and upstream temperature are independently varied. We find ring distributions appear in all ten simulations we perform, and the major and minor radii depend on the upstream plasma parameters in the predicted manner. We further show that the associated electron temperature and temperature anisotropy largely scale according to analytical predictions of the major and minor radii, with the perpendicular temperature in excellent agreement and the parallel temperature being more complicated because there are counterpropagating electron beams along the magnetic field that are not incorporated in the present model. We find the electron ring distributions are associated with the highest electron temperature observed in the simulations, justifying their systematic study here. We confirm that the location at which electron ring distributions appear is associated with the location where the radius of curvature of the magnetic field exceeds the gyroradius based on the bulk flow speed, validating the suggestion by (Shuster et al., 2014) and (Bessho et al., 2014) that the ring distributions form as a result of remagnetization of the electrons. We also show the ring distributions are suppressed by the presence of a background guide field, as is expected if they are caused by remagnetization. Moreover, we show that electron ring distributions consistently appear where there is a plateau, or shoulder, in the profile of the normal magnetic field B_z downstream

of the reconnection exhaust, which may be a useful signature for future observational studies. Finally, we show that the electron temperatures predicted from the theory are comparable to observed temperatures when applied to dipolarization fronts in Earth's magnetotail and super-hot solar flares in the solar corona.

This Appendix is organized as follows. Section A.2 relates the major and minor radii of the ring distributions to upstream (lobe) plasma parameters and provides the associated analytical expressions of the temperature of ring distributions. Section A.3 describes the PIC simulations used in this Appendix. Section A.4 shows the simulation results, revealing ring distributions in all the simulations. Their major and minor radii are extracted and compared to the theory. The location of the ring distributions is related to features in the temperature and magnetic field profiles, and we confirm the rings are caused by remagnetization of the electron outflow jet. We discuss applications to dipolarization fronts and super-hot solar flares in Section A.5. We also discuss extending the theory to asymmetric reconnection for dayside magnetopause applications, and discuss implications for direct *in situ* observations of ring distributions. The manuscript concludes with Section A.6, where the key findings and limitations of our study are gathered, and future work is discussed.

A.2 Theory

We aim to relate the major and minor radii of ring distributions to macroscopic upstream properties of the reconnection process, *i.e.*, number density, temperature and magnetic field. One form of an ideal ring velocity distribution function $f_r(v_\perp, v_\parallel)$

is (Wu et al., 1989; Min & Liu, 2016)

$$f_r(v_{\perp}, v_{\parallel}) = \frac{n_r}{\pi^{3/2} v_{Th}^3 \Lambda} e^{-\frac{v_{\parallel}^2}{v_{Th}^2}} e^{-\frac{(v_{\perp} - v_{\perp 0})^2}{v_{Th}^2}}, \quad (\text{A.1})$$

where n_r is the number density, v_{\parallel} and v_{\perp} are the velocity space coordinates parallel and perpendicular to the central axis of the ring distribution, $v_{\perp 0}$ is the major radius of the ring distribution, and v_{Th} is the minor radius of the ring distribution, assumed to be Gaussian and isotropic in the parallel and perpendicular directions. The normalization factor Λ , defined by $\Lambda = r\sqrt{\pi} \operatorname{erfc}(-r) + e^{-r^2}$, enforces that $n_r = \int d^3v f_r$; here $r = v_{\perp 0}/v_{Th}$ and $\operatorname{erfc}(-r) = (2/\sqrt{\pi}) \int_{-r}^{\infty} e^{-z^2} dz$ is the complementary error function.

It was previously suggested (Shuster et al., 2014; Bessho et al., 2014) that electron ring distributions form when the electron jet from reconnection gets magnetized by the strong normal (reconnected) magnetic field occurring as a result of compression at the dipolarization front. In principle, the same effect can happen for ions, but we only see rings in our simulations for electrons so we focus on them here. We expect the major radius of the ring distribution $v_{\perp 0}$ to be the electron outflow speed before the beam gets magnetized, which scales as the electron Alfvén speed $c_{Aup,e}$ (Shay et al., 2001; Hoshino et al., 2001) based on the reconnecting magnetic field strength $B_{up,e}$ at the upstream edge of the EDR,

$$v_{\perp 0} = \frac{B_{up,e}}{\sqrt{4\pi m_e n_{up}}}, \quad (\text{A.2})$$

where m_e is the electron mass and n_{up} is the density upstream of the EDR which is comparable to the density upstream of the ion diffusion region (IDR) and therefore the upstream (lobe) plasma.

For the minor radius v_{Th} , we propose that it is governed by the thermal speed v_{Th} of the electron upstream of the reconnection site, *i.e.*,

$$v_{Th} = \sqrt{\frac{2k_B T_{e,up}}{m_e}}, \quad (\text{A.3})$$

where k_B is Boltzmann's constant and $T_{e,up}$ is the temperature upstream of the EDR, which is essentially the same as the (lobe) temperature upstream of the IDR at the early times when reconnection that forms a dipolarization front takes place. This effectively assumes that the increase in temperature that takes place as electrons flow through the EDR or across separatrices as they go into the exhaust (Shay et al., 2014) is small. Using Eqs. (A.2) and (A.3), we write the parameter r in terms of upstream parameters as

$$r = \frac{B_{up,e}}{\sqrt{8\pi n_{up} k_B T_{e,up}}}, \quad (\text{A.4})$$

which is related to a form of the upstream electron plasma $\beta_{e,up}$ as $r = \beta_{e,up}^{-1/2}$. Using these expressions, we have the parameters necessary to write Eq. (A.1) solely in terms of upstream plasma parameters.

The perpendicular and parallel temperatures T_{\perp} and T_{\parallel} associated with the ring distribution in Eq. (A.1) are calculated in the standard way using the second velocity moment of f_r , *i.e.*, $T_{\perp} = [m/(2n_r k_B)] \int d^3v (\vec{v}_{\perp} - \vec{u}_{\perp})^2 f_r$ and $T_{\parallel} =$

$[m/(n_r k_B)] \int d^3v (v_{\parallel} - u_{\parallel})^2 f_r$, where \vec{u}_{\perp} and u_{\parallel} are the perpendicular and parallel components of the bulk flow velocity calculated from the first velocity moment of the distribution function, $\vec{u}_{\perp} = (1/n_r) \int d^3v \vec{v}_{\perp} f_r$ and $u_{\parallel} = (1/n_r) \int d^3v v_{\parallel} f_r$. Since both \vec{u}_{\perp} and u_{\parallel} are zero for f_r as given in Eq. (A.1), the resulting T_{\perp} and T_{\parallel} are (Wu et al., 1989)

$$T_{\perp} = \mathcal{M} T_{e,up}, \quad T_{\parallel} = T_{e,up}, \quad (\text{A.5})$$

where

$$\mathcal{M} = \frac{2e^{-r^2} (1 + r^2) + \sqrt{\pi} r (3 + 2r^2) \operatorname{erfc}(-r)}{2\Lambda} \quad (\text{A.6})$$

$$= \frac{3}{2} + r^2 - \frac{e^{-r^2}}{2\Lambda}. \quad (\text{A.7})$$

A plot of \mathcal{M} as a function of r is shown in Fig. A.1(a). The effective temperature $T_{\text{eff}} = (2T_{\perp} + T_{\parallel})/3$ is

$$T_{\text{eff}} = T_{e,up} \left(\frac{2\mathcal{M} + 1}{3} \right). \quad (\text{A.8})$$

The temperature anisotropy, defined as $A_{\perp} = T_{\perp}/T_{\parallel} - 1$, is

$$A_{\perp} = \mathcal{M} - 1. \quad (\text{A.9})$$

Thus, Eq. (A.8) is equivalent to $T_{\text{eff}} = T_{e,up}(1 + 2A_{\perp}/3)$ for this distribution. These expressions give the properties associated with the ring distribution in terms of upstream parameters.

It has been shown (Shuster et al., 2014; Egedal et al., 2016) that ring-type dis-

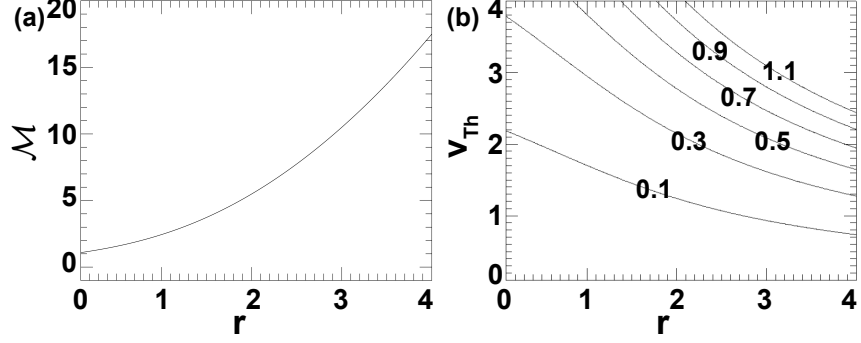


Figure A.1: (a) Line plot of \mathcal{M} from Eq. (A.7) as a function of $r = v_{\perp 0}/v_{Th}$. (b) Contour plot of T_{\perp} from Eq. (A.10) as a function of r and v_{Th} for a ring population plus a Maxwellian core population assuming $n_M = n_r$ and $v_{Th,M} = v_{Th}$.

tributions in PIC simulations of reconnection are not always ideal like in Eq. (A.1); some also have a Maxwellian core population. It is possible that this population is related to the initial current sheet population in the simulations, but validating this conjecture is not carried out for the present study. It is not clear if this population is a numerical artifact or also present in Nature. Since it is not the focus of the present study and has been seen in previous independent studies, we simply include it in our analysis to give more accurate comparisons to the simulations. Thus, we derive the temperatures associated with a distribution $f = f_r + f_M$ that is the sum of the ideal ring distribution f_r from Eq. (A.1) and a Maxwellian distribution $f_M = (n_M/\pi^{3/2}v_{Th,M}^3)e^{-v^2/v_{Th,M}^2}$ with density n_M and temperature T_M associated with the thermal speed $v_{Th,M} = (2k_B T_M/m)^{1/2}$. The zeroth velocity moment of this distribution gives the total local density as $n = n_r + n_M$. The temperatures generalizing Eqs. (A.5) and (A.8) are

$$T_{\perp} = \mathcal{M} \frac{n_r T_{e,up}}{n} + \frac{n_M T_M}{n}, \quad T_{\parallel} = \frac{n_r T_{e,up}}{n} + \frac{n_M T_M}{n} \quad (\text{A.10})$$

$$T_{\text{eff}} = \left(\frac{2\mathcal{M} + 1}{3} \right) \frac{n_r T_{e,up}}{n} + \frac{n_M T_M}{n}, \quad (\text{A.11})$$

while the temperature anisotropy in Eq. (A.9) becomes

$$A_{\perp} = \frac{(\mathcal{M} - 1)n_r T_{e,up}}{n_r T_{e,up} + n_M T_M}. \quad (\text{A.12})$$

A contour plot of T_{\perp} as a function of r and v_{Th} in the limit that $n_M = n_r$ and $v_{Th,M} = v_{Th}$ is shown for reference in Fig. A.1(b). These expressions will be useful when we analyze ring distributions in our PIC simulations.

A.3 Simulations

We use the PIC code `p3d` (Zeiler et al., 2002) to perform simulations of symmetric antiparallel magnetic reconnection that are 2.5D in position space and 3D in velocity space. `p3d` employs the trapezoidal leapfrog method (Guzdar et al., 1993) to advance electromagnetic fields in time and the particles are advanced in time using a relativistic Boris stepper (Birdsall & Langdon, 1991). The multigrid technique (Trottenberg et al., 2000) is used to clean the divergence of the electric field every 10 particle time-steps.

In the simulations, lengths are normalized to the ion inertial scale $d_{i0} = c/\omega_{pi0}$ based on a reference density n_0 that is the peak density of the initial current sheet population, where $\omega_{pi0} = (4\pi n_0 e^2/m_i)^{1/2}$, e is the ion charge, and c is the speed of light. Magnetic fields are normalized to the initial asymptotic upstream reconnecting magnetic field B_0 . Velocities are normalized to the Alfvén speed

$c_{A0} = B_0/(4\pi m_i n_0)^{1/2}$. Times are normalized to the inverse ion cyclotron frequency $\Omega_{ci0}^{-1} = (eB_0/m_i c)^{-1}$. Temperatures are normalized to $m_i c_{A0}^2/k_B$. Reduced velocity distribution functions are normalized to n_0/c_{A0}^2 .

The simulation coordinate system is defined such that reconnection outflows are along $\pm\hat{x}$ and inflows are along $\pm\hat{z}$, with periodic boundary conditions in both directions. The simulations are initialized with two Harris current sheets and a uniform background plasma population. The initial magnetic field profile is

$$B_x(z) = \tanh\left(\frac{z - l_z/4}{w_0}\right) - \tanh\left(\frac{z - 3l_z/4}{w_0}\right) - 1, \quad (\text{A.13})$$

with no initial out-of-plane guide magnetic field unless otherwise stated. Here, w_0 is the thickness of the current sheet and l_z is the length of the computational domain in the \hat{z} direction. The temperature and density of the background populations can be varied independently of the current sheet population. The initial electron and ion density profiles are

$$n(z) = \frac{1}{2(T_{e,CS} + T_{i,CS})} \left[\text{sech}^2\left(\frac{z - l_z/4}{w_0}\right) + \text{sech}^2\left(\frac{z - 3l_z/4}{w_0}\right) \right] + n_{up}, \quad (\text{A.14})$$

where n_{up} is the initial density of the background plasma. The current sheet electron temperature $T_{e,CS}$ is uniform with a value of 1/12, and the current sheet ion temperature $T_{i,CS}$ is uniform with a value $5T_{e,CS}$.

The speed of light c is 15, and the electron to ion mass ratio is $m_e/m_i = 0.04$. There are 4096×2048 grid cells in all the simulations, initialized with 100 weighted

Table A.1: Numerical parameters for two sets of simulations with varying (top) upstream total temperature $T_{TOT,up}$ and (bottom) upstream number density n_{up} . l_x and l_z are system sizes along \hat{x} and \hat{z} , respectively, w_0 is the initial current sheet thickness, Δx is the grid scale along \hat{x} and \hat{z} , and Δt is the time step.

$T_{TOT,up}$	$l_x \times l_z$	w_0	Δx	Δt
0.2	51.20×25.60	0.50	0.0125	0.00100
0.4	51.20×25.60	0.50	0.0125	0.00100
0.6	51.20×25.60	0.50	0.0125	0.00100
0.8	51.20×25.60	0.50	0.0125	0.00100
1.0	51.20×25.60	0.50	0.0125	0.00100
n_{up}	$l_x \times l_z$	w_0	Δx	Δt
0.2	51.20×25.60	0.50	0.0125	0.00100
0.4	47.41×23.71	0.46	0.0116	0.00093
0.6	44.35×22.17	0.43	0.0108	0.00087
0.8	41.81×20.91	0.41	0.0102	0.00082
1.0	39.68×19.84	0.39	0.0097	0.00078

particles per grid (PPG). A weak initial magnetic perturbation of the form $\delta B_x = -B_{pert} \sin(2\pi x/l_x) \sin(4\pi z/l_z)$ and $\delta B_z = B_{pert} l_z / (2l_x) \cos(2\pi x/l_x) [1 - \cos(4\pi z/l_z)]$ with $B_{pert} = 0.025$ is used to seed an X- and O-line pair in each of the two current sheets, where l_x is the computational domain size in the \hat{x} direction.

Two sets of five simulations are performed. Table A.1 lists relevant simulation parameters, including the system size $l_x \times l_z$, the initial current sheet half-thickness w_0 , the grid scale Δx in both directions, and the time step Δt . In all simulations, the ion to electron temperature ratio $T_{i,up}/T_{e,up}$ of the background plasma is initially 5. One set of simulations has varying $T_{TOT,up} = T_{i,up} + T_{e,up}$, while the initial background density is kept fixed at $n_{up} = 0.2$. The other set has varying n_{up} , with the initial background temperatures kept fixed at $T_{e,up} = 1/12$ and $T_{i,up} = 5T_{e,up}$. The smallest length scale for each of the simulations is the electron Debye length λ_{De} based on the total initial density at the center of the current sheet $1 + n_{up}$.

Thus, λ_{De} decreases as n_{up} is increased from 0.2 to 1 by a factor of $(1.2/2)^{1/2}$, *i.e.*, it is 22.5% lower for the $n_{up} = 1$ simulation than the $n_{up} = 0.2$ simulation. Thus, for the $n_{up} = 1$ simulation, the system size, grid length, initial current sheet thickness, and time step are also reduced by 22.5% (as listed in Table A.1). For other n_{up} values, a similar approach is used to determine their simulation parameters.

Since we use periodic boundary conditions, the minimum system size that allows the ions to fully couple back to the reconnection process is approximately $40 d_{i0}$ (Sharma Pyakurel et al., 2019). Since l_x is smaller than necessary for ions to fully couple back to the reconnected magnetic field, this study focuses on electron dynamics. In some of the simulations, the upper current sheet develops secondary islands which do not coalesce with the primary island by the time the system reaches steady-state. Hence we focus on the lower current sheet. Finally, we note that the ion and electron inertial lengths d_i and d_e based on the upstream (background) density are related to the length scale used for normalization via $d_i = d_{i0}/\sqrt{n_{up}}$ and $d_e = 0.2d_i$ for the mass ratio used in the simulations. Since n_{up} is fixed at 0.2 for the simulations with varying $T_{TOT,up}$, $d_i = 2.24 d_{i0}$ and $d_e = 0.45 d_{i0}$ for those simulations. For simulations with varying n_{up} , the length scales change with n_{up} ; for example, for $n_{up} = 1$, we have $d_i = d_{i0}$ and $d_e = 0.2 d_{i0}$. Each simulation is carried out long enough for the reconnection to reach a steady-state, meaning that the reconnection rate becomes approximately constant in time.

For plotting reduced electron velocity distribution functions (rEVDFs), which are 2D velocity distributions produced from the full 3D distributions after integrating over one of the three velocity directions, a domain of size $0.5 d_{i0} \times 0.5 d_{i0}$ centered

at the location of interest is used. A velocity space bin of size $0.1 c_{A0}$ is used in all velocity directions.

A.4 Methods and Results

A.4.1 Presence of ring distributions

A result of this simulation study is that all ten simulations reveal electron ring distributions beyond the downstream edge of the EDR near the region of the dipolarization fronts. This is ascertained by plotting rEVDFs in the plane perpendicular to the local magnetic field. Since the magnetic field in the region of interest is predominantly in the \hat{z} direction, we identify $\hat{x} \approx (\hat{u} \times \hat{b}) \times \hat{b} \equiv \perp 1$, $\hat{y} \approx \hat{u} \times \hat{b} \equiv \perp 2$, and $\hat{z} \approx \hat{b} \equiv \parallel$, where \hat{b} and \hat{u} are the unit vectors along the magnetic field \vec{B} and the bulk flow velocity \vec{u} . Defining the X-line location as (x_0, z_0) , the rEVDFs are plotted along the horizontal line $z = z_0$ as a function of x from the X-line to the magnetic island. At the earliest times in the steady-state reconnection time interval for all simulations, we find that rEVDFs near the X-line have striations, and they are rotated by the reconnected magnetic field B_z as one moves in the outflow direction within the EDR. Beyond the downstream edge of the EDR, ring-like features begin to arise in the distributions as some electrons complete at least one full gyration around B_z , leading to swirls and arcs (not shown), and finally to electron ring distributions for which most electrons complete at least one full gyration. These results are consistent with previous simulation studies (Bessho et al., 2014; Shuster et al., 2014, 2015; Egedal et al., 2016)

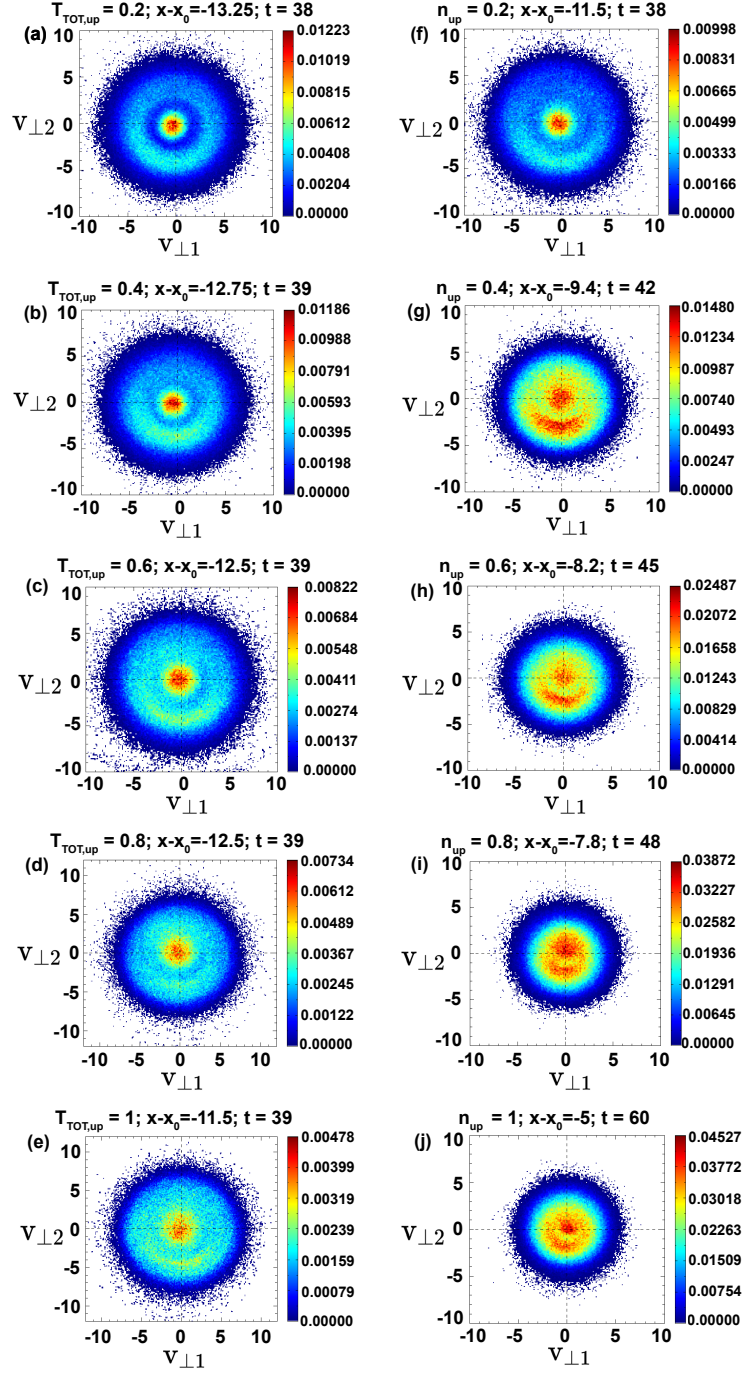


Figure A.2: reVDFs in the $v_{\perp 1} - v_{\perp 2}$ plane (where velocities are given in units of the normalized Alfvén speed c_{A0}) for simulations with (a) - (e) varying $T_{TOT,up}$ and (f) - (j) varying n_{up} . The title of each panel gives its background temperature or density as appropriate, the position $x - x_0$ where the reVDF is measured relative to the X-line, and the time t . For all panels, $z - z_0 = 0$.

The panels of Fig. A.2 show rEVDFs as a function of $v_{\perp 1}$ and $v_{\perp 2}$ for representative ring distributions seen in all ten simulations, with varying $T_{TOT,up}$ on the left from 0.2 to 1 in (a)-(e) and varying n_{up} on the right from 0.2 to 1 in (f)-(j). The title on each panel provides the locations $x - x_0$ and times t at which each rEVDF is plotted. The plotted rEVDFs reveal that there is a noticeable agyrotropy in the ring distributions, but the major and minor radii are well-formed. It is likely that the cause of the agyrotropy is that not all particles complete one full gyration, as also seen in previous studies (Shuster et al., 2014), but we do not study this feature further in the present Appendix. Looking at the rEVDFs in other planes (not shown), we find that along with the ring population and the colder Maxwellian core also seen in previous simulations studies (Shuster et al., 2014), a population of counterstreaming beams is also present in every simulation in every rEVDF. As elevated values of $T_{e,\parallel}$ that would be associated with parallel propagating beams are not seen at the reconnecting magnetic field reversal region in the study by (Shay et al., 2014) [see their Fig. 2(d)], we believe it is likely that this population is an artifact due to our simulation size being smaller than in that previous study, leading to accelerated electrons to be transmitted through the boundary to the location we are measuring distributions, but we leave verifying this conjecture for future work. These rEVDFs reveal that the ring distributions follow clear qualitative trends: with increasing background temperature $T_{TOT,up}$, the rings stay approximately the same size but are thicker in the $v_{\perp 1} - v_{\perp 2}$ plane [Fig. A.2(a)-(e)], whereas with increasing background density n_{up} , the rings shrink in size [Fig. A.2(f)-(j)] while maintaining a similar thickness.

A.4.2 Parametric dependence of ring distribution major and minor radii

We now quantitatively investigate the parametric dependence of the ring distributions by extracting their major and minor radii from the simulations. For each distribution in Fig. A.2, we take separate 1D cuts of the rEVDF along $v_{\perp 1} = 0$ and $v_{\perp 2} = 0$. For each 1D cut, we fit three Gaussians to the distribution given by $\sum_{i=1}^3 a_i e^{-[(x-b_i)/c_i]^2}$ using the *Curvefit* tool in *MATLAB R2020a*. The outer two Gaussians are used to fit the ring portion of the distribution and the central Gaussian is used to fit the core. The coefficients a_i are used to calculate n_r and n_M , b_i give the bulk flow of each component of the distribution and are related to $v_{\perp 0}$, and c_i give the associated thermal speeds v_{Th} and $v_{Th,M}$.

As a case study, 1D cuts and the associated fits are shown in Fig. A.3 for the $n_{up} = 0.2$ simulation from Fig. A.2(f). The black curve is the raw distribution function and the red curve is the best fit. Because the rEVDFs are not perfectly symmetric, the best fit coefficients and associated major and minor radii $v_{\perp 0}$ and v_{Th} are different in the $v_{\perp 1} = 0$ and $v_{\perp 2} = 0$ cuts. We calculate average values for $v_{\perp 0}$ and v_{Th} and their standard deviations σ derived from propagating the errors in quadrature. The best fit procedure also provides 95% confidence bounds, which we take as another estimate of the uncertainty of the values. The results of this procedure for all ten simulations are listed in Table A.2.

We now compare the theoretical predictions for the major and minor radii to the simulation results. For the theoretical predictions, we need to obtain $B_{up,e}, n_{up}$

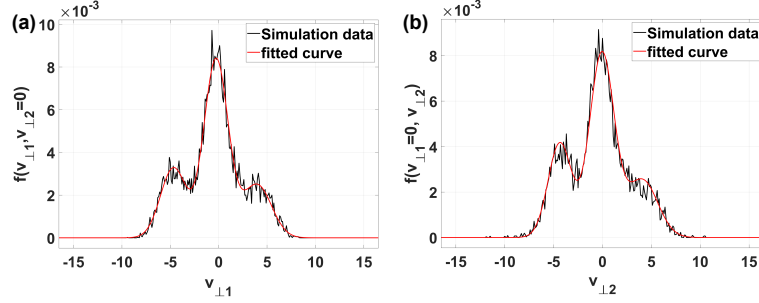


Figure A.3: 1D cuts of the rEVDF from Fig. A.2(f) for the simulation with $n_{up} = 0.2$ (black solid curve). The red solid curve is the best fit to three Maxwellians. The cuts are (a) $f(v_{\perp 1}, v_{\perp 2}=0)$ and (b) $f(v_{\perp 1}=0, v_{\perp 2})$.

Table A.2: Data from the fitting method described in Sec. A.4.2 for all simulations. The first column gives the value being varied, and $n_r, v_{\perp 0}$, and v_{Th} are the ring density, major radius, and minor radius. The σ values are standard deviations from the mean from cuts in the $\perp 1$ and $\perp 2$ directions, and 95% err is the error calculated using 95% confidence bounds from the fit.

$T_{TOT,up}$	n_r	$v_{\perp 0}$	$\sigma_{v_{\perp 0}}$	95% err $_{v_{\perp 0}}$	v_{Th}	$\sigma_{v_{Th}}$	95% err $_{v_{Th}}$
0.2	0.30	4.29	0.19	0.15	1.47	0.05	0.22
0.4	0.36	4.33	0.27	0.22	1.81	0.04	0.32
0.6	0.31	4.24	0.17	0.26	2.13	0.12	0.35
0.8	0.33	4.23	0.19	0.49	2.41	0.05	0.57
1.0	0.26	4.42	0.49	0.49	2.59	0.09	0.49
n_{up}	n_r	$v_{\perp 0}$	$\sigma_{v_{\perp 0}}$	95% err $_{v_{\perp 0}}$	v_{Th}	$\sigma_{v_{Th}}$	95% err $_{v_{Th}}$
0.2	0.28	4.26	0.32	0.12	1.99	0.23	0.17
0.4	0.46	2.93	0.32	0.19	2.11	0.19	0.19
0.6	0.91	2.52	0.29	0.19	2.08	0.15	0.17
0.8	1.17	1.99	0.13	0.35	1.99	0.07	0.28
1.0	1.28	1.89	0.07	0.12	1.94	0.11	0.12

and $T_{e,up}$ to evaluate $v_{\perp 0}$ in Eq. (A.2) and v_{Th} in Eq. (A.3). We define the upstream edge of the EDR where the electron bulk inflow speed starts to differ from the \hat{z} component of the $\vec{E} \times \vec{B}$ velocity. Then, the measured plasma parameters are obtained by averaging quantities over $0.06 d_{i0}$ centered around this location. We find that the upstream parameters vary in time, changing between the transient time when reconnection onset takes place and when a steady-state is reached. We reason that the dipolarization fronts occur due to jets that arise in the transient initial phase of reconnection. Therefore, we measure the upstream parameters at early times when the reconnection rate starts to increase. For the simulations with varying $T_{TOT,up}$, this time is $t = 5$ whereas for n_{up} simulations, the time varies from $t = 5$ for $n_{up} = 0.2$ to $t = 10$ for $n_{up} = 1$ since increasing n_{up} from 0.2 to 1 decreases the speeds by a factor of $5^{1/2}$. At the chosen time, we average the desired upstream quantities over five code time units. We find that the data variations are small (within 5%) during this interval. We also confirm the densities and temperatures do not vary appreciably between the upstream value at the electron layer and the upstream value at the ion layer. The results of this procedure are listed in Table A.3, along with theoretical predictions of $v_{\perp 0}$ using Eq. (A.2) and v_{Th} using Eq. (A.3).

The simulation data and theoretical predictions are plotted in Fig. A.4. The simulation data are displayed as black dots connected by solid black lines. The error bars are the larger of the two errors associated with each measurement given in Table A.2. The theoretical predictions, given in the last two columns of Table A.3, are displayed as red dots connected by red lines. The simulations with varying upstream temperature are shown in Figs. A.4(a) and (b), displaying $v_{\perp 0}$ and v_{Th} ,

Table A.3: Upstream plasma parameters from the simulations using the method described in Sec. A.4.2. The first column gives the value being varied, $B_{up,e}$ is the upstream magnetic field, n_{up} is the upstream density, and $T_{e,up}$ is the upstream temperature at the EDR edge. The last two columns give the theoretical predictions for the major radius $v_{\perp 0}$ and minor radius v_{Th} based on the upstream values using Eqs. (A.2) and (A.3), respectively.

$T_{TOT,up}$	$B_{up,e}$	n_{up}	$T_{e,up}$	Theoretical $v_{\perp 0}$	Theoretical v_{Th}
0.2	0.33	0.14	0.034	4.41	1.30
0.4	0.34	0.14	0.068	4.54	1.84
0.6	0.33	0.14	0.10	4.41	2.24
0.8	0.36	0.16	0.13	4.50	2.55
1.0	0.35	0.15	0.17	4.52	2.92
n_{up}	$B_{up,e}$	n_{up}	$T_{e,up}$	Theoretical $v_{\perp 0}$	Theoretical v_{Th}
0.2	0.35	0.15	0.084	4.51	2.05
0.4	0.36	0.32	0.086	3.18	2.07
0.6	0.38	0.51	0.087	2.66	2.08
0.8	0.36	0.69	0.086	2.17	2.07
1.0	0.37	1.01	0.083	1.84	2.04

respectively, as a function of $T_{TOT,up}$. The theoretical results are within the error bars from the simulations, confirming that $v_{\perp 0}$ is not dependent on $T_{e,up}$ while v_{Th} scales as $T_{e,up}^{1/2}$. Analogous results for the simulations with varying upstream density are shown in Figs. A.4(c) and (d). The predictions again are within the error bars from the simulations, and confirm the scaling of $v_{\perp 0}$ with $n_{up}^{-1/2}$ and the independence of v_{Th} on n_{up} . In summary, we find excellent agreement between the predicted values of both the major and minor radii of the ring distribution and the measured values from the ten simulations.

We now compare the electron temperatures associated with the ring distributions with the analytical expressions from Section A.2 by using Eq. (A.10) and (A.11) to find the predicted $T_{e,\perp}$, $T_{e,\parallel}$, and $T_{e,eff}$. For the core population parameters, we use the fitting results for the central Gaussian described earlier in this

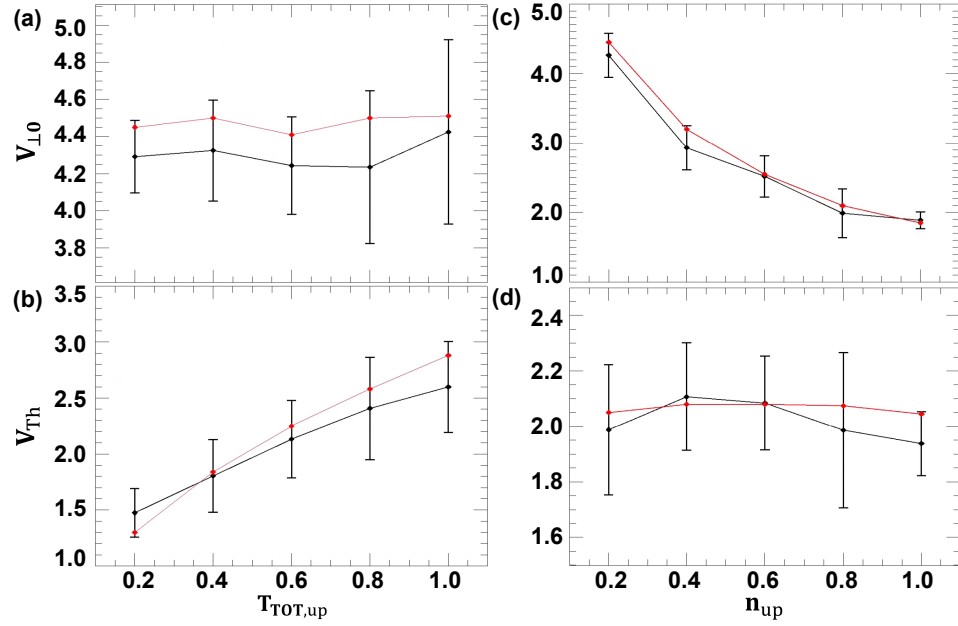


Figure A.4: Ring distribution (a) and (c) major radius $v_{\perp,0}$ and (b) and (d) minor radius v_{Th} from simulations with varying (a) and (b) upstream temperature $T_{TOT,up}$ and (c) and (d) upstream density n_{up} . Data in black (with error bars) are from the simulations as given in Table A.2, and data in red are from the theoretical predictions in Eqs. (A.2) and (A.3). Note that the vertical axes of each panel have a different range.

section. We find that the core population thermal speed $v_{Th,M}$ values are not those associated with the upstream electron temperatures, but a study of how the core population parameters scale with upstream plasma parameters is beyond the scope of this work. In the simulations, ring distributions are seen over a finite region of space, so the presented temperature values are mean values over that range. The error is estimated as the standard deviation of the mean.

The results are shown in Fig. A.5, with simulation results in black and theoretical results in red. The perpendicular temperatures, in panel (a) for simulations with varying $T_{TOT,up}$ and (d) for simulations with varying n_{up} , show excellent agreement between the theory and simulations. For the parallel electron temperature in panels (b) and (e), we observe a sizable difference between the simulated and predicted values. This is attributed to our theory not accounting for the parallel propagating counter-streaming beams mentioned in the previous subsection. However, we do find some qualitative agreement. Since $T_{e,\parallel}$ has a smaller weight than $T_{e,\perp}$ in $T_{e,eff}$, we find good qualitative agreement between simulation results and predicted values of $T_{e,eff}$ for all ten simulations, shown in panels (c) and (f). The results for varying n_{up} in panel (f) have very good quantitative agreement, as well. In summary, we find that the temperature in the region where rings are present increases with increasing upstream temperature and decreases with increasing upstream density, and the model based on ring distributions is quite effective at predicting the scaling and the absolute perpendicular temperatures.

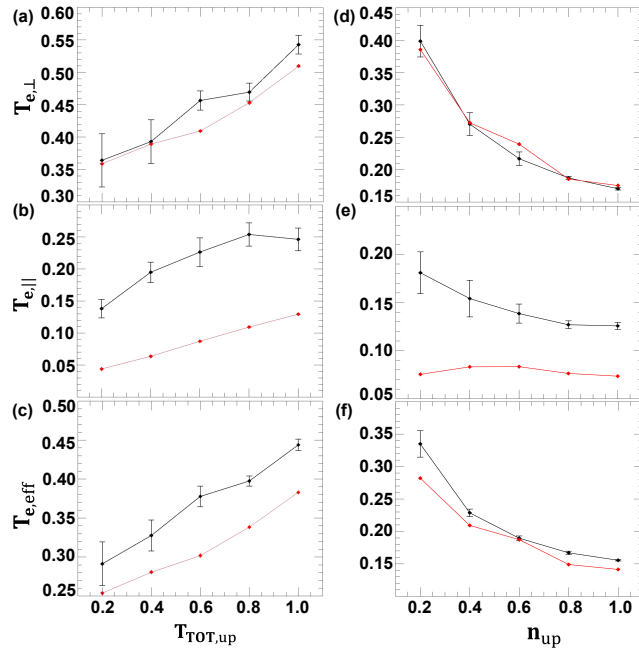


Figure A.5: Comparison between predicted electron temperatures $T_{e,\perp}$, $T_{e,\parallel}$ and $T_{e,eff}$ (red lines) and the simulation results (black lines with error bars). (a)-(c) are for the simulations with varying $T_{TOT,up}$, and (d)-(f) are for varying n_{up} . Note that the vertical axes of each panel has a different range.

A.4.3 Relation of ring distributions to temperature and magnetic field profiles

We now consider the location of the electron ring distributions in relation to the plasma parameter profiles in the region downstream of the EDR. Some plasma parameter profiles in the downstream region are shown in Fig. A.6. Panels (a) and (f) show 2D plots of $T_{e,\text{eff}}$ from the $T_{TOT,up} = 0.2$ simulation and the $n_{up} = 0.2$ simulation, both at $t = 38$. In both cases, the highest electron temperatures observed in the simulation are in the dipolarization front region, between positions $x - x_0$ of -10 and -15. There are also high temperature regions along the separatrix, but these are potentially impacted by the periodic boundary conditions of the simulation and are not treated further here. From previous work (Fu et al., 2012b; Egedal et al., 2016), we expect higher temperatures to arise from betatron acceleration of the electrons in the compressed magnetic field. However, the rEVDFs at later times during the steady-state time period (not shown) reveal the ring distributions do not increase in size in our simulations. We believe we do not observe this because our computational domain is smaller than in the previous study, preventing ions from coupling back to the magnetic field in the exhaust region.

The rest of the panels show comparisons of horizontal cuts of various quantities along the line $z = z_0$ for all $T_{TOT,up}$ (left plots) and n_{up} (right plots) simulations. The times t that each profile is taken are given in panels (b) and (g). Panels (b) and (g) show the perpendicular electron temperature $T_{e,\perp}$, revealing similar profiles for each upstream temperature with peak values near the dipolarization front, increasing

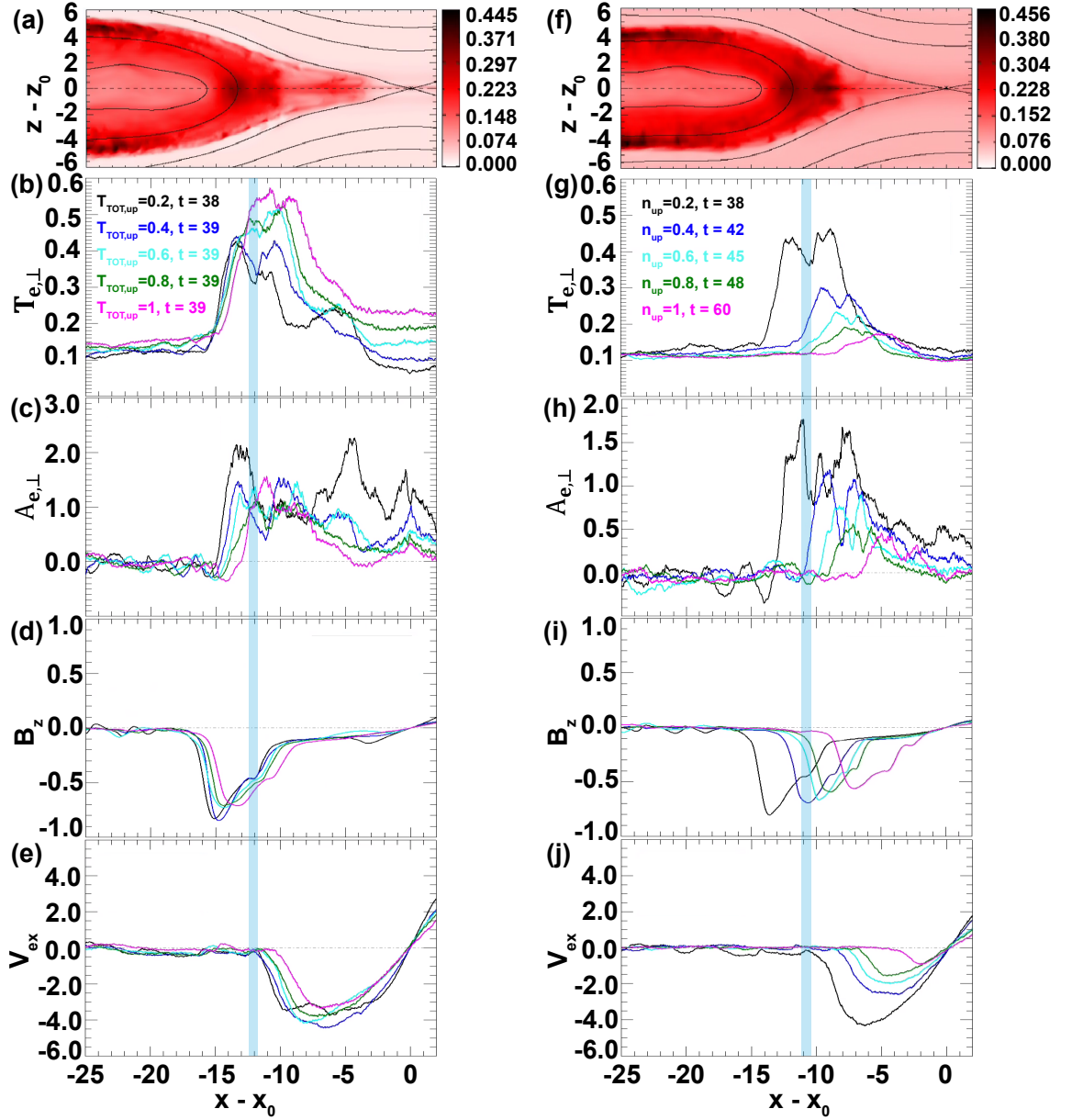


Figure A.6: Profiles of plasma parameters downstream of the reconnection site. (a) 2D plot of electron temperature $T_{e,\text{eff}}$ for the $T_{TOT,up} = 0.2$ simulation at $t = 38$. Horizontal cuts through the X-line as a function of $x - x_0$ of (b) perpendicular electron temperature $T_{e,\perp}$, (c) electron temperature anisotropy $A_{e,\perp}$, (d) reconnected magnetic field B_z , and (e) horizontal velocity V_{ex} for the simulations with varying $T_{TOT,up}$. Panels (g) to (j) repeat (b) to (e), but for the simulations with varying n_{up} . Panel (f) shows T_e for the $n_{up} = 0.2$ simulation at $t = 38$. The vertical blue lines highlight the shoulder in the reconnected magnetic field B_z for the $T_{TOT,up} = 0.2$ and $n_{up} = 0.2$ simulations.

with upstream temperature and decreasing with higher density. Panels (c) and (h) show the temperature anisotropy $A_{e,\perp}$. We observe strong electron temperature anisotropies with all the upstream temperature simulations having similar values. We also find a systematic reduction in $A_{e,\perp}$ with increasing upstream densities in the dipolarization front region.

Panels (d) and (i) show the reconnected magnetic field B_z . The profiles have the characteristic appearance of a dipolarization front, with a sharply peaked value at the front that decreases towards the X-line. Importantly, in all simulations, we observe a plateau, or shoulder, in B_z that occurs upstream of the dipolarization front. Blue vertical lines are used to highlight the shoulder in B_z for the $T_{TOT,up} = 0.2$ and $n_{up} = 0.2$ simulations. We find that for all the simulations, the B_z shoulder is spatially correlated with the regions of high $T_{e,\perp}$ and $A_{e,\perp}$.

Finally, panels (e) and (j) show the horizontal electron velocity V_{ex} , showing the characteristic increase in speed with distance from the X-line before rolling over and decreasing for all simulations as electron outflows exit the EDR. The horizontal velocity is close to zero in the region of peaked perpendicular temperature and the shoulder in B_z . The spatial profiles in Fig. A.6 are very similar to previous simulations by (Fujimoto & Sydora, 2008) (see their Figure 2), *i.e.*, the peak in $A_{e,\perp}$ (due to an enhancement in $T_{e,\perp}$) appears in the magnetic pileup region where the electron outflow speed goes to zero.

We now discuss the locations of the ring distributions relative to these profiles. We find that the ring distributions shown in Fig. A.2 are co-located with the shoulder region of B_z for all simulations. For simulations with increasing upstream

temperature, the shoulder regions in B_z are in similar locations and the ring distributions accordingly appear over a similar region in all five simulations (see the location of the ring distributions in the left column of Fig. A.2). However, as upstream density is increased, the shoulder in B_z appears closer to the X-line and so does the location of ring distributions (see the location of ring distributions in the right column of Fig. A.2). For all simulations, we find that the shoulder in B_z has an extent of $\sim 1 d_{i0}$, with a field strength of $\sim 0.5B_0$.

A possible mechanism for the presence of a shoulder in B_z at the location where there are ring distributions is the diamagnetic effect of the electrons that are magnetized by the strong reconnected magnetic field. The associated current reduces the magnetic field strength in the region where rings are present and increase the field strength outside. This change to the magnetic field appears as a plateau on the B_z profile as it ramps up with distance from the X-line.

To estimate the amount by which the reconnected magnetic field decreases in the presence of ring distributions, we use conservation of energy. Using Eq. (A.7) and (A.10) to rewrite Eq. (A.11) for the effective temperature of electrons as an energy equation gives

$$\frac{3}{2}k_B T_{e,\text{eff}} \simeq \frac{3}{2}k_B T_{e,up} + \frac{1}{2}m_e c_{Aup,e}^2 + \left(1 - \frac{e^{-r^2}}{2\Lambda}\right) k_B T_{e,up}. \quad (\text{A.15})$$

The left-hand side term gives the plasma energy at the location where rings are seen because the electron bulk speed vanishes so all energy is thermal. The first two terms on the right-hand side approximately describe the thermal plus kinetic energy

of electrons as they leave the EDR. The last term on the right side is associated with the thermal energy arising from the generation of the ring distribution. This extra energy is approximately the energy that is lost by the magnetic field as it decreases due to diamagnetism of the remagnetized electrons. The term in parentheses goes from 0.5 to 1 as $r = v_{\perp 0}/v_{Th}$ goes from 0 to ∞ . In order to conserve total energy, we expect the magnetic field energy to decrease by

$$\Delta \left(\frac{B^2}{8\pi} \right) \sim \left(1 - \frac{e^{-r^2}}{2\Lambda} \right) k_B T_{e,up}, \quad (\text{A.16})$$

where $\Delta(B^2/8\pi)$ is the change in magnetic field energy. Assuming the change in the magnetic field is weak, this decrease is approximately $B\Delta B/(4\pi)$ where ΔB is the change in the magnetic field.

In the normalized units of our simulations, $B \simeq 0.5$ at the shoulder, and $r \geq 1$ so $(1 - e^{-r^2}/(2\Lambda))$ is close to 1. For the varying n_{up} simulations where $T_{e,up}$ is kept fixed at 0.0833, this prediction gives a change in magnetic field of $\Delta B \simeq 0.2$. For the varying $T_{TOT,up}$ simulations where $T_{e,up}$ goes from 0.033 to 0.167, this prediction gives a change in magnetic field of $\Delta B \sim 0.1 - 0.3$. From the profiles of B_z in Fig. A.6(d) and (i), we find that the difference of the profile from a linearly increasing ramp away from the X-line is approximately 0.1 - 0.3, in reasonable agreement with the prediction.

A.4.4 Confirmation that ring distributions are caused by remagnetization

We now confirm the proposed model that electron rings are associated with their remagnetization in the reconnected magnetic field (Shuster et al., 2014; Bessho et al., 2014). We calculate two quantities as a function of x : (1) the magnetic field radius of curvature $R_c = |(\hat{b} \cdot \nabla)\hat{b}|^{-1}$, where \hat{b} is the unit vector along the local magnetic field, and (2) the electron gyroradius $\rho_{\text{bfs}} = V_{ex}/\Omega_{ce}$ based on the horizontal bulk flow speed V_{ex} and the local electron gyrofrequency $\Omega_{ce} = eB/m_e c$. The bulk flow speed is the appropriate speed because the ring distributions are proposed to be formed by outflowing electron beams that get remagnetized. The condition for remagnetization is $\sqrt{\kappa} = R_c/\rho_{\text{bfs}} \approx 1$ (Büchner & Zelenyi, 1989).

We plot R_c/ρ_{bfs} as a function of $x - x_0$ in Fig. A.7(a) for the $n_{up} = 0.2$ simulation at $t = 38$. A horizontal red dashed line marks where $R_c/\rho_{\text{bfs}} = 1$, which is $x - x_0 \approx -9$ as marked by the vertical red dashed line. Fig. A.7(b) shows ρ_{bfs} as a function of $x - x_0$. Its value where $R_c/\rho_{\text{bfs}} = 1$ is $\approx 0.5 d_{i0}$, which for this simulation is $\approx 1.1 d_e$.

We now compare this to the location where ring distributions are observed in this simulation. Ring distributions are seen throughout the blue shaded region of Fig. A.6(g)-(j). This is located $\simeq 2d_e$ downstream of the location where $R_c/\rho_{\text{bfs}} = 1$. Since the gyroradius of the electron beam is $\sim 1d_e$, the ring distributions are observed one gyro-diameter downstream of the location where the remagnetization condition is first met. This same behavior is seen in each of the other nine simulations

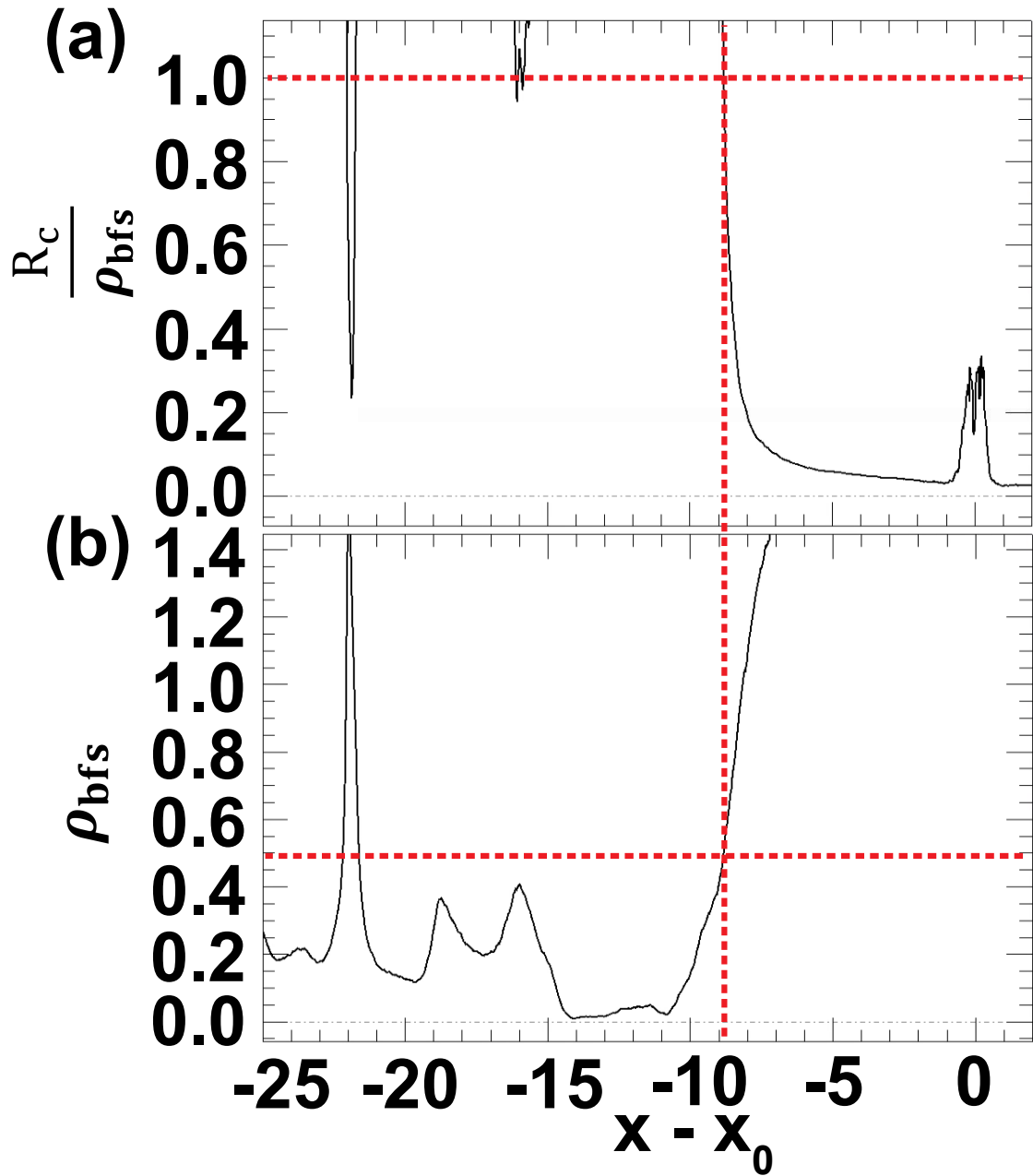


Figure A.7: (a) Ratio of the magnetic field radius of curvature R_c to the electron gyroradius ρ_{bfs} based on the bulk flow speed as a function of $x - x_0$ in a horizontal cut through the X-line for the $n_{up} = 0.2$ simulation at $t = 38$. The horizontal red dashed line at $R_c/\rho_{\text{bfs}} = 1$ is where electrons are expected to remagnetize. The vertical dashed red line marks the $x - x_0$ location where this condition is met. (b) ρ_{bfs} vs. $x - x_0$ for the same simulation, with the horizontal dashed line marking the value of ρ_{bfs} where electrons remagnetize.

studied here (not shown). This confirms that the remagnetization of the electron outflow jet is responsible for the generation of the ring distributions.

A further test that the ring distributions are caused by remagnetization of electron exhaust beams is that they should cease to be present with the addition of a sufficiently strong out of plane (guide) magnetic field. To test this, we perform simulations with initial guide fields B_g of 0.05 and 0.25 for $n_{up} = 0.2$, with all other parameters the same as before. A similar analysis as shown in Fig. A.7 (not shown) reveals that for the $B_g = 0.05$ simulation, R_c/ρ_{bfs} is very similar to the no guide field case, *i.e.*, away from the X-line, R_c/ρ_{bfs} increases and then crosses 1 signalling remagnetization of the electron outflow jet. The plasma parameter profiles are similar to those seen in Fig. A.6 for the no guide field case (not shown). A scan of rEVDFs as described in previous sections shows ring distributions in the region of a B_z shoulder (not shown). However, for the $B_g = 0.25$ simulation, R_c/ρ_{bfs} (not shown) is never less than 1 in the downstream region, implying that electrons are never demagnetized so no remagnetization occurs downstream. We also find no presence of ring EVDFs (not shown) in our scan. This provides additional evidence that the rings are formed by magnetization of the electron exhaust beams.

A.5 Discussion and Applications

The results of this research are potentially useful for a variety of reasons. By relating the properties of the ring distribution to the upstream (lobe) plasma parameters in Sec. A.2, we can make quantitative predictions of the electron temperatures

achieved downstream of reconnection exhausts, such as a dipolarization front or a solar flare reconnection outflow. We can also approximately account for the betatron acceleration that is expected to occur following the generation of ring distributions (Fu et al., 2012b; Egedal et al., 2016). We characteristically see the B_z shoulder at a magnetic field strength of about 0.5 as shown in Fig. A.6, and it further compresses to a strength of 1. If betatron acceleration were to occur and assuming that the magnetic moment is conserved, we expect the perpendicular temperature to increase by a factor of ~ 2 from our predicted values.

To apply the theory to real systems, we also need to estimate the magnetic field $B_{up,e}$ at the upstream edge of the electron layer from the asymptotic magnetic field strength B_{up} . There is no widely accepted theory for this, so we discuss two possible options. In model 1, we use

$$B_{up,e} \approx 2 \left(\frac{m_e}{m_i} \right)^{1/2} B_{up}, \quad (\text{A.17})$$

which captures that the electron outflow velocity at the EDR is often observed to be approximately twice the ion Alfvén speed. In model 2, we use (Liu et al., 2022)

$$B_{up,e} \approx \left(\frac{m_e}{m_i} \right)^{1/4} B_{up}, \quad (\text{A.18})$$

which follows from conservation of magnetic flux at the electron and ion layers.

We first consider Earth’s magnetotail, where there is typically only a weak guide field and typical plasma parameters may be taken as $B_{up} \approx 20$ nT, $n_{up} \approx 0.1$

cm^{-3} , and $T_{e,up} \approx 700$ eV, although there is significant uncertainty in all three values. Using the expressions in Sec. A.2, we find the predicted $v_{\perp 0}$ to be $(2.8 - 9.2) \times 10^8$ cm/s. Here and in what follows, the first number in the provided range is using model 1 and the second is using model 2. We also get $v_{Th} = 1.6 \times 10^9$ cm/s, so the perpendicular and effective temperatures associated with ring distributions is $T_{\perp} = 890 - 1270$ eV and $T_{\text{eff}} = 850 - 1100$ eV, with an anisotropy of $A_{e,\perp} = 0.2 - 0.7$. For comparison, the DF studied in Fig. 4 of (Runov et al., 2010) had electron temperatures reaching about 1800 eV with perpendicular temperature $T_{e,\perp} \sim 2000$ eV. Doubling our prediction to account for betatron acceleration, we find the predicted values are broadly consistent with the observations.

We next consider implications for reconnection in solar flares. The presence of a guide field may suppress the mechanism in the present Appendix entirely. However, a range of guide fields is observed including examples with little to no guide field (Qiu et al., 2017). Moreover, a leading model for the observed heating from MHD simulation studies also requires a low guide field strength (Longcope et al., 2010, 2016). We assume typical values of a background coronal temperature of $T_{e,up} = 1$ MK, a density of $n_{up} = 10^9$ cm^{-3} , and an ambient magnetic field for a large flare of $B \sim 100$ G, the latter of which is consistent with values inferred from radio and other measurements for large flares (Asai et al., 2006; Krucker et al., 2010; Caspi et al., 2014). The associated upstream magnetic field at the electron layer is estimated to be $B_{up,e} = 4.6 - 15.6$ G using model 1 and 2. Then, the predicted major and minor radii of the ring distributions are $v_{\perp 0} = 1.4 - 4.6 \times 10^9$ cm/s and $v_{Th} = 5.5 \times 10^8$ cm/s. This implies $r = 3 - 8$, $A_{e,\perp} = 7 - 70$, and $T_{e,\perp} = 8 - 70$ MK.

Since the coronal plasma β is small, r is significantly larger than 1, much higher than its magnetotail counterpart, leading to a much more dramatic increase in temperature due to remagnetizing the electrons. Taking an asymptotic expansion for the large r limit of Eq. (A.7) gives

$$\mathcal{M} \approx \frac{3}{2} + r^2. \quad (\text{A.19})$$

Using Eqs. (A.3) and (A.4) for v_{Th} and r , Eq. (A.8) gives an expression for T_{eff} for large r as

$$T_{e,\text{eff}} \approx T_{e,up} \left(\frac{4}{3} + \frac{B_{up,e}^2}{12\pi n_{up} k_B T_{e,up}} \right). \quad (\text{A.20})$$

Evaluating this expression in terms of the typical coronal parameters provided above, we get

$$T_{e,\text{eff}} = 1.33 \text{ MK} \left(\frac{T_{e,up}}{1 \text{ MK}} \right) + (4.2 \text{ MK} - 45 \text{ MK}) \left(\frac{B_{up}}{100 \text{ G}} \right)^2 \left(\frac{n_{up}}{10^9 \text{ cm}^{-3}} \right)^{-1}, \quad (\text{A.21})$$

where the range in the second term is for model 1 and 2 of $B_{up,e}$. Therefore, the predicted effective temperature is $T_{e,\text{eff}} = 5 - 46 \text{ MK}$ using models 1 and 2 for the typical coronal parameters employed here. This relation predicts a scaling dependence of the temperature approximately as B_{up}^2 . The temperatures predicted here, even when doubled to account for betatron acceleration, are in the same range as the 10s of MK observed during super-hot flares (Caspi & Lin, 2010; Caspi et al., 2014; Warmuth & Mann, 2016). The heating mechanism in our models is the reconnection process, significant heating occurs for magnetic fields starting at about 100 G, and

there is an increase in temperature with magnetic field strength. These features are broadly consistent with the relationships derived from a statistical study of X-ray observations of intense flares (Caspi et al., 2014). We therefore suggest it may be possible that the super-hot temperatures in such flares are generated by electron beams getting magnetized in reconnected fields, and potentially also subsequently heated further by betatron acceleration as the reconnected magnetic field continues to compress. This compression likely leads to higher densities than the ambient coronal value, as has been previously suggested (Caspi, 2010; Longcope & Guidoni, 2011). The proposed mechanism would also help explain the observed association of super-hot temperatures with coronal non-thermal emission and energy content (Caspi et al., 2015; Warmuth & Mann, 2016). Significant future studies to further explore the viability of the present model for explaining observed temperatures in super-hot solar flares is needed, including a parametric test of Eq. (A.21), determining whether this mechanism is consistent with the high level of compression seen in observations, studying if the small regions where the ring distributions are generated can transmit to the large scales endemic to solar flares, and determining whether guide field strengths in solar flares would magnetize the ring distributions.

The results of this Appendix could also be applicable to Earth’s dayside magnetopause, where ring distributions and whistler mode generation were recently observed both in simulations of asymmetric reconnection with a guide field and in Magnetospheric Multiscale (MMS) Mission observations (Yoo et al., 2019; Choi et al., 2022). The theory presented in this Appendix is exclusively for symmetric reconnection, but dayside reconnection is typically asymmetric. We expect the

mechanism for ring distribution generation to be similar in asymmetric reconnection. We hypothesize that in asymmetric reconnection, the speed that sets the major radius $v_{\perp 0}$ in Eq. (A.2) becomes the asymmetric version of the Alfvén speed that controls the outflow speed of asymmetric reconnection,

$$v_{\perp 0, asym} = \frac{B_{up, asym, e}}{\sqrt{4\pi m_e n_{up, asym}}}, \quad (\text{A.22})$$

and the thermal speed that sets the minor radius is replaced by

$$v_{Th, asym} = \sqrt{\frac{2k_B T_{e, up, asym}}{m_e}}, \quad (\text{A.23})$$

where

$$B_{up, asym, e} = \frac{B_{up, 1, e} B_{up, 2, e}}{(B_{up, 1, e} + B_{up, 2, e})}, \quad (\text{A.24})$$

$$n_{up, asym} = \frac{(n_{up, 1} B_{up, 2, e} + n_{up, 2} B_{up, 1, e})}{(B_{up, 1, e} + B_{up, 2, e})}, \quad (\text{A.25})$$

from previous work (Cassak & Shay, 2007, 2008). Moreover, Shay et al. (2014) gives

$$T_{e, up, asym} = \frac{(T_{e, up, 1} n_{up, 1} B_{up, 2, e} + T_{e, up, 2} n_{up, 2} B_{up, 1, e})}{(n_{up, 2} B_{up, 1, e} + n_{up, 1} B_{up, 2, e})}. \quad (\text{A.26})$$

It is beyond the scope of the present study to test this hypothesis, but it would be interesting to do so for future work.

We now discuss implications for direct measurements of ring distributions in reconnection events, especially in dipolarization fronts that are accessible to *in situ*

observations. The simulations suggest that the physical size of the region where ring distributions are present is relatively small. In the simulations, the range over which rings are seen is about $1 d_i$, corresponding to approximately 720 km (based on a lobe density of 0.1 cm^{-3}) in Earth's magnetotail. Temporally, we expect that they appear transiently at the dipolarization front. Simulations of reconnection in large domains do not reveal temperature peaks in the downstream region in the steady-state (Shay et al., 2014). Moreover, since ring distributions are unstable to wave generation (Gary & Madland, 1985), they are expected to rapidly decay, making their direct observation even more challenging. It is also challenging to observe ring distributions when the major radius is smaller than the minor radius, *i.e.*, when $r < 1$. For typical parameters in Earth's magnetotail, r is theoretically expected to be approximately 0.2 - 0.6, so *in situ* observations of rings might be challenging but can be potentially possible. Rings are more likely to be identifiable in large r (low electron plasma beta) systems.

To illustrate the challenges of direct measurement of a ring distribution, we describe an unsuccessful attempt to identify one in Earth's magnetotail using the THEMIS spacecraft (Angelopoulos, 2009). On February 27, 2009, four of the five THEMIS spacecraft traversed a DF between 0750 and 0800 UT (Runov et al., 2010), and burst mode data were available during this time. Their Figs. 4 and 5 reveal classic signatures of a DF, with a significant decrease in density and an increase in B_z (in GSM coordinates). The P1 (THEMIS B) spacecraft passed through the DF at 07:51:26 UT, shown on the left side of their Fig. 4, with the vertical dashed line denoting the DF. Immediately upstream of the DF (around 07:51:30 UT), the

electron temperature in both directions perpendicular to the magnetic field exceeds the parallel electron temperature, making this location a candidate for having an electron ring distribution.

To determine whether there is an electron ring distribution at this time, we investigate the EVDFs in the time interval when $T_{e,\perp} > T_{e,\parallel}$. The distributions are averaged over two spacecraft spin periods (6 s), between 07:51:30 and 07:51:36 UT, to get better statistics than a single spin. The low-energy cutoff due to spacecraft charging is ~ 60 eV, which is smaller than the predicted major radius for this event, so we expect it to be ostensibly possible to resolve a ring distribution if it is present. Two-dimensional cuts of the EVDF are produced from recombined ElectroStatic Analyzer (ESA) and Solid State Telescope (SST) data in this time range (not shown). Clear signatures of counterstreaming electron beams along the magnetic field are seen in both $\perp - \parallel$ planes. When the raw data is smoothed, a weak signature of what appears to be a ring population is seen. However, a closer examination of the uncombined ESA-only burst mode data with no smoothing reveals that the weak ring population signal is not present in the $\perp 1 - \perp 2$ cut where it should be, judging from the $\perp - \parallel$ plane cuts.

There are a few reasons for the misidentification of a ring distribution structure. In the $\perp 1 - \perp 2$ plane, there is a substantial population of low-energy particles which are of ionospheric origin. When the distribution function is smoothed, this population gives the appearance of a ring. However, the ionospheric population is not what would cause the appearance of a ring distribution by the mechanism studied here and must be excluded. The reason that $T_{e,\perp} > T_{e,\parallel}$ for this distribu-

tion is that the more diffuse magnetotail population is rather elongated in the \perp directions. To determine if this higher-energy magnetotail population is part of a ring distribution, we look at the \parallel - \perp planes. Because of the strong field-aligned counterpropagating beams, it makes it difficult to tell if removing that population would leave a ring in the high-energy population, but the population in question does not clearly disappear for more field-aligned angles. Consequently, we are unable to definitively claim there is an electron ring distribution in this particular THEMIS event. We suggest that observing a ring distribution in situ likely requires higher temporal resolution than available to THEMIS, but it may be accessible to MMS (Schmid et al., 2016; Liu et al., 2018; Zhao et al., 2019; Grigorenko et al., 2020; Ma et al., 2020) which has a much higher temporal resolution.

A.6 Conclusions

The appearance of ring distributions of electrons has been previously identified in particle-in-cell simulations near dipolarization fronts (Shuster et al., 2014; Bessho et al., 2014) and for dayside reconnection (Choi et al., 2022). It was suggested that they are caused by remagnetization of the electrons in the reconnected magnetic field (Shuster et al., 2014; Bessho et al., 2014). In this Appendix, we carry out a theoretical and numerical analysis that verifies and quantifies this prediction. Our analysis gives the major and minor radii of the ring distribution in terms of upstream conditions that dictate the properties of the reconnection, *i.e.*, the plasma density, electron temperature, and reconnecting magnetic field strength. In particular, the

major radius is given by the electron Alfvén speed based on the magnetic field and density upstream of the electron current layer, while the minor radius is governed by the electron thermal speed in the upstream region.

We employ 2.5D PIC simulations to test our predictions using five simulations with varying upstream temperature (with the upstream density held fixed) and five simulations with varying upstream density (with the upstream temperature held fixed). We find ring distributions in all 10 simulations. We extract the major and minor radii of the ring distributions for all ten simulations by fitting Gaussians to 1D cuts of the reduced distributions. We find that the major radius $v_{\perp 0}$ is independent of upstream temperature but decreases for increasing upstream density, while the minor radius v_{Th} increases for increasing upstream temperature and is independent of upstream density. The results are qualitatively and quantitatively consistent with the theoretical predictions, with agreement within one standard deviation of the theoretical predictions for all simulations.

Next, we use the major and minor radii of the ring distributions to compare the electron temperature associated with ring distributions to analytical predictions. We find that the predicted and measured perpendicular electron temperature agrees very well, within 12%. The parallel electron temperature is consistently different by about a factor of 2 between theory and simulation because the simulated plasma also contains counterstreaming beams in the parallel direction that are omitted from the analytical model. Since the perpendicular electron temperature contributes to the total electron temperature more than the parallel, the simulated total temperature is within 20% of the theoretical predictions.

By investigating the plasma parameter profiles in the region where the ring distributions are observed, we find the ring distributions, and their associated perpendicular temperature anisotropy, are spatially coincident with a plateau, or shoulder, in the profile of the reconnected magnetic field B_z . The shoulder in B_z is present where the ring distributions are because the remagnetized electrons are diamagnetic, thereby slightly lowering B_z within the electron orbit and slightly increasing B_z outside the orbit, thereby setting up a plateau in the B_z profile. A simple calculation using conservation of energy reproduces the approximate perturbed magnetic field due to this effect.

We show that the ring distributions appear approximately two electron gyroradii (one diameter of the gyromotion) downstream from the location where the electrons are remagnetized by the strong reconnected magnetic field, *i.e.*, the location where the radius of curvature of the magnetic field exceeds the gyroradius of the electrons based on the bulk flow speed. This result is consistent with the prediction that the ring distributions are associated with reconnection jets that are remagnetized by the reconnected field in a dipolarization front (Shuster et al., 2014; Bessho et al., 2014). We further confirm this by showing that the ring distributions become weaker and then are completely suppressed as an increasingly strong guide field is added.

Finally, we discuss applications of the present results in magnetospheric and solar settings. For dipolarization fronts in Earth's magnetotail, the electron temperatures predicted by the scaling analysis presented here are in the few keV range (when subsequent heating via betatron acceleration is accounted for), which is com-

parable to the observed electron temperatures. When applied to solar flares, we predict electron temperatures up to 10s of MK for very energetic flares, and an increase in temperature with the square of the reconnecting magnetic field. Such temperatures are consistent with those observed in super-hot flares, which are highly likely to come from the coronal reconnection process but for which there is not yet a widely accepted mechanism for their production. We further motivate a possible extension of the present work to antiparallel asymmetric systems, which may be important for applications to the dayside magnetopause.

The direct *in situ* measurement of ring distributions in the magnetotail is expected to be difficult, but potentially possible. Various characteristic pitch-angle distributions have been observed in dipolarization fronts (Liu et al., 2017b,a) and studied using simulations (Huang et al., 2021). It is possible that pancakes and/or the perpendicular features of rolling pins are ring distributions, and testing this would be interesting future work. We note that a pitch-angle distribution plot of a ring distribution would have a pancake-type structure, but it is not possible using a pitch-angle distribution plot to confirm the lack of low energy particles that is characteristic of a ring distribution. Rather, a direct investigation of the velocity distribution function is required. Based on a case study using THEMIS observations, we find that it is difficult to identify ring distributions. Higher temporal resolution, such as that afforded by MMS, would facilitate their identification.

It is known that the significant anisotropy arising in ring distributions makes them unstable to the generation of waves, especially whistlers (Gary & Madland, 1985; Umeda et al., 2007; Fujimoto & Sydora, 2008; Winske & Daughton, 2012).

More broadly, (Grigorenko et al., 2020) showed that electrons at 1–5 keV with a perpendicular temperature anisotropy generate whistler waves near DFs. By knowing the major and minor radii of the ring distributions in terms of upstream parameters, the temperature anisotropy can be calculated, which allows for a quantitative estimate of the linear growth rate of these modes. Such information is an important aspect of understanding particle acceleration and heating as a result of wave-particle interactions (Roytershteyn & Delzanno, 2018).

While whistler waves associated with temperature anisotropies are regularly measured *in situ* in Earth’s magnetosphere, much less has been studied for the possibility of whistler wave generation associated with solar flares. There has been theoretical work on understanding whistler wave generation in solar coronal loops (Vocks & Mann, 2006). In their work, the whistlers are generated from loss cone distributions rather than the mechanism discussed here. Since the characteristic length scale for the ring distributions is d_e , we expect the frequency of whistler waves associated with ring distributions to be comparable to the electron cyclotron frequency $\Omega_{ce} = eB/m_e c$. For the characteristic solar flare plasma parameters used here, we find that the whistler frequencies would be at least on the order of 0.3 GHz. Interestingly, an observational study has seen a long-lived source at 0.327 GHz (Aurass et al., 2006). Whether the mechanism discussed here can account for observed frequencies and whether this can be used as remote evidence in favor of the model presented here would be an interesting topic for future work.

There are many avenues for future work. The present simulations are two-dimensional; we do not expect the fundamental aspects of the results to change in

three dimensions, especially given that there is no guide field in the system studied here, but it would be interesting to confirm that 3D effects known to occur in magnetotail-type settings (Pritchett, 2013; Sitnov et al., 2014) do not alter the conclusions. The initial conditions of the present simulations did not include an equilibrium normal magnetic field, which is important for magnetotail reconnection (Lembege & Pellat, 1982); we do not anticipate this normal magnetic field would appreciably change the results herein, but it should be verified. The simulation domain size we employ is too small to allow ions to fully couple back to the plasma, so future work should confirm that the results are valid for larger system sizes. For dayside magnetopause applications, the proposed generalization incorporating asymmetries needs to be tested. For solar corona applications, electron-ion collisions may need to be taken into account, and observations should be used to test the functional dependence of the temperature on the magnetic field strength during solar flares predicted here, as well as whether a guide field suppresses such high temperatures. The physical size of the region where electrons are remagnetized is expected from the simulations to be relatively small, so questions about how ring distributions thermalize and whether they control the temperature over a greater volume, as would be necessary to explain the temperatures seen in super-hot flares, would be excellent topics for future work. Future work to quantify the rate of production of anisotropy-driven wave modes such as whistlers and their interaction with the downstream plasma would be important for applications.

Appendix B

Kinetic Entropy-Based Measures of Distribution Function

Non-Maxwellianity: Theory

B.1 Kaufmann and Paterson Kinetic Entropy-based Non-Maxwellianity

Here, we review the kinetic entropy-based measure developed by Kaufmann & Paterson (2009) to measure the non-Maxwellianity of an arbitrary given distribution function $f(\vec{r}, \vec{v}, t)$ as a function of position \vec{r} and velocity \vec{v} at a fixed time t . (We henceforth suppress the \vec{r} and t dependence for simplicity.) First, one calculates the density $n = \int d^3v f(\vec{v})$, bulk velocity $\vec{u} = (1/n) \int d^3v \vec{v} f(\vec{v})$ and effective temperature $T = (m/3nk_B) \int d^3v (\vec{v} - \vec{u})^2 f(\vec{v})$, where k_B is Boltzmann's constant and m is the mass of a particle. The Maxwellianized distribution $f_M(\vec{v})$ associated with $f(\vec{v})$ is defined as

$$f_M(\vec{v}) = n \left(\frac{m}{2\pi k_B T} \right)^{3/2} e^{-m(\vec{v} - \vec{u})^2 / 2k_B T}. \quad (\text{B.1})$$

part of J. Plasma Phys., 86, 825860502 (2020)

Contributing authors: Haoming Liang, M. Hasan Barbhuiya, Paul A. Cassak, Oreste Pezzi, S. Servidio, F. Valentini, Gary P. Zank

The local (continuous) kinetic entropy density s [*e.g.*, Eq. (3) in Liang et al. (2019)] of the full distribution function $f(\vec{v})$ is

$$s = -k_B \int d^3v f(\vec{v}) \ln f(\vec{v}). \quad (\text{B.2})$$

The kinetic entropy density s_M associated with the Maxwellianized distribution $f_M(\vec{v})$ is

$$s_M = -k_B \int d^3v f_M(\vec{v}) \ln f_M(\vec{v}). \quad (\text{B.3})$$

Equation (B.3) is analytically solvable using direct substitution of Eq. (B.1), giving

$$s_M = \frac{3}{2}k_B n \left[1 + \ln \left(\frac{2\pi k_B T}{m n^{2/3}} \right) \right]. \quad (\text{B.4})$$

This form motivated Kaufmann & Paterson (2009) to define a non-Maxwellianity measure, which we denote \bar{M}_{KP} , as

$$\bar{M}_{KP} = \frac{s_M - s}{(3/2)k_B n}. \quad (\text{B.5})$$

They chose to normalize to $(3/2)k_B n = c_v n$, where $c_v = (3/2)k_B$ is the specific heat per particle at constant volume for an ideal gas, so that \bar{M}_{KP} is dimensionless. They note, however, that the dimensions of s and s_M individually are not well-defined because they include a natural logarithm of the dimensional quantity $f(\vec{v})$. This is not an issue for differences in entropy density, which can be written as having a natural logarithm of a dimensionless quantity. [See also Appendix B4 of Liang

et al. (2019)].

B.2 Theory of the Kaufmann and Paterson Non-Maxwellianity

B.2.1 Basic Properties of Kaufmann and Paterson Non-Maxwellianity

Here, we gather some basic properties about the Kaufmann and Paterson non-Maxwellianity measure \bar{M}_{KP} . First, obviously, if $f(\vec{v})$ is Maxwellian, then $f_M(\vec{v}) = f(\vec{v})$ and $\bar{M}_{KP} = 0$. Second, it has long been known that $f_M(\vec{v})$ is the distribution with the maximum kinetic entropy for a fixed number of particles and total energy (in the absence of electromagnetic fields, net charge, and net current) [e.g., (Boltzmann, 1877; Bellan, 2008)]. Thus, s_M is the maximum entropy density for a fixed number of particles and energy. Therefore, if $\bar{M}_{KP} = 0$, then $f(\vec{v})$ is Maxwellian, and one expects \bar{M}_{KP} to be strictly non-negative. For these reasons, \bar{M}_{KP} is a good measure of non-Maxwellianity.

It is potentially a useful measure because it is a local measure which can identify regions with non-Maxwellian distributions. This is worthwhile to know because the rate of change of the local entropy density s is [e.g., (Eyink, 2018)]

$$\frac{\partial s}{\partial t} + \nabla \cdot \vec{\mathcal{J}} = -k_B \int d^3v C[f(\vec{v})][1 + \ln f(\vec{v})], \quad (\text{B.6})$$

where $\vec{\mathcal{J}} = -k_B \int d^3v \vec{v} f(\vec{v}) \ln f(\vec{v})$ is the entropy density flux and $C[f(\vec{v})]$ is the collision operator. The collision operator for a single species typically vanishes if $f(\vec{v})$ is Maxwellian, so the degree of non-Maxwellianity can be related to dissipation

through collisions [*e.g.*, (Liang et al., 2020a)]. Caution is necessary, however, because there are systems where dissipation occurs even if distributions are Maxwellian everywhere. One example is if the constituent species have come to equilibrium with themselves, but are at different temperatures than each other; there can be dissipation through inter-species collisions even though each distribution is Maxwellian [*e.g.*, (Guo et al., 2017; Grošelj et al., 2017; Parashar et al., 2018; Arzamasskiy et al., 2019; Kawazura et al., 2019; Cerri et al., 2019; Parashar & Gary, 2019; Rowan et al., 2019; Zhdankin et al., 2019)]. A second example is at an infinitely thin shock; the non-Maxwellianity is zero everywhere in such a system, but there is dissipation and entropy production at the discontinuity.

The quantity \bar{M}_{KP} is fluid-like, obtained from velocity space integrals of a function of the local distribution function. Thus, it should be able to be calculated using satellite, simulation, or laboratory experiment data not very differently than calculating moments of the distribution function such as density or temperature.

Another important property of \bar{M}_{KP} is that it is independent of density, as we now derive. Dividing Eq. (B.2) by n , then adding and subtracting $[f(\vec{v})/n] \ln n$ inside the integrand and simplifying gives

$$\frac{s}{n} = -k_B \int d^3v \frac{f(\vec{v})}{n} \ln \left(\frac{f(\vec{v})}{n} \right) - k_B \ln n. \quad (\text{B.7})$$

Using this result to directly calculate $\bar{M}_{KP} = (s_M - s)/(3/2)k_B n$ reveals that the $k_B \ln n$ term cancels because the densities associated with $f(\vec{v})$ and $f_M(\vec{v})$ are the

same, so

$$\bar{M}_{KP} = \frac{2}{3} \left[- \int d^3v \left(\frac{f_M(\vec{v})}{n} \right) \ln \left(\frac{f_M(\vec{v})}{n} \right) + \int d^3v \left(\frac{f(\vec{v})}{n} \right) \ln \left(\frac{f(\vec{v})}{n} \right) \right]. \quad (\text{B.8})$$

This shows that if one uses the convention where the distribution function is a probability density instead of a phase space density, *i.e.*, $f(\vec{v}) \rightarrow f(\vec{v})/n$, then the result for \bar{M}_{KP} is unchanged. It also shows that \bar{M}_{KP} has no explicit dependence on the plasma density n .

We note that \bar{M}_{KP} contains similar information to the non-Maxwellianity parameter ϵ introduced by Greco et al. (2012) and the enstrophy non-Maxwellianity Ω (Servidio et al., 2017). In our notation, ϵ is

$$\epsilon = \frac{1}{n} \sqrt{\int d^3v [f(\vec{v}) - f_M(\vec{v})]^2} \quad (\text{B.9})$$

and $\Omega = n^2 \epsilon^2$. The latter was simplified by expanding $f(\vec{v})$ in a Hermite expansion, which relates Ω to the Hermite spectrum of $f(\vec{v})$. In the limit that the departure from a Maxwellian is small, we can write $f(\vec{v}) = f_M(\vec{v}) + \delta f(\vec{v})$. Doing an expansion of \bar{M}_{KP} to second order in $\delta f(\vec{v})$ gives

$$\bar{M}_{KP} \simeq \frac{1}{3n} \int d^3v \frac{[f(\vec{v}) - f_M(\vec{v})]^2}{f_M(\vec{v})}, \quad (\text{B.10})$$

as is well-known in gyrokinetic theory [*e.g.*, (Howes et al., 2006; Grošelj et al., 2017; Cerri et al., 2018; Kawazura et al., 2019)]. This is quadratic in $\delta f(\vec{v})$, similar to ϵ and Ω . Thus, one would expect ϵ , Ω , and \bar{M}_{KP} to have similar structure

in strongly collisional systems where the deviation from Maxwellian distributions is small. When deviations from Maxwellianity are large, the two measures likely are different. These measures are compared with each other and other dissipation measures for weakly collisional systems in a companion study (Pezzi et al., 2021).

This section provides some insight into the properties of \bar{M}_{KP} , but it does not address how to interpret what it means for the non-Maxwellianity to be a particular number. The following sections introduce three examples where analytical values of \bar{M}_{KP} are calculated for common non-Maxwellian distribution functions.

B.2.2 Kaufmann and Paterson Non-Maxwellianity for Two Beams

We calculate \bar{M}_{KP} analytically for a two-population plasma that are each Maxwellian but drift parallel or anti-parallel to each other, and we require that the relative velocity of the beams is large enough that the overlap between the two populations in velocity space is negligible. A condition for this is derived below. The distribution function $f_{beam}(\vec{v})$ for such a system is given by

$$f_{beam}(\vec{v}) = n_1 \left(\frac{m}{2\pi k_B T_1} \right)^{3/2} e^{-m(\vec{v}-u_{z1}\hat{\mathbf{z}})^2/2k_B T_1} + n_2 \left(\frac{m}{2\pi k_B T_2} \right)^{3/2} e^{-m(\vec{v}-u_{z2}\hat{\mathbf{z}})^2/2k_B T_2}, \quad (\text{B.11})$$

where n_1 and n_2 are the densities of the two beams, u_{z1} and u_{z2} are the bulk velocities of the two beams, assumed parallel or anti-parallel, and T_1 and T_2 are the temperatures of the two individual beams. By taking moments, it is straight-forward

to show that the density, bulk flow, and effective temperature are

$$n = n_1 + n_2, \quad (\text{B.12})$$

$$u_z = \frac{n_1 u_{z1} + n_2 u_{z2}}{n_1 + n_2}, \quad (\text{B.13})$$

$$T_{beam} = \frac{mn_1 n_2}{3k_B(n_1 + n_2)^2} (u_{z1} - u_{z2})^2 + \frac{n_1 T_1 + n_2 T_2}{n_1 + n_2}. \quad (\text{B.14})$$

These bulk properties are valid independent of whether the two populations overlap in velocity space. The kinetic entropy density, however, is not exactly solvable unless the overlap between the two distributions is negligible, which occurs when the first term in Eq. (B.14) dominates the second term. In that limit, the kinetic entropy density s_{beam} from Eq. (B.2) is just the sum of the kinetic entropies of the individual beams,

$$s_{beam} \simeq \frac{3}{2}k_B(n_1 + n_2) + \frac{3}{2}k_B \left[n_1 \ln \left(\frac{2\pi k_B T_1}{mn_1^{2/3}} \right) + n_2 \ln \left(\frac{2\pi k_B T_2}{mn_2^{2/3}} \right) \right]. \quad (\text{B.15})$$

Eq. (B.5) and (B.4) give an associated non-Maxwellianity of

$$\bar{M}_{KP,beam} \simeq \ln \left(\frac{T_{beam}/n^{2/3}}{(T_1/n_1^{2/3})^{n_1/n} (T_2/n_2^{2/3})^{n_2/n}} \right). \quad (\text{B.16})$$

As a special case, if the beams are identical plasmas ($n_1 = n_2$ and $T_1 = T_2$) and they are counter-propagating ($u_{z1} = -u_{z2}$), then

$$\bar{M}_{KP,beam} \simeq \ln \left(\frac{T_{beam}}{2^{2/3} T_1} \right) \simeq \ln \left(\frac{mu_{z1}^2/3 + k_B T_1}{2^{2/3} k_B T_1} \right). \quad (\text{B.17})$$

Letting $u_{z1}^2 = \mathcal{M}^2 k_B T_1 / m$ with $\mathcal{M} \gg 1$, where \mathcal{M} is an effective Mach number of the flow (leaving out a factor of the ratio of specific heats γ), then the Kaufmann and Paterson non-Maxwellianity for this distribution is $\bar{M}_{KP,beam} \simeq \ln[(\mathcal{M}^2/3 + 1)/2^{2/3}]$.

B.2.3 Kaufmann and Paterson Non-Maxwellianity for Bi-Maxwellian Distributions

A bi-Maxwellian distribution function $f_{biM}(\vec{v})$ is defined as

$$f_{biM}(\vec{v}) = n \left(\frac{m}{2\pi k_B T_{\perp}} \right) \left(\frac{m}{2\pi k_B T_{\parallel}} \right)^{1/2} e^{-m(\vec{v}-\vec{u})_{\perp}^2 / 2k_B T_{\perp}} e^{-m(\vec{v}-\vec{u})_{\parallel}^2 / 2k_B T_{\parallel}}, \quad (\text{B.18})$$

where the \perp and \parallel subscripts allow for anisotropic velocities and temperatures, typically relative to the direction of a magnetic field. Straight-forward calculation of the associated kinetic entropy density from Eq. (B.2) gives

$$s_{biM} = \frac{3}{2} k_B n \left[1 + \ln \left(\frac{2\pi k_B T_{\perp}^{2/3} T_{\parallel}^{1/3}}{m n^{2/3}} \right) \right], \quad (\text{B.19})$$

and Eq. (B.5) gives an associated non-Maxwellianity of

$$\bar{M}_{KP,biM} = \ln \left(\frac{T}{T_{\perp}^{2/3} T_{\parallel}^{1/3}} \right) = \ln \left[\frac{2}{3} \left(\frac{T_{\perp}}{T_{\parallel}} \right)^{1/3} + \frac{1}{3} \left(\frac{T_{\parallel}}{T_{\perp}} \right)^{2/3} \right], \quad (\text{B.20})$$

where the second form eliminates the effective temperature using $T = (2/3)T_{\perp} + (1/3)T_{\parallel}$.

A plot of $\bar{M}_{KP,biM}$ as a function of T_{\perp}/T_{\parallel} is given in black on a linear scale

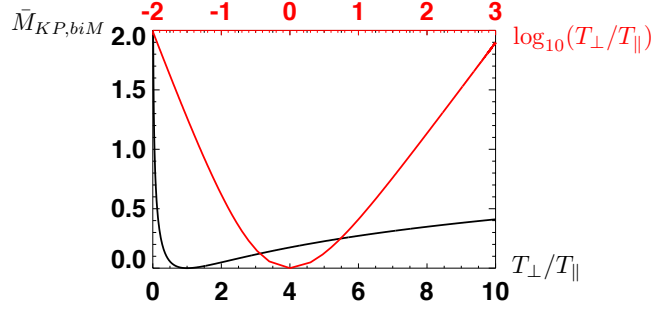


Figure B.1: Plot of the Kaufmann and Paterson non-Maxwellianity $\bar{M}_{KP,biM}$ for a bi-Maxwellian distribution function $f_{biM}(\vec{v})$ as a function of the ratio of perpendicular to parallel temperature T_{\perp}/T_{\parallel} . The black line uses a linear horizontal scale on the bottom axis, and the red line uses a logarithmic horizontal scale on the top axis over a wider range of T_{\perp}/T_{\parallel} to show that it diverges for small and large T_{\perp}/T_{\parallel} .

in Fig. B.1. This helps give perspective on values of the Kaufmann and Paterson non-Maxwellianity measure for a bi-Maxwellian distribution function. In particular, $\bar{M}_{KP,biM} = 0$ for a Maxwellian plasma ($T_{\perp}/T_{\parallel} = 1$), as expected. For example values, $\bar{M}_{KP,biM} \simeq 0.17$ for $T_{\perp}/T_{\parallel} = 4$ and $\bar{M}_{KP,biM} \simeq 0.23$ for $T_{\perp}/T_{\parallel} = 1/4$.

Interestingly, Eq. (B.20) reveals that $\bar{M}_{KP,biM}$ diverges to infinity as T_{\perp}/T_{\parallel} goes to either zero or infinity. The red line in Fig. B.1 uses a logarithmic horizontal scale over a broader range of T_{\perp}/T_{\parallel} to motivate this.

B.2.4 Kaufmann and Paterson Non-Maxwellianity for Egedal Distributions

During magnetic reconnection, magnetic fields in the upstream region bend as they approach the reconnection site. A magnetic field-aligned electric field accelerates electrons into this region, leading to a population of electrons that gets trapped in the mirror field (Egedal et al., 2013). The electron velocity distribution

functions in these regions are elongated in the direction parallel to the magnetic field, leading to a gyrotropic distribution. The distribution is a double adiabatic and reversible solution to the electron drift kinetic equation obtained in the limit of short electron transit/bounce time (Egedal et al., 2013). Here, we call it an Egedal distribution $f_{Eg}(\vec{v})$, and it is given by

$$f_{Eg}(\vec{v}) = \begin{cases} n_{\infty} \left(\frac{2\pi k_B T_{\infty}}{m}\right)^{-3/2} e^{-\frac{mv_{\perp}^2 B_{\infty}}{2k_B T_{\infty} B}} & \text{trapped} \\ n_{\infty} \left(\frac{2\pi k_B T_{\infty}}{m}\right)^{-3/2} e^{-\frac{m(v_{\perp}^2 + v_{\parallel}^2)}{2k_B T_{\infty}}} e^{\frac{e\phi_{\parallel}}{k_B T_{\infty}}} & \text{passing} \end{cases} \quad (\text{B.21})$$

where n_{∞} , T_{∞} and B_{∞} are the density, temperature and magnetic field strength far upstream, B is the local magnetic field strength, ϕ_{\parallel} is the parallel acceleration potential, and v_{\perp} and v_{\parallel} are the speeds perpendicular and parallel to the magnetic field. The trapped/passing boundary is given by

$$\frac{1}{2}m(v_{\parallel}^2 + v_{\perp}^2) - e\phi_{\parallel} - \frac{1}{2}\frac{mv_{\perp}^2}{B}B_{\infty} = 0. \quad (\text{B.22})$$

Calculating the local number density $n = \int d^3v f_{Eg}(\vec{v})$ for this distribution gives (Le et al., 2009)

$$\frac{n}{n_{\infty}} = 2b\sqrt{\frac{\Phi}{\pi}} + \text{erfcx}\left(\sqrt{\Phi}\right) - (1-b)^{3/2}\text{erfcx}\left(\sqrt{\frac{\Phi}{1-b}}\right) \quad (\text{B.23})$$

where $\text{erfcx}(x) = e^{x^2} \text{erfc}(x) = e^{x^2} [1 - \text{erf}(x)]$ is the scaled complementary error function, $\text{erfc}(x) = (2/\sqrt{\pi}) \int_x^{\infty} e^{-z^2} dz$, $b = B/B_{\infty}$, and $\Phi = e\phi_{\parallel}/k_B T_{\infty}$. Note, in the limit of $\Phi \rightarrow 0$ and $b \rightarrow 1$, the trapped/passing boundary from Eq. (B.22) reduces to

a point at $v_{\parallel} = 0$, and the distribution function $f_{Eg}(\vec{v})$ reduces to a Maxwellian, so the Maxwellian results should be recovered. Since $\text{erfcx}(0) = 1$, we recover $n = n_{\infty}$ in this limit, as expected.

The kinetic entropy density s_{Eg} for an Egedal distribution follows from direct application of Eq. (B.2). A lengthy calculation gives

$$s_{Eg} = \frac{3}{2}k_B n \left[\frac{n_{\infty} G}{n} + \ln \left(\frac{2\pi k_B T_{\infty}}{m n_{\infty}^{2/3}} \right) \right], \quad (\text{B.24})$$

where

$$G = 2b\sqrt{\frac{\Phi}{\pi}} + \left(1 - \frac{2\Phi}{3}\right) \text{erfcx}(\sqrt{\Phi}) - \sqrt{1-b} \left(1 - b - \frac{2\Phi}{3}\right) \text{erfcx}\left(\sqrt{\frac{\Phi}{1-b}}\right). \quad (\text{B.25})$$

As a check, in the $\Phi \rightarrow 0, b \rightarrow 1$ limit, $G \rightarrow 1$, so Eq. (B.24) reduces to Eq. (B.4), as expected. We also note that, since $\text{erfcx}(x) \rightarrow 1/(x\sqrt{\pi})$ asymptotically in the $x \rightarrow \infty$ limit, s_{Eg} diverges as $\Phi \rightarrow \infty$.

To calculate $\bar{M}_{KP,Eg}$ for Egedal distributions from Eq. (B.5), one needs the effective temperature T_{Eg} for Egedal distributions to get the entropy density of the Maxwellianized distribution. The parallel temperature $T_{\parallel,Eg} = [m/(nk_B)] \int d^3v (v_{\parallel} - u_{\parallel})^2 f(\vec{v})$ and perpendicular temperature $T_{\perp,Eg} = [m/(2nk_B)] \int d^3v (\vec{v}_{\perp} - \vec{u}_{\perp})^2 f(\vec{v})$,

following lengthy calculations, are

$$T_{\parallel,Eg} = \frac{n_{\infty}T_{\infty}}{n} \left[\operatorname{erfcx}(\sqrt{\Phi}) + 2b \left(2 - b + \frac{2\Phi}{3} \right) \sqrt{\frac{\Phi}{\pi}} - (1-b)^{5/2} \operatorname{erfcx} \left(\sqrt{\frac{\Phi}{1-b}} \right) \right], \quad (\text{B.26})$$

$$T_{\perp,Eg} = \frac{n_{\infty}T_{\infty}}{n} \left\{ \operatorname{erfcx}(\sqrt{\Phi}) + b(3b-1) \sqrt{\frac{\Phi}{\pi}} + (1-b)^{3/2} \left[\frac{\Phi b}{1-b} - \left(\frac{3b}{2} + 1 \right) \right] \operatorname{erfcx} \left(\sqrt{\frac{\Phi}{1-b}} \right) \right\}, \quad (\text{B.27})$$

$$T_{Eg} = \frac{2}{3}T_{\perp,Eg} + \frac{1}{3}T_{\parallel,Eg}. \quad (\text{B.28})$$

As a check, $T_{\parallel,Eg}$, $T_{\perp,Eg}$, and T_{Eg} all go to T_{∞} in the $\Phi \rightarrow 0, b \rightarrow 1$ limit, as expected.

Then, s_M is calculated from Eq. (B.4) and using the result with Eqs. (B.24) and (B.5), the closed-form non-Maxwellianity $\bar{M}_{KP,Eg}$ for Egedal distribution functions is

$$\bar{M}_{KP,Eg} = 1 - \frac{n_{\infty}G}{n} + \ln \left(\frac{T_{Eg}/n^{2/3}}{T_{\infty}/n_{\infty}^{2/3}} \right). \quad (\text{B.29})$$

For reference, plots of kinetic entropy density s_{Eg} and Kaufmann and Paterson non-Maxwellianity $\bar{M}_{KP,Eg}$ for an Egedal distribution are in Fig. B.2, using a density of $n/n_{\infty}=0.805$ and $T_{\infty} = 0.08 B_{\infty}^2/4\pi k_B n_{\infty}$. Panels (a) and (d) are contour plots of s_{Eg} and $\bar{M}_{KP,Eg}$, respectively, as a function of b and Φ . The former is normalized to $k_B n_{\infty}$. Panels (b) and (e) give cuts as a function of b at $\Phi = 2, 4, 6, 8,$ and 10 . Panels (c) and (f) give cuts as a function of Φ at $b = 0.15, 0.30, 0.45, 0.60$ and 0.75 . The plots show that the non-Maxwellianity increases as Φ increases, which makes sense physically because this increases the temperature anisotropy leading to an

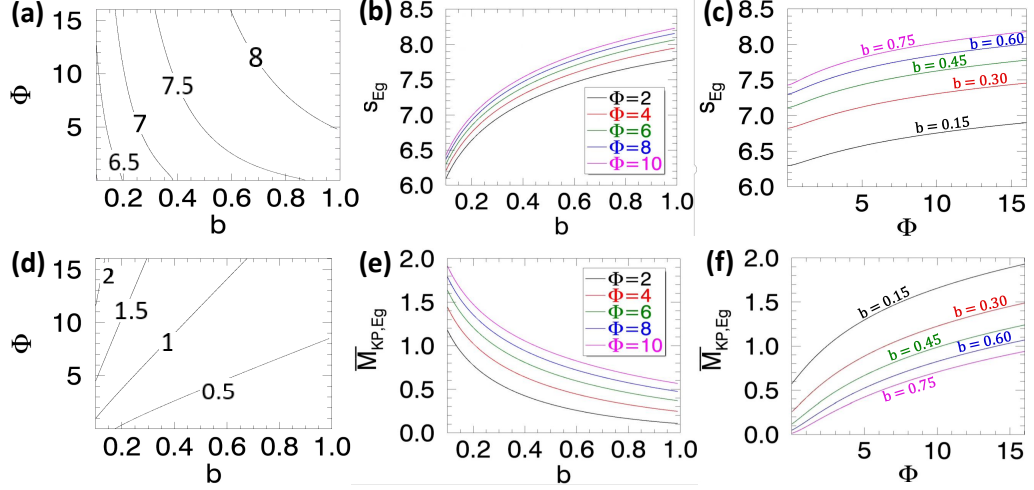


Figure B.2: Kinetic entropy density s_{Eg} and Kaufmann and Paterson non-Maxwellianity $\bar{M}_{KP,Eg}$ for an Egedal distribution function from Eq. (B.24) and Eq. (B.29) assuming $n/n_\infty=0.805$ and $T_\infty = 0.08 B_\infty^2/4\pi k_B n_\infty$. (a) and (d) are contour plots of s_{Eg} and $\bar{M}_{KP,Eg}$, respectively, as a function of $b = B/B_\infty$ and $\Phi = e\phi_{\parallel}/k_B T_\infty$. (b) and (e) are cuts of these as a function of b for five representative values of Φ . (c) and (f) are cuts of these as a function of Φ for five representative values of b .

increase in \bar{M}_{KP} , similar to bi-Maxwellian distributions in the previous section.

Following Le et al. (2009), it is typically more useful to eliminate Φ in favor of n/n_∞ and b by numerically inverting Eq. (B.23). The result is then in terms of quantities more easily found in observations and simulations. Plots analogous to Fig. B.2 but as a function of n/n_∞ and b are in Fig. B.3. Panels (a) and (d) are contour plots of s_{Eg} and $\bar{M}_{KP,Eg}$, respectively. Panels (b) and (e) give cuts as a function of b for $n/n_\infty = 0.6, 0.8, 1.0, 1.2$, and 1.4 . Panels (c) and (f) give cuts as a function of n/n_∞ for fixed b ; only $b = 0.3$ is shown in (c) since the dependence on b is weak, while (f) shows cuts for $b = 0.15, 0.30, 0.45, 0.60$ and 0.75 . Note that numerically inverting Eq. (B.23) gives negative Φ or extremely high $\Phi (\geq 80)$ for some values of n/n_∞ and b . Such values are eliminated from the plots and are denoted by shaded gray regions in Fig. B.3(a) and (d).

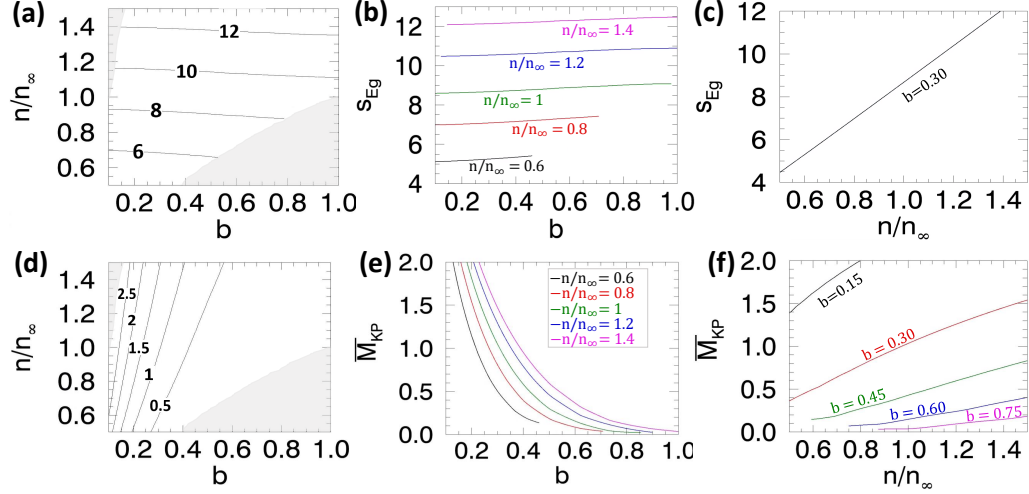


Figure B.3: Analogous to Fig. B.2, except plotted as a function of n/n_∞ and $b = B/B_\infty$ upon inversion of Eq. (B.23). The shaded regions in (a) and (d) correspond to parameters for which the inversion gives values of Φ below 0 or above 80, and are removed from the plot.

The past three subsections provide exact solutions for the non-Maxwellianity measure of analytic forms of three common non-Maxwellian velocity distribution functions. These are potentially useful to quantify the non-Maxwellianity of self-consistently generated distribution functions in physical systems, such as those undergoing reconnection, turbulence, or shocks in magnetized plasmas. In self-consistent plasmas, the distributions undoubtedly are not exactly given by the expressions analyzed here, but should provide a reasonable approximation in some settings.

B.2.5 Kaufmann and Paterson Non-Maxwellianity for Ring Distributions

In Appendix A, we discussed the increase in electron temperature caused by remagnetization of the electron jets outflowing from the diffusion region by the

reconnected magnetic field in the flux pile-up regions. Remagnetization of electron beams turn the electron velocity distribution functions (VDFs) to turn into a torus or ring shape (in velocity-space), which are again non-Maxwellian. As we did in Sec. B.2.4, here we derive the kinetic entropy density for ring VDFs first, and then \bar{M}_{KP} .

We previously used one form of an ideal ring VDF given by (Wu et al., 1989; Min & Liu, 2016)

$$f_r(v_{\perp}, v_{\parallel}) = \frac{n_r}{\pi^{3/2} v_{Th}^3 \Lambda} e^{-\frac{v_{\parallel}^2}{v_{Th}^2}} e^{-\frac{(v_{\perp} - v_{\perp 0})^2}{v_{Th}^2}}, \quad (\text{B.30})$$

where n_r is the number density, v_{\parallel} and v_{\perp} are the velocity space coordinates parallel and perpendicular to the central axis of the ring distribution, $v_{\perp 0}$ is the major radius of the ring distribution, and v_{Th} is the minor radius of the ring distribution, assumed to be Gaussian and isotropic in the parallel and perpendicular directions, given by $v_{Th} = (2k_B T/m)^{1/2}$. The normalization factor Λ , defined by $\Lambda = r\sqrt{\pi} \operatorname{erfc}(-r) + e^{-r^2}$, enforces that $n_r = \int d^3v f_r$; here $r = v_{\perp 0}/v_{Th}$ and $\operatorname{erfc}(-r) = (2/\sqrt{\pi}) \int_{-r}^{\infty} e^{-z^2} dz$ is the complementary error function. We use Eq. B.2 and after some algebra get

$$s_r = \frac{3}{2} n k_B \left[H + \ln \left(\frac{\pi v_{Th}^2 \Lambda^{2/3}}{n^{2/3}} \right) \right], \quad (\text{B.31})$$

where

$$H = 1 - \frac{1}{3} \frac{v_{\perp 0}}{v_{Th}} \frac{\sqrt{\pi}}{\Lambda} \operatorname{erfc} \left(\frac{-v_{\perp 0}}{v_{Th}} \right). \quad (\text{B.32})$$

Note that in the limit of $v_{\perp 0} \rightarrow 0$, $\Lambda \rightarrow 1$, $H \rightarrow 1$, and thus $s_r \rightarrow s_M$ (seen in

Eq. B.3).

Using Eq. B.5, we derive a closed-form expression for non-Maxwellianity $\bar{M}_{KP,r}$ for ring VDFs which after a brief calculation comes out as

$$\bar{M}_{KP,r} = 1 - H - \frac{2}{3} \ln \Lambda. \quad (\text{B.33})$$

Appendix C

Kinetic Entropy in an EDR - Theory, Observations, and Simulations of Kinetic Entropy in a Magnetotail Electron Diffusion Region

C.1 Review of Kinetic Entropy with a Uniform Velocity Space Grid

Kinetic entropy S as defined by Boltzmann (Boltzmann, 1877) is written as

$$S = k_B \ln \Omega, \tag{C.1}$$

where k_B is Boltzmann’s constant, $\Omega = N_{tot}! / \prod_{j,k} N_{j,k}!$ is the total number of microstates that correspond to a given macrostate, N_{tot} is the total number of particles in the system, $N_{j,k}$ is the number of particles in the j, k ’th cell of phase space, and the product over j and k is over all position- and velocity-space cells, respectively. We suppress writing a possible time t dependence here and throughout for simplicity. We call this form “combinatorial entropy” because of how the microstates are counted.

By breaking up phase space into discrete bins and applying Stirling’s approximation, combinatorial entropy can be written in terms of the particle distribution

part of Phys. Plasmas, 29, 022902 (2022)

Contributing authors: Matthew R. Argall, M. Hasan Barbhuiya, Paul A. Cassak, Shan Wang, Jason Shuster, Haoming Liang, Daniel J. Gershman, R. B. Torbert, and Jim L. Burch

function $f(\mathbf{r}, \mathbf{v}) = N_{j,k}/(\Delta^3 r \Delta^3 v)$ as (Boltzmann, 1877; Liang et al., 2019)

$$S = k_B \left\{ N_{tot} \ln \left(\frac{N_{tot}}{\Delta^3 r \Delta^3 v} \right) - \int d^3 r \int d^3 v f(\mathbf{r}, \mathbf{v}) \ln [f(\mathbf{r}, \mathbf{v})] \right\}. \quad (\text{C.2})$$

where the small phase space cells have uniform dimensions of size $\Delta^3 r$ and $\Delta^3 v$. In writing this expression, the phase space volume has been written as infinitesimals $d^3 r d^3 v$ in the integral in the second term but remains $\Delta^3 r \Delta^3 v$ in the first term. This implies that Eq. C.2 is only semi-continuous and that the finite grid size of any practical simulation or measurement device factors into the total entropy (Liang et al., 2019, 2020a).

By considering the permutation of particles in position- and velocity-space separately, the total combinatorial entropy can be decomposed into position-space combinatorial entropy S_r and velocity-space combinatorial entropy S_V , each of which has a semi-continuous representation similar to Eq. C.2 (Mouhot & Villani, 2011; Liang et al., 2019). It is illustrative to note that the same semi-continuous forms of position- and velocity-space entropy can be derived directly from Eq. C.2. After adding and subtracting $\int d^3 r n(\mathbf{r}) \ln [n(\mathbf{r})]$ and some simplification, Eq. C.2 becomes

$$S = S_r + S_V \quad (\text{C.3})$$

where

$$S_r = k_B \left\{ N_{tot} \ln \left(\frac{N_{tot}}{\Delta^3 r} \right) - \int d^3 r n(\mathbf{r}) \ln [n(\mathbf{r})] \right\} \quad (\text{C.4})$$

$$S_V = \int d^3 r s_V(\mathbf{r}) \quad (\text{C.5})$$

$$s_V(\mathbf{r}) = k_B \left\{ n(\mathbf{r}) \ln \left[\frac{n(\mathbf{r})}{\Delta^3 v} \right] - \int d^3 v f(\mathbf{r}, \mathbf{v}) \ln [f(\mathbf{r}, \mathbf{v})] \right\} \quad (\text{C.6})$$

The second term in Eq. C.6 is often referred to as the total kinetic entropy density $s(\mathbf{r})$,

$$s = -k_B \int d^3 v f(\mathbf{v}) \ln [f(\mathbf{v})], \quad (\text{C.7})$$

where we begin to suppress the \mathbf{r} dependence except where it is important to retain. This is the density of S because its position space integral gives the total kinetic entropy S in Eq. C.2 (up to a constant).

For a drifting Maxwellian distribution of the form

$$f_M(\mathbf{v}) = n \left(\frac{m}{2\pi k_B T} \right)^{3/2} e^{-m(\mathbf{v}-\mathbf{u})^2/2k_B T}, \quad (\text{C.8})$$

where m is the mass of the particles, n is the number density, \mathbf{u} is the bulk flow velocity, and T is the temperature, Eq. C.7 is exactly solvable, and gives the kinetic entropy density s_M of a Maxwellian distribution:

$$s_M = \frac{3}{2} k_B n \left[1 + \ln \left(\frac{2\pi k_B T}{m n^{2/3}} \right) \right]. \quad (\text{C.9})$$

Substituting this into Eq. C.6 gives

$$s_{M,V} = \frac{3}{2}k_B n \left[1 + \ln \left(\frac{2\pi k_B T}{m (\Delta^3 v)^{2/3}} \right) \right], \quad (\text{C.10})$$

the velocity-space entropy density of a Maxwellian distribution.

Because the Maxwellian distribution describes a plasma in local thermodynamic equilibrium, and because that equilibrium state has the highest entropy of all distributions with the same energy and number of particles (Boltzmann, 1877), the difference in kinetic entropy density between an observed distribution and its associated Maxwellian, or the non-Maxwellianity of the distribution (Kaufmann & Paterson, 2009),

$$\bar{M}_{KP} = \frac{s_M - s}{(3/2)k_B n}, \quad (\text{C.11})$$

is a measure of the departure from Maxwellianity of a local distribution function and gives a measure for the possibility for dissipation to occur. Eq. C.11 was defined by Kaufmann & Paterson (2009) and is normalized by $\frac{3}{2}k_B n = c_v n$, where c_v is the specific heat per particle at constant volume for an ideal gas, to make \bar{M}_{KP} dimensionless.

One disadvantage of \bar{M}_{KP} is that it is not bounded, making its interpretation difficult (Liang et al., 2020a). To remedy this, a new non-Maxwellianity measure formed from the velocity-space entropy density (Eq. C.6) was introduced (Liang et al., 2020a)

$$\bar{M} = \frac{s_{M,V} - s_V}{s_{M,V}}. \quad (\text{C.12})$$

Provided the velocity space grid is chosen appropriately, as discussed in Liang et al. (2020a), this measure is not only dimensionless, positive definite, and vanishes when the distribution is a Maxwellian (similar to \bar{M}_{KP}), but is also bounded. It can be written in terms of total entropy density s (Eq. C.7)

$$\bar{M} = \frac{s_M - s}{s_M + k_B n \ln(n/\Delta^3 v)}$$

but we will evaluate it in terms of \bar{M}_{KP} (Eq. C.11) (Liang et al., 2020a)

$$\bar{M} = \frac{\bar{M}_{KP}}{1 + \ln \left\{ (2\pi k_B T) / \left[m (\Delta^3 v)^{2/3} \right] \right\}}. \quad (\text{C.13})$$

because this allows us to isolate the effects that discretizing phase space has on our ability to measure entropy and non-Maxwellianity.

C.2 Simulation

The observed reconnection event was nearly symmetric and reasonably laminar, and previous studies employing 2.5D PIC simulations have shown good agreement with the observations (Torbert et al., 2018; Nakamura et al., 2018, 2019; Egedal et al., 2019). We therefore also employ 2.5D PIC simulations to compare with the observations. We use the massively parallel PIC code P3D (Zeiler et al., 2002), where particles are stepped forward in time using the relativistic Boris particle stepper (Birdsall & Langdon, 1991) and electromagnetic fields are stepped forward using the trapezoidal leapfrog method (Guzdar et al., 1993); the fields can have a smaller

time-step than that of the particles. P3D employs the multigrid approach to clean the electric field, \mathbf{E} , to enforce $\nabla \cdot \mathbf{E} = \rho/\epsilon_0$, where ρ is the net charge density, every 10 particle time-steps. We employ periodic boundary conditions in both directions with a large enough computational domain that the boundaries are not expected to play much of a role in the region of interest at the time examined. A motivation for choosing periodic boundary conditions over open ones is to see if the local kinetic entropy densities obtained in a closed system are representative of the local kinetic entropy obtained in the (open) real system.

The initial setup of the simulation has two Harris current sheets (CS) and a uniform background (BG) plasma population for which the density n_{BG} and temperature $T_{s,BG}$ for species s (either e for electrons or i for ions) can be chosen independently from the Harris sheet parameters. The initial magnetic field profile is $B_L(N) = B_0[\tanh[(N - l_N/4)/w_0] - \tanh[(N - 3l_N/4)/w_0] - 1]$, where B_0 is the asymptotic reconnecting magnetic field far upstream, w_0 is the half-thickness of the current sheet and l_N is the width of the computational domain in the \hat{e}_N direction. Initially, the electrons and ions in the Harris sheets have the same density profile, $n_{CS}(N) = n_0(\text{sech}^2[(N - l_N/4)/w_0] + \text{sech}^2[(N - 3l_N/4)/w_0])$, where $n_0 = B_0^2/[8\pi k_B(T_{e,CS} + T_{i,CS})]$ and $T_{s,CS}$ are the temperatures of the current sheet population for each species.

For the plasma parameters in the simulations, we employ the same values used by Nakamura et al. (2018) The upstream (lobe) magnetic field is $B_0 = 12 \text{ nT}$ and the density at the center of the initial CS is $n_0 = 0.0896 \text{ cm}^{-3}$. The electron CS temperature $T_{e,CS} = 1.053 \text{ keV} = 0.125 T_0$ and ion CS temperature $T_{i,CS} = 3 T_{e,CS}$,

where $T_0 = m_i V_{Ai0}^2 / k_B = 8.424 \text{ keV}$ and $V_{Ai0} = 875 \text{ km/s}$ is the Alfvén speed based on n_0 and B_0 . The background (lobe) electron temperature $T_{e,BG} = 0.351 \text{ keV} = 0.04167 T_0$ and the background ion temperature $T_{i,BG} = 3 T_{e,BG}$. The BG density is $n_{BG} = 0.0296 \text{ cm}^{-3} = 0.33 n_0$. These parameters result in an upstream electron Debye length of $\lambda_{De} = 0.018 d_{i0} = 1.37 \times 10^4 \text{ m}$, and upstream total beta of $\beta = 0.11$.

The speed of light c is $1.75 \times 10^4 \text{ km/s}$ which is smaller than that of Nakamura et al. (2018) but is sufficiently larger than other speeds of our system. The initial current sheet half-thickness $w_0 = 456 \text{ km} = 0.6 d_{i0}$, where $d_{i0} = c / \omega_{pi0} = 760 \text{ km}$ is the ion inertial length based on n_0 , $\omega_{pi0} = (n_0 e^2 / \epsilon_0 m_i)^{1/2}$ is the ion plasma frequency, and e is the proton charge, which is the same as in Nakamura et al. (2018). The electron to ion mass ratio is $m_e / m_i = 0.01$ which is larger than in Nakamura et al. (2018) and is a factor of 18.36 larger than the realistic value. This means the electron-to-ion inertial length ratio in the simulations is a factor of 4.28 larger than the realistic length ratio. This difference will be noted while drawing comparisons between observation and simulation results, but we do not expect that electron scale properties of the reconnection region are altered when properly normalized to a realistic value.

The length of the computational domain is $l_L = 2.66 \times 10^4 \text{ km} = 35 d_{i0}$ and its width is $l_N = 1.33 \times 10^4 \text{ km} = 17.5 d_{i0}$. The system size is smaller than that of Nakamura et al. (2018) but since the focus of our study is a trajectory which passes very close to the electron diffusion region, a smaller system size is sufficient; our system size is not large enough for ions to fully couple to the reconnected field downstream of the X-point, but this is not expected to affect dynamics at the

electron scale that are the focus of this study. The grid-length Δ in both directions = 6.5 km = 0.008545 d_{i0} , which is chosen to be smaller than the smallest length scale of the system (the electron Debye length). The time-step $\Delta t = 0.652$ ms = 0.00075 Ω_{ci0}^{-1} is chosen to be smaller than the smallest time scale of the system (the electron plasma frequency), where Ω_{ci0} is the ion cyclotron frequency based on B_0 . The time step for electromagnetic fields is half of that for the particles. There are 4096×2048 grid cells which are initialized with 100 weighted particles per grid (PPG). To initiate reconnection, an X point/O point pair are seeded in both current sheets using a weak magnetic field perturbation of the form $\delta B_L = -0.08B_0 \sin(2\pi L/l_L) \sin(4\pi N/l_N)$ and $\delta B_N = 0.08B_0[l_N/(2l_L)] \cos(2\pi L/l_L)[1 - \cos(4\pi N/l_N)]$.

Kinetic entropy is calculated in the simulations employing the implementation from Liang et al. (2019) with one noteworthy difference. The velocity-space grid scale Δv_i for ions and Δv_e for electrons was imposed to be equal to each other in previous works (Liang et al., 2019, 2020a). In the present study, we allow Δv_i and Δv_e to be chosen independently. Moreover, this study employs two populations in the initial Harris sheet profile, compared to a single drifting Maxwellian distribution in previous works. Therefore, we optimize the velocity-space grid scale analogously to the previous works, but specifically check the agreement between kinetic entropy density calculated by the simulation and the theoretical value in both the background plasma and the current sheet center simultaneously. We calculate the kinetic entropy density for each species in the simulations with varying velocity-space grids in order to find the optimal velocity-space grid scale at $t = 0$. This is an important step because if the velocity space grid is too small, the distribution is over-

resolved, meaning there is not a statistically significant number of particles per grid cell. Meanwhile, if the grid size is too large, the distribution is under-resolved and important structures are lost. The kinetic entropy density for either species is given by Eq. C.7 with $f = f_{CS} + f_{BG}$, consisting of both the current sheet and background populations at $t = 0$. Since these integrals cannot be done analytically, we carry out these integrals numerically. After we choose a (Cartesian) velocity-space grid scale for electrons, we numerically compute the entropy and compare it to the theoretical value. This results in agreement to within $\pm 1\%$ in the upstream region and $\pm 2\%$ at the center of the current sheet. The optimal velocity-space grid scale for each species is 60 – 65% of the smaller of the background and current sheet thermal speeds. For electrons, each velocity-space direction is binned from $(-1.67, 1.67) \times 10^4$ km/s = $(-18.71, 18.71) V_{Ai0}$ with 22 bins of size $\Delta v_e = 1.48 \times 10^3$ km/s = $1.7005 V_{Ai0}$. For ions, the binning range is $(-7.34, 7.34) \times 10^3$ km/s = $(-8.38, 8.38) V_{Ai0}$ with 54 bins with bin-size $\Delta v_i = 2.72 \times 10^2$ km/s = $0.3105 V_{Ai0}$.

Previous simulation studies (Liang et al., 2019, 2020a) employed a look-up table. A look-up table for the simulation is advantageous because the simulated plasma has PIC noise while the analytical expression does not. Using raw density and temperature values with an analytical expression for the Maxwellianized entropy leads to disagreement with the theoretical value. The look-up table allows comparable amounts of error in the simulated and theoretical values, which improves the agreement with theory.

For the present study, we find that unlike in Liang et al. (2020a), the results for s_M when using a look-up table are significantly different than when not using one.

The reason for the disagreement is mixing between macroparticles of different numerical weight; previous studies employed a look-up table that assumed the weights were the same for all macroparticles. As macroparticles of different weight mix, the look-up table becomes less accurate. This could be addressed by including a third axis of the look-up table to incorporate particle weight, but that is not undertaken for the present study. We therefore directly calculate s_M to get simulated values of the non-Maxwellianity parameters.

The simulation results we present are carried out with no initial out of plane (guide) magnetic field B_g . It is important to put this choice in the context of previous numerical simulations of the observed event that employed a weak initial guide field (Egedal et al., 2019; Nakamura et al., 2018). We perform and compare results from test simulations with and without a weak initial guide field of $B_g = -0.36$ nT $= -0.03B_0$. Figure C.1 shows 2D plots of the out-of-plane magnetic field component B_M , where the X-line is located at $(0, 0)$ and the separatrices are the black curves. In the presence of the weak guide field (Fig. C.1a), we find that B_M has a value of about -0.6 nT $= -0.05 B_0$ in the vicinity of the EDR. This is not seen in MMS3 data (see Figure C.2e; B_M does not become appreciably negative in the shaded region). In our simulations without an initial guide field (Fig. C.1b) we find that B_M is again negative in the vicinity of the X-line along the virtual spacecraft trajectory marked by the thick black curve, but has a smaller value of -0.24 nT $= -0.02B_0$, closer to the MMS3 observations. We find no comparable virtual trajectory in the simulation with an initial guide field that reproduces the signature of B_M observed by MMS3, so we use the $B_g = 0$ simulation for this study. Egedal et al. (2019) also used a

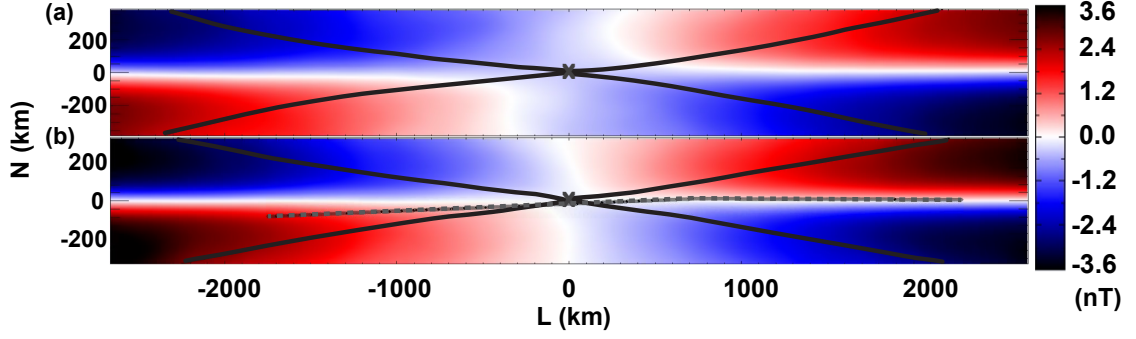


Figure C.1: Out of plane magnetic field B_M from simulations (a) with and (b) without an initial guide field of $B_g = -0.36 \text{ nT} = 0.03B_0$. The separatrices are thick black curves and the thick black line in (b) is our selected virtual spacecraft trajectory. [Associated dataset available at <https://doi.org/10.5281/zenodo.5807744>].

guide field weaker than that of Nakamura et al. (2018) for similar reasons.

Finally, we note that the virtual spacecraft trajectory is selected from a set of possible trajectories, chosen by eye (as opposed to using more systematic approaches to determine the trajectory (Nakamura et al., 2019; Egedal et al., 2019; Shuster et al., 2017)). The selected trajectory is one which produces qualitatively similar trends of magnetic field and electron flow speeds when compared with MMS3 observations. We do not anticipate significantly different values by employing more systematic approaches. In what follows, all plots are made from the lower current sheet at the simulation time of $23.4 \text{ s} = 27 \Omega_{ci0}^{-1}$, when the system has achieved a steady-state reconnection rate (not shown).

C.3 Results

C.3.1 Comparison between Observations and the PIC Simulation

Figure C.2 shows a comparison between observations (left) and the PIC simulation (right) in the same format as Figure 7 of Nakamura et al. (2018) MMS3 passed closest to the reconnection X-line and its data is plotted during the 5 second interval starting at 22:34:00 UT because this is the time interval surrounding the EDR most commonly shown in previous studies (Torbert et al., 2018; Genestreti et al., 2018; Hasegawa et al., 2019; Nakamura et al., 2018, 2019). In this study, we focus on the electron entropy in and immediately surrounding the EDR in the subinterval from 1.95 s to 3.315 s, which is highlighted by the gold box in the MMS panels. Since the structure velocity is $V_L = -170$ km/s and the electron inertial length is $d_e = 30$ km (Torbert et al., 2018), the spacecraft traversed a distance of $7.7 d_e$ during this time.

The corresponding path of the virtual spacecraft trajectory through the simulation is $5.3 d_{i0} = 30.64 d_e$ long, where (no) subscript 0 indicates that the (current sheet density, n_0) upstream density was used. This would correspond to a path length of $7.1 d_e$ in a simulation with a realistic mass ratio (with m_e 18.36 times lighter), which is nearly the same as the path length in the observations. The data is taken at a single time after the simulation has reached a steady state. We include simulation results both in normalized units (left vertical axis) and physical units (right vertical axis), the latter of which allows for a quantitative comparison with the MMS data.

Quantitatively, the density (Fig. C.2a,b); electron temperature anisotropy $A = T_{e,\parallel}/T_{e,\perp} - 1$, where $T_{e,\parallel}$ and $T_{e,\perp}$ are the electron temperatures parallel and perpendicular to the magnetic field (Fig. C.2c,d); and magnetic field (Fig. C.2e,f) are similar between observations and the simulation. The electron bulk flow (Figure C.2g,h) has similar structure but is smaller in the simulation by about a factor of 4; this is because the simulated electron mass is 18.36 times larger than the realistic value, so the electron Alfvén speed is 4.28 times smaller. The electric field components in the simulation reference frame \mathbf{E} and in the electron rest frame \mathbf{E}' (Fig. C.2i-n) all have similar profiles to the observations, but the L and N components are about 2 times smaller in amplitude in the simulations than in the observations. Similarly, the rate of energy conversion between the electric field and the electrons (Fig. C.2o,p) is a factor of about 4 lower in the simulations. We note that there is good agreement in the normalized simulation values and those presented in Nakamura et al. (2018) (see their Figure 7), so the quantitative differences with the observations seen here are consistent with previous studies. The overall agreement between the simulation and observations gives us confidence in our comparison and interpretations of entropy that follow (§C.3.2).

Some differences in density visible in Figure C.2a,b can be attributed to the trajectory of the virtual spacecraft through the simulation EDR. Along the trajectory, the density profiles both increase, but the simulation profile exhibits a local minimum not present in the observations. The density profile along a vertical cut through the EDR has a double peak with the peaks appearing just upstream of the X-line at the turning points of the meandering motion (Chen et al., 2011). If

our virtual trajectory began closer to, but still below, the central current sheet and sloped gently downward, the density profile would gradually increase as in the observations. However, the qualitative agreement between the fields and flows just described would suffer. We choose to keep this trajectory because of the importance of \mathbf{B} and \mathbf{V}_e to reconnection. We will revisit this issue when comparing entropy in the next section.

C.3.2 Kinetic Entropy: Application

We now compare observations and simulation results of kinetic entropy parameters along the satellite trajectory to a) determine if local kinetic entropy measurements in a large, open system can be interpreted in a similar manner to those of a closed system and b) draw a link between kinetic entropy and the dissipation processes of reconnection. Figure C.3 again shows the virtual satellite trajectory through the simulation domain during the gold highlighted interval, as well as a 2D snapshot of \bar{M} from Eq. C.12. We then plot total and velocity-space entropy densities s and s_V along with their associated Maxwellianized values s_M and $s_{M,V}$, and the non-Maxwellianity measures \bar{M} and \bar{M}_{KP} from both MMS (left) and the simulation (right) in the same format as Figure C.2. We note that s and s_M do not have real units on the right-axis because the units are not physical (Liang et al., 2019). From 22:34:00-1.95 (the left-edge of the gold box), MMS3 made a brief excursion into the inflow region (Torbert et al., 2018) where entropy reaches a maximum during the separatrix crossing and a minimum at the furthest excursion. During the

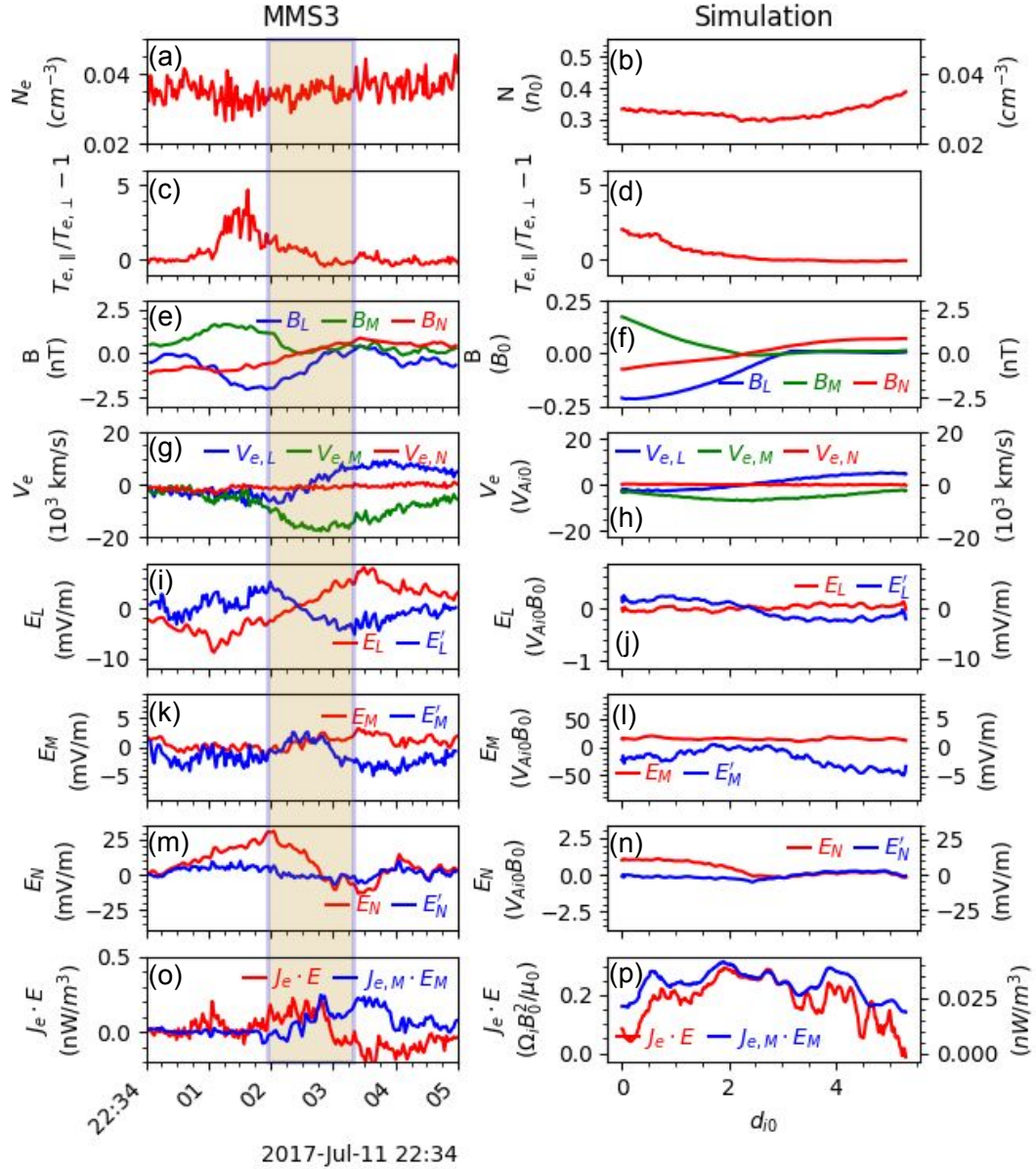


Figure C.2: Comparison between MMS observations (left) and a PIC simulation (right) of a magnetotail EDR encounter. MMS observations are shown over an extended region to provide context and comparison to previous results (see text). The gold rectangle highlights the EDR and region of overlap with simulation. Comparisons are made between (a,b) electron density, (c,d) electron temperature anisotropy, (e,f) magnetic field, (g,h) electron bulk velocity, (i-n) electric field in the spacecraft and electron rest frame, (o,p) total and M-component of the rate of energy conversion between the electric field and the electrons. Simulation data is shown in real units (right-axis) on the same scale as MMS observations with the exception of panel (p), which is much smaller in magnitude. Overall, observations and simulations are in qualitative agreement. [Associated simulation dataset available at <https://doi.org/10.5281/zenodo.5807744>]

same interval, the non-Maxwellianity peaks in the inflow region, a characteristic that has been noted in previous simulations of reconnection (Liang et al., 2020b). That non-Maxwellianity peaks outside of the regions where energy is being dissipated will be discussed below in the context of the electron distribution functions.

As MMS3 enters into the EDR (the gold box), passes southward of the X-line, and exits into the tailward exhaust, entropy density gradually increases in the observations; however, in the simulation, entropy density has a U-shaped profile with a minimum below the EDR. As expected from Eq. C.9, these traces have the same overall structure as the density profiles in Figure C.2a,i.

The non-Maxwellianity measure \bar{M}_{KP} (Eq. C.11, Fig. C.3d,g) is computed using both s (Eq. C.7, blue) and s_V (by using the version of Eq. C.6 in spherical coordinates (Argall et al., 2022), green). The MMS observations result in unphysical values within the EDR of the electron Kaufmann and Paterson non-Maxwellianity $\bar{M}_{KP,s,e}$ based on s , where it becomes negative. The Maxwellian distribution should have the highest entropy of any distribution with the same number of particles and energy, so $\bar{M}_{KP,s,e}$ should be positive. The reason $\bar{M}_{KP,s,e}$ is negative is explained in detail in Argall et al. (2022). In contrast, the electron Kaufmann and Paterson non-Maxwellianity $\bar{M}_{KP,s_V,e}$ using the velocity space entropy density s_V is always positive, consistent with theoretical constraints.

The other non-Maxwellianity measure \bar{M} (Fig. C.2d,g, orange) is computed using the appropriate version of Eq. C.12 for MMS and the simulation. It is smaller in magnitude than \bar{M}_{KP} because its normalization term s_V ensures that \bar{M} is bounded to the range [0,1] for a properly defined velocity space grid (Liang et al., 2020a).

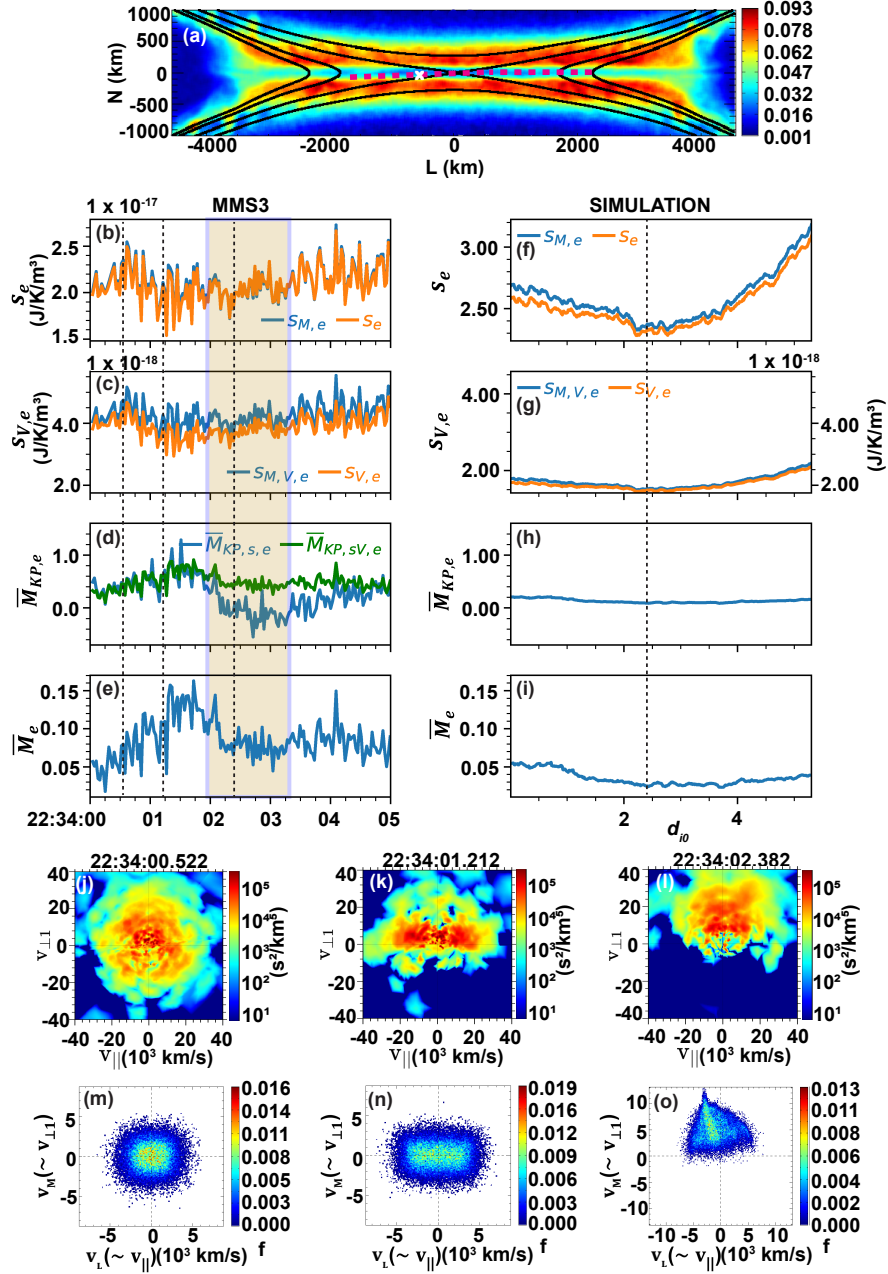


Figure C.3: Kinetic entropy and non-Maxwellianity in an EDR and their relationship to structures in the distribution function. (a) 2D plot of electron non-Maxwellianity \bar{M}_e in the PIC simulation, the virtual satellite trajectory through the EDR, representative magnetic field lines, and the location of the EDR distribution in panel o, marked by an “x”. (b,f) Total and (c,g) velocity space kinetic entropy density for the measured (orange) and Maxwellianized (blue) distributions. (d,h) Kaufmann and Paterson non-Maxwellianity \bar{M}_{KP} using total (blue) and velocity space (green) entropy density. (e,i) Velocity space non-Maxwellianity \bar{M} (orange). For (b)-(i), MMS data is in the left column and simulation data is in the right column. (j,m) Upstream, (k,n) inflow, and (l,o) EDR electron distribution functions from MMS3 (j-l) and the PIC simulation (m-o). [Associated simulation dataset available at <https://doi.org/10.5281/zenodo.5807744>].

When comparing observations to simulations, both \bar{M} and \bar{M}_{KP} have similar shapes within the EDR despite the fact that s and s_V are different. In addition, both values of \bar{M} are more similar in magnitude than the values of \bar{M}_{KP} . This implies that the local measure of kinetic entropy density s_V as measured in the closed simulation can be interpreted in the same manner as it is in the large, open magnetotail system by MMS.

Now we relate kinetic entropy measurements to various kinetic processes that occur during reconnection by examining the electron distribution functions in the MMS data (Fig. C.3j-l) and the PIC simulation (Fig. C.3m-o) at the times and locations indicated by vertical dashed lines in Figures C.3b-i and by the “x” in the EDR of Figure C.3a. The simulated distributions are on a different scale; as noted, multiplying the axes by $\sqrt{m_i/m_e} \approx 4.3$ will give the proper ranges for a real mass ratio simulation. The two simulated distributions corresponding to the MMS observations outside the EDR were taken from representative upstream locations in the simulation. The first distribution (Fig. C.3j,m) is taken from the Earthward exhaust after the electrons have re-magnetized and become mostly Maxwellian. The second distribution (Fig. C.3k,n) is from the inflow region where parallel potential structures generate a temperature anisotropy (Egedal et al., 2008, 2010). Here s_V is lower, but the non-Maxwellianity is relatively large. The third distribution (Fig. C.3l,o) is from the heart of the EDR where meandering motion in the current sheet creates crescents and striations (Ng et al., 2011; Shuster et al., 2015; Torbert et al., 2018). Here, the non-Maxwellianity is intermediate between the inflow and Maxwellian distributions. That regions of elevated non-Maxwellianity in the MMS

observations can be related to kinetic processes during reconnection is consistent with previous numerical simulations (Liang et al., 2020b) and motivates the utility of the entropy-based non-Maxwellianity measure as an indicator of kinetic-scale energy conversion and dissipation processes that occur during reconnection.

C.4 Data Availability

MMS data is publicly available at the MMS science data center (<https://lasp.colorado.edu/mms/sdc/public/>) (Burch, 2015). MMS data was processed and visualized with the help of the PyMMS Python library (Argall et al., 2020b,a). Simulation data used in this manuscript is available on Zenodo (<https://doi.org/10.5281/zenodo.5807744>)

Bibliography

- Aarseth, S. J., & Aarseth, S. J. 2003, Gravitational N-body simulations: tools and algorithms (Cambridge University Press)
- Afshari, A. S., Howes, G. G., Kletzing, C. A., Hartley, D. P., & Boardsen, S. A. 2021, Journal of Geophysical Research: Space Physics, 126, e2021JA029578, doi: 10.1029/2021JA029578
- Allred, J. C., Alaoui, M., Kowalski, A. F., & Kerr, G. S. 2020, Ap. J., 902, 16
- Angelopoulos, V. 2009, The THEMIS Mission, ed. J. L. Burch & V. Angelopoulos (New York, NY: Springer New York), 5–34, doi: 10.1007/978-0-387-89820-9_2
- Angelopoulos, V., Runov, A., Zhou, X.-Z., et al. 2013, Science, 341, 1478, doi: 10.1126/science.1236992
- Angelopoulos, V., Baumjohann, W., Kennel, C. F., et al. 1992, Journal of Geophysical Research: Space Physics, 97, 4027, doi: 10.1029/91JA02701
- Angelopoulos, V., McFadden, J. P., Larson, D., et al. 2008, Science, 321, 931, doi: 10.1126/science.1160495
- Argall, M. R., Small, C. R., & Petrik, M. 2020a, PyMMS: A Python Library for NASA's Magnetospheric Multiscale (MMS) Mission, Zenodo, doi: 10.5281/zenodo.3840766
- Argall, M. R., Small, C. R., Piatt, S., et al. 2020b, Frontiers in Astronomy and Space Sciences, 7, 54, doi: 10.3389/fspas.2020.00054

- Argall, M. R., Barbhuiya, M. H., Cassak, P. A., et al. 2022, *Physics of Plasmas*, 29, 022902, doi: 10.1063/5.0073248
- Arró, G., Califano, F., & Lapenta, G. 2022, *A&A*, 668, A33, doi: 10.1051/0004-6361/202243352
- Arzamasskiy, L., Kunz, M. W., Chandran, B. D. G., & Quataert, E. 2019, *The Astrophysical Journal*, 879, 53, doi: 10.3847/1538-4357/ab20cc
- Asai, A., Nakajima, H., Shimojo, M., et al. 2006, *Publications of the Astronomical Society of Japan*, 58, L1, doi: 10.1093/pasj/58.1.L1
- Ashour-Abdalla, M., El-Alaoui, M., Goldstein, M. L., et al. 2011, *Nature Physics*, 7, 360, doi: 10.1038/nphys1903
- Aurass, H., Mann, G., Rausche, G., & Warmuth, A. 2006, *Astronomy & Astrophysics*, 457, 681, doi: 10.1051/0004-6361:20065238
- Axford, W. I. 1984, in *Magnetic Reconnection in Space and Laboratory Plasmas*, ed. J. Edward W. Hones, *Geophysical Monograph 30* (American Geophysical Union), 1–8
- Baez, J. C., & Pollard, B. S. 2016, *Entropy*, 18, doi: 10.3390/e18020046
- Bandyopadhyay, R., Matthaeus, W. H., Parashar, T. N., et al. 2020a, *Phys. Rev. Lett.*, 124, 255101, doi: 10.1103/PhysRevLett.124.255101
- Bandyopadhyay, R., Yang, Y., Matthaeus, W. H., et al. 2020b, *Ap. J. Lett.*, 893, L25, doi: 10.3847/2041-8213/ab846e

- Bandyopadhyay, R., Chasapis, A., Matthaeus, W. H., et al. 2021, *Physics of Plasmas*, 28, 112305, doi: 10.1063/5.0071015
- Barbhuiya, M. H., Cassak, P., Shay, M., et al. 2022, *Journal of Geophysical Research: Space Physics*, 127, e2022JA030610
- Barbhuiya, M. H., & Cassak, P. A. 2022, *Physics of Plasmas*, 29, 122308, doi: 10.1063/5.0125256
- Batchelor, G. K. 2000, *An Introduction to Fluid Dynamics*, Cambridge Mathematical Library (Cambridge University Press), doi: 10.1017/CB09780511800955
- Bellan, P. M. 2008, *Fundamentals of Plasma Physics* (Cambridge University Press)
- Berthelin, F., Tzavaras, A. E., & Vasseur, A. 2009, *Journal of Statistical Physics*, 135, 153
- Bessho, N., & Bhattacharjee, A. 2005, *Phys. Rev. Lett.*, 95, doi: 10.1103/PhysRevLett.95.245001
- Bessho, N., Chen, L.-J., Shuster, J. R., & Wang, S. 2014, *Geophysical Research Letters*, 41, 8688, doi: 10.1002/2014g1062034
- Birdsall, C. K., & Langdon, A. B. 1991, *Plasma Physics via Computer Simulation* (Philadelphia: Institute of Physics Publishing)
- Birn, J., Borovsky, J. E., Hesse, M., & Schindler, K. 2010, *Phys. Plasmas*, 17, 052108
- Birn, J., Hesse, M., Nakamura, R., & Zaharia, S. 2013, *Journal of Geophysical Research: Space Physics*, 118, 1960, doi: 10.1002/jgra.50132

- Birn, J., & Priest, E., eds. 2007, Reconnection of Magnetic Fields (Cambridge University Press)
- Birn, J., Drake, J. F., Shay, M. A., et al. 2001, *J. Geophys. Res.*, 106, 3715
- Biskamp, D. 2000, *Magnetic Reconnection in Plasmas* (Cambridge, UK: Cambridge University Press)
- Boltzmann, L. 1872, *Wiener Berichte*, 66, 275
- . 1877, *Wiener Berichte*, 76, 373
- Brackbill, J. 2011, *Physics of Plasmas*, 18, 032309
- Braginskii, S. I. 1965, *Reviews of Plasma Physics*, 1, 205
- Büchner, J., & Zelenyi, L. M. 1989, *Journal of Geophysical Research: Space Physics*, 94, 11821, doi: 10.1029/JA094iA09p11821
- Burch, J. L. 2015, Data from NASA's Magnetospheric Multiscale (MMS) mission, MMS Mission. <https://lasp.colorado.edu/mms/sdc/public/>
- Burch, J. L., Moore, T. E., Torbert, R. B., & Giles, B. L. 2016a, *Space Sci. Rev.*, 199, 5
- Burch, J. L., Torbert, R. B., Phan, T. D., et al. 2016b, *Science*, 352, 6290
- Caspi, A. 2010, PhD thesis, University of California, Berkeley
- Caspi, A., Krucker, S., & Lin, R. P. 2014, *Ap. J.*, 781, 43

- Caspi, A., & Lin, R. P. 2010, *Ap. J. Lett.*, 725, L161
- Caspi, A., Shih, A. Y., McTiernan, J. M., & Krucker, S. 2015, *Ap. J. Lett.*, 811, L1
- Cassak, P. A., & Barbhuiya, M. H. 2022, *Physics of Plasmas*, 29, 122306, doi: 10.1063/5.0125248
- Cassak, P. A., Barbhuiya, M. H., Liang, H., & Argall, M. R. 2023, *Physical Review Letters*, 130, 085201, doi: 10.1103/PhysRevLett.130.085201
- Cassak, P. A., Barbhuiya, M. H., & Weldon, H. A. 2022, *Physics of Plasmas*, 29, 122307, doi: 10.1063/5.0125252
- Cassak, P. A., & Shay, M. A. 2007, *Phys. Plasmas*, 14, 102114
- . 2008, *Geophys. Res. Lett.*, 35, L19102
- Cerri, S., Kunz, M. W., & Califano, F. 2018, *The Astrophysical Journal Letters*, 856, L13
- Cerri, S. S., Grošelj, D., & Franci, L. 2019, *Frontiers in Astronomy and Space Sciences*, 6, 64, doi: 10.3389/fspas.2019.00064
- Chan Eu, B. 2006, *The Journal of Chemical Physics*, 125, 064110, doi: 10.1063/1.2208360
- Chapman, S., & Cowling, T. G. 1970, *The mathematical theory of non-uniform gases. an account of the kinetic theory of viscosity, thermal conduction and diffusion in gases*, 3rd edn. (Cambridge University Press)

- Chasapis, A., Yang, Y., Matthaeus, W. H., et al. 2018, *The Astrophysical Journal*, 862, 32, doi: 10.3847/1538-4357/aac775
- Chen, C. H. K., Klein, K. G., & Howes, G. G. 2019, *Nature Communications*, 10, 740
- Chen, F. F. 1974, *Introduction to Plasma Physics* (Plenum Press)
- Chen, L.-J., Daughton, W. S., Lefebvre, B., & Torbert, R. B. 2011, *Physics of Plasmas*, 18, 012904, doi: 10.1063/1.3529365
- Cheung, M. C. M., Rempel, M., Chintzoglou, G., et al. 2019, *Nature Astronomy*, 3, 160, doi: 10.1038/s41550-018-0629-3
- Chew, G. F., Goldberger, M. L., & Low, F. E. 1956, *Proceedings of the Royal Society of London. Series A. Mathematical and Physical Sciences*, 236, 112, doi: 10.1098/rspa.1956.0116
- Choi, S., Bessho, N., Wang, S., Chen, L.-J., & Hesse, M. 2022, *Physics of Plasmas*, 29, 012903, doi: 10.1063/5.0059884
- Clausius, R. 1850, *Annalen der Physik*, 155, 500, doi: 10.1002/andp.18501550403
- Cozzani, G., Retinò, A., Califano, F., et al. 2019, *Phys. Rev. E*, 99, 043204, doi: 10.1103/PhysRevE.99.043204
- Dafermos, C. M. 1979, *Archive for Rational Mechanics and Analysis*, 70, 167, doi: 10.1007/BF00250353

- Dal Pino, E. d. G., Piovezan, P., & Kadowaki, L. 2010, *Astronomy & Astrophysics*, 518, A5
- Daughton, W., & Karimabadi, H. 2007, *Phys. Plasmas*, 14, doi: 10.1063/1.2749494
- Del Sarto, D., & Pegoraro, F. 2018, *MNRAS*, 475, 181, doi: doi:10.1093/mnras/stx3083
- Del Sarto, D., Pegoraro, F., & Califano, F. 2016, *Physical Review E*, 93, 053203, doi: 10.1103/PhysRevE.93.053203
- Deng, X., Ashour-Abdalla, M., Zhou, M., et al. 2010, *Journal of Geophysical Research: Space Physics*, 115, A09225, doi: 10.1029/2009JA015107
- Diperna, R. J. 1979, *Indiana University Mathematics Journal*, 28, 137. <http://www.jstor.org/stable/24892290>
- Divin, A. V., Sitnov, M. I., Swisdak, M., & Drake, J. F. 2007, *Geophys. Res. Lett.*, 34, 09109, doi: 10.1029/2007GL029292
- Du, S., Guo, F., Zank, G. P., Li, X., & Stanier, A. 2018, *Ap. J.*, 867, 16, doi: 10.3847/1538-4357/aae30e
- Du, S., Zank, G. P., Li, X., & Guo, F. 2020, *Phys. Rev. E*, 101, 033208, doi: 10.1103/PhysRevE.101.033208
- Dungey, J. W. 1953, *Phil. Mag.*, 44, 725
- . 1958, *Cosmic Electrodynamics* (Cambridge University Press)

- Eastwood, J., Goldman, M., Phan, T., et al. 2020, Physical Review Letters, 125, 265102, doi: 10.1103/PhysRevLett.125.265102
- Eastwood, J. P., Phan, T. D., Drake, J. F., et al. 2013, Physical Review Letters, 110, 225001, doi: 10.1103/PhysRevLett.110.225001
- Egedal, J., Fox, W., Katz, N., et al. 2008, Journal of Geophysical Research: Space Physics, 113, A12207, doi: 10.1029/2008JA013520
- Egedal, J., Le, A., & Daughton, W. 2013, Physics of Plasmas, 20, 061201, doi: 10.1063/1.4811092
- Egedal, J., Lê, A., Zhu, Y., et al. 2010, Geophysical Research Letters, 37, L10102, doi: 10.1029/2010GL043487
- Egedal, J., Ng, J., Le, A., et al. 2019, Physical Review Letters, 123, doi: 10.1103/physrevlett.123.225101
- Egedal, J., Wetherton, B., Daughton, W., & Le, A. 2016, Physics of Plasmas, 23, 122904, doi: 10.1063/1.4972135
- Egedal, J., Le, A., Daughton, W., et al. 2018, Phys. Rev. Lett., 120, 055101, doi: 10.1103/PhysRevLett.120.055101
- Eu, B. C. 1995, The Journal of chemical physics, 102, 7169
- Evans, D. J., & Hoover, W. G. 1986, Annual Review of Fluid Mechanics, 18, 243, doi: 10.1146/annurev.fl.18.010186.001331

- Eyink, G. L. 2018, *Phys. Rev. X*, 8, 041020
- Fadanelli, S., Lavraud, B., Califano, F., et al. 2021, *Journal of Geophysical Research: Space Physics*, 126, e2020JA028333, doi: 10.1029/2020JA028333
- Fletcher, L., Dennis, B. R., Hudson, H. S., et al. 2011, *Space Science Reviews*, 159, 19, doi: 10.1007/s11214-010-9701-8
- Floerchinger, S., & Haas, T. 2020, *Phys. Rev. E*, 102, 052117, doi: 10.1103/PhysRevE.102.052117
- Fu, H., Grigorenko, E. E., Gabrielse, C., et al. 2020, *Sci. China Earth Sci.*, 63, 235, doi: 10.1007/s11430-019-9551-y
- Fu, H. S., Khotyaintsev, Y. V., André, M., & Vaivads, A. 2011, *Geophysical Research Letters*, 38, L16104, doi: 10.1029/2011GL048528
- Fu, H. S., Khotyaintsev, Y. V., Vaivads, A., André, M., & Huang, S. Y. 2012a, *Geophysical Research Letters*, 39, L10101, doi: 10.1029/2012GL051784
- Fu, H. S., Khotyaintsev, Y. V., Vaivads, A., et al. 2012b, *Journal of Geophysical Research: Space Physics*, 117, A12221, doi: 10.1029/2012JA018141
- Fu, H. S., Cao, J. B., Khotyaintsev, Y. V., et al. 2013, *Geophysical Research Letters*, 40, 6023, doi: 10.1002/2013GL058620
- Fujimoto, K., & Sydora, R. D. 2008, *Geophysical Research Letters*, 35, doi: 10.1029/2008GL035201

- Gary, S. P., & Madland, C. D. 1985, *Journal of Geophysical Research: Space Physics*, 90, 7607, doi: 10.1029/JA090iA08p07607
- Genestreti, K. J., Nakamura, T. K. M., Nakamura, R., et al. 2018, *Journal of Geophysical Research: Space Physics*, 123, 9130, doi: 10.1029/2018JA025711
- Giannios, D. 2010, *Monthly Notices of the Royal Astronomical Society: Letters*, 408, L46, doi: 10.1111/j.1745-3933.2010.00925.x
- Giovanelli, R. G. 1947, *MNRAS*, 107, 338
- Gonzalez, W., & Parker, E. 2016, *Magnetic Reconnection* (Springer)
- Grad, H. 1965, *Journal of the Society for Industrial and Applied Mathematics*, 13, 259
- Grandy, W. 2004, *Foundations of Physics*, 34, 21, doi: 10.1023/B:F00P.0000012008.36856.c1
- Greco, A., Valentini, F., Servidio, S., & Matthaeus, W. 2012, *Physical Review E*, 86, 066405
- Grigorenko, E. E., Malykhin, A. Y., Shklyar, D. R., et al. 2020, *Journal of Geophysical Research: Space Physics*, 125, e2020JA028268, doi: 10.1029/2020JA028268
- Grošelj, D., Cerri, S. S., Navarro, A. B., et al. 2017, *The Astrophysical Journal*, 847, 28, doi: 10.3847/1538-4357/aa894d
- Guo, X., Sironi, L., & Narayan, R. 2017, *The Astrophysical Journal*, 851, 134

- Guzdar, P. N., Drake, J. F., McCarthy, D., Hassam, A. B., & Liu, C. S. 1993, *Phys. Fluids B*, 5, 3712
- Haggerty, C. C., Shay, M. A., Drake, J. F., Phan, T. D., & McHugh, C. T. 2015, *Geophysical Research Letters*, 42, 9657, doi: 10.1002/2015GL065961
- Hallatschek, K. 2004, *Physical review letters*, 93, 125001
- Harris, E. G. 1962, *Nuovo Cimento*, 23, 115
- Hasegawa, H., Denton, R. E., Nakamura, R., et al. 2019, *Journal of Geophysical Research: Space Physics*, 124, 122, doi: 10.1029/2018JA026051
- Hazeltine, R. D., Mahajan, S. M., & Morrison, P. J. 2013, *Physics of Plasmas*, 20, 022506, doi: 10.1063/1.4793735
- Hazeltine, R. D., & Waelbroeck, F. L. 2018, *The framework of plasma physics* (CRC Press)
- Hellinger, P., Montagud-Camps, V., Franci, L., et al. 2022, *Ap. J.*, 930, 48
- Hesse, M., & Birn, J. 1991, *Journal of Geophysical Research: Space Physics*, 96, 19417, doi: 10.1029/91JA01953
- . 1992, *J. Geophys. Res.*, 97, 10643
- Hesse, M., Kuznetsova, M., & Hoshino, M. 2002, *Geophys. Res. Lett.*, 29, 1563
- Hesse, M., Neukirch, T., Schindler, K., Kuznetsova, M., & Zenitani, S. 2011, *Space Sci. Rev.*, 160, 3

- Hesse, M., & Zenitani, S. 2007, *Phys. Plasmas*, 14, 112102
- Holman, G. D., Aschwanden, M. J., Aurass, H., et al. 2011, *Space Science Reviews*, 159, 107, doi: 10.1007/s11214-010-9680-9
- Hoshino, M., Mukai, T., Terasawa, T., & Shinohara, I. 2001, *J. Geophys. Res.*, 106, 25,979
- Howes, G. G. 2017, *Physics of Plasmas*, 24, 055907, doi: 10.1063/1.4983993
- Howes, G. G., Cowley, S. C., Dorland, W., et al. 2006, *The Astrophysical Journal*, 651, 590
- Howes, G. G., Klein, K. G., & Li, T. C. 2017, *Journal of Plasma Physics*, 83
- Howes, G. G., McCubbin, A. J., & Klein, K. G. 2018, *Journal of Plasma Physics*, 84
- Huang, K., Lu, Q., Lu, S., Wang, R., & Wang, S. 2021, *Journal of Geophysical Research: Space Physics*, 126, e2021JA029939, doi: 10.1029/2021JA029939
- Huang, S. Y., Zhang, J., Sahraoui, F., et al. 2020, *Ap. J. Lett.*, 898, L18, doi: 10.3847/2041-8213/aba263
- Hwang, K.-J., Goldstein, M. L., Lee, E., & Pickett, J. S. 2011, *Journal of Geophysical Research: Space Physics*, 116, doi: 10.1029/2010JA015742
- Jaeger, H. M., & Liu, A. J. 2010, arXiv preprint arXiv:1009.4874

- Jara-Almonte, J., & Ji, H. 2021, *Phys. Rev. Lett.*, 127, 055102, doi: 10.1103/PhysRevLett.127.055102
- Jarzynski, C. 1997, *Phys. Rev. Lett.*, 78, 2690, doi: 10.1103/PhysRevLett.78.2690
- Jaynes, E. T. 1963, *Information Theory and Statistical Mechanics*, In: K. Ford, Ed., *Statistical Physics* (New York: Benjamin), 181
- Jou, D., Lebon, G., & Casas-Vázquez, J. 2010, *Extended Irreversible Thermodynamics*, 4th edn. (Springer, Dordrecht)
- Jun, G., & Quan-Ming, L. 2007, *Chinese Physics Letters*, 24, 3199
- Juno, J., Howes, G. G., TenBarge, J. M., et al. 2021, *Journal of Plasma Physics*, 87
- Kadomtsev, B. B. 1975, *Sov. J. Plasma Phys.*, 1, 389
- Karplus, M., & Petsko, G. A. 1990, *Nature*, 347, 631
- Kaspi, V. M., & Beloborodov, A. M. 2017, *Annual Review of Astronomy and Astrophysics*, 55, 261, doi: 10.1146/annurev-astro-081915-023329
- Kaufmann, R. L., & Paterson, W. R. 2009, *J. Geophys. Res.*, 114, A00D04
- Kawazura, Y., Barnes, M., & Schekochihin, A. A. 2019, *PNAS*, 116, 771
- Klein, K. G. 2017, *Physics of Plasmas*, 24, 055901
- Klein, K. G., & Howes, G. G. 2016, *The Astrophysical Journal Letters*, 826, L30
- Klein, K. G., Howes, G. G., & TenBarge, J. M. 2017, *Journal of Plasma Physics*, 83

- Klein, K. G., Howes, G. G., TenBarge, J. M., & Valentini, F. 2020, *Journal of Plasma Physics*, 86
- Krucker, S., Hudson, H. S., Glesener, L., et al. 2010, *Ap. J.*, 714, 1108, doi: 10.1088/0004-637X/714/2/1108
- Kullback, S., & Leibler, R. A. 1951, *The annals of mathematical statistics*, 22, 79
- Kuznetsova, M. M., Hesse, M., & Winske, D. 1998, *J. Geophys. Res.*, 103, 199
- Landau, L. 1936, *Collected papers of LD Landau*, 163
- Laperre, B., Amaya, J., & Lapenta, G. 2022, *Phys. Plasmas*, 29, 032706
- Le, A., Egedal, J., Daughton, W., Fox, W., & Katz, N. 2009, *Phys. Rev. Lett.*, 102, 085001
- Le Contel, O., Roux, A., Jacquy, C., et al. 2009, *Annales Geophysicae*, 27, 2259, doi: 10.5194/angeo-27-2259-2009
- Lembege, B., & Pellat, R. 1982, *Phys. Fluids*, 25, 1995
- Li, H., Zhou, M., Deng, X., et al. 2015, *Journal of Geophysical Research: Space Physics*, 120, 1086, doi: 10.1002/2014JA020474
- Li, T. C., Howes, G. G., Klein, K. G., Liu, Y.-H., & TenBarge, J. M. 2019, *Journal of Plasma Physics*, 85
- Liang, H., Barbhuiya, M. H., Cassak, P. A., et al. 2020a, *Journal of Plasma Physics*, 86, 825860502, doi: 10.1017/S0022377820001270

- Liang, H., Cassak, P. A., Swisdak, M., & Servidio, S. 2020b, *Journal of Physics: Conference Series*, 1620, 012009, doi: 10.1088/1742-6596/1620/1/012009
- Liang, H., Cassak, P. A., Servidio, S., et al. 2019, *Physics of Plasmas*, 26, 082903, doi: 10.1063/1.5098888
- Lidar, D. A. 2020, arXiv preprint arXiv:1902.00967v2
- Liu, C. M., & Fu, F. S. 2019, *Ap. J. Lett.*, 873, L2
- Liu, C. M., Fu, H. S., Cao, J. B., et al. 2017a, *Geophysical Research Letters*, 44, 10,116, doi: 10.1002/2017GL075007
- Liu, C. M., Fu, H. S., Xu, Y., Cao, J. B., & Liu, W. L. 2017b, *Geophysical Research Letters*, 44, 6492, doi: 10.1002/2017GL074029
- Liu, C. M., Fu, H. S., Xu, Y., et al. 2018, *Geophysical Research Letters*, 45, 4628, doi: 10.1029/2018GL077928
- Liu, Y.-H., Cassak, P., Li, X., et al. 2022, *Communications Physics*, 5, 1, doi: 10.1038/s42005-022-00854-x
- Livadiotis, G. 2018, *Europhysics Letters*, 122, 50001, doi: 10.1209/0295-5075/122/50001
- Longcope, D. W., & Guidoni, S. 2011, *Ap. J.*, 740, 73
- Longcope, D. W., Jardins, A. C. D., Carranza-Fulmer, T., & Qiu, J. 2010, *Solar Phys.*, 267, 107

- Longcope, D. W., Qiu, J., & Brewer, J. 2016, *Ap. J.*, 833, 211
- Lu, S., Angelopoulos, V., & Fu, H. 2016, *Journal of Geophysical Research: Space Physics*, 121, doi: 10.1002/2016JA022815
- Lynden-Bell, D. 1967, *Monthly Notices of the Royal Astronomical Society*, 136, 101, doi: 10.1093/mnras/136.1.101
- Lyutikov, M. 2003, *Monthly Notices of the Royal Astronomical Society*, 346, 540
- . 2006, *Mon. Not. Astron. Soc.*, 367, 1594
- Ma, W., Zhou, M., Zhong, Z., & Deng, X. 2020, *Ap. J.*, 903, 84
- Mandt, M. E., Denton, R. E., & Drake, J. F. 1994, *Geophys. Res. Lett.*, 21, 73
- Matsumoto, Y., Amano, T., Kato, T., & Hoshino, M. 2015, *Science*, 347, 974
- Matthaeus, W. H., & Lamkin, S. L. 1986, *Phys. Fluids*, 29, 2513
- Matthaeus, W. H., Yang, Y., Wan, M., et al. 2020, *Astrophys. J.*, 891, 101
- McPherron, R. L. 1979, *Reviews of Geophysics*, 17, 657, doi: 10.1029/RG017i004p00657
- Min, K., & Liu, K. 2016, *Journal of Geophysical Research: Space Physics*, 121, 475, doi: 10.1002/2015ja022042
- Montag, P., & Howes, G. G. 2022, *Physics of Plasmas*, 29, 032901
- Mouhot, C., & Villani, C. 2011, *Acta Math.*, 207, 29, doi: 10.1007/s11511-011-0068-9

- Nakamura, R., Genestreti, K. J., Nakamura, T., et al. 2019, *Journal of Geophysical Research: Space Physics*, 124, 1173, doi: 10.1029/2018JA026028
- Nakamura, T. K. M., Genestreti, K. J., Liu, Y.-H., et al. 2018, *Journal of Geophysical Research: Space Physics*, 123, 9150, doi: 10.1029/2018JA025713
- Ng, J., Egedal, J., Le, A., Daughton, W., & Chen, L.-J. 2011, *Phys. Rev. Lett.*, 106, 65002, doi: 10.1103/PhysRevLett.106.065002
- Ohtani, S.-i., Shay, M. A., & Mukai, T. 2004, *Journal of Geophysical Research: Space Physics*, 109, doi: 10.1029/2003JA010002
- Onsager, L. 1931, *Phys. Rev.*, 37, 405, doi: 10.1103/PhysRev.37.405
- Pan, Q., Ashour-Abdalla, M., El-Alaoui, M., Walker, R. J., & Goldstein, M. L. 2012, *Journal of Geophysical Research: Space Physics*, 117, A12224, doi: 10.1029/2012JA018156
- Parashar, T. N., & Gary, S. P. 2019, *The Astrophysical Journal*, 882, 29, doi: 10.3847/1538-4357/ab2fc8
- Parashar, T. N., Matthaeus, W. H., & Shay, M. A. 2018, *The Astrophysical Journal*, 864, L21, doi: 10.3847/2041-8213/aadb8b
- Parker, E. N. 1957, *J. Geophys. Res.*, 62, 509
- . 1963, *Ap. J.*, 8, 177
- Patrikalakis, N. M., & Maekawa, T. 2002, *Shape interrogation for computer aided design and manufacturing*, Vol. 15 (Springer)

- Pezzi, O., Servidio, S., Perrone, D., et al. 2018, *Physics of Plasmas*, 25, 060704
- Pezzi, O., Yang, Y., Valentini, F., et al. 2019, *Physics of Plasmas*, 26, 072301,
doi: 10.1063/1.5100125
- Pezzi, O., Liang, H., Juno, J. L., et al. 2021, *MNRAS*, 505, 4857, doi: 10.1093/
mnras/stab1516
- Phan, T. D., Gosling, J. T., Davis, M. S., et al. 2006, *Nature*, 439, 175
- Pollock, C., Moore, T., Jacques, A., et al. 2016, *Space Sci. Rev.*, 199, 331
- Popielawski, J., & Gorecki, J. 1991, *Far-from-Equilibrium Dynamics of Chemical Systems* (World Scientific), doi: 10.1142/1307
- Priest, E., & Forbes, T. 2000, *Magnetic Reconnection* (Cambridge University Press)
- Priest, E. R., & Forbes, T. R. 2002, *Astron. Astrophs. Rev.*, 10, 313
- Prigogine, I. 1978, *Science*, 201, 777
- Pritchett, P. L. 2013, *Phys. Plasmas*, 20, 080703
- Pulkkinen, T. 2007, *Living Reviews in Solar Physics*, 4, 1, doi: 10.12942/
lrsp-2007-1
- Qi, Y., Strangeway, R., Russell, C., et al. 2019, in *Geophysical Research Abstracts*,
Vol. 21
- Qiu, J., Longcope, D. W., Cassak, P. A., & Priest, E. R. 2017, *Ap. J.*, 838, 17

- Reeves, K. K., Guild, T. B., Hughes, W. J., et al. 2008, *J. Geophys. Res.*, 113, A00B02
- Retinò, A., Sundkvist, D., Vaivads, A., et al. 2007, *Nature Physics*, 3, 235, doi: 10.1038/nphys574
- Ricci, P., Lapenta, G., & Brackbill, J. 2002, *Geophysical research letters*, 29, 3
- Richardson, A. S. 2019, 2019 NRL plasma formulary, Tech. rep., US Naval Research Laboratory
- Robertson, J. C., Tallman, E. W., & Whiteman, C. H. 2005, *Journal of Money, Credit, and Banking*, 37, 383
- Rogers, A. J., Farrugia, C. J., Torbert, R. B., & Rogers, T. J. 2021, Applying Magnetic Curvature to MMS data to identify thin current sheets relative to tail reconnection, arXiv, doi: 10.48550/ARXIV.2112.04646
- Rowan, M. E., Sironi, L., & Narayan, R. 2019, *The Astrophysical Journal*, 873, 2, doi: 10.3847/1538-4357/ab03d7
- Roytershteyn, V., & Delzanno, G. L. 2018, *Frontiers in Astronomy and Space Sciences*, 5
- Runov, A., Angelopoulos, V., Gabrielse, C., et al. 2015, *Journal of Geophysical Research: Space Physics*, 120, 4369, doi: 10.1002/2015JA021166
- . 2013, *Journal of Geophysical Research: Space Physics*, 118, 744, doi: 10.1002/jgra.50121

- Runov, A., Angelopoulos, V., Zhou, X.-Z., et al. 2011, *Journal of Geophysical Research: Space Physics*, 116, doi: 10.1029/2010JA016316
- Runov, A., Angelopoulos, V., Sitnov, M. I., et al. 2009, *Geophysical Research Letters*, 36, doi: 10.1029/2009GL038980
- Runov, A., Angelopoulos, V., Sitnov, M., et al. 2010, *Planetary and Space Science*, 59, 517, doi: 10.1016/j.pss.2010.06.006
- Sakurai, J. J. 1994, *Modern quantum mechanics; rev. ed.* (Reading, MA: Addison-Wesley). <https://cds.cern.ch/record/1167961>
- Schaller, G. 2014, *Open Quantum Systems Far from Equilibrium* (Springer International Publishing)
- Schekochihin, A., Cowley, S., Dorland, W., et al. 2009, *The Astrophysical Journal Supplement Series*, 182, 310
- Schmid, D., Volwerk, M., Nakamura, R., Baumjohann, W., & Heyn, M. 2011, *Annales Geophysicae*, 29, 1537, doi: 10.5194/angeo-29-1537-2011
- Schmid, D., Nakamura, R., Volwerk, M., et al. 2016, *Geophysical Research Letters*, 43, 6012, doi: 10.1002/2016GL069520
- Servidio, S., Matthaeus, W. H., Shay, M. A., Cassak, P. A., & Dmitruk, P. 2009, *Phys. Rev. Lett.*, 102, 115003, doi: 10.1103/PhysRevLett.102.115003
- Servidio, S., Valentini, F., Califano, F., & Veltri, P. 2012, *Phys. Rev. Lett.*, 108, 045001, doi: 10.1103/PhysRevLett.108.045001

- Servidio, S., Chasapis, A., Matthaeus, W., et al. 2017, *Physical review letters*, 119, 205101
- Sharma Pyakurel, P., Shay, M. A., Phan, T. D., et al. 2019, *Physics of Plasmas*, 26, 082307, doi: 10.1063/1.5090403
- Shay, M. A., Drake, J. F., Denton, R. E., & Biskamp, D. 1998, *Journal of Geophysical Research: Space Physics*, 103, 9165, doi: 10.1029/97JA03528
- Shay, M. A., Drake, J. F., Rogers, B. N., & Denton, R. E. 1999, *Geophys. Res. Lett.*, 26, 2163
- . 2001, *J. Geophys. Res.*, 106, 3751
- Shay, M. A., Haggerty, C. C., Phan, T. D., et al. 2014, *Phys. Plasmas*, 21, 122902
- Shell, M. S. 2008, *The Journal of chemical physics*, 129, 144108
- Shi, P., Srivastav, P., Barbhuiya, M. H., et al. 2022a, *Physical Review Letters*, 128, 025002, doi: 10.1103/PhysRevLett.128.025002
- . 2022b, *Physics of Plasmas*, 29, 032101, doi: 10.1063/5.0082633
- Shuster, J. R., Chen, L.-J., Hesse, M., et al. 2015, *Geophysical Research Letters*, 42, 2586, doi: 10.1002/2015GL063601
- Shuster, J. R., Chen, L.-J., Daughton, W. S., et al. 2014, *Geophysical Research Letters*, 41, 5389, doi: 10.1002/2014gl060608

- Shuster, J. R., Argall, M. R., Torbert, R. B., et al. 2017, *Geophysical Research Letters*, 44, 1625, doi: 10.1002/2017GL072570
- Shuster, J. R., Gershman, D. J., Chen, L.-J., et al. 2019, *Geophysical Research Letters*, 46, 7862, doi: 10.1029/2019GL083549
- Shuster, J. R., Gershman, D. J., Dorelli, J. C., et al. 2021, *Nature Phys.*, 17, 1056, doi: 10.1038/s41567-021-01280-6
- Sitnov, M. I., Buzulukova, N., Swisdak, M., Merkin, V. G., & Moore, T. E. 2013, *Geophys. Res. Lett.*, 40, 22, doi: 10.1029/2012GL054701
- Sitnov, M. I., Merkin, V. G., Roytershteyn, V., & Swisdak, M. 2018, *Geophys. Res. Lett.*, 45, 4639
- Sitnov, M. I., Merkin, V. G., Swisdak, M., et al. 2014, *Journal of Geophysical Research: Space Physics*, 119, 7151, doi: 10.1002/2014JA020205
- Sitnov, M. I., & Swisdak, M. 2011, *J. Geophys. Res.*, 116, 12216, doi: 10.1029/2011JA016920
- Sitnov, M. I., Swisdak, M., & Divin, A. V. 2009, *Journal of Geophysical Research: Space Physics*, 114, doi: 10.1029/2008JA013980
- Smith, A. W., Jackman, C. M., Thomsen, M. F., et al. 2018, *Journal of Geophysical Research: Space Physics*, 123, 2714, doi: 10.1002/2017JA024904
- Song, L., Zhou, M., Yi, Y., et al. 2020, *Journal of Geophysical Research: Space Physics*, 125, e2020JA028278, doi: 10.1029/2020JA028278

- Sonnerup, B. U. Ö. 1979, in *Solar System Plasma Physics*, ed. L. J. Lanzerotti, C. F. Kennel, & E. N. Parker, Vol. 3 (North Halland Pub., Amsterdam), 46
- Speiser, T. W. 1965, *Journal of Geophysical Research (1896-1977)*, 70, 4219, doi: 10.1029/JZ070i017p04219
- Struik, D. J. 1961, *Lectures on classical differential geometry* (Courier Corporation)
- Sweet, P. A. 1958, in *Electromagnetic Phenomena in Cosmical Physics*, ed. B. Lehnert (Cambridge University Press, New York), 123
- Swisdak, M. 2016, *Geophysical Research Letters*, 43, 43, doi: 10.1002/2015GL066980
- Tang, C. L., Wang, X., & Zhou, M. 2021, *Journal of Geophysical Research: Space Physics*, 126, e2020JA028787, doi: 10.1029/2020JA028787
- Tatsuno, T., Dorland, W., Schekochihin, A., et al. 2009, *Physical review letters*, 103, 015003
- Torbert, R. B., Burch, J. L., Phan, T. D., et al. 2018, *Science*, 362, 1391, doi: 10.1126/science.aat2998
- Trottenberg, U., Oosterlee, C. W., & Schuller, A. 2000, *Multigrid* (Academic Press, San Diego)
- Tzavaras, A. E. 2005, *Communications in Mathematical Sciences*, 3, 119

- Umeda, T., Ashour-Abdalla, M., Schriver, D., Richard, R. L., & Coroniti, F. V. 2007, *Journal of Geophysical Research: Space Physics*, 112, doi: 10.1029/2006JA012124
- Uzdensky, D. A. 2011, *Space Science Reviews*, 160, 45, doi: 10.1007/s11214-011-9744-5
- Vasyliunas, V. M. 1975, *Rev. Geophys.*, 13, 303
- Vedral, V. 2002, *Reviews of Modern Physics*, 74, 197
- Verniero, J., Howes, G., Stewart, D., & Klein, K. 2021, *Journal of Geophysical Research: Space Physics*, 126, e2020JA028940
- Viberg, H., Khotyaintsev, Y. V., Vaivads, A., et al. 2014, *Journal of Geophysical Research: Space Physics*, 119, 2605, doi: 10.1002/2014JA019892
- Vlasov, A. A. 1968, *Soviet Physics Uspekhi*, 10, 721, doi: 10.1070/PU1968v010n06ABEH003709
- Vocks, C., & Mann, G. 2006, *Astronomy & Astrophysics*, 452, 331, doi: 10.1051/0004-6361:20054042
- Von Neumann, J. 1927, *Nachrichten von der Gesellschaft der Wissenschaften zu Göttingen, Mathematisch-Physikalische Klasse*, 1927, 273
- Wang, K., Lin, C.-H., Wang, L.-Y., et al. 2014, *Journal of Geophysical Research: Space Physics*, 119, 9747, doi: 10.1002/2014JA020176

- Wang, L., Hakim, A. H., Bhattacharjee, A., & Germaschewski, K. 2015, *Physics of Plasmas*, 22, 012108
- Wang, S., Chen, L., Bessho, N., et al. 2016, *Journal of Geophysical Research: Space Physics*, 121, 2104, doi: 10.1002/2015ja021892
- Wang, Y., Bandyopadhyay, R., Chhiber, R., et al. 2021, *Journal of Geophysical Research: Space Physics*, 126, e2020JA029000, doi: 10.1029/2020JA029000
- Warmuth, A., & Mann, G. 2016, *Astronomy and Astrophysics*, 588, A115, doi: 10.1051/0004-6361/201527474
- Wilder, F. D., Ergun, R. E., Burch, J. L., et al. 2018, *Journal of Geophysical Research: Space Physics*, 123, 6533, doi: 10.1029/2018JA025529
- Winske, D., & Daughton, W. 2012, *Physics of Plasmas*, 19, 072109, doi: 10.1063/1.4736983
- Wu, C. S., Yoon, P. H., & Freund, H. P. 1989, *Geophysical Research Letters*, 16, 1461, doi: 10.1029/g1016i012p01461
- Wu, M., Lu, Q., Volwerk, M., et al. 2013, *Journal of Geophysical Research: Space Physics*, 118, 4804, doi: 10.1002/jgra.50456
- Wu, P., Fritz, T. A., Larvaud, B., & Lucek, E. 2006, *Geophysical Research Letters*, 33, L17101, doi: 10.1029/2006GL026595
- Xu, S. B., Huang, S. Y., Yuan, Z. G., et al. 2021, *Geophysical Research Letters*, 48, e2021GL092701, doi: 10.1029/2021GL092701

- Xu, Y., Fu, H. S., Liu, C. M., & Wang, T. Y. 2018, *Ap. J.* , 853, 11
- Yamada, M., Levinton, F. M., Pomphrey, N., et al. 1994, *Phys. Plasmas*, 1, 3269
- Yamada, M., Yoo, J., Jara-Almonte, J., et al. 2014, *Nature Communications*, 5, 4774, doi: 10.1038/ncomms5774
- Yang, Y., Matthaeus, W. H., Roy, S., et al. 2022, *The Astrophysical Journal*, 929, 142, doi: 10.3847/1538-4357/ac5d3e
- Yang, Y., Wan, M., Matthaeus, W. H., et al. 2019a, *Physics of Plasmas*, 26, 072306, doi: 10.1063/1.5099360
- . 2019b, *Monthly Notices of the Royal Astronomical Society*, 482, 4933, doi: 10.1093/mnras/sty2977
- Yang, Y., Matthaeus, W. H., Parashar, T. N., et al. 2017a, *Phys. Rev. E*, 95, 061201, doi: 10.1103/PhysRevE.95.061201
- . 2017b, *Physics of Plasmas*, 24, 072306, doi: 10.1063/1.4990421
- Yin, L., & Winske, D. 2003, *Physics of Plasmas*, 10, 1595
- Yoo, J., Wang, S., Yerger, E., et al. 2019, *Physics of Plasmas*, 26, 052902, doi: 10.1063/1.5094636
- Yuen, K. H., & Lazarian, A. 2020, *Ap. J.*, 898, 66, doi: 10.3847/1538-4357/ab9360
- Zeiler, A., Biskamp, D., Drake, J. F., et al. 2002, *J. Geophys. Res.*, 107, 1230, doi: 10.1029/2001JA000287

- Zenitani, S., Hesse, M., Klimas, A., & Kuznetsova, M. 2011, *Phys. Rev. Lett.*, 106, 195003
- Zhao, M. J., Fu, H. S., Liu, C. M., et al. 2019, *Geophysical Research Letters*, 46, 2390, doi: 10.1029/2019GL082100
- Zhdankin, V. 2022a, *Phys. Rev. X*, 12, 031011, doi: 10.1103/PhysRevX.12.031011
- . 2022b, *Journal of Plasma Physics*, 88, doi: 10.1017/s0022377822000551
- Zhdankin, V., Uzdensky, D. A., Werner, G. R., & Begelman, M. C. 2019, *Phys. Rev. Lett.*, 122, 055101, doi: 10.1103/PhysRevLett.122.055101
- Zhong, Z. H., Deng, X. H., Zhou, M., et al. 2019, *Geophysical Research Letters*, 46, 12693, doi: 10.1029/2019GL085409
- Zhou, M., Man, H., Yang, Y., Zhong, Z., & Deng, X. 2021, *Geophysical Research Letters*, 48, e2021GL096372, doi: 10.1029/2021GL096372